

Corrosion Behavior of Alloys in Molten Fluoride Salts

By

Guiqiu Zheng

A dissertation submitted in partial fulfillment of
the requirements for the degree of

Doctor of Philosophy
(Materials Science)

at the

UNIVERSITY OF WISCONSIN-MADISON

2015

Date of final oral examination: 4/17/2015

The dissertation is approved by the following members of the Final Oral Committee:

Kumar Sridharan, Distinguished Research Professor, Engineering Physics
Todd Allen, Professor, Engineering Physics
Dane Morgan, Professor, Materials Science and Engineering
Chang-Beom Eom, Professor, Materials Science and Engineering
Xudong Wang, Associate Professor, Materials Science and Engineering

© Copyright by Guiqiu Zheng, 2015

All Rights Reserved

Acknowledgements

First of all, I would like to acknowledge that this work was supported by the grant from the U.S. Department of Energy Nuclear Energy University Program under Contract No. DE-AC07-05ID14517, and the high purity FLiBe salt used in this study was provided by Oak Ridge National Laboratory.

I would like to express my sincere gratitude to my advisor, Distinguished Research Professor Kumar Sridharan, and co-advisor Professor Todd Allen, for their inspiring guidance and consistent support throughout the pursuit of PhD degree in past five and half years, and for their effort on reviewing papers and this dissertation. I also thank Professor Dane Morgan, Professor Chang-Beom Eom and Professor Xudong Wang for serving as my committee members and providing invaluable suggestions on my dissertation.

I would also like to thank Research Professor Mark Anderson and Instrument Specialist Paul Brooks for their design guidance in the fabrication of molten salt facilities, and for their smart ideas to setup and to troubleshoot high temperature control systems. I would like to thank Brian Kelleher for his assistance in molten salt handling and chemistry measurement, thank Dr. Guoping Cao, Dr. Lingfeng He and Dr. Bin Leng for preparing samples and assistance in microscopic analysis, thank Dr. Beata Tyburska-Püschel, Kim Kriewaldt, Alexander Mairov and Sam Briggs for their help on irradiation experiments, thank undergraduate students Josh Greife, Jon King, Kieran Dolan, Neil Roberts and Nickolas Trocinski for sample preparation and characterization, thank staff in Materials Science Center and the Department of Engineering Physics.

I would like to express my appreciation to my parents for their spiritual support and best wishes, and to my lovely wife, Suhong Yu, for her unconditional support and for her love that always cheers me up.

Finally, I would like to mention my son Andrew who was born in Madison during my PhD studies and has brought great happiness and joy into my life. His charming smile always encourages me to pursue my dream without fear.

Abstract

The molten fluoride salt-cooled high-temperature nuclear reactor (FHR) has been proposed as a candidate Generation IV nuclear reactor. This reactor combines the latest nuclear technology with the use of molten fluoride salt as coolant to significantly enhance safety and efficiency. However, an important challenge in FHR development is the corrosion of structural materials in high-temperature molten fluoride salt. The structural alloys' degradation, particularly in terms of chromium depletion, and the molten salt chemistry are key factors that impact the lifetime of nuclear reactors and the development of future FHR designs. In support of materials development for the FHR, the nickel base alloy of Hastelloy N and iron-chromium base alloy 316 stainless steel are being actively considered as critical structural alloys. Enriched 2^7LiF-BeF_2 (named as FLiBe) is a promising coolant for the FHR because of its neutronic properties and heat transfer characteristics while operating at atmospheric pressure. In this study, the corrosion behavior of Ni-5Cr and Ni-20Cr binary model alloys, and Hastelloy N and 316 stainless steel in molten FLiBe with and without graphite were investigated.

Due to the toxicity of beryllium in FLiBe and the hygroscopicity of fluoride salts in general, molten salt experiments are inherently challenging in regards to experimental design, data acquisition, and safety. A series of preparatory apparatus and facilities were successfully built for safely preparing and handling fluoride salts as well as performing corrosion tests. These facilities at present are unique to the University of Wisconsin-Madison and have been used to successfully complete corrosion tests in molten FLiBe.

The corrosion tests of model binary Ni-5Cr and Ni-20Cr alloys in molten FLiBe were performed in pure nickel capsules at 700°C for exposure durations of up to 1000 hours. Notable intergranular corrosion attack was observed in these alloys largely by way of Cr depletion of the alloys into the molten salt. Cr depletion was accompanied by a shrinkage in the lattice parameter of the alloys, with the higher Cr alloys exhibiting greater shrinkage. K-alpha x-ray photoelectron spectroscopy (XPS) identified the Cr concentration on the corrosion surface to be zero which provided the boundary condition for long-term

corrosion prediction. Crystallographic analysis suggested that the coincident sites lattice (CSL) grain boundaries especially for $\Sigma 3$ s are resistant to the Cr depletion in molten fluoride salt.

Hastelloy N was also tested in molten FLiBe at 700°C for up to 1000 hours, in both pure nickel and graphite capsules. In the nickel capsule tests, the alloy was attacked to approximately 3.5 μm depth by way of dealloying of Cr, and developed an about 200nm porous structure. In tests performed in graphite capsules, the samples gained weight due to the formation of Cr_3C_2 , Cr_7C_3 , Mo_2C and Cr_{23}C_6 carbide phases on the surface and in the subsurface regions of the alloy. An approximately 1.4 μm thick Ni_3Fe layer devoid of Cr depletion was also observed. The Cr_{23}C_6 carbide containing layer extended to about 7 μm in depth underneath the Ni_3Fe layer. Graphite in molten salt accelerated alloy corrosion, but the formation of Cr_{23}C_6 phase might stabilize Cr and mitigate its dissolution in molten FLiBe salt in long term.

Finally, 316 stainless steel, an ASME code certified alloy for the use in nuclear energy systems, was tested in molten FLiBe in both 316 stainless steel and graphite capsules at 700°C for an exposure durations up to 3000 hours. The use of graphite crucible accelerated chromium depletion from alloy by a factor of two deeper than those tested in 316 stainless steel capsules, and promoted the formation of Cr_7C_3 , Mo_2C , and Al_4C_3 particulate phases in corrosion layer. Regardless of the crucible materials, MoSi_2 phase formed on surface due to increased activity of Mo and Si as a result of Cr depletion, and furthermore the massive Cr removal from alloy induced a γ -austenite to α -ferrite phase transformation. Crystallographic analysis suggested that Cr preferentially depleted along random high angle grain boundaries (15-180°), and CSL $\Sigma 3$ s grain boundaries were immune to Cr depletion. From the fitting profiles, the corrosion attack depths of 17.1 $\mu\text{m}/\text{year}$ and 31.2 $\mu\text{m}/\text{year}$ were predicted for 316 stainless steel tested in 316 stainless steel and in graphite capsules, respectively.

Based on the understanding of the corrosion behavior and data of above four alloys in molten FLiBe, a long-term corrosion prediction model has been developed that is applicable specifically for these four materials in FLiBe at 700°C. The model uses Cr concentration profile $C(x, t)$ as a function of corrosion distance in the materials and duration fundamentally derived from the Fick's diffusion laws. This model was validated with reasonable accuracy for the four alloys by fitting the calculated profiles with

experimental data and can be applied to evaluate corrosion attack depth over the long-term. The critical constant of the overall diffusion coefficient (D_{eff}) in this model can be quickly calculated from the experimental measurement of alloys' weight loss due to Cr depletion. While many factors affect the D_{eff} such as the grain boundary type, grain size, precipitates, initial Cr concentration as well as temperature, this model provides a methodology for estimating corrosion attack depth of alloys in molten fluoride salts obviating the need for difficult and challenging experiment.

Table of Contents

Acknowledgements.....	i
Abstract.....	ii
List of Figures.....	ix
List of Tables	xvii
Chapter 1: Introduction	1
1.1 Historical perspective on molten salt reactors	2
1.2 Selection of molten fluoride salts.....	6
1.3 Materials challenges in molten fluoride salt-cooled reactor	7
1.4 Corrosion mechanisms of alloys in molten fluoride salt.....	9
1.4.1 Thermodynamics of corrosion reactions	9
1.4.2 Impurity-driven corrosion	11
1.4.3 Temperature gradient-driven corrosion	14
1.4.4 Dissimilar materials corrosion.....	18
1.4.5 Redox potential controlled corrosion	19
1.4.6 Fission products-driven corrosion.....	20
1.5 Corrosion control	21
1.6 Experimental techniques in molten salt corrosion research	22
1.7 Prediction of Cr depletion in alloys	24
Chapter 2: Experimental procedures.....	31
2.1 Fluoride salts preparation.....	31
2.1.1 Experimental challenges associated with molten fluoride salt	31
2.1.2 Pre-drying salts.....	32
2.1.3 Preparation of KF-ZrF ₄	33
2.1.4 Preparation of FLiNaK	34
2.1.5 Preparation of FLiBe.....	35
2.2 Test samples preparation.....	39
2.2.1 Ni-5Cr and Ni-20Cr model alloys.....	39
2.2.2 Hastelloy N	41
2.2.3 316 stainless steel	41
2.2.4 Ceramics and graphite samples	42
2.3 High temperature corrosion tests	44

2.3.1 Assisting facilities for corrosion tests in FLiBe	44
2.3.2 Practice of high temperature corrosion tests in KF-ZrF ₄	48
2.3.3 Ni-Cr model alloys corrosion in FLiBe	49
2.3.4 Structural materials corrosion in FLiBe	51
2.4 Post-corrosion examination	53
2.4.1 Weight change	54
2.4.2 Microstructural characterization	54
2.4.3 Size distribution of graphite particles in FLiBe.....	57
Chapter 3: Results and discussion.....	58
3.1 Corrosion of Ni-Cr model alloys in high temperature FLiBe	58
3.1.1 Overview	58
3.1.2 Characterization methods.....	60
3.1.3 Microstructure of pre-corrosion alloys	60
3.1.4 Surface morphology of annealed alloys.....	61
3.1.5 Cross-sectional microstructure of annealed alloys.....	63
3.1.6 Weight change of post-corrosion alloys	66
3.1.7 Cr depletion induced lattice parameter change	68
3.1.8 Surface morphology of post-corrosion alloys	71
3.1.9 Cross-sectional microstructure of post-corrosion alloys	72
3.1.10 Cr depletion distance in post-corrosion alloys	76
3.1.11 Texture analysis of post-corrosion alloys.....	77
3.1.12 Effect of crystallographic orientation on Cr depletion	79
3.1.13 Chemical state of Cr on post-corrosion alloys surface.....	84
3.1.14 Discussion about Cr depletion approach in Ni-Cr alloys	86
3.1.15 Summary	89
3.2 Corrosion of Hastelloy N in high temperature FLiBE	91
3.2.1 Overview	91
3.2.2 Characterization methods.....	92
3.2.3 Weight change	93
3.2.4 Surface morphology of post-corrosion Hastelloy N.....	94
3.2.5 Elemental analysis on corrosion surface.....	95
3.2.6 XRD analysis on corrosion surface	96

3.2.7 Microstructural instability of Hastelloy N at high temperature	97
3.2.8 Microstructure of FIB milled cross-section	99
3.2.9 Carbide particles formed within Hastelloy N	101
3.2.10 Cross-sectional microstructure of post-corrosion Hastelloy N	102
3.2.11 Quantitative analysis of graphite effect on Hastelloy N corrosion	104
3.2.12 Kinetics of carbides formation	107
3.2.13 Summary	108
3.3 Corrosion of 316 stainless steel in high temperature FLiBe	109
3.3.1 Overview	109
3.3.2 Characterization methods	111
3.3.3 Weight change	112
3.3.4 Observation on corrosion surface	113
3.3.5 Microstructure of particulate phase on corrosion surface	115
3.3.6 XRD analysis on corrosion surface	116
3.3.7 Cr depletion induced phase transformation	118
3.3.8 Cross-sectional microstructure	119
3.3.9 Intergranular corrosion attack in alloy	120
3.3.10 Quantitative analysis of Cr depletion	123
3.3.11 Prediction of corrosion attack depth	124
3.3.12 Grain boundary dependence of Cr depletion	125
3.3.13 Microstructure of carbides formed within alloy	127
3.3.14 Thermodynamics of carbides formation	130
3.3.15 Redox potential effect on corrosion	133
3.3.16 Summary	134
3.4 Discussion	135
3.4.1 Thermal diffusion controlled corrosion model (TDCCM)	135
3.4.2 Validation of TDCCM	142
3.4.3 Effect of grain boundary precipitates on Cr depletion	145
3.4.4 Effect of crystallographic texture on the alloys corrosion	147
3.4.5 Effect of graphite on the alloys corrosion	149
Chapter 4 Conclusions	151
Chapter 5 Future work	154

5.1 Irradiation effect on alloys corrosion in molten salt	154
5.2 Redox potential controlled corrosion tests	158
Bibliography	161

List of Figures

Figure 1: Schematic illustration of FHR presenting inside construction of reactor core and entire system. Arrows denote flow direction of molten salt in reactor core. Inset shows the structure of pebble fuel[10].	2
Figure 2: Multiple criteria for molten salt selection in nuclear reactors[23].	7
Figure 3: Schematic illustration of FHR cross-section showing the various structural materials of interests[2].	8
Figure 4: Comparison of tensile ductility of MSRE surveillance specimen and control Hastelloy N as function of temperature at a strain rate of 0.05 min^{-1} [33].	9
Figure 5: Gibbs free energy of formation of various fluorides at 700°C .	10
Figure 6: Photograph of a thermal convection corrosion loop constructed with Hastelloy N (courtesy ORNL).	15
Figure 7: Weight change as a function of exposure time for Hastelloy N specimens exposed to MSRE fuel salt at 566 , 635 and 704°C in thermal convection corrosion loop 21A[45].	16
Figure 8: Schematic of temperature gradient mass transfer in a convection loop constructed with Hastelloy N[53].	17
Figure 9: Cross-sectional SEM images and EDS maps of 316 stainless steel specimens exposed to KCl-MgCl_2 in different crucible materials[38].	18
Figure 10: Weight change results of type 316 stainless steel samples exposed to the corrosion loop filled with LiF-BeF_2 (66-34 mole%) salt with and without Be addition.	20
Figure 11: (left) Fuel pebble and TRISO fuel particle and (right) cross-section of fissioned TRISO particle indicating excellent fission products retention at the temperature up to 1800°C [61].	21
Figure 12: Three different diffusion models showing A, B and C regimes kinetic proposed by Harrison.	26
Figure 13: Schematic illustration of molten salt reactor and TRISO fuel. Red arrows denote the irradiation.	29
Figure 14: Flow chart presenting the effects on alloys corrosion behavior in molten fluoride salt at high temperature.	30
Figure 15: Fluoride salts pre-drying system.	33
Figure 16: Salt prepared at the University of Wisconsin laboratory: (a) Laboratory made 20kg KF-ZrF_4 in SiC-coated tank, (b) bulk salt and (c) salt chunks stored in glass jars.	34

Figure 17: Salt prepared at laboratory (a) 10kg FLiNaK bulk and (b) salt chunks stored in glass jars.	34
Figure 18: Modified glove box for handling FLiBe and for conducting corrosion tests in molten FLiBe.	36
Figure 19: As-received BeF ₂ nuggets and LiF (puffy powder), and laboratory made non-purified FLiBe at room temperature.	37
Figure 20: Purified ORNL FLiBe in (a) liquid state and (b) solid state in pure nickel tray.	38
Figure 21: Be reduced ORNL FLiBe in solid state in pure nickel tray.	39
Figure 22: Polished Ni-5Cr and Ni-20Cr coupons.	40
Figure 23: 2MeV proton irradiated 316 stainless steel. Blue yellow area denotes the proton irradiated region.	42
Figure 24: (a) Tyranno-SA3 CVI SiC-SiC composite and (b) FMI222 C-C composite, provided by Oak Ridge National Laboratory	43
Figure 25: (a) IG-110U and A3-27 nuclear grade graphite and (b) TRISO particles with ZrO ₂ surrogate as kernel.	44
Figure 26: Molten fluoride salt transferring system.	45
Figure 27: Molten fluoride salt dripping system.	46
Figure 28: Graphite corrosion crucible (left) before and (right) after re-melting FLiNaK salt in six cylindrical capsules.	47
Figure 29: Temperature profiles showing the temperature difference from top to bottom of temperature gradient heating rod, and a picture of tested heating rod.	48
Figure 30: (a) Cut away schematic drawing and (b) picture of double-walled corrosion crucible mainly composing of pure nickel inner container and 316 stainless steel outer canister, (c) pure nickel sample holder with five attached samples.	49
Figure 31: (a) Schematic diagram of annealing and corrosion tests in furnace, (b) pure nickel corrosion crucible, (c) pendent coupons under fixture of nickel wire for corrosion tests in FLiBe and (d) sealed coupons in Ar filled quartz tubes for annealing experiments.	50
Figure 32: (a) annealed Ni-5Cr and (b) annealed Ni-20Cr alloys in Ar filled quartz tubes at 700°C for 50, 500 and 1000 hours, (c) FLiBe-exposed Ni-20Cr and Ni-5Cr samples that were cleaned in deionized water.	51
Figure 33: (a, b) FS-1 stage and (c, d) FS-2 stage of structural materials corrosion tests in FLiBe, without and with graphite lids on top.	52

Figure 34: Post-corrosion samples collection system, consisting of 316 stainless steel container with four pins and a stainless steel mesh.	53
Figure 35: Geometry of the sample setup for EBSD measurement. ND, RD, and TD denote normal direction, rolling direction, transverse direction, respectively.	56
Figure 36: (a) Optical image (b) SEM image (c) EBSD auto grain image and (d) grain size distribution of Ni-5Cr alloy before corrosion testing.	61
Figure 37: (a) Optical image (b) SEM image (c) EBSD auto grain image and (d) grain size distribution of as-received Ni-20Cr alloy before corrosion testing.	61
Figure 38: Surface SEM images of (a, b, c) Ni-5Cr and (d, e, f) Ni-20Cr samples annealed at 700°C for 50, 500 and 1000 hours respectively. Inset on upper right corner is high magnification SEM image clearly presenting microstructural features.	62
Figure 39: Cross-sectional SEM images of (a, b, c) Ni-5Cr and (d, e, f) Ni-20Cr annealed at 700°C for 50, 500 and 1000 hours respectively.	63
Figure 40: EDS mapping of Cr, O, Ni and Cu element in the near surface layer of (a) Ni-5Cr and (b) Ni-20Cr. Both were annealed at 700°C for 1000 hours.	64
Figure 41: Quantitative analysis of the Cr and O concentration profile in the near surface of Ni-5Cr sample annealed at 700°C for 1000 hours.	65
Figure 42: Weight loss as a function of square root of the corrosion time for Ni-5Cr (blue) and Ni-20Cr (red) alloys that were exposed to molten FLiBe at 700°C for 50, 500 and 1000 hours. Linear trend lines (dashed lines) and R-squared values are included for both alloys.	68
Figure 43: XRD patterns of Ni-5Cr alloy surface before (blue) and after (red) corrosion test in molten FLiBe for 1000 hours. A part of blue pattern ($2\theta=50^\circ-80^\circ$) was zoomed in to present the existence of (200) and (220) peak.	69
Figure 44: XRD patterns of Ni-20Cr alloy surface before (blue) and after (red) corrosion tests in molten FLiBe for 1000 hours. A vertical dashed line was added on (111) peak to emphasize peak shift between two patterns.	70
Figure 45: Calculated lattice parameters (pm) vs. extrapolation function ($\cos^2\theta/\sin^2\theta + \cos^2\theta/\theta$) of Ni-5Cr and Ni-20Cr before and after corrosion tests in molten FLiBe for 1000 hours.	71
Figure 46: Surface SEM images of (a, b, c) Ni-5Cr and (d, e, f) Ni-20Cr tested in molten FLiBe for 50, 500 and 1000 hours (from left to right) respectively. Inset on upper right corner shows the morphology of grain boundaries.	72

- Figure 47: Cross-sectional SEM images of (a, b, c) Ni-5Cr and (d, e, f) Ni-20Cr exposed to molten FLiBe for 50, 500 and 1000 hours. A layer of Cu was electroplated on all samples surface for edge protection during polishing. Arrow denotes corrosion surface. 73
- Figure 48: EDS mapping of Cr, Ni and Cu elemental distribution in the near surface layer of the Ni-5Cr samples tested in molten FLiBe for (a) 50 hours, (b) 500 hours and (c) 1000 hours..... 74
- Figure 49: EDS mapping of Cr, Ni and Cu elemental distribution in the near surface layer of the Ni-20Cr samples tested in molten FLiBe for (a) 50 hours, (b) 500 hours and (c) 1000 hours..... 75
- Figure 50: Cross-sectional SEM image of (a) annealed Ni-20Cr with 50 hours, (b) (c) and (d) post-corrosion Ni-20Cr in molten FLiBe for 50 hours, 500 hours and 1000 hours respectively. The mechanically polished cross-section was further chemically etched in a solution (45ml HCl+15ml HNO₃+20ml methanol) for 15 seconds..... 76
- Figure 51: Cr depletion distance as a function of corrosion time. All data were collected from EDS Cr mappings and from the calculations in Table 7. 77
- Figure 52: EBSD (a) auto grain, (b) inverse pole figure overlapped grain boundaries distribution, (c) grain size distribution and (d) distribution of misorientation angle relative to [001] on the cross-section of near surface layer of Ni-5Cr that was exposed to molten FLiBe for 1000 hours. 78
- Figure 53: EBSD (a) auto grain, (b) inverse pole figure overlapped grain boundaries distribution, (c) grain size distribution and (d) distribution of misorientation angle relative to [001] on the cross-section of near surface layer of Ni-20Cr that was exposed to molten FLiBe for 1000 hours. 79
- Figure 54: EBSD inverse pole figure [001] in the cross-section of FLiBe-exposed Ni-5Cr for 1000 hours, EDS maps in the red dashed line framed area, and 3-D crystallographic orientation of the specific grains labeled in EBSD image. 80
- Figure 55: Misorientation angle relative to reference direction [001] for grains 1, 2, 3 and 4 labeled in EBSD image. 50 spots were randomly selected within each grain for this analysis..... 81
- Figure 56: (a) EBSD inverse pole figure [001] with grain boundary map (blue line: 15°-180° regular grain boundary; orange line: CSL Σ 3), (b) cross-sectional SEM image, (c) Ni and Cr concentration profiles (wt.%) along the EDS line scanning path labeled in (a, b), and (d) EDS Cr map in the same area as EBSD and SEM for the Ni-20Cr tested in molten FLiBe for 1000 hours..... 82
- Figure 57: (a) EBSD inverse pole figure relative to [001] direction and (b) SEM image in the same area as EBSD. The lattice orientation and Kikuchi patterns on three individual grains are presented..... 83
- Figure 58: K-alpha XPS Cr-2p spectra of as-received Ni-20Cr (black), post-corrosion Ni-20Cr (red) and post-corrosion Ni-5Cr (blue) after testing in molten FLiBe for 1000 hours, focusing on the range of Cr binding energy from 570ev to 595ev. 85

Figure 59: (a) Cleaned surface after soaking in deionized water for 24 hours and (b) further ultrasonically cleaned surface for the FLiBe-exposed Ni-20Cr for 1000 hours. 86

Figure 60: Cr concentration profiles (EDS line-scan) in Ni-5Cr alloys that were exposed to molten FLiBe for 50, 500 and 1000 hours. 87

Figure 61: Cr concentration profiles (EDS line-scan) in Ni-20Cr alloys that were exposed to molten FLiBe for 50, 500 and 1000 hours. 87

Figure 62: Schematic illustration of Cr concentration profile in Ni-5Cr and Ni-20Cr during corrosion in molten FLiBe. 88

Figure 63: Typical Cr depletion at local region nearby grain boundary due to the formation of Cr_{23}C_6 precipitate. 89

Figure 64: (a) Purified Li-enriched FLiBe salt at room temperature used in this study and (b) depictions of graphite crucible used in this study for conducting corrosion tests. Pure nickel liner was inserted into the compartments in effect providing a nickel containment for the corrosion test. 93

Figure 65: (a) Hastelloy N samples after corrosion testing in FLiBe salt in nickel and graphite capsule at 700°C for 1000 hours. (b), (c) and (d) SEM images showing surface morphology of Hastelloy N before and after corrosion tests in nickel and graphite capsules, respectively. 95

Figure 66: EDS elemental mappings of Hastelloy N corrosion surface after testing molten FLiBe in nickel (a, scale bar 25 μm) and in graphite capsule (b, scale bar 2.5 μm). 96

Figure 67: X-ray diffraction patterns of the near-surface regions of Hastelloy N (a) as-received condition, and (b) and (c) after corrosion testing in FLiBe salt at 700°C for 1000 hours in nickel and graphite capsule, respectively. 97

Figure 68: Cross-sectional SEM images and EDS mappings showing the Mo rich precipitates and the elemental distribution of Mo, Si and Ni of as-received and annealed Hastelloy N samples. Annealing temperature was 850°C. Scale bar is 10 μm 99

Figure 69: SEM images showing corrosion surface and FIB milled cross section underneath framed area (orange line) for the Hastelloy N tested in FLiBe salt at 700°C for 1000 hours in (a, b) nickel capsule and (c, d) graphite capsule, respectively. 101

Figure 70: STEM images and EDS mapping showing the microstructure features in near-surface layer of the Hastelloy N tested in graphite capsule. (a) full view of a FIB lift-out sample, (b) a region in near-surface layer with TEM diffraction patterns in region 1 of Ni_3Fe layer and region 2 of Hastelloy N matrix, (c) close view of nanosized carbide particles within Hastelloy N matrix, and (d) quantitative elemental mapping (C, Cr, Mn, Fe, Mo, Si, Ti and Ni) of a particle marked by a square. 102

Figure 71: SEM-EDS analysis of Hastelloy N samples tested in (a) nickel capsule and (b) graphite capsule. Cu coating was electroplated on sample surface prior to polishing. Yellow dashed arrows in cross-sectional SEM images denote the traces of EDS line-scan. 104

Figure 72: Quantitative concentration profiles of the main elements in the near-surface of Hastelloy N tested in pure nickel capsule. 106

Figure 73: Quantitative concentration profiles of main elements in the near-surface of Hastelloy N tested in graphite capsule. 107

Figure 74: Gibbs free energy of formation (ΔG) of carbides per mole carbon as a function of temperature, calculating with HSC7.0. 108

Figure 75: Weight measurements for 316 stainless steel samples tested at 700°C in molten FLiBe salt in 316 stainless steel and graphite corrosion capsules (two samples in each capsule) as a function of square root of corrosion time. 113

Figure 76: Surface SEM images of 316 stainless steel samples after corrosion testing under different conditions. a, b, and c in 316 stainless steel capsules, and d, e, and f in graphite capsules for 1000, 2000, and 3000 hours, respectively. 114

Figure 77: EDS maps showing Mo-rich precipitates on the corrosion surface of 316 stainless steel samples tested in (a) 316 stainless steel lined capsule and (b) graphite capsule after 3000 hours exposure to molten FLiBe salt at 700°C. 115

Figure 78: High magnification (20,000 \times) SEM images of the 316 stainless steel sample's corrosion surface after corrosion testing in (a) 316 stainless steel capsule and (b) graphite capsule for 3000 hour. Mo denotes Mo-rich phase and GB denotes grain boundary. 116

Figure 79: XRD patterns collected from the surface of (a) as-received 316 stainless steel, (b) 316 stainless steel tested in a graphite capsule, and (c) 316 stainless steel tested in a 316 stainless steel capsule. (b) and (c): both tested for 3000 hours. 117

Figure 80: XRD patterns scanned on (a) the original corrosion surface tested in 316 stainless steel capsule for 3000 hours, (b) the surface after grinding down 5 μ m to 10 μ m below the original surface of the sample in (a), and (c), the surface after grinding down 45 μ m to 50 μ m below original corrosion surface of the sample in (a). Photographs on right side show the XRD scanned surface. 118

Figure 81: Cross-sectional SEM images of 316 stainless steel samples after corrosion tests; (a), (b), and (c) tested in 316 stainless steel capsules, and (d), (e) and (f) tested in graphite capsules for 1000, 2000, and 3000 hours respectively. Please note that samples in (c) and (f) were electroplated a Cu layer for edge protection. 120

Figure 82: EDS maps showing Cr distribution in near surface layer of corroded 316 stainless steel samples: (a), (b), and (c) tested in 316 stainless steel capsules and (d), (e), and (f) tested in graphite

capsules at 700°C for 1000, 2000, and 300 hours. Maximum Cr depletion distance was labeled in each EDS Cr map.	122
Figure 83: Main elements Cr, Fe and Ni concentration profiles in the near-surface region of 316 stainless steel samples (a) tested in 316 stainless steel capsule and (b) tested in graphite capsule for 3000 hours.	123
Figure 84: The depth of corrosion attack, in terms of maximum Cr depletion depth, as a function of corrosion time. Experimental data is indicated by a solid line, while the fit is indicated by the dashed line. The fit predicted 17.1µm/year of corrosion in 316 stainless steel capsules and 31.2µm/year in graphite capsules.	125
Figure 85: (a) cross-sectional SEM image, (b-d) EDS Cr, Fe and Ni map and (e-h) EBSD images in same near-to-surface area of 316 stainless steel tested in graphite capsule for 1000 hours. (e) grain distribution, (f) inverse polar figure [001], (g) α phase (red) distribution and (h) grain boundary and α phase maps overlapped on image quality (blue lines and orange lines denote 15-180° and $\Sigma 3$ grain boundaries respectively).	127
Figure 86: STEM images of a 316 stainless steel tested in graphite capsule for 3000 hours, (a) STEM image, (b) and (c) STEM images on a specific location framed in (a), and (d) STEM image on a triple grain boundary junction framed in (b).	129
Figure 87: STEM image and EDS spectra corresponding to the red digit 1, 2, 3 and 4 in STEM image. Primary metallic matrix element is highlighted in each EDS spectrum.	130
Figure 88: (a) solution of the FLiBe salt collected from graphite corrosion capsule (0.173g salt in 60 ml deionized water), (b) filtered graphite particles (denoted with red arrows) from the solution and (c) particle size distribution of the graphite in FLiBe salt.	131
Figure 89: Schematic representation of the 316 stainless steel corrosion processes in molten FLiBe in 316 stainless steel capsule and in graphite capsule materials.	132
Figure 90: Surface SEM image, cross-sectional SEM image and EDS Cr mapping of 316 stainless steel sample tested in (a, b, c) purified FLiBe and (d, e, f) Be metal reduced FLiBe salt in graphite crucible at 700°C for 1000 hours.	133
Figure 91: Schematic illustration of conventional thermal diffusion of infinite diffusion source in infinite medium, and the Cr depletion from the alloy into the molten fluoride salts.	137
Figure 92: Typical concentration profiles of (a) conventional thermal diffusion for the cases with infinite diffusion source through infinite medium, and (b) molten salt corrosion induced Cr depletion profiles by the means of outward diffusion from alloy into molten salt.	140
Figure 93: Cr depletion profiles of the four alloys investigated in this study as a function of the distance, calculated using the TDCCM.	142

Figure 94: Comparison of calculated and experimental (averaged) Cr depletion profiles for Ni-5Cr, Ni-20Cr, 316 stainless steel and Hastelloy N in molten FLiBe at 700°C.....	143
Figure 95: Cross-sectional SEM images focusing on the grain boundaries in the bulk alloy: (a) Ni-5Cr, (b) Ni-20Cr, (c) 316 stainless steel, and (d) Hastelloy N. All samples exposed to molten FLiBe at 700°C for 1000 hours.....	147
Figure 96: (a) Inverse pole figure (IPF) to [001] after rotating -90° about RD axis, (b) pole figure (PF) and (c) misorientation profile along the red arrow trace labeled in (a) for the Ni-20Cr sample tested in molten FLiBe at 700°C for 1000 hours. Grain boundaries distribution map overlapped on IPF, blue lines denote high angle regular grain boundaries (15°-180°), and orange lines denote CSL $\Sigma 3$ grain boundaries.	148
Figure 97: (a) Profile of displacement per atom (dpa) vs. depth and (b) 2 dimensions tracing path of incident protons showing the radiation damage distribution in 316 stainless steel, calculated using The Stopping and Range of Ions in Matter (SRIM, 2010) with Quick Kinchin-Peace calculation mode.	155
Figure 98: (a) two 316 stainless steel samples mounted on Mo plates on stage, (b) assembled sample holder and aperture on stage, and (c) samples loaded into beam line chamber equipped with assisting facilities of cooling system and IR camera.	156
Figure 99: (a) Schematic illustration diagram of corrosion experiment for testing irradiated samples, (b) irradiated 316 stainless steel samples and (c) 316 stainless steel liner for conducting corrosion tests of irradiated and non-irradiated 316 stainless steels in molten FLiBe at 700°C.	157
Figure 100: Diagram of redox potential controlled corrosion system.	159
Figure 101: (a) 3D schematic drawing of redox potential controlled corrosion system, (b) prepared corrosion system in furnace, and (c) corrosion setup with reference voltage measurement and external power supply connection.	160

List of Tables

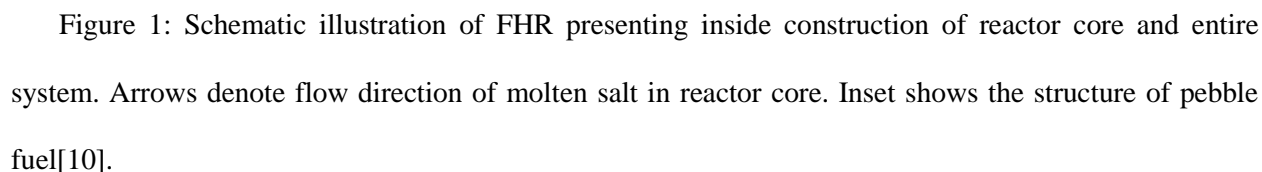
Table 1: Development history of molten salt-related nuclear reactors.	5
Table 2: General chemical specifications for MSRE fluoride mixtures[42].....	12
Table 3: Compositions of the as-received Ni-Cr model alloys	40
Table 4: Nominal composition of the Hastelloy N (wt.%) used in this study.....	41
Table 5: Nominal composition of 316 stainless steel (wt.%) used in this study.....	41
Table 6: Capsule materials, samples and salt conditions for the corrosion tests in molten FLiBe, at 700°C.	52
Table 7: Calculated mean Cr diffusion distance by using two different methods.	68
Table 8: Neighboring grains misorientation angle for the grain boundaries labeled in Figure 57.....	84
Table 9: XPS Cr (2p) peaks and corresponding chemical state of Cr on sample surface.	86
Table 10: Main boundary conditions for the models of conventional thermal diffusion and the Cr depletion due to corrosion in molten fluoride salts.	138
Table 11: Calculated effective diffusion coefficient of Cr in alloys, the experimental and calculated maximum Cr depletion distance in the alloys tested in molten FLiBe at 700°C.	144

Chapter 1: Introduction

The fluoride salt-cooled high-temperature nuclear reactor (abbreviated conventionally as FHR) has been recently proposed as one of the Generation IV nuclear reactors in order to satisfy the increased global energy demand as well as alleviate the consequence of green-house gas emissions[1], [2]. It is a competitive candidate among all Generation IV nuclear reactors because of its high operating temperatures, heat transfer efficiency, safety and reliability[3]. The background of applying molten fluoride salts as heat transfer coolants stems from the successful operation of the molten salt reactor experiment (MSRE) that was conducted at Oak Ridge National Laboratory (ORNL) from 1960s to 1970s[4]–[7]. The development history of molten salt reactor will be briefly described in the historical perspective subsection.

“The success of a molten-salt reactor system is strongly dependent on the compatibility of the materials of construction with the salts comprising the primary and secondary circuits of the reactor”, reported by J. W. Koger who was an expert at ORNL during MSRE program[8]. It is critically important to understand structural materials corrosion behavior in high temperature molten salts for precisely evaluating materials performance and service life in practical applications. An important issue that limits the application of fluoride salts in high temperature systems is materials corrosion mainly due to the inevitable presence of impurities in molten salt[9]. The challenges for handling molten fluoride salt and typical corrosion mechanisms of alloys in molten salts will be discussed in next two subsections.

Unlike most high temperature environments where an oxide layer is relied upon for corrosion resistance, in molten fluoride salt such a protective oxide layer is inherently unstable and chemically dissolves in liquid salt. Also unlike the MSRE, the recent FHR design (as shown in Figure 1) proposes the use of a non-fuel bearing molten salt $2\text{LiF}\cdot\text{BeF}_2$ (FLiBe) as primary coolant with solid fuel pebbles comprising of tristructural-isotropic (TRISO) fuel particles and graphite matrix. With the above background, the present study was aimed at understanding the corrosion behavior of structural alloys in



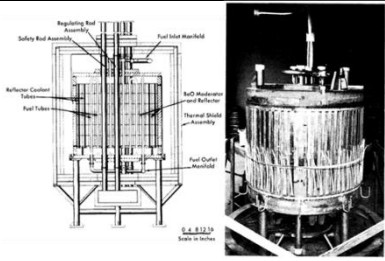
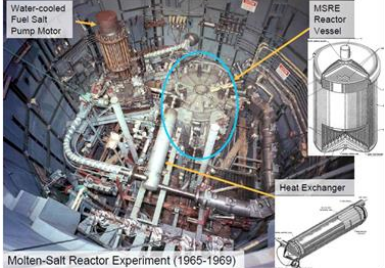
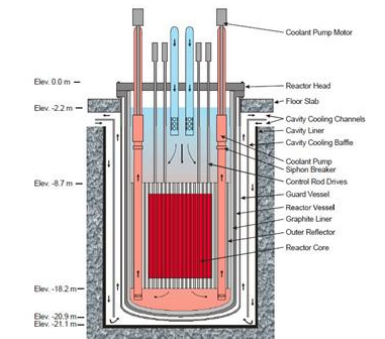
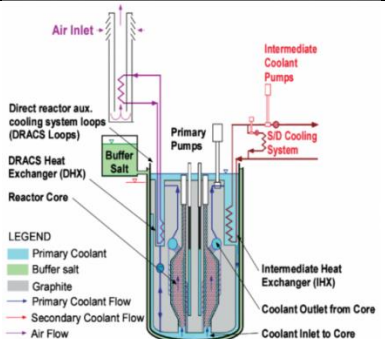
The history of using molten salts as coolant for nuclear reactors dates back 60 years with the work at ORNL for developing a molten salt reactor (MSR) where the U-fuel was dissolved in the coolant[4], [11].

Molten fluoride salts were selected as heat transfer coolants due to their chemical stability both to high-temperature performance and to radiation. MSRs were initially developed for the Aircraft Nuclear Propulsion Program with the goal of powering an aircraft. The project was cancelled after the successful development of Intercontinental Ballistic Missile (ICBM). Then researchers' focus shifted to developing MSRs as a commercial power plant. The Molten Salt Reactor Experiment (MSRE) demonstrated the success of using molten salt as a fuel solvent and heat transfer coolant but the reactor was never commercialized. For a variety of reasons, the molten salt reactor program in the United States was shut down in the mid-1970s. Research on molten salt-cooled, high-temperature reactors was again initiated in 2002 with studies of liquid salt very high temperature reactors (LS-VHTR) aimed at achieving a high core outlet temperature (950°C to 1000°C). With the technology development, in 2010, a Pebble Bed Advanced High-Temperature Reactor (PB-AHTR) was designed at the University of California at Berkeley, which is the prototype of the fluoride salt-cooled high-temperature reactor (FHR)[1], [2].

Table 1 summarizes the typical molten salt-related nuclear reactors in the development history. Fuel was dissolved into molten fluoride salts in the form of uranium tetrafluoride (UF_4) in the ARE and MSRE reactors. Nickel-base alloys of Inconel and Hastelloy N (also named as INOR-8 in ORNL technical reports) were applied to fabricate the reactor vessel and circulating tubes in the ARE and MSRE respectively. The main purpose of the MSRE was to demonstrate the practicality of the key features of molten-salt power reactors. Unlike these two types of molten salt reactors, the recently designed LS-VHTR and updated version FHR propose the use of a non-fuel bearing FLiBe salt as the primary coolant. Furthermore, the FHR combines four established technologies in a new way: (1) coated-particle graphite-matrix fuels (called TRISO fuels) successfully used in helium-cooled high temperature reactors, (2) passive safety systems and plant designs developed for liquid-metal-cooled fast reactors, (3) low-pressure liquid-salt coolants used in liquid-fueled fast reactors, (4) high-temperature Brayton power cycles. Gas-cooled high-temperature reactors have the potential advantages of delivering heat at higher temperatures and power conversion efficiency than light water reactors (LWR), but they require very high gas pressure

to achieve adequate heat transfer. In the FHR, the high volumetric heat capacity of liquid salt allows for a high power density which can significantly minimize the reactor size. Additionally, the ability to operate at near atmospheric pressure enhances FHR safety compared to other reactor designs.

Table 1: Development history of molten salt-related nuclear reactors.

Name/Year	Photo/Schematic	Salt/Coolant	Materials/Peak Temperature
ARE ¹ (1954)		53NaF-41ZrF ₄ -6UF ₄ (mole%) in core; Liquid sodium in 2 nd loop	Inconel vessel and circulating tubes; BeO moderator; 860°C peak temperature
MSRE ² (1965-1969)		65.0 ⁷ LiF-29.1BeF ₂ -5.0ZrF ₄ -0.9UF ₄ (mole%) in core; 66 ⁷ LiF-34BeF ₂ (mole%) in 2 nd loop	Hastelloy N vessel and tubes; Nuclear graphite moderator; 649°C peak temperature
LS-VHTR ³ (2002-)		Considered 66 ⁷ LiF-34BeF ₂ (mole%) as primary coolant and 58KF-42ZrF ₄ (mole%) as intermediate salt	Considered Hastelloy N as main alloy; Designed mean core outlet temperature of 700°C
FHR ⁴		66 ⁷ LiF-34BeF ₂ (mole%) with solid fuel in reactor core	Considered materials: 316 stainless steel, Hastelloy N, graphite, SiC-SiC composite; Designed operation temperature 700°C;
¹ , Aircraft reactor experiment, 2.5MW[12]–[15]			
² , Molten salt reactor experiment, 8MW [16]–[18]			
³ , Liquid salt very high temperature reactor, under design[19][20]			
⁴ , Fluoride salt-cooled high-temperature reactor, under design[1], [2]			

1.2 Selection of molten fluoride salts

Many aspects must be considered to select molten fluoride salts for FHRs. During the MSRE program, Grimes attempted to establish a screening logic for selecting molten salts as fuel solvents and coolants based on thermal neutron capture cross-sections[21][22]. A number of additional screening criteria were applied to candidate salt mixtures that:

1. exhibit chemical stability at $T > 800^{\circ}\text{C}$,
2. are stable under intense radiation,
3. melt at low temperatures ($< 525^{\circ}\text{C}$) and are not volatile,
4. are compatible with high-temperature alloys and graphite,
5. can dissolve required quantities of fertile and fissile materials.

Melting temperature is important for all candidate salts, which must fit with each application. Vapor pressure is minimized to assure salt stability at high temperature. Neutron capture and moderation effect are important for graphite-moderated concepts. The first four requirements listed above are suitable for the FHR. O. Benes et. al. summarized the important aspects that should be considered for salt selection[23], as shown in Figure 2.

The primary coolant in FHR will most likely be ${}^{27}\text{LiF-BeF}_2$ salt, which has a low neutron cross-section and residual radioactivity, and high volumetric heat capacity, boiling point, and thermal conductivity, but has problems of beryllium toxicity and costs associated with lithium enrichment[19], [20], [24]–[26]. Handling FLiBe in practice requires special assistance facilities and equipment due to toxicity and hygroscopicity issues, which causes the experimental challenges whiel purifying and transferring salt.

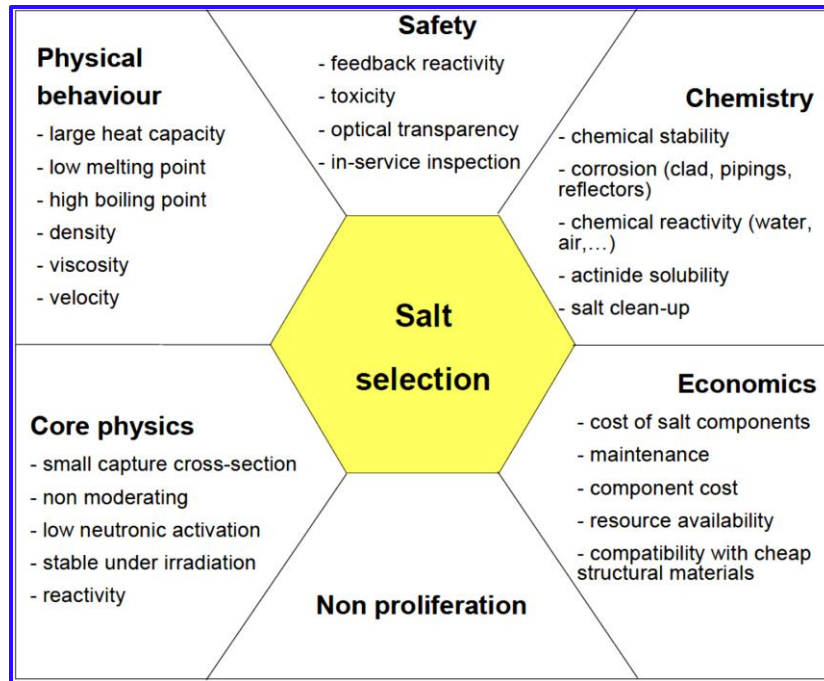


Figure 2: Multiple criteria for molten salt selection in nuclear reactors[23].

1.3 Materials challenges in molten fluoride salt-cooled reactor

The components within a molten-salt-cooled reactor core must be able to tolerate the corrosive fluoride salt, stress, vibration, irradiation, high temperature, temperature gradients, and fission products (accident scenario). Degradation of materials in this extreme environment can lead to reduced performance, and in some cases, sudden failure [27], [28].

A molten-salt-cooled nuclear reactor core is an extremely complex system. Several different types of materials are used to achieve these requirements. As shown in Figure 3, the potential structural materials in FHR include Hastelloy N, 316 stainless steel, SiC, SiC-SiC composites, and nuclear graphite. They are configured in different ways in the reactor core, connecting or disconnecting with other structural materials in the molten salt medium. The molten salt directly contacts all elements except the embedded TRISO particles at normal operation conditions. Molten salt interfaces with all contacted materials, for instance, alloys of reactor vessel, nuclear graphite reflector, control rods and fuel pebbles in the FHR core as well as the alloys of the heat exchanger. The products from the reactions between molten salt and

structural materials might create new reactants which interact with another material. This is the challenge to select suitable materials with acceptable compatibility with other materials.

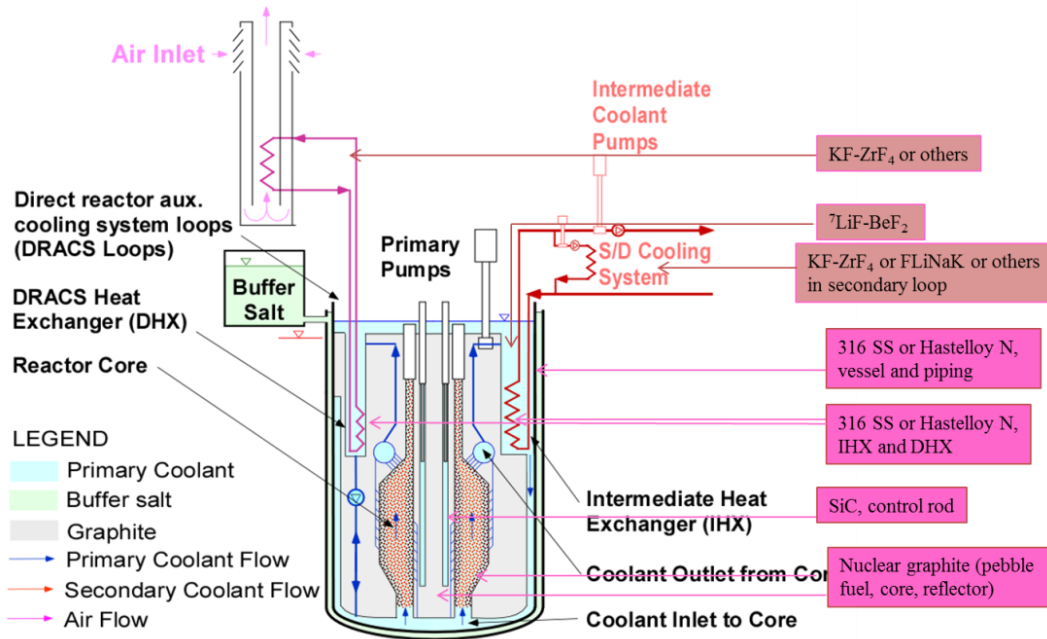


Figure 3: Schematic illustration of FHR cross-section showing the various structural materials of interests[2].

In addition to the degradation caused by chemical reactions, intense radiation reduces materials performance. A number of investigations confirmed that radiation causes various structural defects (such as vacancies, interstitials, voids), segregation at grain boundary[29], [30], and redistribution of elements within materials[31], [32]. For example, as shown in Figure 4, the ductility of Hastelloy N was significantly reduced after experiencing irradiation in MSRE compared to non-irradiated control Hastelloy N, especially at temperatures higher than 700°C. Since the materials microstructure changes after irradiation, for instance the local chemistry at the grain boundaries, irradiation can lead to different corrosion behavior of the materials in molten fluoride salt.

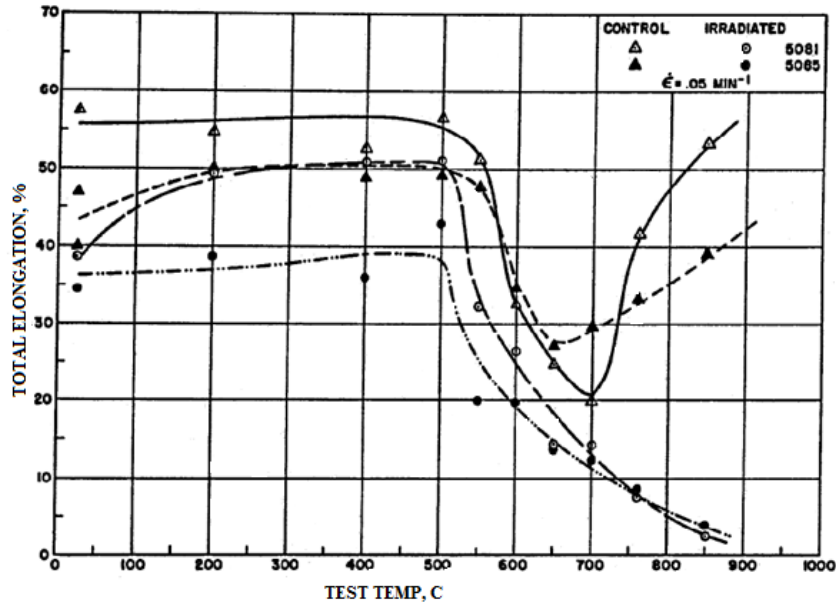


Figure 4: Comparison of tensile ductility of MSRE surveillance specimen and control Hastelloy N as function of temperature at a strain rate of 0.05 min^{-1} [33].

1.4 Corrosion mechanisms of alloys in molten fluoride salt

In a molten fluoride salt system, materials corrosion is driven by a variety of factors. The main corrosion mechanisms include thermodynamically driven corrosion reactions due to the Gibbs free energy of fluorides formation, impurity-driven corrosion due to the presence of moisture, oxygen, and metals, temperature gradient-driven corrosion due to the strong dependence of elemental solubility in molten salt on temperature, galvanic corrosion due to electrochemical potentials between dissimilar materials, and the redox potential of the salt [9].

1.4.1 Thermodynamics of corrosion reactions

The difference in the Gibbs free energy of the salt constituents and the fluorides of alloying elements is a key driving force for the corrosion in molten fluoride salt [34]–[39]. The metals that have more negative free energies of fluoride formation are generally more likely to form fluorides that dissolve in the molten salt. The basic fluorination reaction of metal M can be expressed:

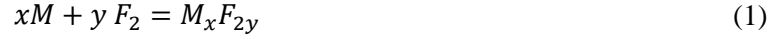


Figure 5 shows the profiles of the Gibbs free energy of the formation of selected fluorides as a function of temperature[39]. BeF_2 has a lower free energy of formation than the LiF in this temperature range. Chromium forms chromium fluorides more readily than other alloying elements. For this reason Cr is the primary constituent in the alloy that is depleted into the molten fluoride salts. The presence of NiF_2 in the salt can also result in the formation of CrF_2 and aggravate the dissolution of Cr in the molten fluoride salt, and further oxidize CrF_2 to CrF_3 at high temperature (Eq. (2)).

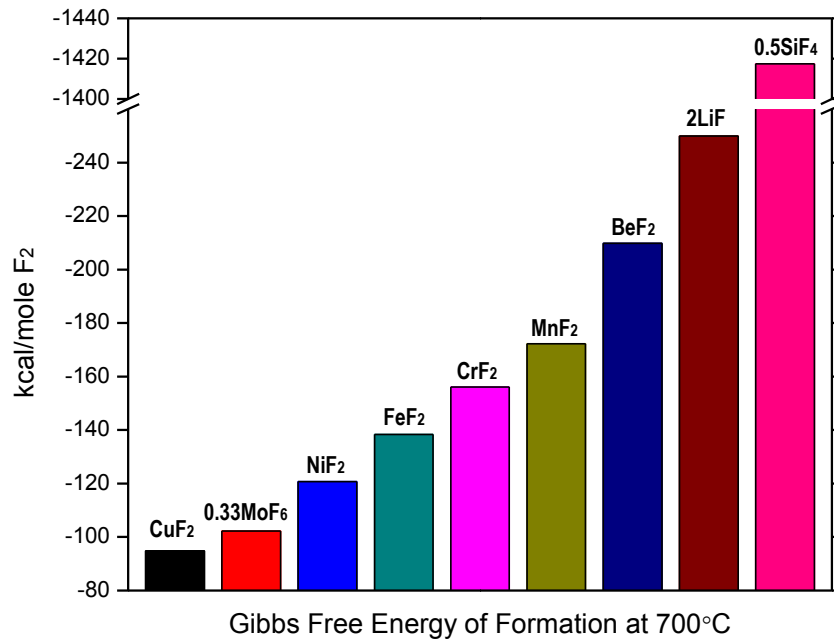


Figure 5: Gibbs free energy of formation of various fluorides at 700°C.



Chromium depletion in Cr -containing alloys in molten fluoride salts can occur through the formation of chromium fluorides on alloys surface as a result of removal of chromium in the alloys matrix, leaving a

depleted zone[40]. In high temperature molten salt, the Cr depletion rate is primarily governed by the rate of outward elemental thermal diffusion through alloys, and the thermal diffusion is highly dependent on the microstructure.

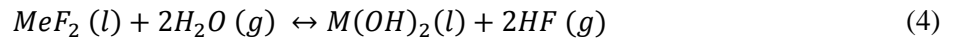
Lewis acid-base properties of the fluoride salt are also an important aspect of understanding corrosion behavior in molten fluoride salt. For example, if an acidic salt, BeF_2 , is to be added to a basic salt, LiF , it would tend to form a complex BeF_4^{2-} , as expressed as:



The result of such complexation is the stabilization of the acid component and a decrease in its chemical activity. The F^- ions coming from the basic salt are tied by the basic salt, which affects the salt activity and influences corrosion in this salt system[41].

1.4.2 Impurity-driven corrosion

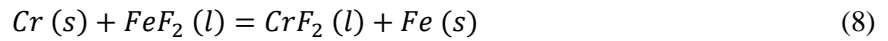
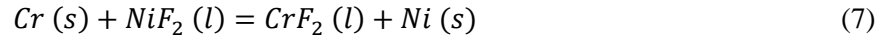
Impurities such as moisture, hydroxides, oxides, sulfur, and metallic constituents in the salt are known to accelerate materials corrosion. Impurity-driven corrosion occurs at a rapid rate in the initial stage of the corrosion process. These impurities can result in attack to most metals at high temperature, even nickel which is relatively immune to fluoride salt attack. Moisture is perhaps the most deleterious contaminant in molten fluoride salts because it reacts with salt fluoride to form the highly corrosive HF gas according to the reactions:



Corrosive gas HF reacts with structural-metals (M^0) and introduces metallic fluorides (MF_x) impurity into molten salt:



Structural-metal impurities in the salt such as Fe and Ni incorporated as fluorides in the salt can react with the Cr depleted from alloy, and result in the following reactions:



These chemical reactions due to the impurities aggravate alloys degradation rate, and affect molten salt conditions. The specifications regulating the maximum allowable impurities in fluorides obtained for the MSRE are listed in Table 2.

Table 2: General chemical specifications for MSRE fluoride mixtures[42].

Impurity	Allowable concentration (wt.%) (1ppm=0.0001 wt.%)
water	0.1
Cu	0.005
Fe	0.01
Ni	0.0025
S	0.025
Cr	0.0025
Al	0.015
Si	0.01
B	0.0005
Na	0.05
Ca	0.01
Mg	0.01
K	0.01
Li (natural)	0.005
Zr (natural)	0.025
Cd	0.001
Rare earths (total)	0.001

In order to remove/control the impurity content in molten salt, several strategies were developed during the MSRE program. Oxides were removed by sparging the molten fluoride salt with anhydrous

hydrogen fluoride, but HF gas can readily attack structural metals. Thus a combined HF-H₂ sparge was used to remove oxides and simultaneously to reduce metallic fluorides, based on the Equations (4), (5) and (6). It is also applicable for sulfur removal. Addition of Be metal into molten FLiBe was shown to be effective in removing sulfate impurities[42].

Because of the toxicity of fluoride salt (particularly for beryllium fluoride), the control and measurement of impurities present challenges. All materials that contact with molten salt are required to be inert to salt at high temperature during transferring and handling of the molten salt. Based on literature review, no satisfactory analytical method appears to exist for determination of impurities in molten fluoride salts[43]. Several techniques has been discussed during the workshops of Integrated Research Project (IRP) of the FHR, for example, inductivity coupled plasma atomic emission spectroscopy (ICP-OES), neutron activation analysis (NAA), Fourier transform infrared spectroscopy (FT-IR), LECO elemental analysis (combustion infrared), electrochemical techniques as well as wet chemistry method. However, low sensitivity, difficulty in sample preparation and high cost and time consumption limits their application in molten salt analysis.

Additionally, in reactors, the transmutation products formed by neutron reactions with the salt introduce another significant source of oxidants in the molten salt. For example, in FLiBe, all three elemental constituents of the salt: lithium, beryllium and fluorine, are expected to undergo transmutation reactions[44]. The reactions between neutron and Li are as the follows:

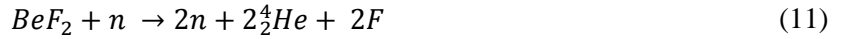


and



The tritium product can combine with fluorine to form corrosive gas of TF which can react with the alloys container to form metallic fluorides impurities.

Transmutation of Be takes place in either of these two ways:



or



The product of He-6 in Equation (12) undergoes beta decay with a 0.8 second half-life. The fluorine products in these Be transmutation reactions can react with alloy container as another source of corrosion to alloys in reactor.

The other transmutation product of the FLiBe components comes from fluorine.



The N-16 ions undergoes beta decay with about a 7 seconds half-life producing O-16 which can react with metal in the reactor causing additional corrosion attack.

1.4.3 Temperature gradient-driven corrosion

The solubility of fluoride corrosion products in molten salts is a strong function of temperature. Thus the dissolved corrosion products (mainly chromium fluorides) at the higher temperature zones can partially plate out in the relatively cooler zones in the flowing salt system. The temperature gradient from hot zone to cold zone is the driving force for this mass transfer. This corrosion mechanism has been studied by operating corrosion tests in thermal convection salt flowing loop as shown in Figure 6.



Figure 6: Photograph of a thermal convection corrosion loop constructed with Hastelloy N (courtesy ORNL).

As mentioned earlier, the Cr depletion from alloy matrix is the primary mechanism of corrosion in molten fluoride salts. The difference in solubility of chromium fluorides in molten salt at different temperatures transfers Cr from hotter sections of the molten salt circulating system to the colder sections and resulting in a partial plate-out in the colder regions. The amount of Cr (ΔM) removed from a unit area of alloy surface is defined by[45]:

$$\Delta M = BC_0\sqrt{Dt} \quad (14)$$

where B is a temperature-dependent constant, C_0 is the initial concentration of chromium in the alloy and D is the diffusivity of chromium in the alloy. Equation (14) shows that the diffusion of chromium through alloys controls the weight loss in static corrosion environments and the mass transfer in circulating corrosion system. Figure 7 shows the typical profiles of weight change of Hastelloy N samples

located at different positions as a function of local temperature. The weight gain increases as decreasing of temperature in colder side, and vice versa in hotter section.

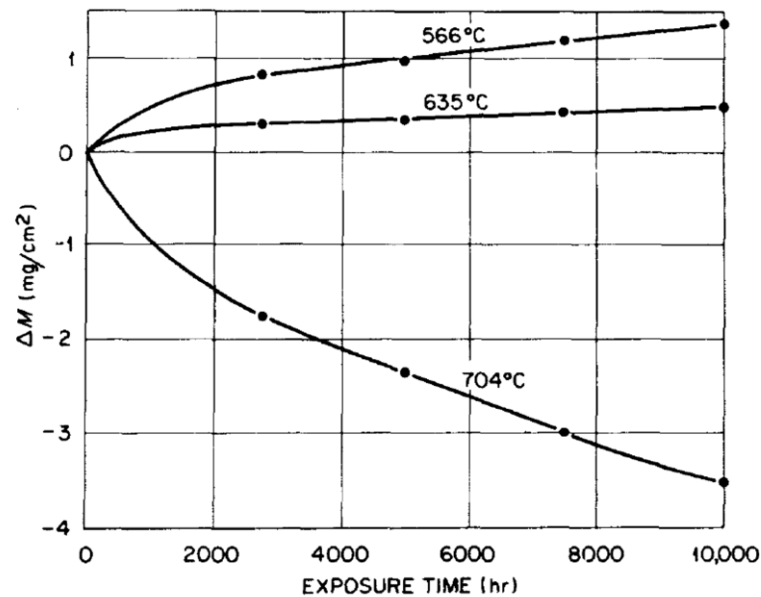


Figure 7: Weight change as a function of exposure time for Hastelloy N specimens exposed to MSRE fuel salt at 566, 635 and 704°C in thermal convection corrosion loop 21A[45].

Figure 8 shows the schematic of temperature gradient mass transfer in a thermal convection loop. In the hotter section, Cr outwardly diffuses to alloy surface and then is oxidized as chromium fluoride. Compared to the thermal diffusion rate through alloy matrix, the reaction on surface is extremely fast. The products immediately dissolve into molten salt because Cr ions diffusion rate in molten salts (10^{-7} m²/second) is much faster than thermal diffusion rate of Cr through a Fe or Ni matrix (10^{-19} ~ 10^{-15} m²/second) at the same temperature[46]–[52]. With increasing exposure time, the corrosion product concentration in the molten salt continues to increase, and the equilibrium temperature begins to move away from the coldest temperature point. At this stage, chromium starts to return to the walls of the coldest point in the circulating system. The rise corrosion product concentration in the flowing salt continues until the amount of chromium depositing on the walls balances the amount of chromium dissolving into the system in hotter regions, based on differential solubility.

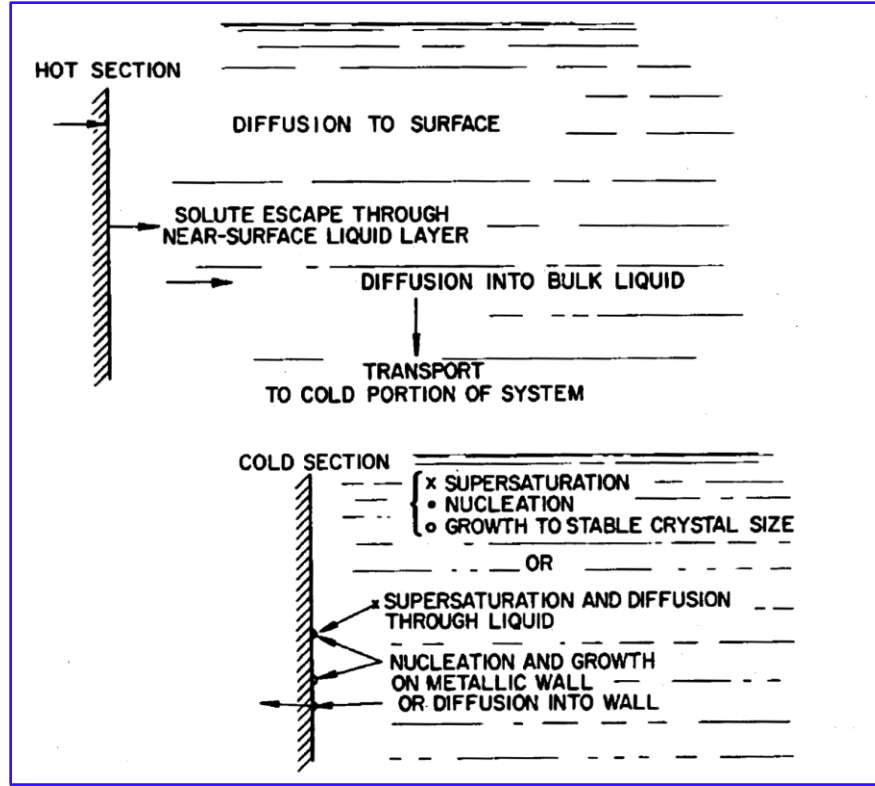


Figure 8: Schematic of temperature gradient mass transfer in a convection loop constructed with Hastelloy N[53].

During the MSRE program, J. W. Koger derived the mass transfer in corrosion loop tubing as[40]:

$$\frac{\Delta M(t)}{A_z} = \int_0^t j_M dt' = -2\rho_a x_a \left(1 - \frac{x_T}{x_a}\right) \left(\frac{Dt}{\pi}\right)^{1/2} \quad (15)$$

where ΔM is the weight of M transferred and A_z is the internal peripheral area of loop tubing, ρ_a is the density with the subscript a denoting alloy, D is diffusion coefficient of M in the alloy, x_a and x_T is the concentration of the alloy constituent in as-received alloy and the surface concentration of alloy constituent as a function of temperature respectively, and t is exposure time.

1.4.4 Dissimilar materials corrosion

The co-existence of dissimilar materials in a molten fluoride salt system can enhance corrosion effects and complicates the understanding of corrosion behavior of individual materials. Usually, the presence of dissimilar materials in the vicinity of each other in molten fluoride salt can accelerate corrosion of the more active material which corrodes in preference to the more noble material by an electrochemical process. Activity-driven corrosion is a particular issue in high-temperature static corrosion studies. An example is the transport of chromium from a steel component through a molten salt with deposition onto a graphite crucible[54]. The effect of crucible materials on the corrosion behavior of 316 stainless steel has been studied in corrosion tests[38]. As shown in Figure 9, the depth of attack on test materials of 316 stainless steel is significantly different in different crucible materials.

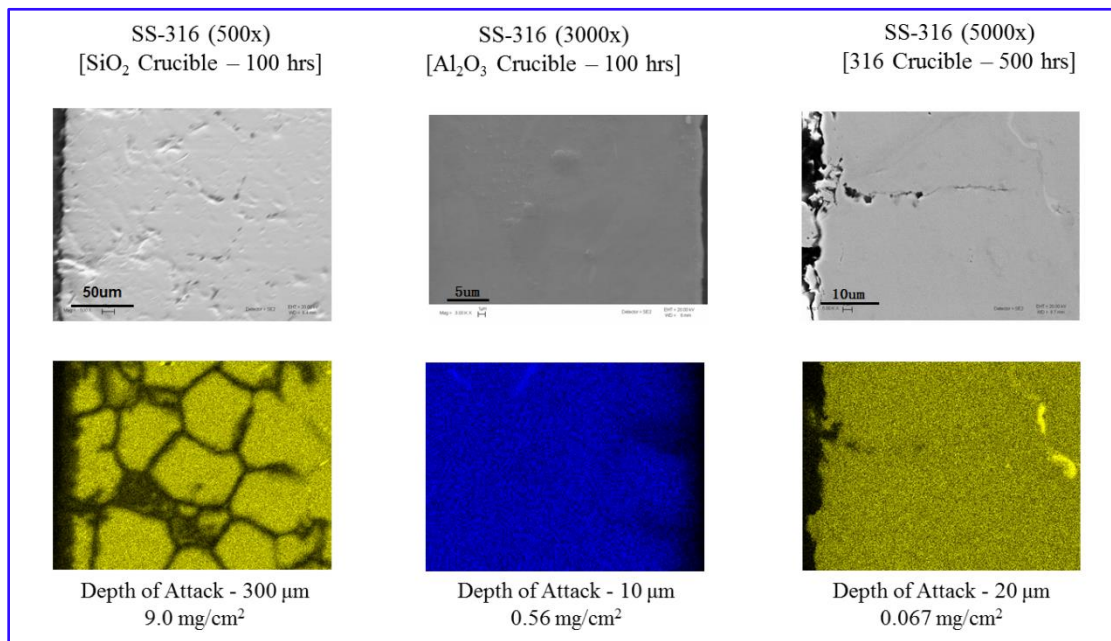


Figure 9: Cross-sectional SEM images and EDS maps of 316 stainless steel specimens exposed to KCl-MgCl₂ in different crucible materials[38].

To mitigate this type of corrosion on the structural materials, using a single structural material to fabricate molten salt reactor vessel has been discussed in FHR project workshops[43].

1.4.5 Redox potential controlled corrosion

The corrosivity of molten fluoride salts may require that the oxidation potential of the salt be lowered by the addition of reducing agents to mitigate corrosion. Reduction-oxidation (redox) potential of molten salt is directly related to the oxidation states of the cations in molten salt that are capable of having multiple oxidation states. For the fluoride fuel salts used in the MSRE, the mole fraction ratio of $[U^{3+}]$ to $[U^{4+}]$ controlled the redox potential that was measured according to the Nernst relation:[55], [56].

$$E_{fuel\ salt} = E_{UF_4/UF_3}^{o'} + \frac{2.3RT}{F} \log \frac{x(UF_4)}{x(UF_3)} \quad (16)$$

where R is the ideal gas constant (J/mole/K), F is the Faraday constant (C/mole), T is the temperature (K) and $E^{o'}$ is the standard potential of the UF_4/UF_3 redox system which combines the standard potential and activity coefficient of UF_4 and UF_3 .

Redox potential of molten salt can be measured experimentally using electrochemistry techniques[39], [55]. Corrosion of materials in molten salt can be reduced by controlling salt redox potential. Beryllium addition in LiF-BeF₂ (66-34 mole%) salt has been shown to reduce 316 stainless steel corrosion. As shown in Figure 10, corrosion of 316 stainless steel was evaluated in LiF-BeF₂ (66-34 mole%) in a thermal convection loop with a maximum temperature of 650°C. It was noted that corrosion in the early stage is rapid due to impurity-driven corrosion. The addition of beryllium drastically reduced the corrosion rate by reducing the oxidation potential of the salt[44], [57].

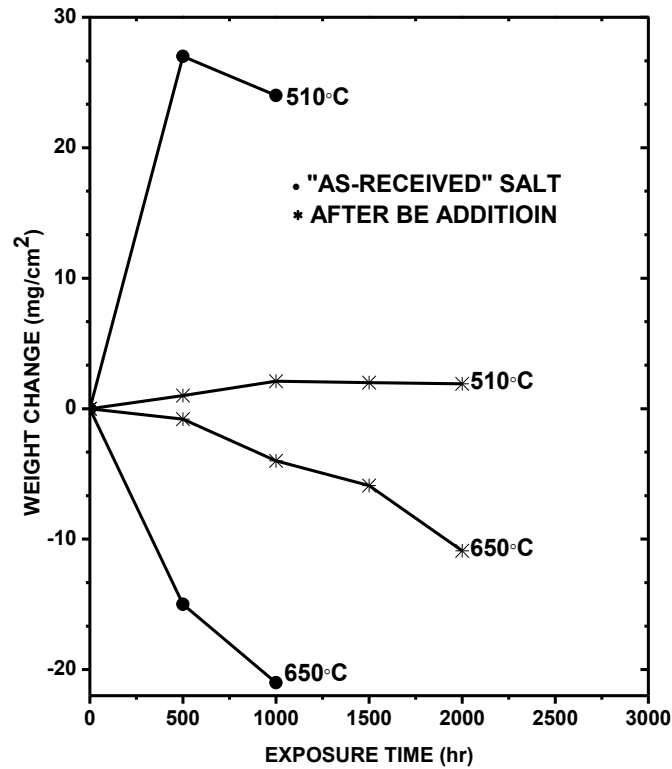


Figure 10: Weight change results of type 316 stainless steel samples exposed to the corrosion loop filled with LiF-BeF₂ (66-34 mole%) salt with and without Be addition.

Additions of rare earths (Sm and Y), Cs, Be, BeC, and Zr have been suggested for corrosion control in non-fuel bearing salts such as LiF-BeF₂ (66-34 mole%), which is being proposed as a primary coolant for the FHR.

1.4.6 Fission products-driven corrosion

In a fuel-bearing molten salt reactor, fission products will accumulate in the salt throughout the fission process. The oxidation state of the fission products depends on the salt redox potential at the time of its formation[58]. As an example, for high values of the salt potential, tellurium in metallic form reacts with structural steel to form Ni_yTe_x or Cr_xTe_y. These compounds form at alloy grain boundaries and are brittle, leading to an intergranular attack[56], [59]. This intergranular embrittlement can be reduced by

adding niobium to the Hastelloy N or controlling the oxidation potential of the molten salt in the reducing stage[60].

In the FHR design, TRISO coated fuel particles will be used to constrain fission products (including gases and metallic constituents) within particles by a coating layer of CVD-SiC, as shown in Figure 11. This new design avoids the corrosion attack to structural materials due to the fission products[10].

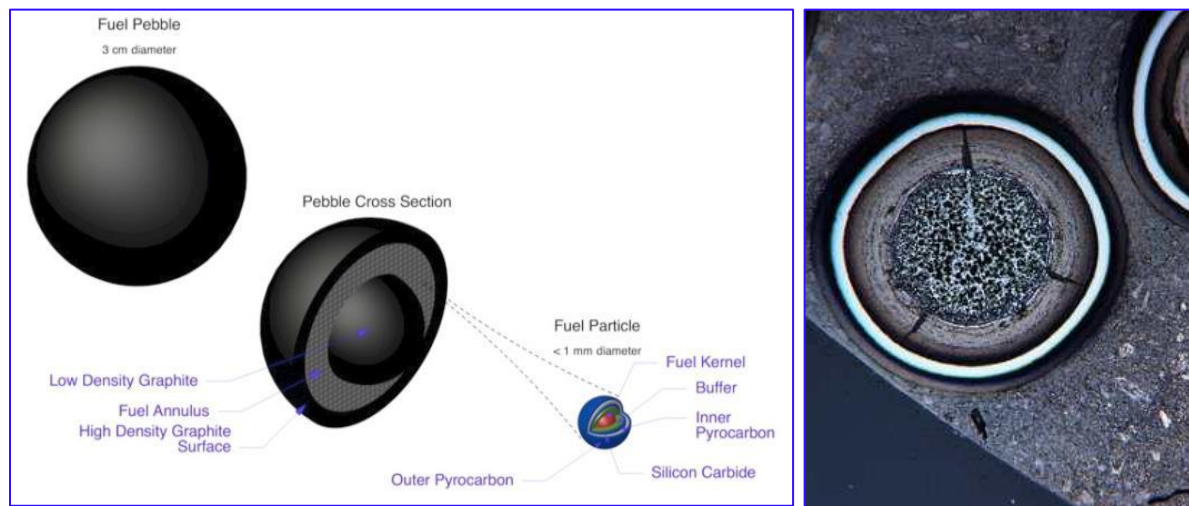


Figure 11: (left) Fuel pebble and TRISO fuel particle and (right) cross-section of fissioned TRISO particle indicating excellent fission products retention at the temperature up to 1800°C[61].

1.5 Corrosion control

Many methods haven been investigated to control structural materials corrosion in molten salts, including protective coating on surface, sacrificial anode protection, alloys modification as well as salt chemistry control[33], [37], [54], [62]. The protective coating layers on alloys surface deposited via chemical or electrochemical processes have been proposed to prevent corrosion of alloys. The important requirements of these coatings are adherence to substrate, homogeneity, and good coverage. Olson has developed passive nickel coatings for corrosion prevention in FLiNaK[54]. However, it is not practical to rely only on a passive system because the aggressiveness of molten salts to corrode is preserved and it is

generally not possible to construct a practical fluoride salt system from noble metals due to cost or strength restrictions.

Numerous molten salt chemistry control systems and corrosion resistant structural alloys were employed during the MSRE program. Ni-based alloy, Hastelloy N, was specially developed to resist corrosion in molten fluoride salts[33], [63], [64]. The alloy contains high concentration of nickel and molybdenum, both of which provide excellent resistance to molten salt corrosion. Redox control method was also implemented based on mole fraction ratio of U^{4+}/U^{3+} in salt. Recent reports show that the oxidation potential control of the non-fuel dissolved molten salt seems to be achievable. However, it is a challenge to measure the salt potential due to reactions on the electrodes. Russian researchers have developed a system using a dynamic reference electrode based on the reference redox systems Be^{2+}/Be [62]. This system has been recently updated in the molten salt group at University of Wisconsin-Madison[65]. Additionally, the redox potential of molten salt can be modified by controlling impurity concentration by adding small amount of Be metal to the salt.

1.6 Experimental techniques in molten salt corrosion research

A number of techniques have been used in the study of molten salt corrosion. Since complicated interactions occur between molten salt and materials at high temperature, it requires the application of multiple disciplines into the understanding corrosion behavior of materials in molten salt, from electrochemistry to materials science. These issues are briefly discussed here to indicate their importance.

Thermogravimetry. Thermogravimetry involves measuring weight change as a function of temperature and exposure time to determine corrosion rate or corrosion kinetics. Here the weight change of coupons is continuously monitored during corrosion tests. Thermogravimetry has been widely applied to predicting long-term corrosion rate of materials in salt based on research data. It also has been applied to study vaporization/decomposition kinetics of molten salt.

Microscopy and x-ray analysis. These are the basic tools for identifying corrosion phases and materials structure to help understand the mechanism of metal-salt interactions. Both traditional metallurgical light microscopy and scanning electron microscopy provide important and unique information on surface microstructural change under different magnifications and resolutions. SEM equipped energy dispersive x-ray analysis can identify elemental distribution and also quantitatively provides elemental composition. X-ray diffraction analysis is valuable to identify phases at the surface and sub-surface regions of the material. Other x-ray/electron interaction techniques such as Auger electron spectroscopy and x-ray photoelectron spectroscopy can give very near surface information on the chemical state of the corrosion products.

Gas analysis. The composition of gases released from the corrosion system usually represents the interactions within molten salt that cannot be observed directly. Attempts of on-line instrumental techniques have been made to collect gas information for monitoring salt state and materials performance. High-temperature solid-state electrodes represent an important new means for analyzing gas composition in molten salt corrosion.

Mass spectrometry. This technique has been widely applied in high temperature chemistry, primarily for identifying the species arising from the vaporization or decomposition of solid phases. In molten salt corrosion, the major use is to determine the composition of salt vapors and the species resulting from the high-temperature reaction of molten salt with metals.

Electrochemistry. This technique can be divided into equilibrium and kinetic methods. The equilibrium method primarily consists of classical potentiometry based on the Nernst equation. It has been successfully applied for analyzing molten salts in which the concentration of some ions change, and for determining the solubility of slightly soluble oxides. The major problem is to find an electrode that is reversible to the ion but does not react with molten salts. A number of kinetic methods such as voltammetry and chronopotentiometry have been developed. In all cases, the controlled variables are

potential, current and time. It is very useful to study the individual steps in the corrosion process[34]. The major application to corrosion research is to evaluate alloys performance in molten salt environments.

In addition to above techniques, some others might be applicable to the molten salt corrosion research such as neutron activation analysis (NAA) for impurities measurement and Rutherford back scatter spectroscopy for profiling components concentration.

1.7 Prediction of Cr depletion in alloys

In pure molten fluoride salt, the degradation of alloys containing Cr is primary due to Cr depletion via two processes of (1) Cr diffusion outward through the alloy to the salt-alloy interface and (2) Cr dissolution by the reduction and oxidation (Equation (17-19)) due to more negative Gibbs free energy of CrF_2 formation.



The extent of the above reaction resulting from equilibration of the salt mixture with a given alloying element (such as Cr) is governed simply by the activity of the element in the alloy and by the stability (or ΔG) of the fluoride compound. For the above reaction, the equilibrium ratio is given by:

$$K_\alpha = \frac{\alpha_{\text{CrF}_2} \cdot \alpha_{\text{M}}}{\alpha_{\text{Cr}} \cdot \alpha_{\text{MF}_2}} \quad (18)$$

where Cr and M are solid-solution alloying elements.

Under a steady-state, isothermal corrosion environment, the overall reaction rate causing Cr depletion from an alloy is controlled by the diffusion rate of Cr in the alloy because it is considerably lower than the other reaction rates of involved in the overall corrosion process. To study the overall diffusion coefficient of Cr in alloy in molten salt, an experiment of self-diffusion of Cr in nickel-base alloys was accomplished during the MSRE program[48]. The radioactive tracer of Cr^{51} was introduced into carrier salt of NaF-ZrF_4 after the salt system had equilibrated at 900°C for several hours and then subjected to lower temperature

prior to immersing the specimen into salt. The diffusion coefficient was determined both by directly monitoring the Cr^{51} intake by the alloys and by analysis of the Cr^{51} concentration profile below the exposed surfaces of the metallic specimen.

Under conditions of a constant surface potential, constant Cr^{51} tracer concentration at the specimen surface with time, the corresponding Cr^{51} transfer equation is calculated by means of the following equation:

$$\Delta M = 2AC_0 \sqrt{\frac{D_{eff} t}{\pi}} \quad (19)$$

where A is the specimen surface area, C_0 is the initial concentration of Cr^{51} introduced into molten salt, D_{eff} is the effective diffusion coefficient (also named overall diffusion coefficient) of Cr in the alloy, and t is the corrosion time[48], [57].

Assuming the diffusion coefficient D is independent of time, at fixed temperature and pressure, the relationship between diffusing source concentration and the diffusion distance and time can be expressed as (Fick's second diffusion law):

$$\frac{\partial C}{\partial t} = D \frac{\partial^2 C}{\partial x^2} \quad (20)$$

The solution of this equation is dependent on the boundary conditions for different diffusion models and environments. Three different diffusion approaches have been discussed to analyze the experimental results by R. B. Evans et. al[48]. One of these is similar to alloy corrosion in molten salt-the placement of tracer atoms is effected by surface reactions. In such an environment, the surface concentration of tracer atoms is brought instantaneously to and maintained at a constant level. A convenient solution of Equation (20) is:

$$C_{cr}(x, t) = C_{0Cr} \operatorname{erfc}\left(\frac{x}{2\sqrt{D_{eff}t}}\right) = C_{0Cr} \left(1 - \operatorname{erf}\left(\frac{x}{2\sqrt{D_{eff}t}}\right)\right) \quad (21)$$

Using these methods, the coefficient of Cr self-diffusion in nickel-base alloys was calculated as follows:

$$D = D_0 e^{-E/RT} \quad (22)$$

Additionally, the results showed that grain size had a marked influence on the overall diffusion coefficient. This indicates that at least two distinct processes contribute to the diffusion of tracer atoms in polycrystalline metals, namely, diffusion occurring along grain boundaries and diffusion through the grain matrix. The effects of these two processes on the overall diffusion coefficient were not separated in this study due to the complexity of microstructure in heat treated metals.

Lattice diffusion (also referred to as volume diffusion) and grain boundary diffusion has been investigated by many researchers[51], [66]–[70]. A classification of diffusion kinetics was proposed for the first time by Harrison who specified three types of kinetic regimes in 1961, as illustrated in Figure 12. In the A regime only, the grain diffusion occurs, and in the C regime, only grain boundary diffusion occurs. Type B kinetic corresponds to conditions where both grain and grain boundary diffusion occur simultaneously. The mechanisms have been discussed by Olson[71].

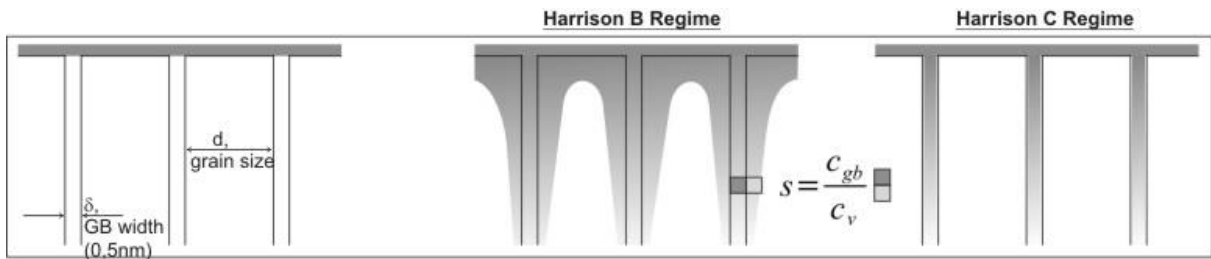


Figure 12: Three different diffusion models showing A, B and C regimes kinetic proposed by Harrison.

An attempt was made recently by T. Chen, et. al. to calculate volume and grain boundary diffusion of Cr in Ni-base Ni-Cr-Fe alloys[51]. In the results, for instantaneous source and a semi-infinite medium, the appropriate solution of Fick's law is given by[51]:

$$C(x, t) = \frac{M}{(\pi D_v t)^{\frac{1}{2}}} \exp\left(-\frac{x^2}{4 D_v t}\right) \quad (23)$$

where $C(x, t)$ is the concentration of the tracer at a distance x from the original surface, D_v is the volume or lattice diffusion coefficient, t is the time of diffusion and M the total amount of deposited tracer at $x=0$ and $t=0$. This equation represents the materials transport within the lattice by volume diffusion. To determine the material transport rate within the lattice as well as the grain boundary simultaneously, an analytical procedure is needed to separate the contributions of the lattice and the grain boundary to the overall depth profile of the diffusing species.

To calculate the grain boundary diffusion coefficient, several methods have been discussed. The important calculations include the analysis by Fisher, Suzuoka and Whipple. Chen et. al.,[51] also proposed the expression:

$$\delta D_{gb} = \left(\frac{\partial \ln \bar{C}}{\partial x^{\frac{6}{5}}} \right)^{-\frac{5}{3}} \left(\frac{4 D_v}{t} \right)^{\frac{1}{2}} \left(\frac{\partial \ln \bar{C}}{\partial \left(\eta \beta^{-\frac{1}{2}} \right)^{\frac{6}{5}}} \right)^{\frac{5}{3}} \quad (24)$$

Here \bar{C} is the average concentration of the tracer at x perpendicular to the diffusion interface. According to Harrison's classification of the preferential diffusion along short-circuiting paths, this corresponds to B regime kinetics, Combining the grain size and grain boundary width, the above expression can be transformed to[51]:

$$\delta D_{gb} = 0.661 \left(\frac{\partial \ln \bar{C}}{\partial x^{\frac{6}{5}}} \right)^{-\frac{5}{3}} \left(\frac{4 D_v}{t} \right)^{\frac{1}{2}} \quad (25)$$

From the plots of $\ln C$ vs. x^2 , the volume diffusion coefficient D_v can be estimated from the initial linear portion of the curve because the volume diffusion is dominant in this region. Subsequently, the grain boundary diffusion coefficient δD_{gb} can be calculated from the linear portion of the plots of $\ln \bar{C}$ vs. $x^{6/5}$. However, the diffusion approach in molten salt environment is in reverse to this semi-infinite thermal diffusion model. Volume diffusion is dominant in the layer close to surface and grain boundary diffusion is predominant in substrate where Cr concentration is close to initial $C_{Cr,0}$.

During MSRE program, the corrosion behavior of INOR-8 (now known as Hastelloy N) in fused fluoride salt was investigated by J. H. DeVan and R. B. Evans[72]. An analytical method was employed to interpret corrosion and mass-transfer behavior in a corrosion loop system. This method was based on the following assumptions: (1) pre-equilibrated process established a steady-state condition for CrF_2 and UF_3 at the beginning of loop operation, (2) overall rate of mass transfer is controlled by the diffusion of chromium in the container material, (3) chemical equilibrium with respect to Cr and the salt mixture exists at every surface point within loop system, (4) at any time the cumulative amount of Cr removed from hot zone equals to the Cr deposited in the cold zone. The applicable diffusion equation at any given temperature position under the boundary condition of constant surface concentration is:

$$C_{Cr}(x, t) = C_s - \Delta C \operatorname{erf} \left(\frac{x}{2\sqrt{D_{eff}t}} \right) \quad (26)$$

where $C(x, t)$ is Cr concentration at depth x after time t , $\Delta C = C_s - C_0$ is the difference between the Cr concentration at surface (C_s) and the original Cr concentration in INOR-8 (C_0). The main purpose of developing this equation in MSRE program was to determine the concentration gradient of Cr and hence the mass of metal removed at a selected temperature. The basic data needed for this determination are (1) the diffusion coefficient for Cr in alloy and (2) equilibrium ratios for the redox (Equation (20)) as a function of temperature. The C_s equals the Cr concentration in molten salt at equilibrium state, which is about 0.0025% in MSRE fluoride salt (Table 2). Comparing to the initial Cr concentration in the alloy (~7% in INOR-8), C_s is negligible ($C_s \sim 0$). Then, the Equation (28) can be simplified.

In all calculations of Cr concentration profiles, the D_{eff} is a critical factor that affects alloy corrosion behavior in molten salt and has been discussed in relation to the application of a variety of diffusion models[54], [70], [73]. The results are inconsistent, but a consensus is that the two diffusion processes, volume and grain boundary diffusion (D_v and D_{gb}), mainly contribute to the effective diffusion coefficient. At high temperature, these two diffusion mechanisms are determined by the microstructure of alloys. Therefore, in addition to the attack depth calculation, the microstructure of tested alloys must be analyzed using varying techniques to better understand the corrosion behavior of the alloy in molten salt.

In a molten salt reactor, the structural alloys are exposed to both molten salt and intense irradiation, as demonstrated in Figure 13. The irradiation usually causes Cr segregation at grain boundaries, which is termed radiation induced segregation (RIS)[29], [30], [74], [75]. Additionally, the redox potential of molten salt controls the chemical reaction rate of the Cr at alloy-salt interface.

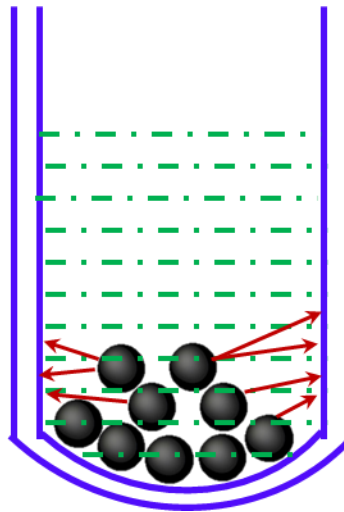


Figure 13: Schematic illustration of molten salt reactor and TRISO fuel. Red arrows denote the irradiation.

After understanding the structural alloys exposure environments in molten salt nuclear reactor, there are three main aspects that must be considered in the study of corrosion behavior of alloys in high temperature molten fluoride salts, as illustrated in Figure 14. They are the thermal effect on

microstructure, the irradiation effect on microstructure, and the effect of salt redox potential. The first two factors have a strong effect on alloy microstructure. Therefore, it is important to characterize the microstructure of corrosion samples including grain orientation, grain boundary type, and elemental distribution and so on. Additionally, the interaction between molten salt and the alloy is important to alloy corrosion. Moreover, with graphite in molten salt, carbon liberated from graphite quickly diffuses into alloy matrix and forms carbides within alloys. In this study, Ni-Cr model alloys, Hastelloy N and 316 stainless steel were investigated for understanding corrosion behavior in molten FLiBe salt with and without graphite effect.

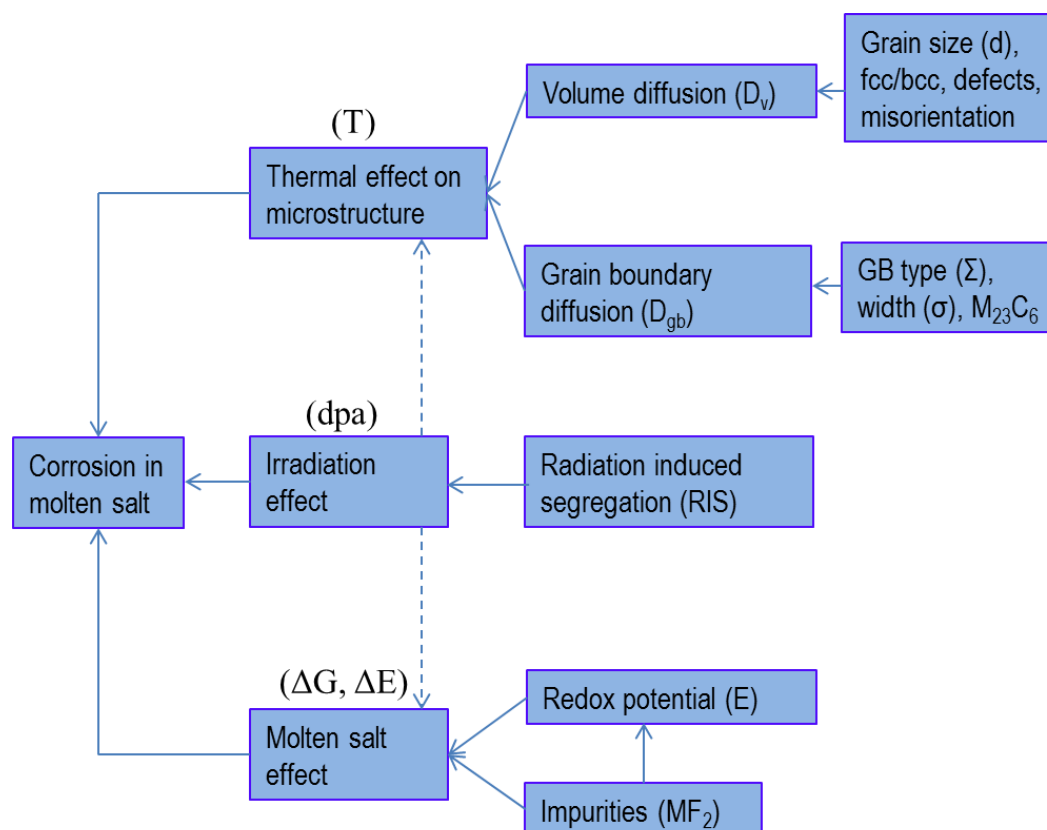


Figure 14: Flow chart presenting the effects on alloys corrosion behavior in molten fluoride salt at high temperature.

Chapter 2: Experimental procedures

2.1 Fluoride salts preparation

This study focuses on the corrosion of structural materials in molten FLiBe salt. However, handling FLiBe salt requires specially designed facilities and high precautions due to the hygroscopicity of the salt, corrosive effects of fluoride species, and the toxicity of beryllium. To test new designed facilities, KF-ZrF₄ (58-42 mole%) and LiF-NaF-KF (46.5-11.5-42 mole%, usually called FLiNaK) were prepared in laboratory prior to starting tests in FLiBe salt. Valuable experience was accumulated from these two fluoride salts in regards to preparation and handling for the corrosion tests of structural materials in high temperature FLiBe. The challenges for handling FLiBe salt and the samples exposed to FLiBe are described in the following section.

2.1.1 Experimental challenges associated with molten fluoride salt

The hygroscopicity and toxicity of beryllium as well as high melting point (460°C) requires special facilities and environment to transfer FLiBe at liquid state. Safety must always be the top priority. Chronic Beryllium Disease (CBD) might occur if a person is exposed to beryllium or beryllium compounds over a safe level and one can develop an immune response (beryllium sensitization). However, unlike the monitoring of radiation exposure using a sensitive meter, no instrument is available to monitor beryllium contaminant on-line. Inductively coupled plasma atomic emission spectroscopy (ICP-OES), the most feasible method with sufficient sensitivity, was employed to measure beryllium content.

In order to minimize exposure to beryllium and beryllium compounds, all operation procedures were discussed and standardized in advance and in consultation with the office of occupational health at the University of Wisconsin-Madison which was involved in this project to regulate and monitor any possible beryllium contamination in our laboratory. Additionally, all personnel working on this project were required to take annual physical exams including blood test and lung function. All blood samples are sent to National Jewish Health Laboratory where is authorized for CBD diagnosis.

To mitigate the introduction of impurities during salt handling in the experiments, a pure nickel container and tubing are selected because nickel is noble to molten fluoride salts, and it has good machinability and acceptable mechanical properties at high temperature. In this work, several pure nickel crucibles were designed and fabricated particularly for fluoride salts. For example, the purification system was mainly composed of a pure nickel container that was sealed in a 316 stainless steel canister. Since the strength of pure nickel dramatically decreases with increasing temperature, this double-walled purification system enhanced its structural durability during the pressurizing process to drive liquid salt through transfer system to the storage canister.

Unlike the transfer of other liquid media, molten fluoride salts must be melted and maintained at liquid state with a temperature above their melting points (460°C for FLiBe). Therefore, the entire storage and transferring system must be wrapped with external heaters and thermal insulation. Any cold point in this system could freeze the salt which would block the whole system. It is a challenge to homogeneously wrap heaters on this system due to the shape complexity, particularly at the connection joints and filter. Furthermore, cleaning graphite crucibles, oxygen and moisture control (ppm level), precisely filling salt (0.1g accuracy) into small corrosion capsules (~10mm in diameter), as well as re-melting loaded salt in graphite crucibles are also challenges in this work.

2.1.2 Pre-drying salts

Since most fluoride salts are hygroscopic in air, it is necessary to pre-dry all as-received salts prior to melting mixed salts. As shown in Figure 15, as-received individual salts such as KF, NaF, LiF and ZrF₄ were added into SiC-coated graphite tank that was surrounded by clam shell heaters. This tank was also used to melt salt mixture of KF-ZrF₄ and FLiNaK. A gas sparging system consisting of moisture trap and a filter at bottom was embedded into salt for carrying out moisture during pre-drying. Herein, it should be noted that the temperature for pre-drying ZrF₄ was controlled at lower than 220°C in order to mitigate the product of HF gas from the following chemical reaction.

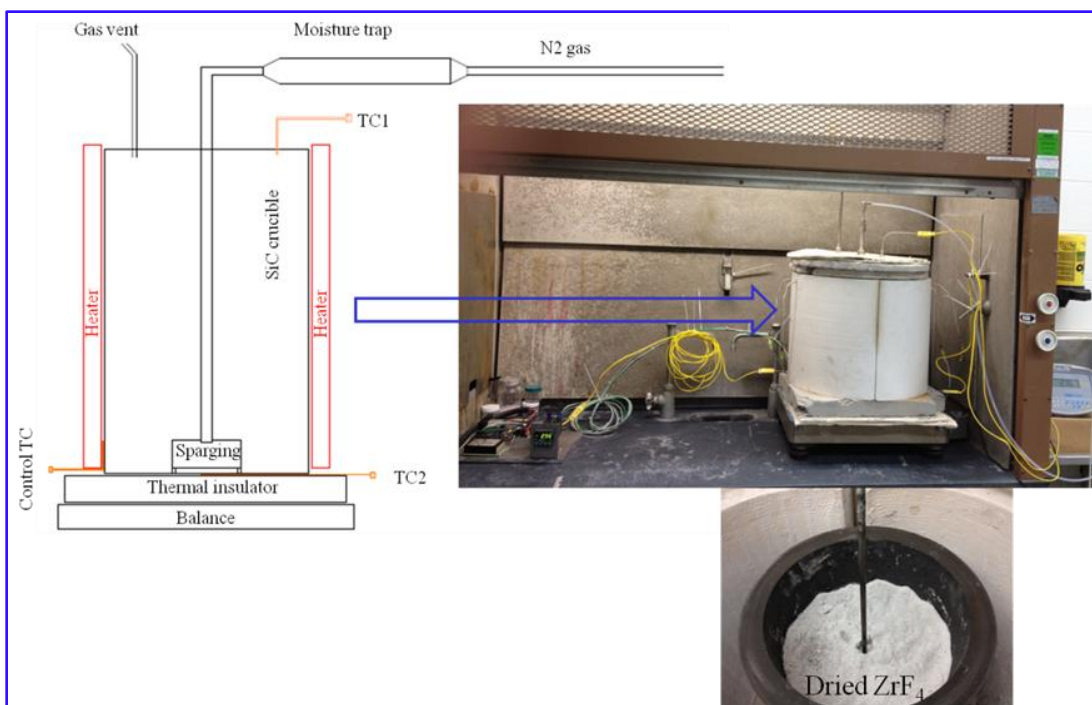
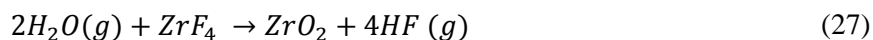


Figure 15: Fluoride salts pre-drying system.



This pre-drying temperature was selected based on the thermodynamic calculation (HSC Chemistry 7.0). If the pre-drying temperature is higher than 220°C (1 mole% ZrO₂ criterion at equilibrium state), the amount of oxides and corrosive HF gas would dramatically increase, then the impurity content in the salt would increase.

2.1.3 Preparation of KF-ZrF₄

The pre-dried KF and ZrF₄ was mixed in 0.58 to 0.42 mole ratio and melted in SiC-coated graphite tank. Salt mixture was maintained at 550°C for 12 hours. Precaution is required to melt KF and ZrF₄ mixture because of the HF gas that might be produced due to the existence of moisture in salts. An HF gas removal system is therefore strongly recommended at the end of system. Following this method, approximately 20kg of non-purified KF-ZrF₄ was prepared, as shown in Figure 16. Apparent density of

this salt is approximately $2.64\text{g}/\text{cm}^3$ based on the mass and dimensions of the salt bulk shown in Figure 16b.



Figure 16: Salt prepared at the University of Wisconsin laboratory: (a) Laboratory made 20kg KF-ZrF₄ in SiC-coated tank, (b) bulk salt and (c) salt chunks stored in glass jars.

2.1.4 Preparation of FLiNaK

Using above system and methods, about 10kg FLiNaK was prepared, as shown in Figure 17. The bulk surface of this salt was much cleaner than the KF-ZrF₄ (Figure 16b) because of less attack to the tank wall due to the HF product. The apparent density of this salt was about $1.36\text{g}/\text{cm}^3$ calculated from the mass and dimensions of laboratory made FLiNaK bulk, which is lower than the theoretical density because of the presence of voids.

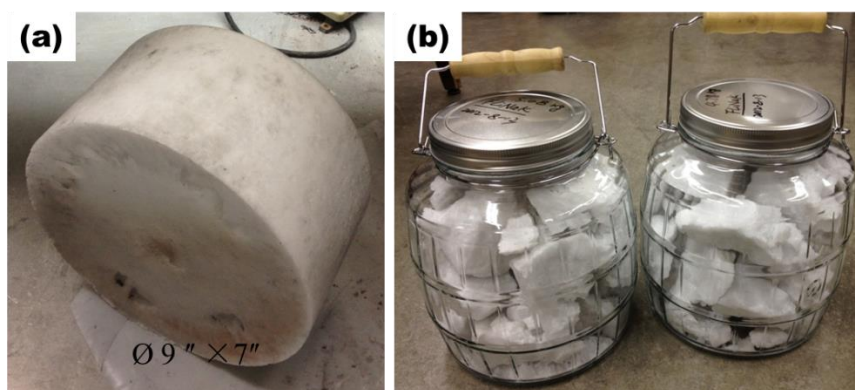


Figure 17: Salt prepared at laboratory (a) 10kg FLiNaK bulk and (b) salt chunks stored in glass jars.

2.1.5 Preparation of FLiBe

In order to efficiently prevent the beryllium salt from any exposure to air or contact with humans, a specially modified glove box, as shown in Figure 18, was set up in laboratory prior to starting FLiBe salt preparation. Oxygen and moisture levels were monitored on-line using two separate instruments (on top of glove box). Both levels are lower than 10 ppm during regular operation. The circulating gas in the glove box was purified through regeneration system. The copper purifier in the regeneration system could efficiently absorb moisture and oxygen, thus controlling the gas impurities to provide an inert atmosphere for corrosion testing in molten fluoride salt. Additionally, a high temperature heating system was placed in the same glove box. This system was remotely modulated through a Labview program. This specifically designed glove box is critically important for safe preparation and handling of FLiBe salt.

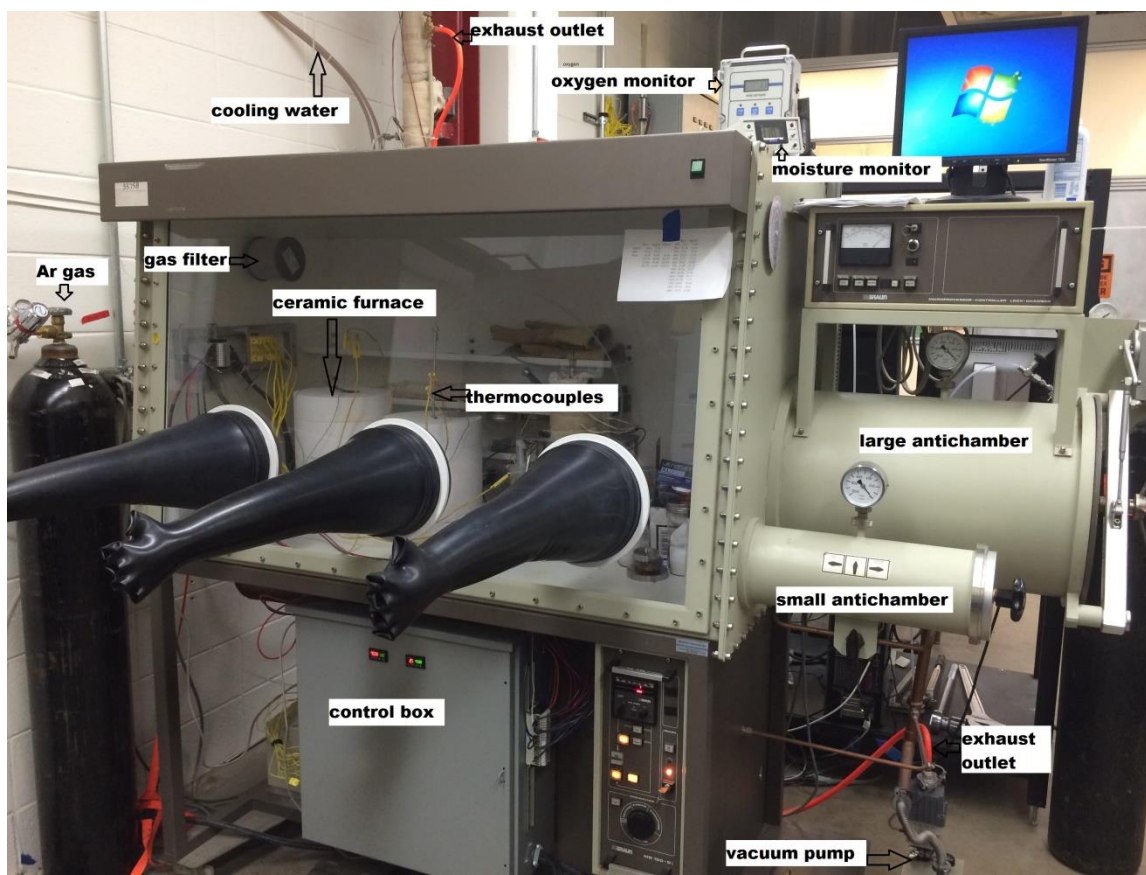


Figure 18: Modified glove box for handling FLiBe and for conducting corrosion tests in molten FLiBe.

As shown in Figure 19, the as-received LiF and BeF₂ were mixed in a mole fraction ratio of 2:1 in a pure nickel container. Then, the mixture was heated up to 550°C and maintained for about six hours. This laboratory made FLiBe salt contained black impurity particles that were determined to be graphite presnet initially in the as-received BeF₂ nuggets. To remove impurities from FLiBe salt, many solutions and facilities were developed during the MSRE program. The high purity enriched FLiBe used for corrosion tests in this study originated from the secondary cooling system of MSRE, and was provided by Oak Ridge National Laboratory (ORNL).

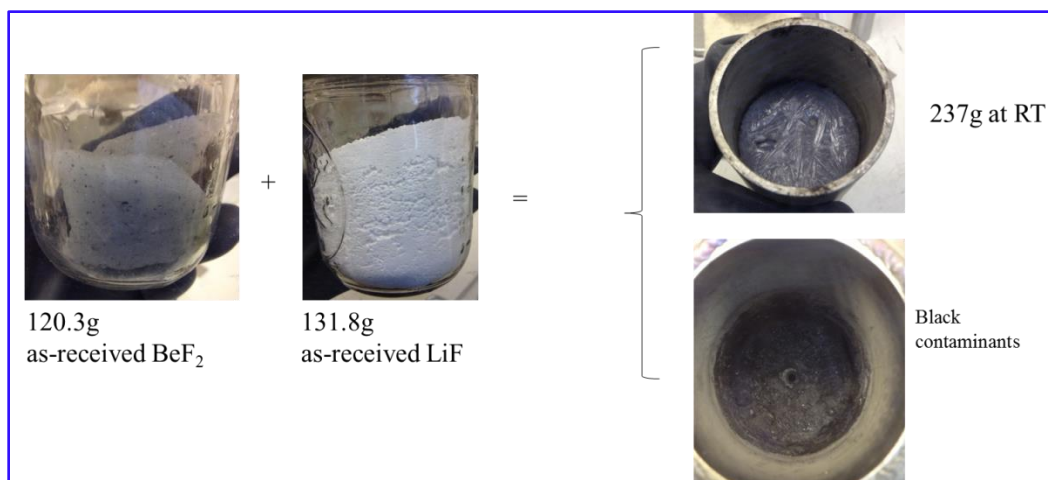


Figure 19: As-received BeF_2 nuggets and LiF (puffy powder), and laboratory made non-purified FLiBe at room temperature.

The as-received ORNL FLiBe salt had been stored in stainless steel tank for longer than forty years. The salt was subjected to re-purification by the hydrofluorination process prior to corrosion tests because the corrosion in molten fluoride salts is primarily impurity driven. This process insures a high quality salt even after forty years of storage. Five hundred grams of the as-received FLiBe were transferred in molten state into a small nickel vessel where it was bubbled with hydrogen-fluoride and hydrogen gas with a ratio of 1:10 HF/H_2 , flowing at 1.5 L/min, at approximately 550°C , for two hours. The hydrofluorination process time though short was deemed acceptable as the salt was being regenerated rather than being manufactured from raw materials. The hydrofluorination process was then followed with a 12 hour sparge with hydrogen. The purified salt was transferred into pure nickel tray through an open ended transfer line with a $40\text{ }\mu\text{m}$ stainless steel filter on the end[76]. Figure 20 shows purified FLiBe that was originally from secondary loop of MSRE. Liquid salt was transparent to light and cracks were visible in solid salt due to volume shrink during solidification.

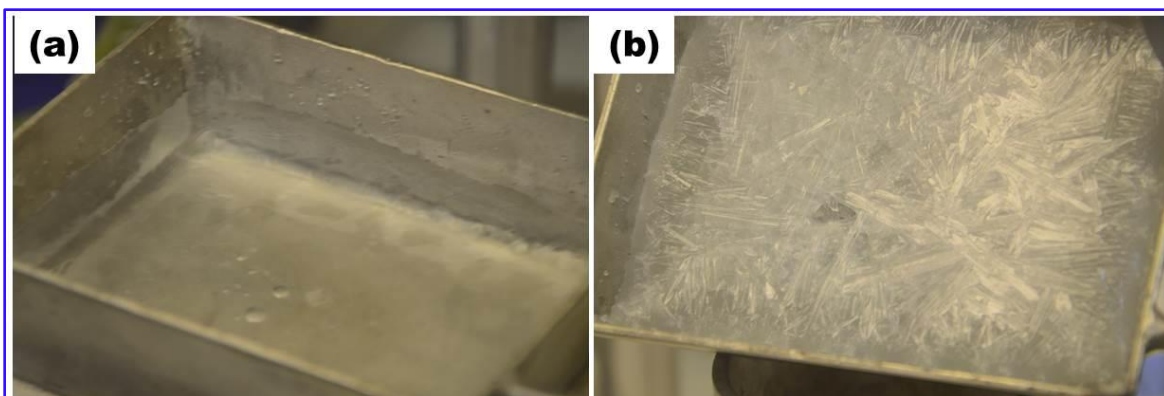


Figure 20: Purified ORNL FLiBe in (a) liquid state and (b) solid state in pure nickel tray.

To prepare more reducing FLiBe salt, beryllium (Be) was added into purification canister after purifying with hydrogen fluorine and hydrogen gases. Be reacts with other metallic fluorides impurities such as Cr^{2+} and the redox potential of the salt becomes more negative, around -0.49V (reference $E^0_{\text{HF}/\text{H}_2} = 0$) using glass carbon and molybdenum electrodes. This further Be-reduced FLiBe was transferred into pure nickel tray through the same stainless steel filter. As shown in Figure 21, transparent salt crystallized in a nickel tray in the glove box and formed large crystalline grains. This salt was filled into separate corrosion capsules to investigate the salt redox potential effect on materials corrosion behavior.



Figure 21: Be reduced ORNL FLiBe in solid state in pure nickel tray.

2.2 Test samples preparation

In support of structural materials development for the FHR, the materials tested in molten fluorides involved in this work include nickel-based Hastelloy N, 316 stainless steel, chemical vapor deposition (CVD) SiC, SiC-SiC composites, tristructural-isotropic (TRISO) particles with ZrO_2 surrogate in kernel and nuclear grade graphite as well as C-C composite. To fundamentally understand the Cr depletion from alloys in molten fluoride salt, binary alloys of Ni-5Cr and Ni-20Cr (wt.%) were also tested. For comparison purposes, the binary alloys were also tested in argon back-filled quartz tubes for the same temperature (700°C) and exposure times as the corrosion tests. This study focuses on the corrosion of Ni-Cr model alloys, Hastelloy N and 316 stainless steel.

2.2.1 Ni-5Cr and Ni-20Cr model alloys

The compositions of model alloys Ni-5Cr and Ni-20Cr are shown in Table 3 and they were procured from the manufacturer of Sophisticated Alloys Inc. (PA, United States). The coupons with dimensions of 12.7mm×6.3mm×2.3mm were cut from as-received rods and plate using electrical discharge machining

(EDM) cutting, as shown in Figure 22. A small hole was drilled on one end of each coupon for the convenience of suspending samples in molten salt during the corrosion tests. Both sides of these coupons were mechanically polished to mirror finish using silicon carbide paper with last step on a fabric pad (MD-Nap, Struers) with silica suspension. Polished samples were then ultrasonically cleaned in deionized water and acetone.

The polishing quality was inspected under optical microscope. It was found that the grain size of as-received Ni-5Cr is over one hundred microns, which is much larger than the as-received Ni-20Cr with several tens microns grains. To refine the grain size, the as-received Ni-5Cr was subjected to cold rolling (thinning thickness from 2.3mm to 0.58mm) and annealing at 700°C for an hour. The surface of these samples was re-polished with the same polishing procedures.

Table 3: Compositions of the as-received Ni-Cr model alloys

Alloy	Cr, wt. %	Ni, wt. %	Purity, %	Apparent density (g/cm ³)	Manufacturing
Ni-5Cr	5	95	99.95	8.7	Vacuum induction melting, HIPed rod ~1"Ø x 8" ~4" x 4" x 0.490" plate
Ni-20Cr	20	80	99.95	8.57	

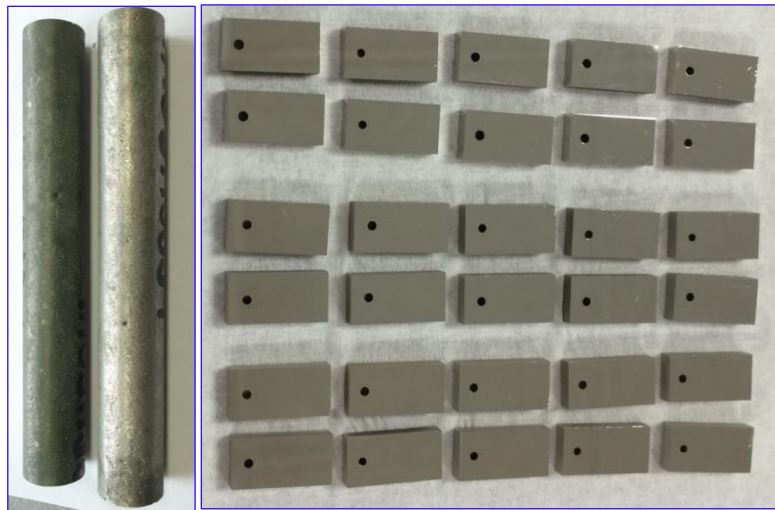


Figure 22: Polished Ni-5Cr and Ni-20Cr coupons.

2.2.2 Hastelloy N

Hastelloy N samples with dimensions of $\sim 1\text{mm} \times 7\text{mm} \times 13\text{mm}$ were cut from sheet stock procured from the company, Haynes International. The nominal composition of the alloy as provided by the manufacturer is shown in Table 4. For the convenience of suspending samples in liquid FLiBe salt, a 1.6 mm hole was drilled on the Hastelloy N coupons. All coupons were mechanically polished to 1200-grit final finish with silicon-carbide paper, and cleaned with deionized water and acetone prior to corrosion tests.

Table 4: Nominal composition of the Hastelloy N (wt.%) used in this study.

Nickel ^a	Cr	Mo	Fe	Si	Mn	C	others
71	7	16	4 [*]	1 [*]	0.80 [*]	0.08 [*]	Co=0.20 [*] Cu=0.35 [*] W=0.50 [*] Al+Ti=0.35 [*]

a As balance, * Maximum

To investigate the development of Mo rich precipitate at grain boundary, a series of Hastelloy N samples were annealed at 850°C for the duration varying from 20 hours to 500 hours.

2.2.3 316 stainless steel

Commercial purity, 316L stainless steel for corrosion testing was procured in sheet form from a commercial vendor in the U.S. and the nominal chemical composition of this material is listed in Table 5. 7mm \times 13mm \times 1mm test samples were cut from the sheet stock. The sample surfaces were mechanically polished to a 1200-grit final finish with silicon-carbide paper, and cleaned with deionized water and acetone.

Table 5: Nominal composition of 316 stainless steel (wt.%) used in this study.

C	Cr	Cu	Mn	Mo	N	Ni	P	S	Si	Fe [*]
0.0225	16.825	0.3795	1.5305	2.0115	0.051	10.025	0.031	0.0016	0.309	68.8134

* As balance

To evaluate the effect of irradiation damage on the corrosion behavior of 316 stainless steel in molten FLiBe, two samples with dimensions of $25\text{mm} \times 10\text{mm} \times 2\text{mm}$ were polished to mirror surface for irradiation experiment. 2MeV proton beams was applied to introduce 0.5 dpa irradiation damage into the samples at around $420^\circ\text{C} \pm 10^\circ\text{C}$ in the ion beam laboratory at the University of Wisconsin-Madison. The target constant irradiation damaged region with 0.5 dpa is in the range from $2\mu\text{m}$ to $10\mu\text{m}$ deep from surface. Figure 23 displays two irradiated 316 stainless steel samples. The blue yellow area in each sample center is the irradiated region. Other surface areas were covered by face molybdenum plate during irradiation experiment.

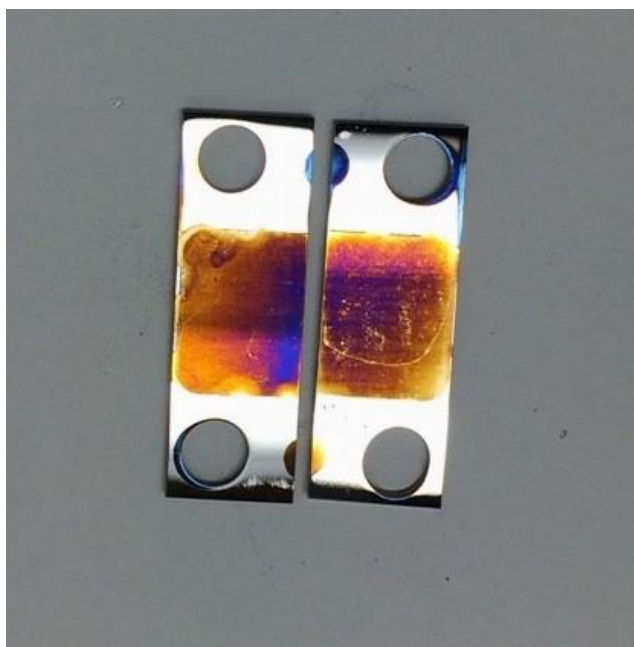


Figure 23: 2MeV proton irradiated 316 stainless steel. Blue yellow area denotes the proton irradiated region.

2.2.4 Ceramics and graphite samples

Although the primary focus of this study was on metallic samples, ceramics and graphite samples were also tested and are briefly described in this thesis. High purity, polycrystalline Rohm-Haas chemically vapor deposited (CVD) SiC, two types of chemically vapor infiltrated (CVI) SiC fibers

reinforced polycrystalline cubic SiC composites, Tyranno™ -SA3 CVI SiC-SiC and Hi-Nicalon™ Type-S CVI SiC-SiC, were also tested. The SiC fibers used for these two SiC-SiC composites are from Ube Industries, Ltd., Ube, Japan and Nippon Carbon Company, Tokyo, Japan respectively.

Carbon fiber reinforced carbon composite, named FMI-222 C-C composite from Fiber Materials Inc., was selected as carbon materials to compare corrosion behavior with nuclear grades graphite. Figure 24 shows pictures and SEM images of polished SiC-SiC composite and C-C composite samples.

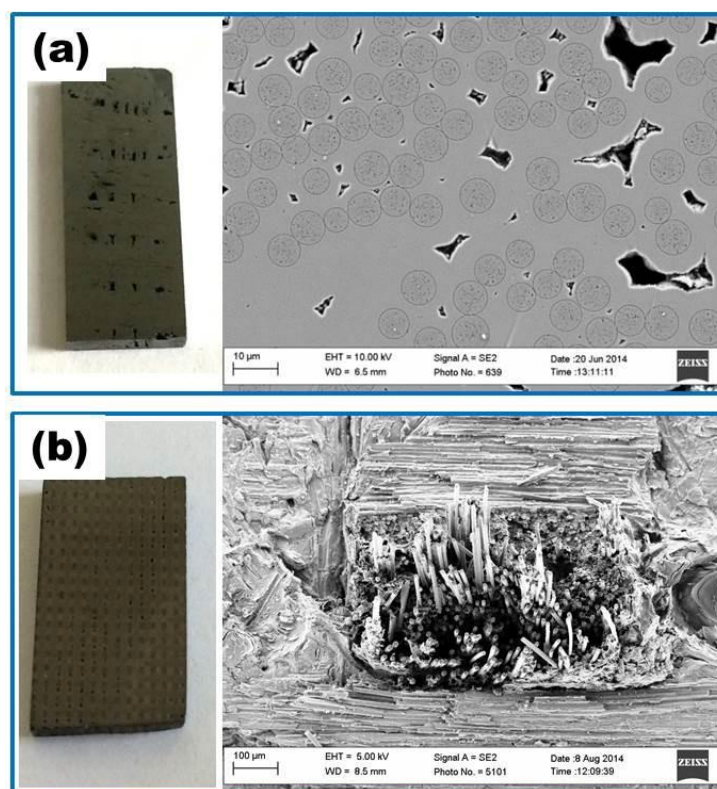


Figure 24: (a) Tyranno-SA3 CVI SiC-SiC composite and (b) FMI222 C-C composite, provided by Oak Ridge National Laboratory

Figure 25 displays the samples of nuclear grades graphite IG-110U and A3-27 as well as TRISO particles. Graphite samples were dry polished and cleaned prior to corrosion tests in molten FLiBe. TRISO particles with ZrO_2 surrogate fuel as kernel were provided by Oak Ridge National Laboratory.

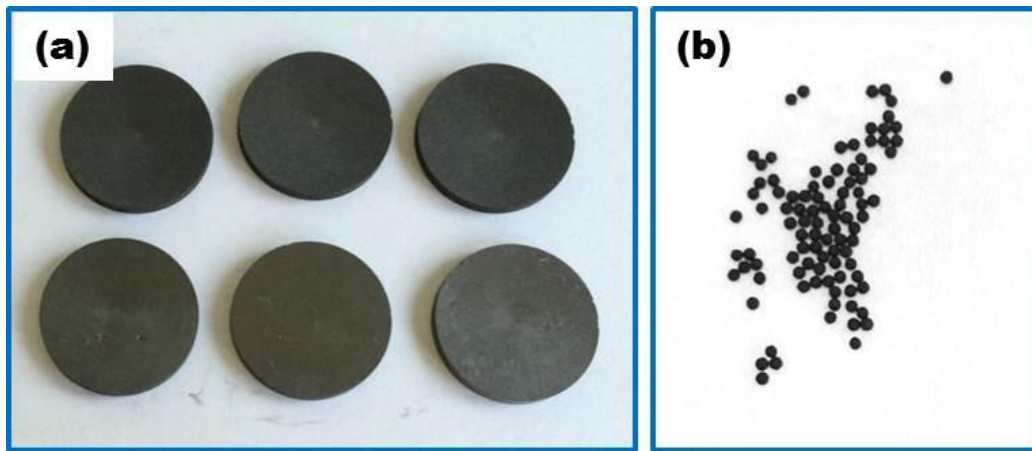


Figure 25: (a) IG-110U and A3-27 nuclear grade graphite and (b) TRISO particles with ZrO_2 surrogate as kernel.

2.3 High temperature corrosion tests

As mentioned, alloys, ceramics and graphite samples were tested in molten fluoride salts to support materials development for FHR. This study, however, focuses on the alloys corrosion in high-temperature FLiBe that is actively considering as coolant in primary cooling system in FHR. To successfully conduct corrosion tests in high temperature FLiBe, specific facilities were required to handle salt in glove box.

2.3.1 Assisting facilities for corrosion tests in FLiBe

Corrosion tests in FLiBe possess multiple experimental challenges. In addition to the glove box for the corrosion tests in molten fluoride salt, several other facilities were designed, fabricated and tested using FLiNaK salt, including molten salt transferring system, salt dripping system and temperature gradient heating rod.

First challenge was to transfer salt from purification vessel to small corrosion crucible. As shown in Figure 26, a prototype of transferring system was designed, mainly composing of molten salt vessel, furnace, pressure gas inlet and liquid salt outlet. The purified liquid salt in the vessel in furnace was pushed out by applying pressurized gas (about 2 psi) into the vessel. The liquid salt moves out through a

transferring tube that is wrapped with heating wire and thermal insulators. The temperature of salt vessel was controlled at 550°C and temperature on transferring tube was maintained at 500°C. FLiNaK salt was added in vessel to test this system. Consequently, liquid salt was efficiently transferred out, but the flow rate was difficult to control. In practice, the connection joints between transferring tube and salt vessel are the coldest points where salt is favorable to freeze and blocks whole system. Furthermore, without the use of high temperature anti-seize compound, the bolts for tightening the flange at the top of vessel were difficult to unscrew after heat treatment, which increased the difficulty to refill solid salt into the vessel. Therefore, this system was adjusted for only purifying salt in small scale (about 500g) and then salt was transferred into nickel canister or nickel tray.

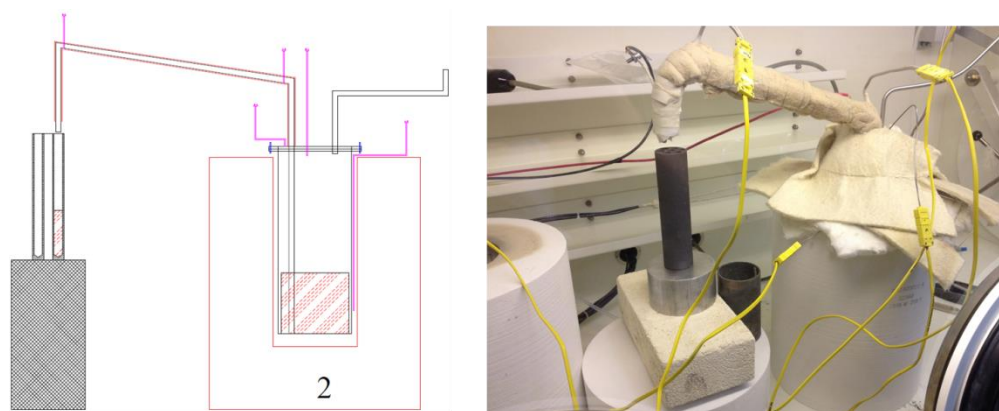


Figure 26: Molten fluoride salt transferring system.

To conduct corrosion tests in the identical crucible as in-core corrosion tests in MIT research reactor, a nuclear grade graphite corrosion crucible was selected. To fabricate this crucible, a 38.1mm diameter cylinder of nuclear graphite was cut to a 152.4mm in height. The crucible was partitioned with six, 10.3mm diameter, cylindrical capsules. However, it was a challenge to precisely fill liquid salt (~500°C) into the corrosion capsules with 10.3 mm in diameter. As shown in Figure 27, a dripping system was designed, which consists of a pure nickel container with an outlet tube at bottom and a “V” shape graphite plug connected with a rotation bar on top. Heating elements and thermal insulators were wrapped on the outer surface of nickel container and outlet tube to maintain the salt in liquid state. Rotating top handler to

release or to lock the graphite plug centered in outlet tube can control the dripping rate of liquid salt with an accuracy of 0.1g. This system mitigates the introduction of impurities into molten fluoride salt by the use of pure nickel material except for the tiny graphite plug. This whole system was flushed with purified FLiBe prior to filling salt into graphite crucible for corrosion tests. Using this system in glove box, desired mass of molten FLiBe was accurately filled into the graphite capsules, and 316 stainless steel and pure nickel lined capsules.

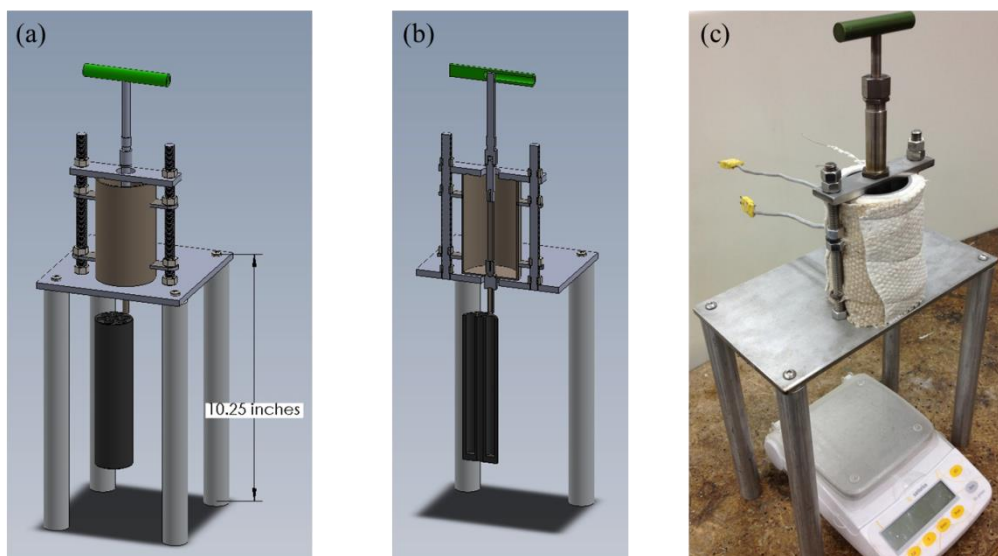


Figure 27: Molten fluoride salt dripping system.

Another challenge was the cracking of graphite crucible during re-melting the filled salt for loading samples and for starting corrosion tests in furnace. Salt volume usually expands as it transitions from solid state to liquid state, which causes graphite crucible cracking if salt starts re-melting from bottom. As shown in Figure 28, salt leaked out from the cylindrical capsule but the crack was invisible. In the practice runs with FLiNaK salt, the bottom of graphite crucible broke and salt leaked out into graphite holder after repeating freezing-thawing twice.

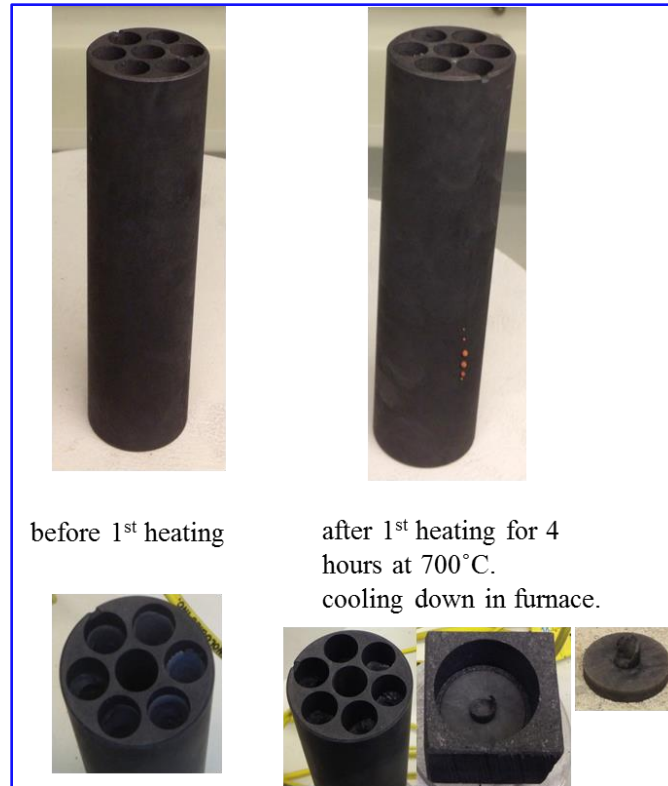


Figure 28: Graphite corrosion crucible (left) before and (right) after re-melting FLiNaK salt in six cylindrical capsules.

To simulate the re-melting approach in reactor, a temperature gradient heating rod was designed and fabricated. The temperature distribution from top to bottom on this rod was governed by the wrapping density of heating wire. The main purpose of using this heating rod was to re-melt salt from top to bottom which avoids the crack of graphite crucible due to salt volume expansion. To examine the temperature differences, three thermocouples were attached on three different spots of rod heater. Figure 29 shows the temperatures profiles on three spots and about 100°C difference exists on the rod from top to bottom. With the assistance of this rod heater, the graphite crack problem was addressed while re-melting FLiNaK salt in graphite capsules. This system was applied to the corrosion tests of materials in molten FLiBe and no leakage was observed.

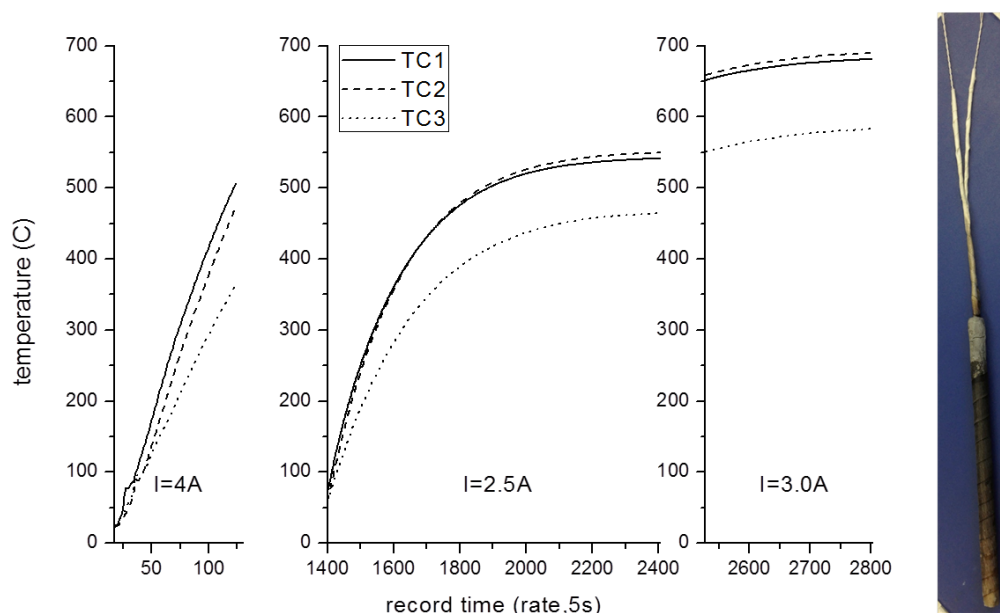


Figure 29: Temperature profiles showing the temperature difference from top to bottom of temperature gradient heating rod, and a picture of tested heating rod.

2.3.2 Practice of high temperature corrosion tests in $KF-ZrF_4$

The main purpose of performing corrosion tests in $KF-ZrF_4$ (58-42 mole%) was to pre-examine the feasibility of double-walled corrosion crucibles for processing FLiBe. As shown in Figure 30, double-walled corrosion crucible is mainly consisted of inner pure nickel container and outer 316 stainless steel canister. The use of inner pure nickel container is to mitigate the impurities from corrosion of crucible material during high temperature corrosion tests. The diameter of the pure nickel container was 141.3mm and the 316 stainless steel canister was 168.3mm. The nickel container could accommodate 4.5kg molten $KF-ZrF_4$ (58-42 mole%). Three 316 stainless steel tubes ($\Phi=44.5mm$) with sealing flanges were welded on the top of 316 stainless steel canister. A stainless steel ring was welded inside of each tube for holding samples assembly (Figure 30(c)). Thermocouples shielded by pure nickel tubing ($\Phi=6.4mm$) were inserted into molten salt for monitoring and controlling salt temperature. Other two tubes ($\Phi=12.7mm$) on

top of stainless steel canister are inlet and outlet of carry gas. This design enables the sample holders vertically sliding up and down at high temperature. In this corrosion system, all materials contacting with molten salt are made of pure nickel.

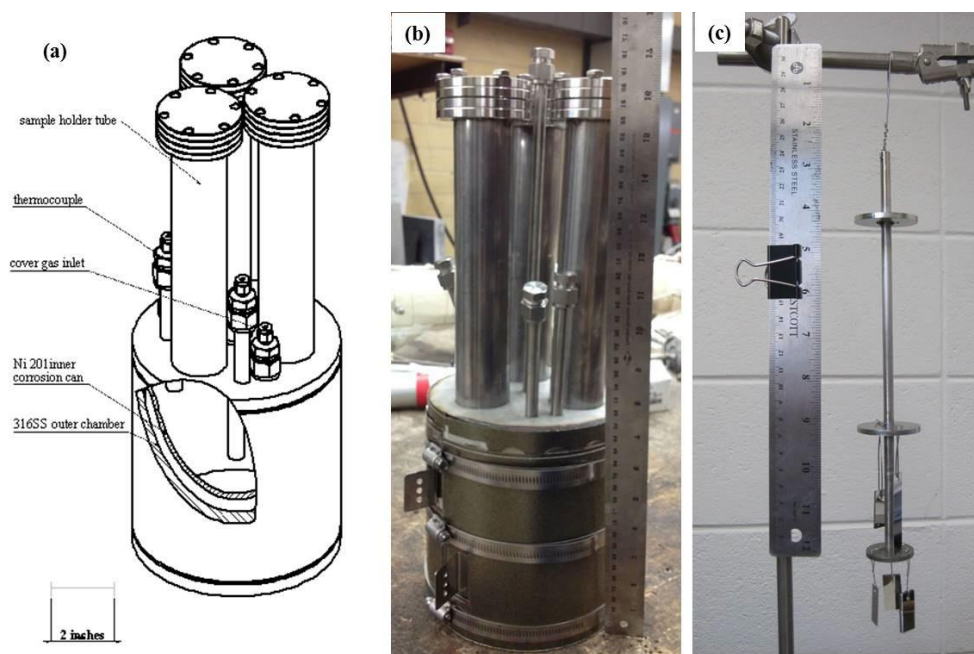


Figure 30: (a) Cut away schematic drawing and (b) picture of double-walled corrosion crucible mainly composing of pure nickel inner container and 316 stainless steel outer canister, (c) pure nickel sample holder with five attached samples.

2.3.3 Ni-Cr model alloys corrosion in FLiBe

As shown in Figure 31(b), pure nickel corrosion crucibles were used for the corrosion tests to avoid the crucible material effect on corrosion behavior in molten FLiBe. To remove possible impurities on crucible wall, the cleaned nickel crucibles were further baked at 850°C for 24 hours with flowing gas of 10% H₂ balanced N₂ through furnace. The depth of liquid salt in each capsule was about 127 mm. The salt in capsules was pre-heated to about 550°C for suspending samples in molten salt through a pure nickel wire (0.5 mm in diameter). The nickel wire was fixed on the top lid. The position of samples in liquid salt for corrosion tests is demonstrated in Figure 31(a).

Simultaneously, three samples of Ni-5Cr and Ni-20Cr encapsulated in quartz tubes were heated in the same furnace as that for corrosion tests in FLiBe. To minimize the oxidation during annealing tests, as shown in Figure 31(d), cleaned samples were sealed in Ar filled quartz tubes. The quartz tubes were repeatedly pumped and filled Ar gas three times to create an inert atmosphere for annealing alloys. The temperature of furnace was maintained at $700 \pm 1^\circ\text{C}$ for annealing and corrosion tests in an inert atmosphere glove box. Two devices associated with glove box monitor the oxygen and moisture level of experimental environment, both less than 5ppm.

The heat treated samples were removed after periods of 50 hours, 500 hours and 1000 hours in furnace. The system for testing the salt samples and the quartz tube encapsulated samples is shown in Figure 32. All samples cooled down in glove box. FLiBe-exposed samples were cleaned in deionized water and then dried in air for microstructural analysis, as shown in Figure 32(c).

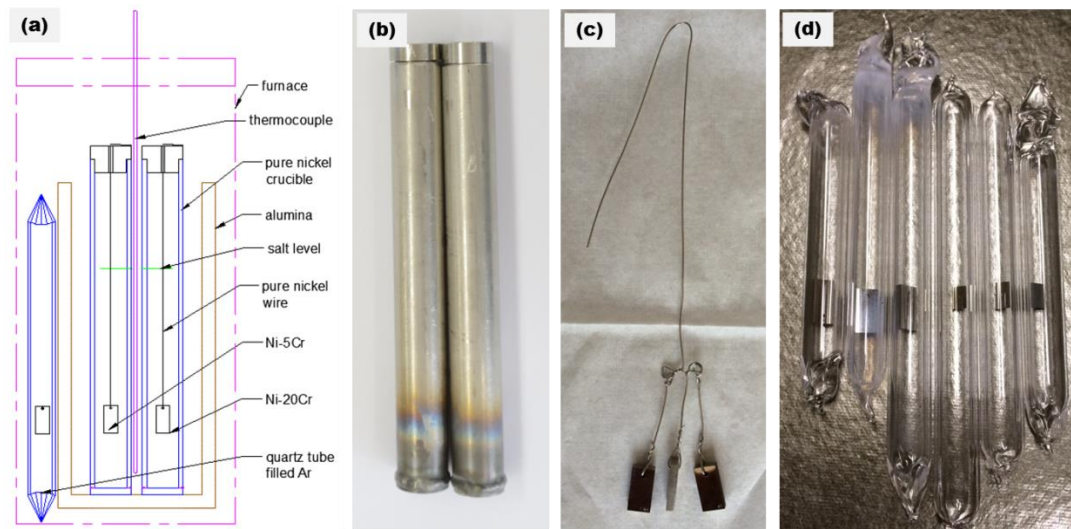


Figure 31: (a) Schematic diagram of annealing and corrosion tests in furnace, (b) pure nickel corrosion crucible, (c) pendent coupons under fixture of nickel wire for corrosion tests in FLiBe and (d) sealed coupons in Ar filled quartz tubes for annealing experiments.

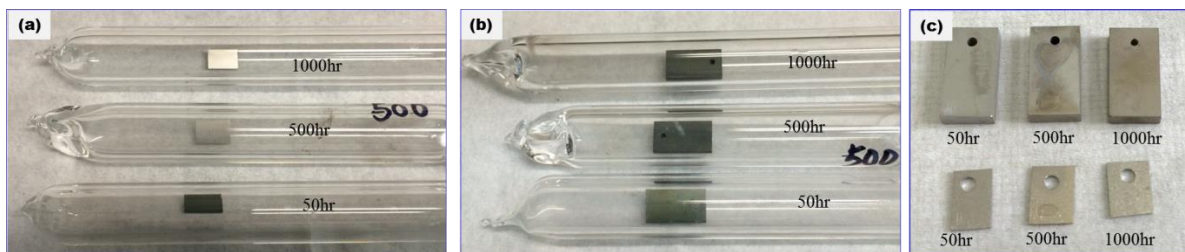


Figure 32:(a) annealed Ni-5Cr and (b) annealed Ni-20Cr alloys in Ar filled quartz tubes at 700°C for 50, 500 and 1000 hours, (c) FLiBe-exposed Ni-20Cr and Ni-5Cr samples that were cleaned in deionized water.

2.3.4 Structural materials corrosion in FLiBe

In support of materials development, different candidate structural materials were discussed in the workshops of FHR (2012-2014). To evaluate the compatibility of these materials with molten FLiBe, two stages of static corrosion tests were accomplished in the identical corrosion crucible to the in-core corrosion tests performed in MIT research reactor. Table 6 summarizes the capsule materials, samples and salt conditions for the corrosion tests in high temperature molten FLiBe. Pure nickel liner and 316 stainless steel liner were inserted into graphite capsules to separate liquid salt from contacting the graphite. The graphite effect on alloys corrosion behavior in molten salt was investigated by comparing the corrosion tests in liners to those in graphite. Additionally, the corrosion tests of 316 stainless steel and SiC-SiC composites in Be-reduced FLiBe were completed to investigate the salt redox potential effect on materials corrosion. The corrosion temperature and duration for all tests in Table 6 was 700°C and 1000 hours respectively. The corrosion temperature of 700°C was selected as this is the presently intended FHR outlet temperature.

Table 6: Capsule materials, samples and salt conditions for the corrosion tests in molten FLiBe, at 700°C.

Test stage	Crucible order	Capsule materials	Samples	FLiBe condition
FS-1 (2013)	1	1-1, graphite IG-110	Hastelloy N	HF and H ₂ sparge
		1-2, pure nickel liner	Hastelloy N	
		1-3, graphite IG-110	TRISO particles	
		1-4, graphite IG-100	316 stainless steel	
		1-5, 316 stainless steel	316 stainless steel	
		1-6, graphite IG-110	CVD-SiC, SiC-SiC	
FS-2 (2014)	2	2-1, graphite IG-110U	IG-110U, A3-27	HF and H ₂ sparge
		2-2, graphite IG-110U	SiC-SiC, TRISO	
		2-3, graphite IG-110U	C-C composite	
	3	3-1, graphite IG-110U	316 stainless steel	Be further reduced
		3-2, graphite IG-110U	316 stainless steel	
		3-3, graphite IG-110U	SiC-SiC, TRISO	

Figure 33 displays the pictures of two stages of corrosion tests in high temperature FLiBe. All these crucibles with filled FLiBe and samples were in inert atmosphere glove box while taking these pictures. The outer diameter of all graphite crucibles is 38mm due to the space limitation in MIT research reactor. In the first stage corrosion tests (FS-1), six capsules were machined on a graphite (IG-110) cylinder (Figure 33(a)). In the second stage corrosion tests (FS-2), only three capsules were machined on graphite cylinder to enlarge the volume of molten salt per capsules. As shown in Figure 33(b) and Figure 33(d), the wires for suspending alloy coupons in molten salt were fixed on the top graphite lids.

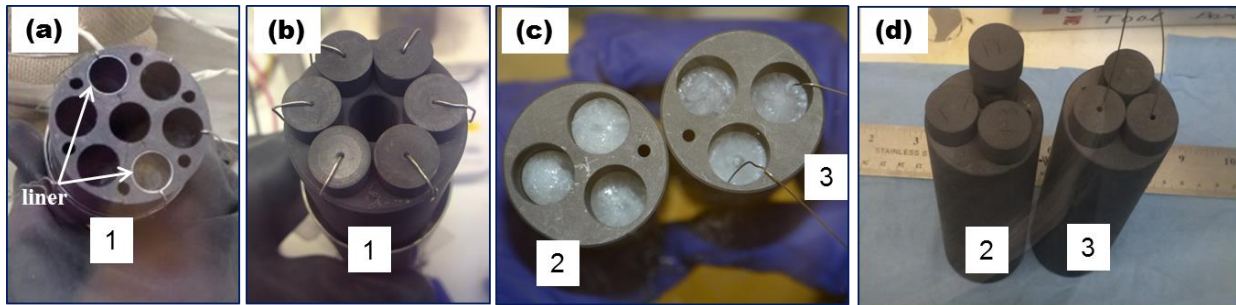


Figure 33: (a, b) FS-1 stage and (c, d) FS-2 stage of structural materials corrosion tests in FLiBe, without and with graphite lids on top.

Furthermore, to investigate the corrosion rate as a function of corrosion time, a long-term corrosion tests of 316 stainless steel in FLiBe were carried out using the same corrosion crucible as shown in Figure 33(a, b). Alloy coupons were exposed to purified FLiBe salt at 700°C for 1000, 2000 and 3000 hours, in both graphite and in 316 stainless steel lined capsules.

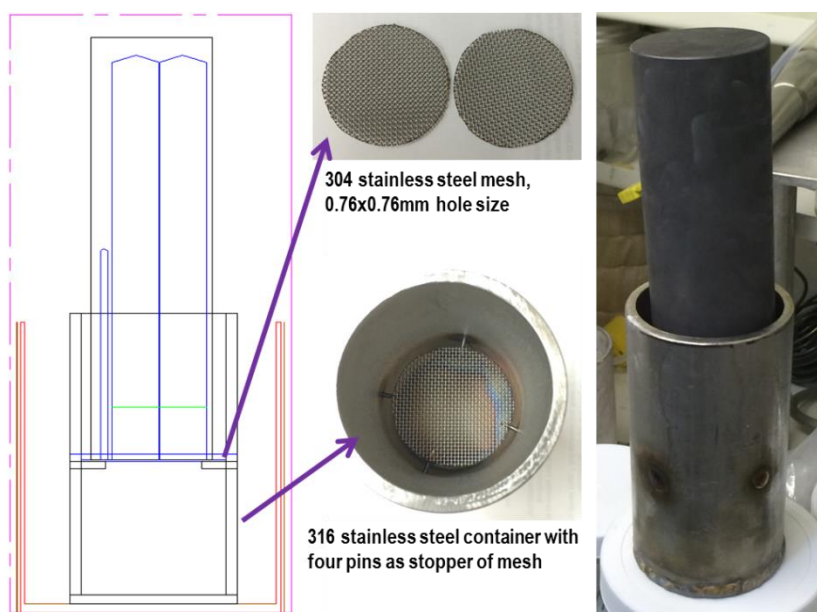


Figure 34: Post-corrosion samples collection system, consisting of 316 stainless steel container with four pins and a stainless steel mesh.

After corrosion test, alloy samples which were suspended with wires were easily removed from liquid salt by vertically lifting wires. Other post-corrosion samples such as SiC, graphite as well as TRISO particles were collected from molten FLiBe using the system shown in Figure 34. The graphite crucible was flipped over and put it on a stainless steel mesh that functioned as a filter. All post-corrosion samples were cleaned by soaking and rinsing in deionized water, and dried in air for microstructural analysis.

2.4 Post-corrosion examination

For safety consideration, cleaned post-corrosion samples were pre-examined using elemental analysis technique to ensure no residual Be remained on corrosion surface prior to microstructure characterization.

Experiments indicated that FLiBe-exposed alloys samples can be cleaned by soaking samples in deionized water for 24 hours.

2.4.1 Weight change

In most reports on the evaluation of materials corrosion, weight change is a typical parameter to compare corrosion rate by assuming uniform constituent depletion or uniform oxides formation. It is simply calculated from the weight change before and after corrosion tests divided by exposure area. In this study, weight change (mg/cm^2) of the samples tested in molten FLiBe was calculated from formula $\Delta W = (M - M_0)/A$, where M_0 and M is the mass of samples before and after corrosion test, A is exposure area of samples.

Weight change criteria assumes uniform Cr depletion through thermal diffusion outwardly from alloy matrix, or homogeneous oxide layer formation on surface. However, in practice, grain boundary diffusion more severe in depth than volume diffusion occurs in molten salt. For instance, Cr outward diffusion and C inwardly diffusion takes place simultaneously while alloys submerging into the molten fluoride salts in graphite crucible. For such situation, weight change cannot provide sufficient information to understand materials corrosion behavior in molten fluoride salt. Therefore, microstructural analysis was deemed as the most direct approach to reveal the reactions between alloys and their surroundings.

2.4.2 Microstructural characterization

The surface morphology of post-corrosion samples was observed under field emission Scanning Electron Microscope (SEM, LEO 1530) operated with 5 keV acceleration high voltage and $30\mu\text{m}$ aperture size. SEM equipped with Energy Dispersive Spectroscopy (EDS) was employed to map elemental distribution. Operational parameters of EDS analysis are 15 keV acceleration high voltage and $120\mu\text{m}$ aperture size.

The structure of post-corrosion samples surface was analyzed by using x-ray powder diffractometer (XRD, Siemens Stoe), using Cu radiation ($K\alpha=0.15418\text{nm}$), at a step size of 0.02° in 2θ scanning mode. According to the profiles of characteristic d-spacing calculated from Bragg's law of $n\lambda=2d\sin\theta$ vs. extrapolation function of $\cos^2\theta/\sin\theta+\cos^2\theta/\theta$, the accurate lattice parameter was obtained from the intercepts of profiles on y axis.

K-Alpha x-ray photoelectron spectroscopy (XPS) is a surface-sensitive quantitative spectroscopic technique that measures the elemental composition, chemical state and electronic state of the elements within a material. This technique was applied to analyze Cr on both as-received and FLiBe-exposed Ni-Cr model alloys' surface using characteristic spectrum in the range of binding energy from 570ev to 595ev.

The cross-sectional microstructure of post-corrosion sample was analyzed by combining SEM-EDS and Electron Backscatter Diffraction (EBSD) techniques. EBSD analysis was performed on LEO-1530 SEM incorporated with TSL (TexSEM Laboratory, Inc.) Orientation Imaging Microscopy (OIM). OIM measurements can be used to create visualizations of the spatial distribution of crystallographic orientation providing a practical and innovative tool to link orientation and microstructure. The SEM was operated at 15keV for EDS scanning and at 20keV for EBSD data collection. Alpha phase and gamma phase iron data were pre-loaded into OIM data collecting system to identify both phases distribution in cross-section. Grain size distribution, grain orientation, phase distribution as well as grain boundary character distribution were collected from the same region as EDS scanning. Collected EBSD data was then cleaned up using TSL-OIM data analysis software, as standard cleanup processes[77], [78].

For EBSD measurements, sample was mounted on a sample holder, and then the sample holder was tilted 70° for better pattern quality. Figure 35 shows the geometry of the sample setup after tilting sample holder. Using default setting of the sample direction [001], inverse pole figure (IPF) can present crystal direction relative to the crystal reference frame. In this thesis, if not specifically explained, all IPF maps are created on TD-RD plane, without any rotation during processing collected data, and are relative to the

default [001] reference crystal direction. The neighbor grains misorientation angle was measured by defining one grain's orientation (that was originally relative to [001]) as the reference direction.

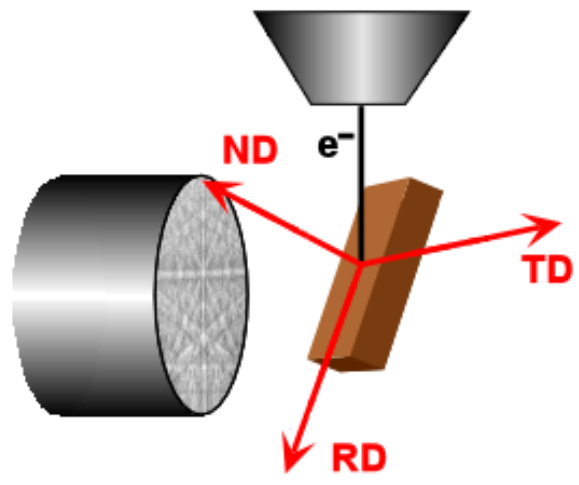


Figure 35: Geometry of the sample setup for EBSD measurement. ND, RD, and TD denote normal direction, rolling direction, transverse direction, respectively.

To further analyze the microstructure of near surface corrosion region, particularly on carbide containing layer, Hastelloy N and 316 stainless steel samples tested in graphite capsule were selected for Scanning Transmission Electron Microscope (STEM, Titan, FEI) and EDS analysis studies. Focused Ion Beam (FIB, ZEISS 1540XB CrossBeam) milling technique was applied to prepare STEM sample. Approximately 2 μ m thick Pt cap was deposited on a target area to protect original corrosion surface before FIB milling. Subsequently, a sample with dimensions of 20 μ m \times 15 μ m \times 2 μ m was lifted out, and then welded on a STEM sample grid. Both sides of the lift-out sample were gently milled to electron transparency using low milling current for the following STEM analysis. Bright field and dark field STEM images were collected from an area near to corrosion surface. The composition of particles was analyzed using STEM-EDX technique.

2.4.3 Size distribution of graphite particles in FLiBe

Zetasizer (Malvern Instruments) was applied to measure graphite particle size distribution (PSD) in the molten FLiBe in graphite corrosion capsule. After corrosion test, 0.173g solid salt was dissolved into 60 ml deionized water on magnetic stirrer at room temperature. About 1 ml solution was added into a disposable polystyrene cuvette for PSD measurements, running three cycles. The morphology of the graphite particles were observed under SEM by filtering out particles from the FLiBe solution.

Chapter 3: Results and discussion

This chapter includes four main subsections (1) Ni-Cr model alloys corrosion in molten FLiBe, (2) Hastelloy N corrosion in molten FLiBe, (3) 316 stainless steel corrosion in molten FLiBe, and (4) the thermal diffusion controlled corrosion model and the discussions on the main corrosion factors. Corrosion results are presented and discussed in first three subsections. The corrosion of Ni-Cr model alloys provides insights into the basic corrosion mechanisms of Cr depletion and dissolution in molten fluoride salts. The corrosion of both commercial alloys: Hastelloy N, a type of nickel-base alloys developed during MSRE specifically for the application in molten fluoride salts, and 316 stainless steel, an ASME code certified alloy for applications in nuclear energy systems, gives a full understanding of both alloys corrosion behavior in molten FLiBe, which are valuable references for supporting structural alloys development for FHR. The corrosion rate in terms of the maximum Cr depletion distance in tested alloys was experimentally determined based on the microstructural analysis. In section 4, a long-term corrosion prediction model was fundamentally derived based on the understanding of alloys corrosion in FLiBe, and successfully validated by fitting with experimental profiles of Cr depletion.

3.1 Corrosion of Ni-Cr model alloys in high temperature FLiBe

3.1.1 Overview

Earlier corrosion tests of nickel-base alloys in molten fluoride salts showed excellent corrosion resistance compared to other alloys[36], [53], [79]–[81]. Some investigations suggest that Cr depletion and dissolution into molten salt in terms of Cr ions is the main corrosion mechanism causing alloys degradation[75], [82]–[85]. Since the inner regions of alloys (i. e., bulk) does not contact molten salt, the rate of Cr depletion is highly dependent on the thermal diffusion coefficient of Cr in the alloys. In early corrosion reports, the thermal diffusion coefficient of Cr in the alloys in molten salts was simply calculated from the weight loss by assuming a constant diffusion source and uniform Cr depletion[45],

[48]. However, the microstructure dependence of Cr depletion in the alloys exposed to molten fluoride salts has not been well understood.

Alloys usually experience microstructural changes in the bulk during corrosion in high temperature molten salt such as sensitization and phase transformation[86]–[88]. High temperature induced microstructural instability is complicated due to the multiple constituents interactions within alloys[89]–[91]. To simplify the study of high temperature corrosion, model alloys are usually selected as the samples such as Ni-Cr binary alloys and Ni-Fe-Cr alloys[40], [40], [67], [68], [92]. In those investigations, the thermal diffusion of Cr was studied by introducing a constant diffusion source on the alloys surface or exposing alloys to a high temperature oxidizing environment. The diffusion approach of Cr isotope was from surface to inside of alloys. The oxidation occurred on alloys' surface could induce Cr outward diffusion, but only in a short range because the oxide film on alloys' surface protects alloys from further attack or at least functioned as Cr diffusion barrier.

Unlike the oxidation environment and infinite diffusion couples, in molten salt, the oxide products on alloys surface dissolve into salt, resulting in fresh surface all the time. Compared to the thermal diffusion rate of Cr through alloy matrix ($\sim 10^{-20} - 10^{-15} \text{ m}^2/\text{sec}$), the chemical reactions between Cr metal and F^- ions occur quickly at the interface of alloy and molten salt. The chemical reaction rate depends on the conditions of molten salt such as impurities, redox potential and temperature gradient as well[39], [55], [75]. Under normal conditions, Cr is fluorinated immediately as it diffuses outwardly to the alloys' surface. The Cr^{2+} ions diffuse into molten salt quickly ($D_{\text{Cr}^{2+}/\text{FLiBe}} = 0.73 \pm 0.2 \times 10^{-9} \text{ m}^2/\text{sec}$ at 700°C)[49] compared to the Cr thermal diffusion coefficient within alloys. The concentration of Cr on corrosion surface could be near zero. Therefore, the existence of concentration gradient continuously drives Cr outward diffusion.

This section focuses on the corrosion of Ni-5Cr and Ni-20Cr (wt.%) model alloys in purified molten FLiBe in pure nickel capsules at 700°C . Simultaneously, to investigate the thermal effect on the

microstructure, a series of samples were annealed in Ar filled quartz tubes in the same furnace as the corrosion tests. Then, the Cr depletion induced by molten fluoride salt corrosion can be determined by comparing the microstructure of salt-exposed samples to annealed ones. The crystal orientation dependence on Cr depletion was also studied through crystallographic analysis.

3.1.2 Characterization methods

The details of sample preparation and corrosion tests in molten FLiBe are described in chapter 2. The FLiBe salt used in this work was provided by Oak Ridge National Laboratory (ORNL). It was purified using a hydrofluorination process in our laboratory prior to corrosion tests; the purification procedures are provided in reference[65]. The temperature for corrosion tests and annealing is 700°C and durations are 50 hours, 500 hours and 1000 hours.

Weight change (mg/cm^2) of the samples tested in molten FLiBe was calculated and the microstructure of the alloys before and after corrosion tests in molten salt was analyzed using optical microscopy, scanning electron microscopy (SEM), x-ray diffraction patterns (XRD) equipped with energy-dispersive x-ray spectroscopy (EDS), electron backscattering diffraction (EBSD) as well as k-alpha x-ray photoelectron spectroscopy (XPS). The polished surface was slightly etched in a solution of 45ml HCl+15ml HNO₃+20ml methanol for ~10 seconds for EBSD analysis. The d-spacing of (111), (200) and (220) were calculated by using typical Bragg's law $n\lambda=2d\cdot\sin\theta$, where $\lambda=0.15418\text{nm}$ for Cu $k\alpha$ radiation for XRD. To determine the accurate lattice parameters of the alloys before and after corrosion testing, calculated d-spacing was profiled vs. extrapolation function $(\cos^2\theta/\sin\theta + \cos^2\theta/\theta)$, and the profiles intercepted with y-axis.

3.1.3 Microstructure of pre-corrosion alloys

Figure 36 and Figure 37 show the optical image, SEM image and EBSD auto grain image as well as the grain size distribution of Ni-5Cr and Ni-20Cr model alloys before annealing and corrosion tests.

Although Ni-5Cr alloys experienced cold rolling and a one hour heat-treatment, the grain size of Ni-5Cr is still larger than as-received Ni-20Cr. The mean grain size was in the range of $\sim 100\mu\text{m}$ - $200\mu\text{m}$ and $\sim 10\mu\text{m}$ - $30\mu\text{m}$ for Ni-5Cr and Ni-20Cr respectively. The grain size strongly depends on the manufacturing process. The vacuum induction melting, casting and hot isostatic rod shape forming allowed grains to coarsen in the Ni-5Cr samples. The hot rolling of the Ni-20Cr as-received plate led to smaller grain sizes.

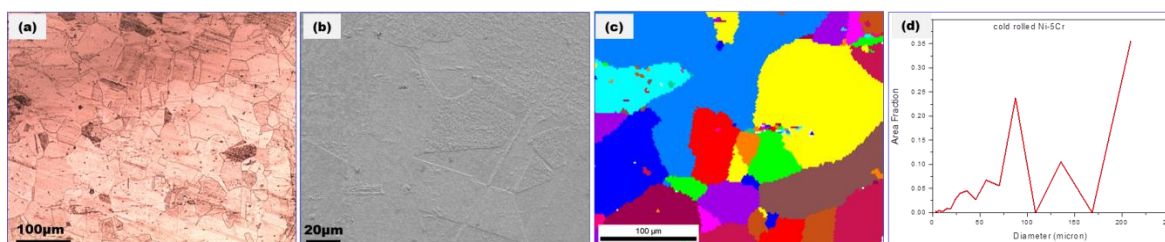


Figure 36: (a) Optical image (b) SEM image (c) EBSD auto grain image and (d) grain size distribution of Ni-5Cr alloy before corrosion testing.

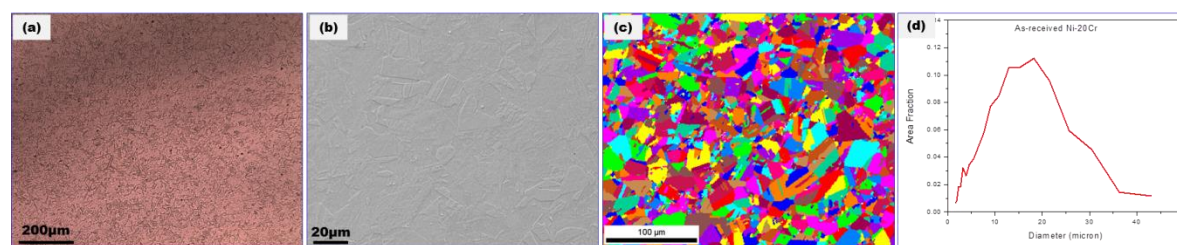


Figure 37: (a) Optical image (b) SEM image (c) EBSD auto grain image and (d) grain size distribution of as-received Ni-20Cr alloy before corrosion testing.

3.1.4 Surface morphology of annealed alloys

The main purpose of annealing the model alloys (in argon back-filled quartz capsules) at the same temperature as corrosion tests was to investigate the thermal effect on the Cr depletion from the alloys that are exposed to an inert atmosphere, without the presence of molten salt. To create an inert atmosphere for annealing, the samples were sealed in Ar filled quartz tubes that were repeatedly vacuumed and refreshed with high purity Ar gas. Although the quartz tubes were filled Ar gas, the surface

of all annealed Ni-Cr samples was oxidized, as shown in Figure 38. These surface SEM images clearly display that a layer of discontinuous Cr_2O_3 film formed on the Ni-5Cr alloy surface after 500 hours, and the surface of Ni-20Cr alloy was fully covered by an oxide layer after the initial 50 hours. Higher magnification SEM images show round oxide particles on Ni-5Cr samples and the mixture of needle-like and hexagonal particles on Ni-20Cr sample surfaces. The difference in the shape of oxide particles between Ni-5Cr and Ni-20Cr is probably relevant to Cr content in the alloys. The size of the oxide particles formed on the Ni-20Cr alloy surface increases with increasing annealing time. This suggests that the alloys containing higher Cr concentration are more favorable to be oxidized under identical high temperature environment. Furthermore, for cold rolled Ni-5Cr samples, the grains obviously coarsened and extruded out from the thin layer of chromium oxides after 50 hours to 500 hours annealing. This is probably indicative of the microstructural instability of Ni-5Cr during annealing at high temperature. For Ni-20Cr, in contrast, the extruded grain was not observed after 1000 hours annealing.

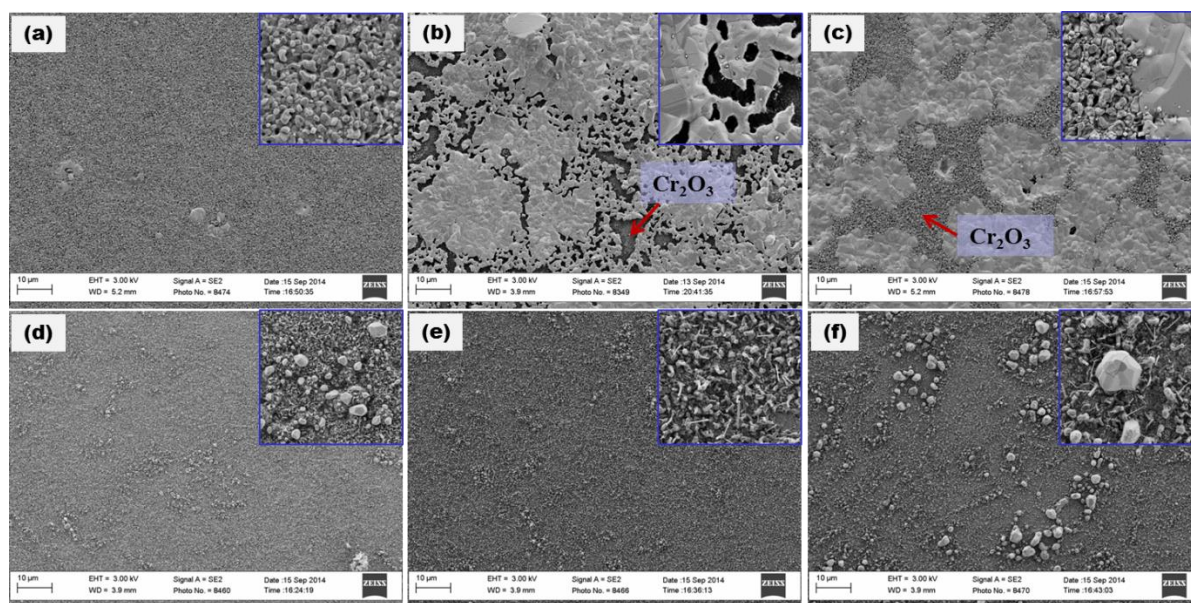


Figure 38: Surface SEM images of (a, b, c) Ni-5Cr and (d, e, f) Ni-20Cr samples annealed at 700°C for 50, 500 and 1000 hours respectively. Inset on upper right corner is high magnification SEM image clearly presenting microstructural features.

3.1.5 Cross-sectional microstructure of annealed alloys

Figure 39 shows the cross-section of annealed alloys with varying annealing time. For the Ni-5Cr alloy, the surface profile is relatively rough compared to Ni-20Cr. This is in agreement with the surface observation of extruded grains and a discontinuous oxide layer. Ni-5Cr samples experienced cold work in laboratory, which introduced lots of structure defects. These defects induced significant change in the microstructure such as grain coarsening and grain boundary reorientation within Ni-5Cr samples during annealing at 700°C. On the surface of annealed Ni-20Cr, a thin oxide layer, approximately 0.5µm, is clearly observed from the cross-sectional images. The thickness of this oxide layer does not change with annealing time. This means this oxide layer is very stable at high temperature, and it functioned as a protective film against further oxidation of the alloy.

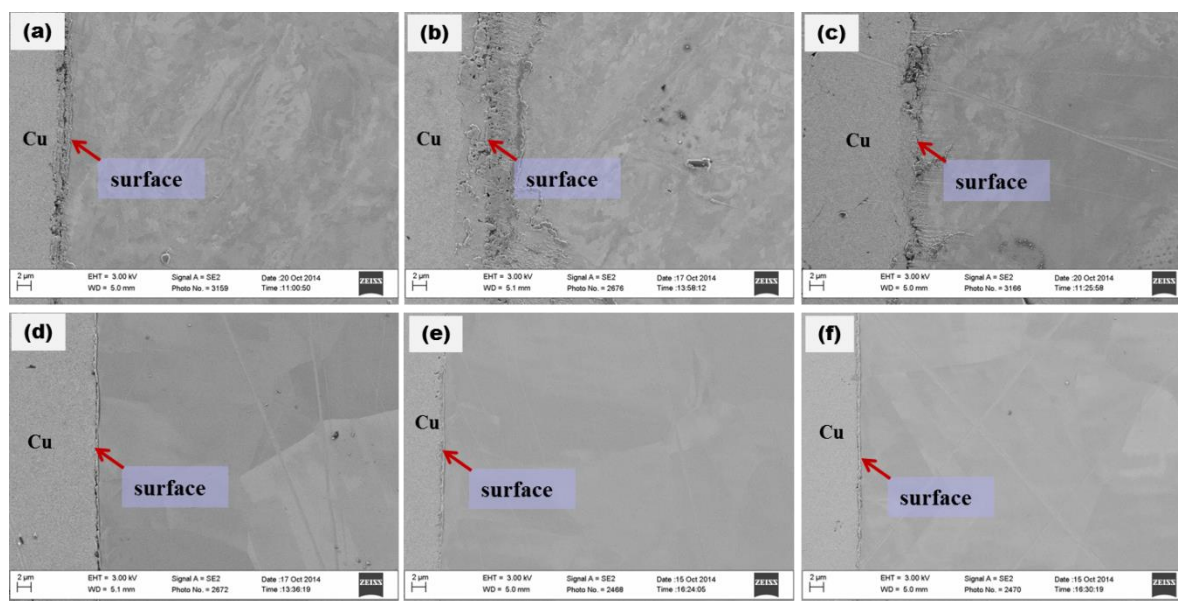


Figure 39: Cross-sectional SEM images of (a, b, c) Ni-5Cr and (d, e, f) Ni-20Cr annealed at 700°C for 50, 500 and 1000 hours respectively.

The elemental distribution in the near surface layer of 1000 hours annealed Ni-5Cr and Ni-20Cr is shown in Figure 40 EDS mappings. The relatively high concentration of Cr and O on the surface of annealed samples indicates the formation of chromium oxide phase that formed on surface during

annealing. Cr depletion in the near surface layer is not observable from Cr distribution mappings. It is possible that the chromium oxides formed on these alloys' surface might lead to very short Cr depletion distance (several nanometers) underneath the oxide layer. Since these alloys were annealed in Ar filled quartz tubes, the result here is different from the reported investigations of the Cr depletion in a range of tens microns as nickel-base alloys were aged in hot air or water[92]–[94]. Furthermore, a discontinuous Ni layer was observed on the surface of annealed Ni-5Cr alloy, which corresponds to the surface observation of coarsened and extruded grains.

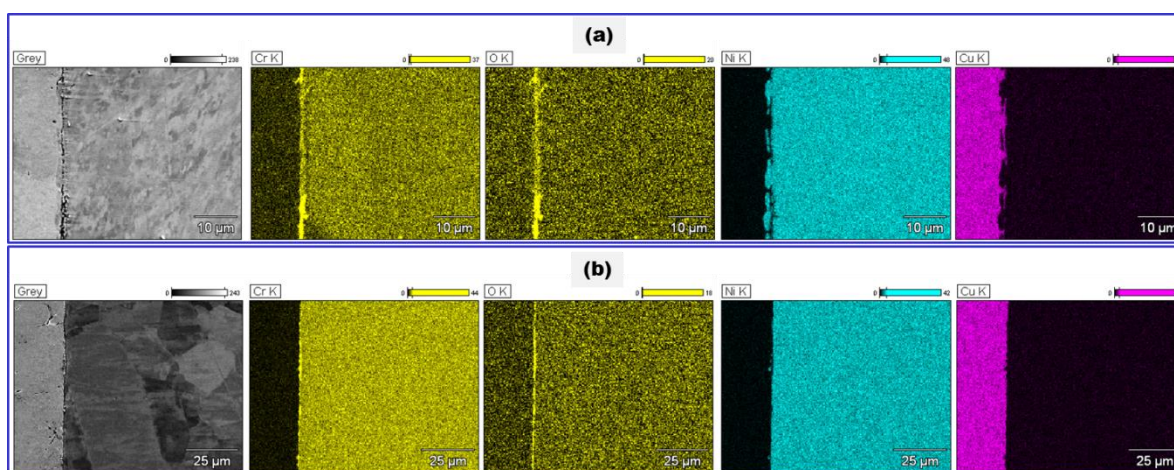


Figure 40: EDS mapping of Cr, O, Ni and Cu element in the near surface layer of (a) Ni-5Cr and (b) Ni-20Cr. Both were annealed at 700°C for 1000 hours.

Figure 41 shows the quantitative Cr and O concentration in the near-surface region of the Ni-5Cr sample that was annealed at 700°C for 1000 hours in an Ar filled quartz tube. From this profile, an approximately 1.6μm thick oxide film formed on the surface, which induced about a 1μm Cr depleted (~80% of initial Cr concentration) zone underneath the oxide layer. All other annealed Ni-Cr alloys show similar Cr and O concentration profiles. The chromium oxide film on the alloy surface protects the alloy from further degradation by the means of Cr depletion. The 1μm layer of slight Cr depletion is negligible compared to the Cr depletion distance observed in 1000 hours corrosion tests on Ni-5Cr sample.

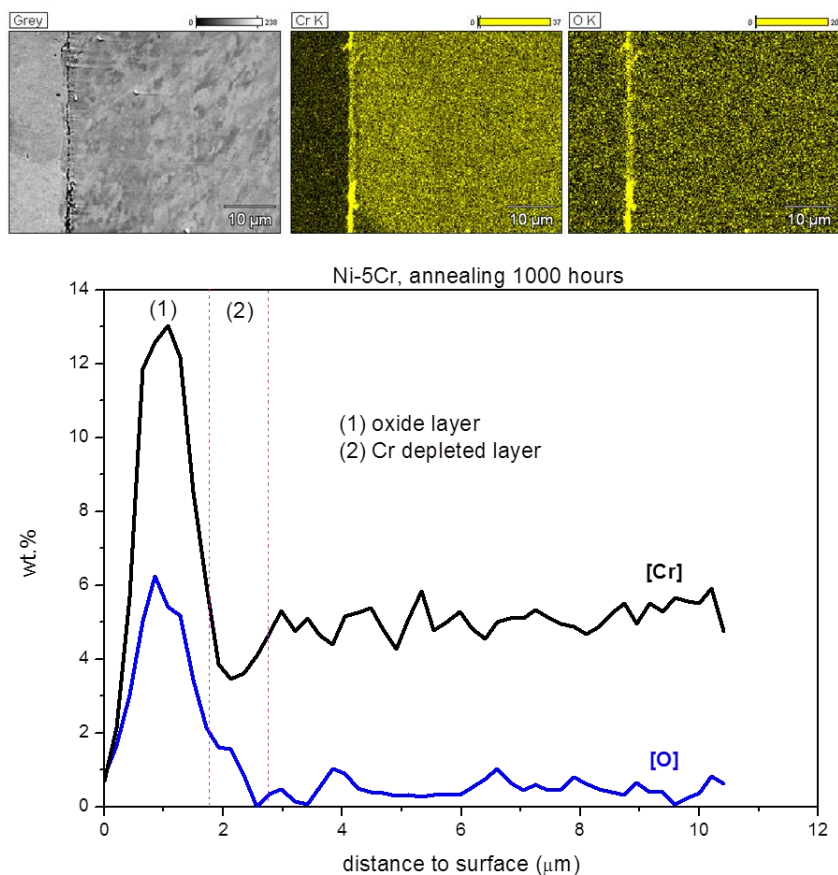


Figure 41: Quantitative analysis of the Cr and O concentration profile in the near surface of Ni-5Cr sample annealed at 700°C for 1000 hours.

The Cr depletion distance in the annealed Ni-Cr alloys is negligible. However, the high temperature treatment might change alloy microstructure such as grain growth and grain boundary migration, and carbides precipitates at grain boundary and phase transformation. This microstructural evolution affects alloys' corrosion behavior in high-temperature molten fluoride salts. These considerations complicate the prediction of Cr depletion distance in Cr containing alloys in high-temperature molten fluoride salt. They will be further discussed in the following analysis.

3.1.6 Weight change of post-corrosion alloys

All post-corrosion Ni-Cr alloys lost weight, ranging from -0.07 to -0.42 mg/cm² and from -0.67 to -7.11 mg/cm² for Ni-5Cr and Ni-20Cr respectively, as shown in Figure 42. The weight loss results from the Cr depletion from alloys and then dissolution into molten salt in form of chromium fluoride. It has been reported that the Cr depletion rate is governed by its thermal diffusion coefficient through the alloy matrix[45], [48]. Assuming uniform Cr depletion from alloys, the calculation of weight loss per unit area (mg/cm²) is expressed in Equation (21) if effective diffusion coefficient (D_{eff}) is known. In reverse, the D_{eff} can be calculated from the known weight loss.

Following this calculation, the weight loss is a linear function of square root of corrosion time. Figure 42 shows the weight loss vs. square root of the corrosion time, and linear trend lines of corrosion Ni-5Cr and Ni-20Cr samples. R^2 -value of 0.9894 and 0.9004 indicates a good fit for both trend lines and the experimentally derived data points. The slope of these trend lines equals to $2C_0(D_{\text{eff}}/\pi)^{1/2}$. As a result, the D_{eff} of Cr is calculated to be 1.66×10^{-17} m²/sec and 2.74×10^{-16} m²/sec for Ni-5Cr and Ni-20Cr at 700°C. The calculated D_{eff} is close to the reported overall diffusion coefficient of Cr in Ni at 700°C, $\sim 10^{-16}$ m²/s[46], [68]. The D_{eff} for Ni-20Cr is about 16.5 times higher than that for Ni-5Cr mainly due to the smaller grain size and higher Cr concentration. The reported data shows that the grain boundary diffusion coefficient ($D_{\text{gb}} = 10^{-19} \sim 10^{-17}$ m²/sec) is approximately one order higher than volume diffusion coefficient ($D_{\text{v}} = 10^{-20} \sim 10^{-18}$ m²/sec) at 700°C for different nickel base alloys[51], [67], [95]. Here, the grain boundary width of $\delta = 1$ nm is assumed. It is very likely that the corrosion in high-temperature molten salt drives Cr outward diffusion faster in Ni-Cr alloys in this work than other high temperature environments.

Although the conventional diffusion approach is from alloy's surface to the inside, the diffusion mechanisms can still be applied for the outward diffusion of Cr for the alloys in high-temperature molten salts. As summarized by Pruthi, the overall diffusion coefficient of Cr decreases with the increasing initial Cr concentration in tested alloys[95]. This indicates that the Cr concentration gradient governs the

diffusion rate in alloy. Since the Cr concentration gradient in Ni-5Cr is smaller than Ni-20Cr in molten salt, the D_{eff} could be smaller in Ni-5Cr than that in Ni-20Cr, which is in a good agreement with the calculated value. Additionally, as discussed by Olson, the diffusion coefficient is also strongly dependent on the alloys' microstructure such as grain size, grain shape and grain boundary types[71].

A characteristic diffusion distance can be conservatively estimated by $x = 2\sqrt{Dt}$, where D is overall diffusion coefficient and t is exposure time[92], [96]. Substituting the D_{eff} calculated above into this formula, the mean Cr diffusion distance is obtained (Table 7). Another method to estimate mean diffusion distance is $x = 2 \left(\frac{\Delta W}{\rho_{\text{Cr},0}} \right)$ by assuming linear Cr depletion profile, where ΔW is weight loss per unit area, and $\rho_{\text{Cr},0}$ is initial Cr density in alloys. All calculated results are summarized in Table 7. Using both methods, similar results are obtained for Ni-5Cr, but the former calculation method generates a higher x value than latter one for Ni-20Cr for $t=50$ hours and $t=500$ hours, in reverse for $t=1000$ hours. The former method is strongly dependent on the correctness of the calculated D_{eff} . The trend line of Ni-20Cr in Figure 42 is obviously higher than experimental data as $t=50$ hours and $t=500$ hours, but lower than experimental data as $t=1000$ hours. This is in agreement with the trend of calculated results.

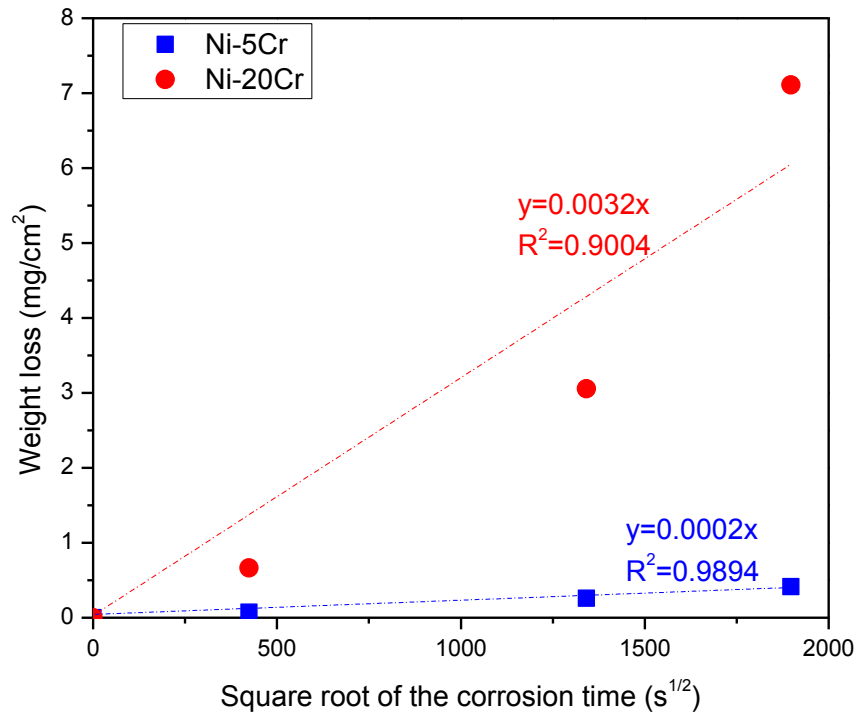


Figure 42: Weight loss as a function of square root of the corrosion time for Ni-5Cr (blue) and Ni-20Cr (red) alloys that were exposed to molten FLiBe at 700°C for 50, 500 and 1000 hours. Linear trend lines (dashed lines) and R-squared values are included for both alloys.

Table 7: Calculated mean Cr diffusion distance by using two different methods.

Corrosion time (s)	Mean Cr diffusion distance (μm)			
	$x = 2\sqrt{Dt}$		$x = 2\left(\frac{\Delta W}{\rho_{Cr,0}}\right)$	
	Ni-5Cr	Ni-20Cr	Ni-5Cr	Ni-20Cr
180000	3.46	14.05	3.34	7.77
1800000	10.93	44.42	11.87	35.66
3600000	15.46	62.81	19.11	82.95

3.1.7 Cr depletion induced lattice parameter change

XRD technique has been widely applied to analyze materials microstructure including lattice parameters, structure defects, grain size and preferential orientation of grains and so on[97]. Figure 43 and

Figure 44 show the XRD patterns of Ni-5Cr and Ni-20Cr alloy surface before and after corrosion tests in molten FLiBe for 1000 hours. In all XRD patterns, the characteristic peaks of (111), (200) and (220) of γ phase nickel alloy with fcc crystal structure were clearly detected. A pronounced intensity of (111) peak on the Ni-5Cr alloy (Figure 43) is indicative of the preferential orientation of grains along $\langle 111 \rangle$ direction due to the cold rolling process before the corrosion test. The significant shrinking of (111) peak intensity after the corrosion tests suggests the grain growth and re-orientation at 700°C in molten salt. For Ni-20Cr, as shown in Figure 44, the characteristic peaks significantly shift to higher 2θ after experiencing 1000 hours corrosion in molten FLiBe, which indicates a decrease in lattice parameters.

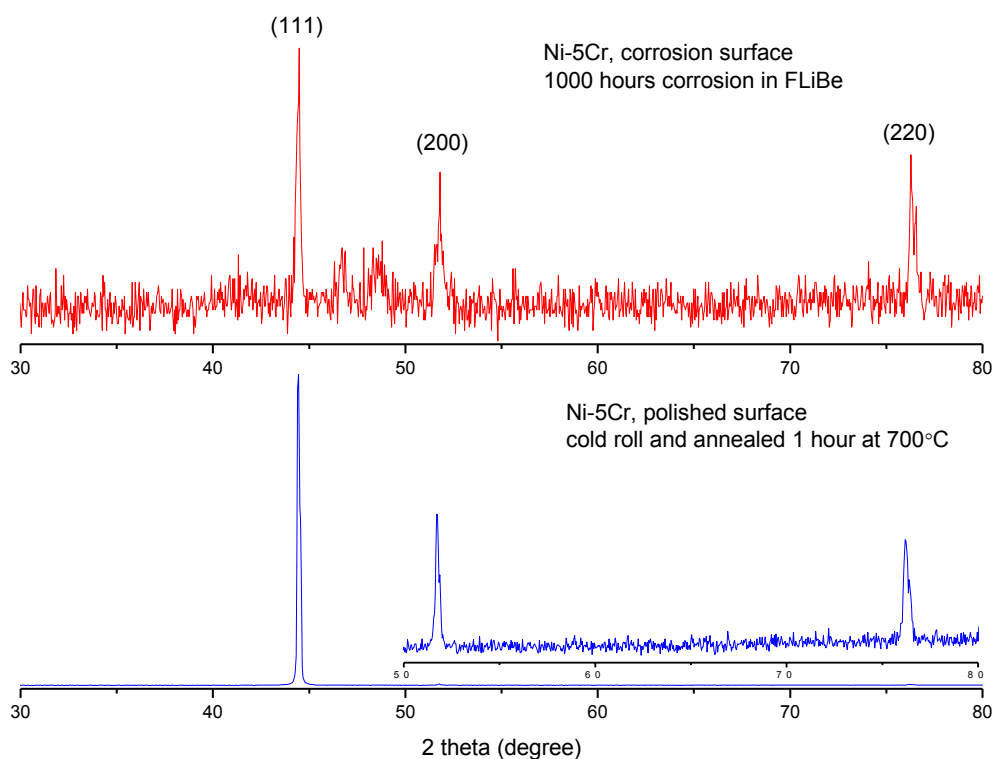


Figure 43: XRD patterns of Ni-5Cr alloy surface before (blue) and after (red) corrosion test in molten FLiBe for 1000 hours. A part of blue pattern ($2\theta=50^{\circ}$ - 80°) was zoomed in to present the existence of (200) and (220) peak.

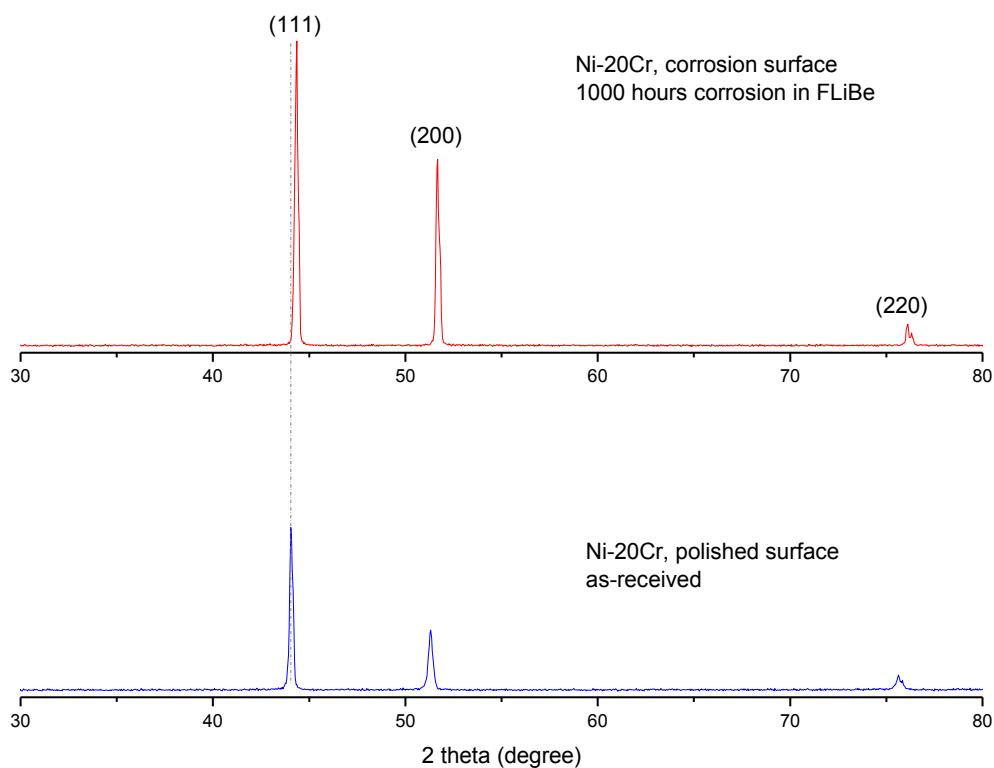


Figure 44: XRD patterns of Ni-20Cr alloy surface before (blue) and after (red) corrosion tests in molten FLiBe for 1000 hours. A vertical dashed line was added on (111) peak to emphasize peak shift between two patterns.

The fitting lines of spacing $d(111)$, $d(200)$ and $d(220)$ vs. extrapolation function $(\cos^2\theta/\sin\theta + \cos^2\theta/\theta)$ were applied to determine accurate lattice parameters of pre- and post-corrosion Ni-5Cr and Ni-20Cr model alloys, as shown in Figure 45. The intercept points on y-axis suggest that the lattice parameter on the alloys surface layer decreases from 353.08pm to 352.75pm, and from 354.66pm to 353.17pm for Ni-5Cr and Ni-20Cr alloy respectively. This indicates that the Cr depletion from the alloys surface layer leads to the decrease of lattice parameter. Cr is present as a substitutional atom in the Ni-Cr solid solution and its release into the molten salt results in a decrease in lattice parameter in accordance with Vegard's law. After 1000 hours corrosion in molten FLiBe, the lattice parameter in the Ni-20Cr alloy surface layer (1.49pm change) shrunk more than Ni-5Cr (0.33pm change) due to more Cr depletion from Ni-20Cr

matrix than from Ni-5Cr (i. e. due to greater driving force for Cr dissolution), which is in a good agreement with the trend of weight loss (Figure 42).

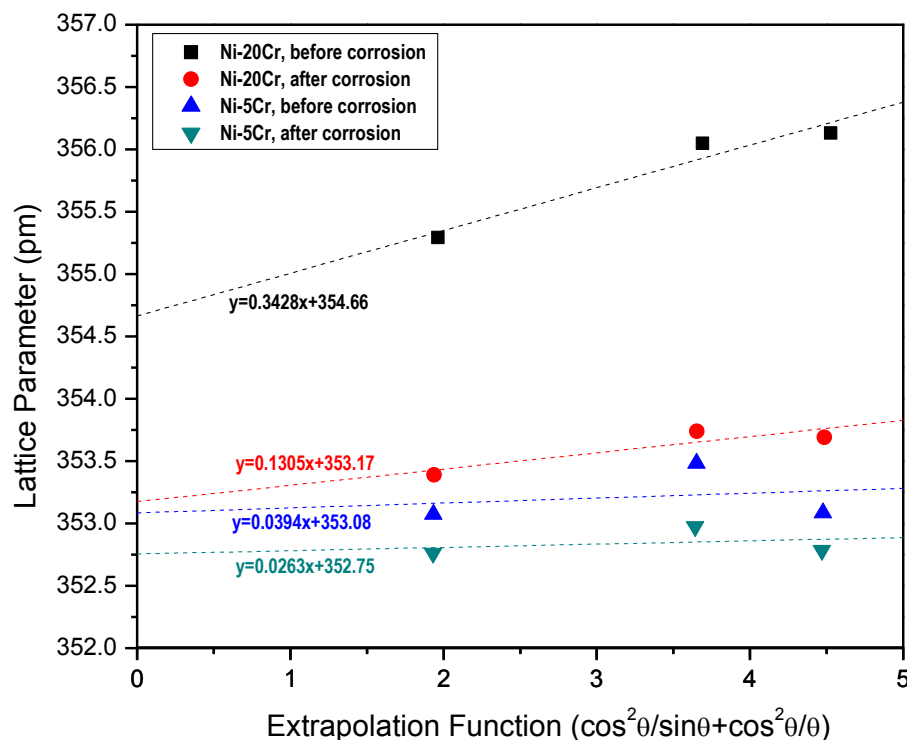


Figure 45: Calculated lattice parameters (pm) vs. extrapolation function $(\cos^2\theta/\sin^2\theta + \cos^2\theta/\theta)$ of Ni-5Cr and Ni-20Cr before and after corrosion tests in molten FLiBe for 1000 hours.

3.1.8 Surface morphology of post-corrosion alloys

Figure 46 shows the surface morphology of all samples tested in molten FLiBe for varying durations. The intergranular corrosion attack was observed on all corrosion samples surface, and the attack becomes deeper and wider with increasing of exposure time. This is indicative of preferential Cr leaching along grain boundaries in the near-surface region. From these corrosion images, it is obvious that the fraction of grain boundaries per unit area on the surface of Ni-20Cr is larger than that on Ni-5Cr, which dominantly

contributes to the overall Cr depletion rate. Using ImageJ, the area fraction of attacked grain boundaries is 3.85% and 28.42% for Ni-5Cr and Ni-20Cr, respectively after 1000 hours corrosion in molten FLiBe. In general, the areal density of grain boundaries is inversely proportional to grain size for polycrystalline materials. Therefore, the Ni-20Cr with a relatively smaller grain size has higher fraction of grain boundaries per unit area. This is consistent with the EBSD analysis on the grain size distribution of pre-corrosion alloys (in Figure 36 and Figure 37).

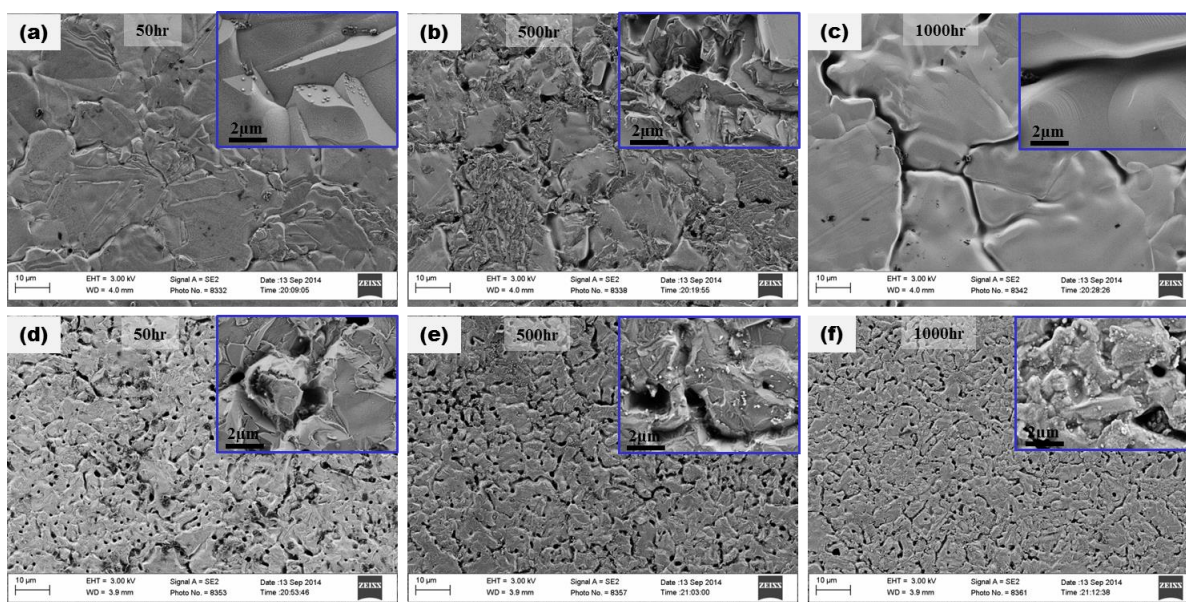


Figure 46: Surface SEM images of (a, b, c) Ni-5Cr and (d, e, f) Ni-20Cr tested in molten FLiBe for 50, 500 and 1000 hours (from left to right) respectively. Inset on upper right corner shows the morphology of grain boundaries.

3.1.9 Cross-sectional microstructure of post-corrosion alloys

The cross-section of the near-surface layer of post-corrosion Ni-5Cr and Ni-20Cr model alloys is shown in Figure 47. The corrosion surface (denoted with red arrow in SEM images) was protected by a layer of electroplated Cu prior to polishing. Voids, a couple of microns in diameter were observed to be randomly distributed within the near-surface layer of Ni-20Cr alloys, but they were not observable in post-corrosion Ni-5Cr alloy. Furthermore, the void size in Ni-20Cr slightly increased with increasing

corrosion time. It has been reported that massive Cr depletion from the alloy matrix contributes to void formation at high temperature due to volume reduction[40]. Generally, these voids form preferentially at grain boundaries where Cr depletion is more significant. However, it was not observed in the cross-sectional SEM images here, though the preferential grain boundary attack was observed on all corrosion samples surface. This might suggest that the preferential grain boundary attack only occurred in a thin layer adjacent to corrosion surface. The Cr depletion mechanism within the alloy is probably different from the surface. This will be further discussed in the following discussion on EDS analysis.

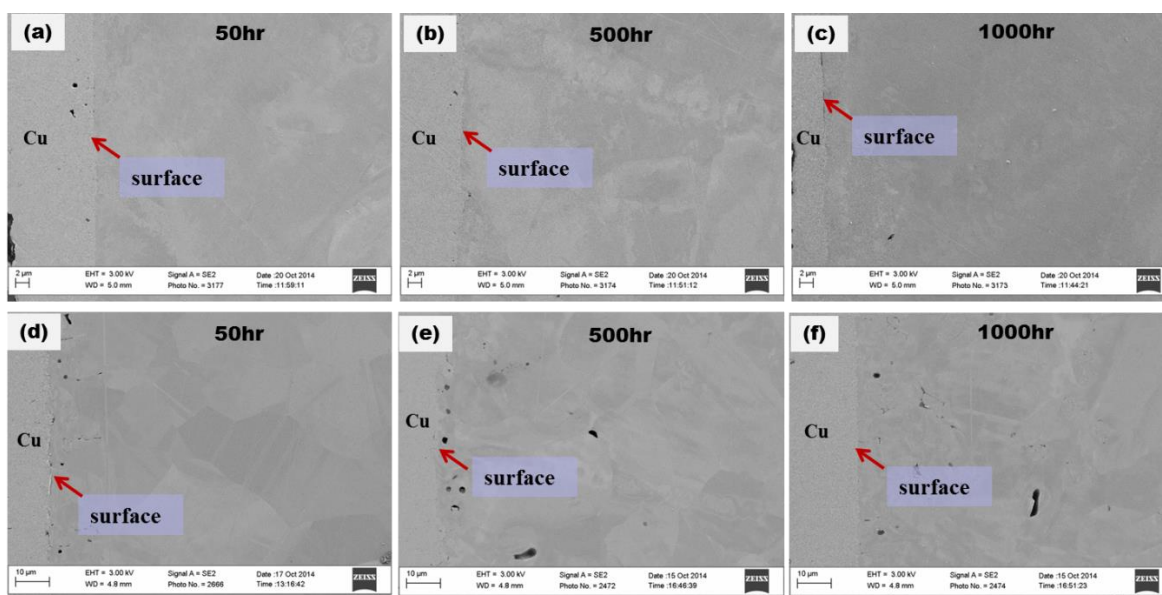


Figure 47: Cross-sectional SEM images of (a, b, c) Ni-5Cr and (d, e, f) Ni-20Cr exposed to molten FLiBe for 50, 500 and 1000 hours. A layer of Cu was electroplated on all samples surface for edge protection during polishing. Arrow denotes corrosion surface.

Figure 48 and Figure 49 show the elemental distributions of main constituents Ni and Cr in the cross-section of the near-surface region in FLiBe-exposed Ni-5Cr and Ni-20Cr for 50, 500 and 1000 hours. The relatively low concentration of Cr was observed in the near-surface region for all corrosion samples. Unlike the corrosion surface where preferential grain boundary attack was observed, the dominant Cr depletion mechanism is through grains, based on the EDS mappings of Cr. It is likely that the Cr depleted grain boundaries are too thin to be identified by EDS imaging technique. This is consistent with cross-

sectional observation. Additionally, the Cr depletion is not uniform in same depth. To evaluate corrosion attack depth, the maximum Cr depletion distance was measured and labeled in EDS Cr mappings. With the increasing of corrosion time, from 50 hours to 1000 hours, the maximum Cr depletion distance increases from 5.4 μm to 21.7 μm and from 18.2 μm to 140.8 μm for Ni-5Cr and Ni-20Cr, respectively.

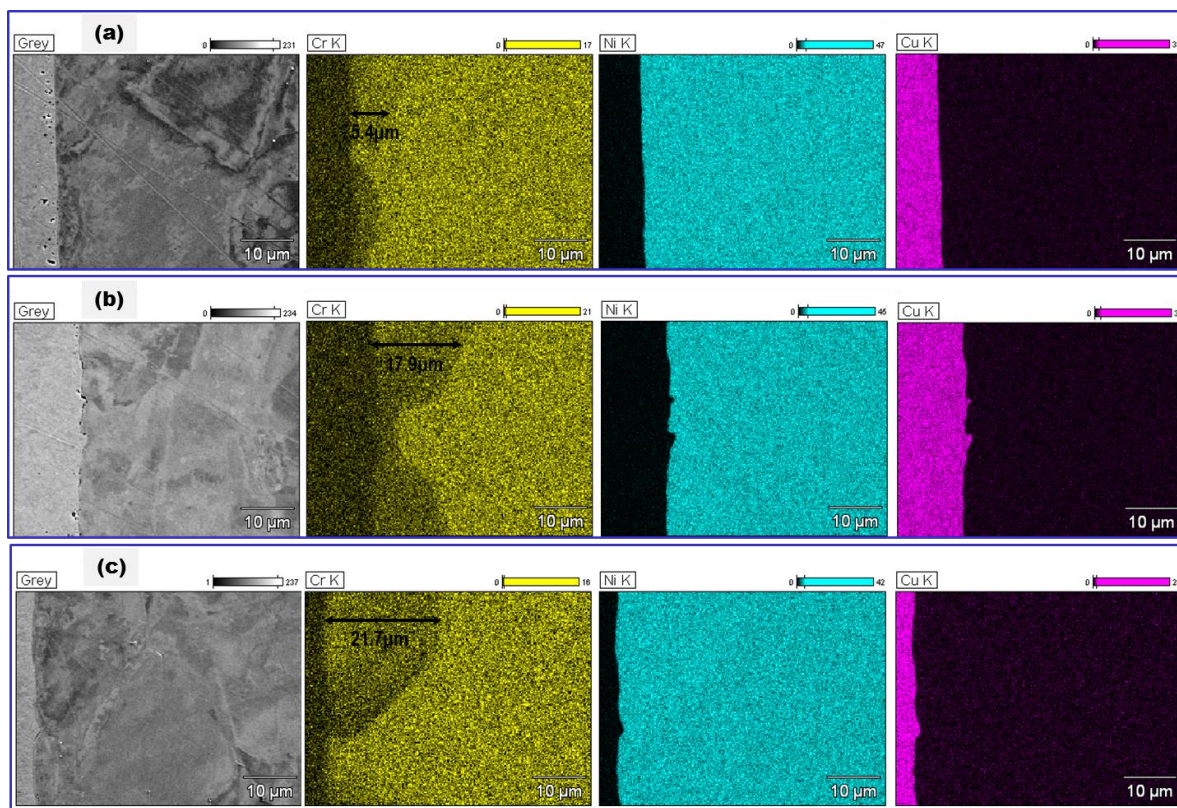


Figure 48: EDS mapping of Cr, Ni and Cu elemental distribution in the near surface layer of the Ni-5Cr samples tested in molten FLiBe for (a) 50 hours, (b) 500 hours and (c) 1000 hours.

The Cr depletion in Ni-5Cr only occurred in a pronounced manner only in certain grains adjacent to the surface. In Ni-20Cr, the Cr depletion occurred in a wide range or multiple connected grains. This is because the grain size in Ni-5Cr ($\sim 100\mu\text{m}$ - $200\mu\text{m}$, in Figure 36) is much larger than Ni-20Cr ($\sim 10\mu\text{m}$ - $30\mu\text{m}$, in Figure 37), even larger than the maximum Cr depletion distance. The reason why Cr depletion preferentially occurred in certain grains, not in all the grains in same depth, was further analyzed using EBSD technique.

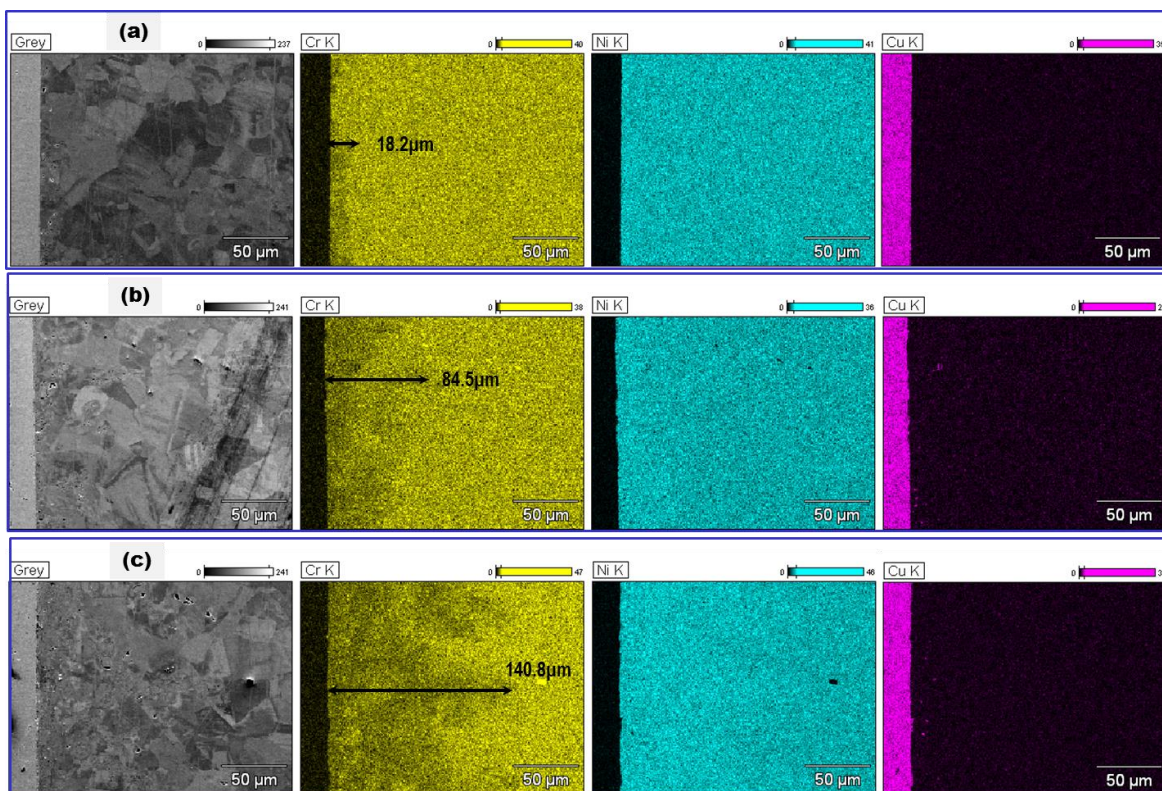


Figure 49: EDS mapping of Cr, Ni and Cu elemental distribution in the near surface layer of the Ni-20Cr samples tested in molten FLiBe for (a) 50 hours, (b) 500 hours and (c) 1000 hours.

To avoid the possible smearing effect on the cross-sectional observation due to mechanically polishing, the polished cross-sections were further etched in a chemical solution (45ml HCl + 15ml HNO₃ + 20ml methanol). After etching, the microstructure of all Ni-5Cr alloys and annealed Ni-20Cr alloys appeared the same as the non-etched cross-section. However, for the Ni-20Cr alloys that were exposed to molten FLiBe, the etching process slightly enlarged the voids and revealed some slits and pitting in the cross-section, as exhibited in Figure 50. EDS mappings of Cr on these etched cross-sections are the same as the mechanically polished ones, although the cross-sectional SEM images changed slightly.

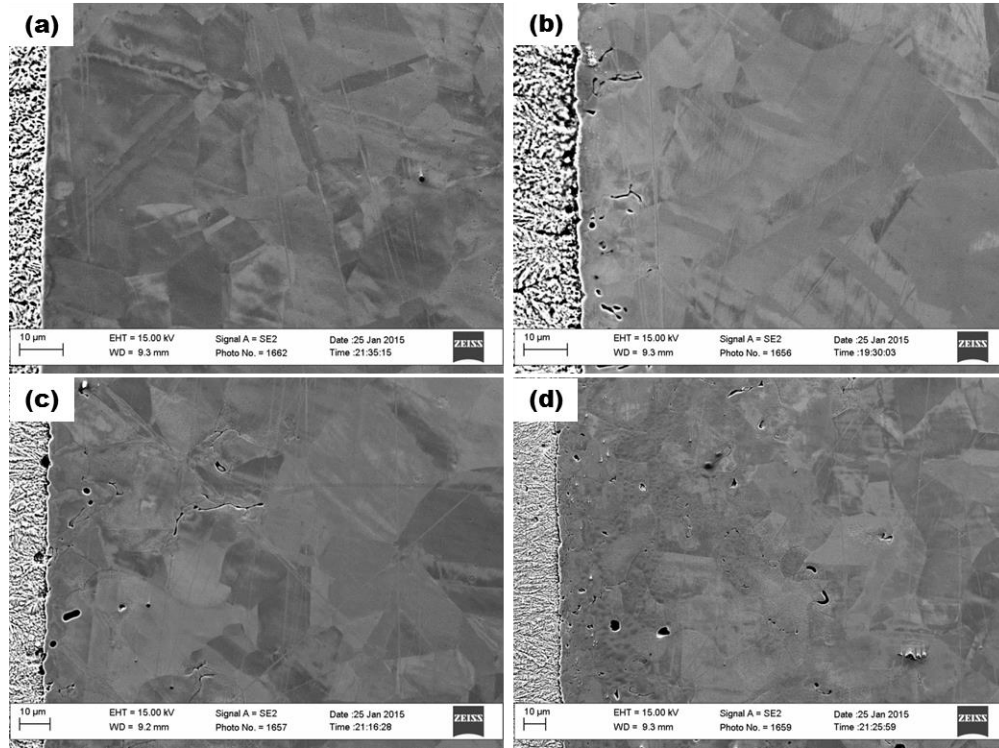


Figure 50: Cross-sectional SEM image of (a) annealed Ni-20Cr with 50 hours, (b) (c) and (d) post-corrosion Ni-20Cr in molten FLiBe for 50 hours, 500 hours and 1000 hours respectively. The mechanically polished cross-section was further chemically etched in a solution (45ml HCl+15ml HNO₃+20ml methanol) for 15 seconds.

3.1.10 Cr depletion distance in post-corrosion alloys

Figure 51 shows the maximum Cr depletion distances obtained from EDS Cr mappings, and the Cr depletion distances calculated using different methods (summarized in Table 7). For both alloys, the experimental data of the maximum Cr depletion distance is larger than the calculated distance. The mean diffusion length ($x=2(Dt)^{1/2}$) and the overall distance of linear Cr depletion ($x=2(\Delta M/C_0)$) are about half of the maximum Cr depletion distance, particularly for Ni-20Cr. This indicates that both calculating methods are inadaptable to the measurement of real Cr depletion distance, although the mean diffusion length was widely considered as effective diffusion distance. Therefore, both calculations were not selected as a model to precisely predict real Cr depletion distance in this work.

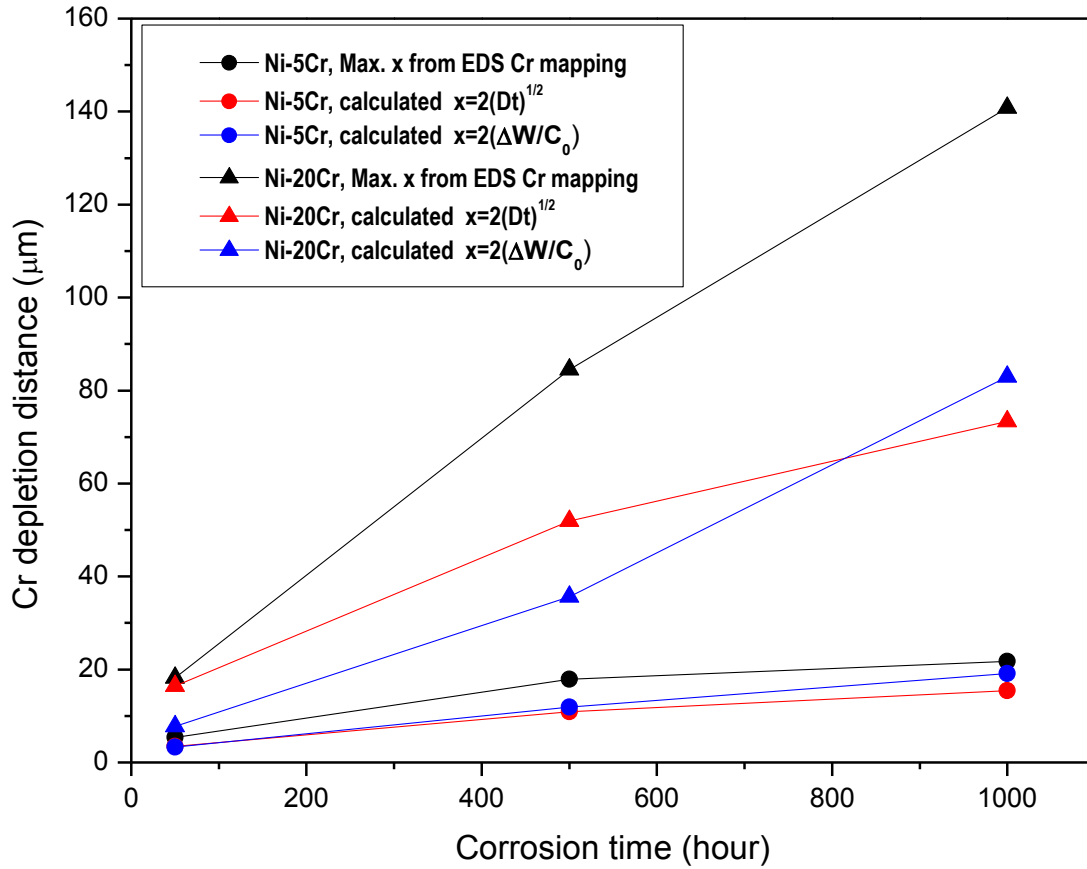


Figure 51: Cr depletion distance as a function of corrosion time. All data were collected from EDS Cr mappings and from the calculations in Table 7.

3.1.11 Texture analysis of post-corrosion alloys

The distribution of grain size, grain boundary and misorientation angle of post-corrosion Ni-5Cr and Ni-20Cr alloys are shown in Figure 52 and Figure 53. From the inverse pole figure (IPF) (Figure 52(b)), it is obvious that the preferential orientation of most grains is [111] in the post-corrosion Ni-5Cr alloy (blue grains). This is consistent with the differences observed in XRD patterns for pre-corrosion and post-corrosion samples of Ni-5Cr surface (in Figure 43). During high temperature corrosion the surface grains in Ni-5Cr dramatically re-orientated and re-distributed due to large free space on surface, which is also proved by the extruded grains on the surface of annealed Ni-5Cr (Figure 38). The grains in the alloy bulk maintained [111] preferential orientation as the pre-corrosion sample. Moreover, the average grain size

becomes relatively small compared to the pre-corrosion Ni-5Cr alloys. As shown in Figure 53(b), a number of low angle coincident site lattice (CSL) grain boundaries (orange lines) exist in Ni-20Cr. These low energy CSL grain boundaries usually have higher corrosion resistance[98]–[100]. Such high density of the low angle grain boundaries in Ni-20Cr might be a reason why dominant volumetric Cr depletion was observed. Figure 53(c) shows that the grain size in Ni-20Cr slightly coarsened during 1000 hours corrosion in molten FLiBe at 700°C due to thermal effect. The distribution of misorientation angle relative to [001] shows slightly more 50-60° misorientation angles in Ni-20Cr than that in Ni-5Cr.

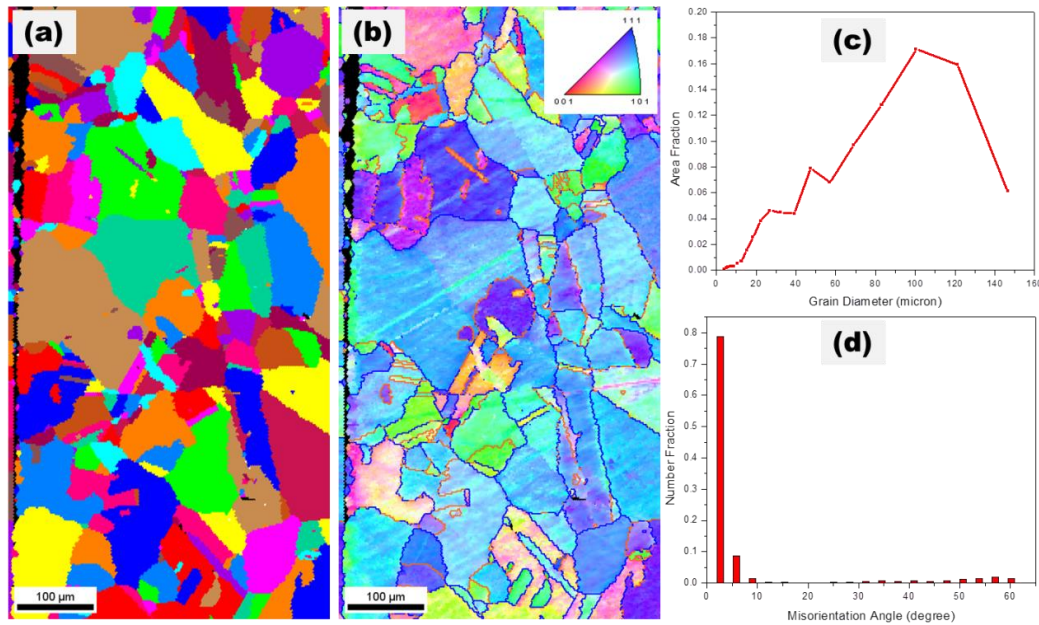


Figure 52: EBSD (a) auto grain, (b) inverse pole figure overlapped grain boundaries distribution, (c) grain size distribution and (d) distribution of misorientation angle relative to [001] on the cross-section of near surface layer of Ni-5Cr that was exposed to molten FLiBe for 1000 hours.

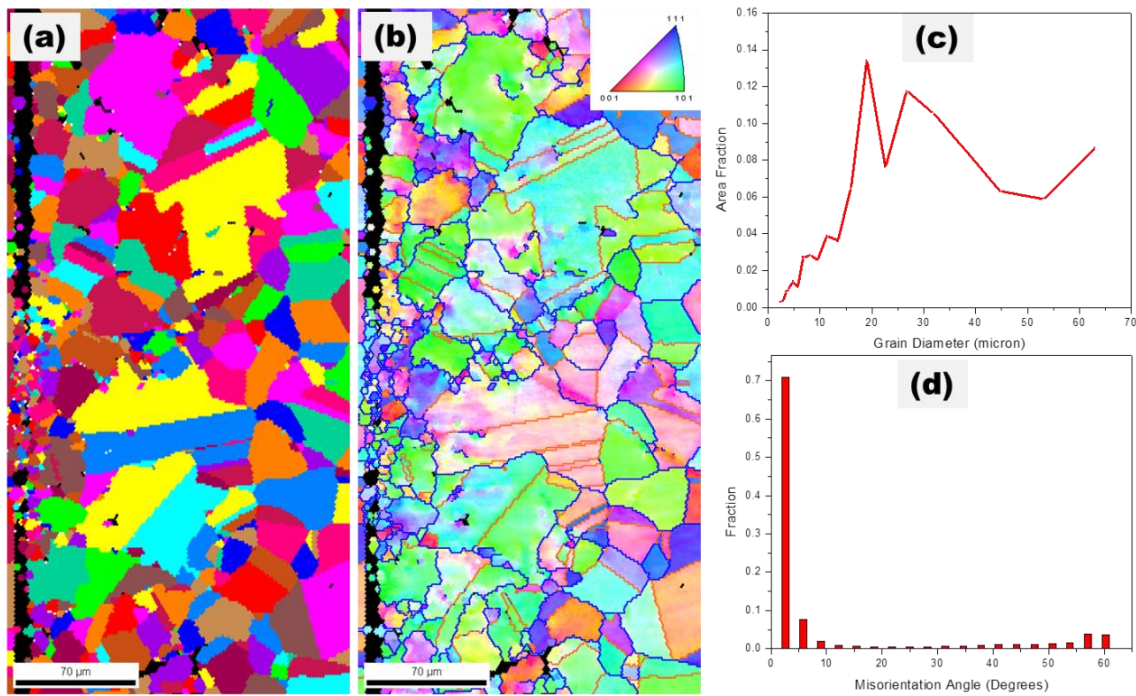


Figure 53: EBSD (a) auto grain, (b) inverse pole figure overlapped grain boundaries distribution, (c) grain size distribution and (d) distribution of misorientation angle relative to [001] on the cross-section of near surface layer of Ni-20Cr that was exposed to molten FLiBe for 1000 hours.

To further understand the effect of molten salt corrosion on the microstructure of alloys, EBSD must be combined with EDS analysis. EBSD only provides the texture information, but EDS can provide elemental distribution in alloys. The evidence of the corrosion in molten fluoride salt is Cr depletion that could induce alloys' microstructural change at high temperature. The combination of EBSD with EDS can trace the corrosion dynamics of alloys in high-temperature molten salt.

3.1.12 Effect of crystallographic orientation on Cr depletion

Figure 54 exhibits an IPF image, EDS mappings of Cr, Ni and Cu in the local area framed in the EBSD image, and the crystallographic orientation of four single grains in FLiBe-exposed Ni-5Cr. From the EDS mapping of Cr, the grains labeled 1 and 2 in the IPF image show partial Cr depletion due to the corrosion in molten FLiBe. Grains 3 and grain 4 have a relatively higher Cr concentration than grains 1

and 2, which indicates higher corrosion resistance of grain 3 and grain 4 in molten FLiBe. This result reveals the dependence of alloy corrosion resistance on the grain orientation, especially for the volume diffusion dominated Cr depletion.

Figure 55 presents the misorientation angle relative to [001] of 50 acquired spots from each single grain labeled in Figure 54. The misorientation angles for each grain oscillate within a range of values. The small difference in the misorientation angles in the same grain is mainly due to the quality of polished cross-section. From these profiles, the mean misorientation angle relative to [001] axis is about 45°, 38°, 29° and 60° for grains 1, 2, 3, and 4, respectively. Combining with the EDS Cr mapping, it is reasonable to conclude that the grains with misorientation angle relative to [001] in the range from 35° to 50° (grain 1 and grain 2) are more vulnerable to Cr depletion from the attack by the molten fluoride salt. In reverse, grains with misorientation angles far from this range (35-50°) have better corrosion resistance to molten fluoride salt.

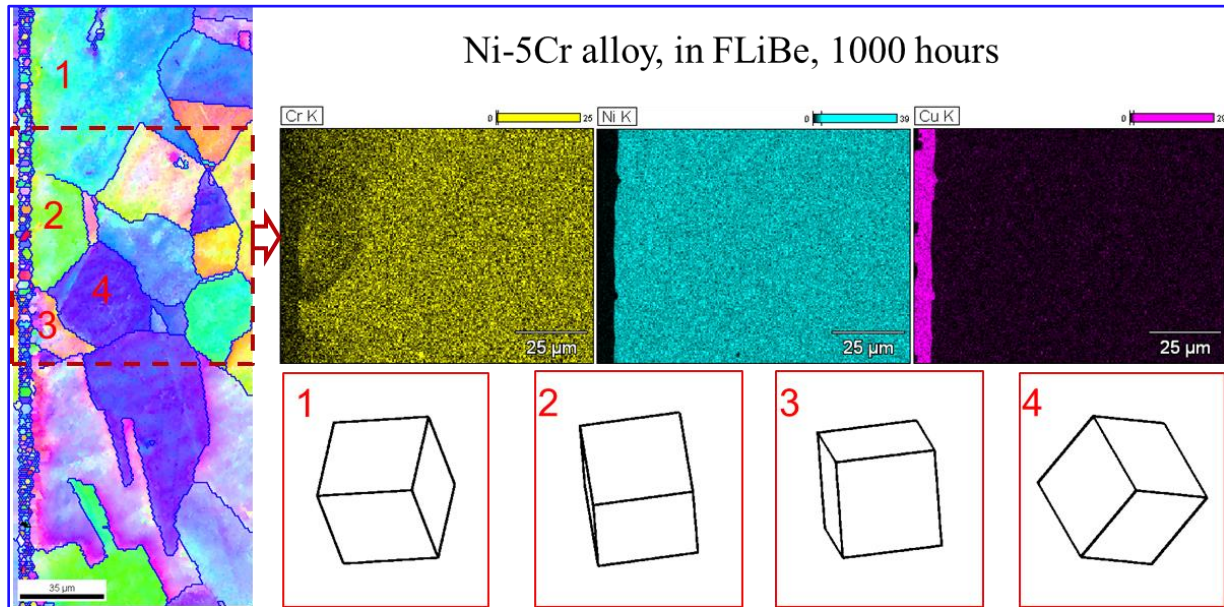


Figure 54: EBSD inverse pole figure [001] in the cross-section of FLiBe-exposed Ni-5Cr for 1000 hours, EDS maps in the red dashed line framed area, and 3-D crystallographic orientation of the specific grains labeled in EBSD image.

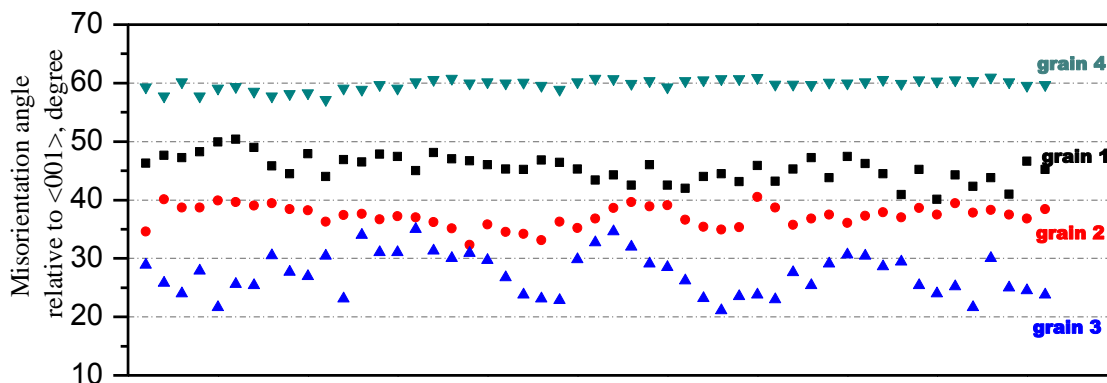


Figure 55: Misorientation angle relative to reference direction [001] for grains 1, 2, 3 and 4 labeled in EBSD image. 50 spots were randomly selected within each grain for this analysis.

From the previous analysis, Ni-20Cr shows more complicated corrosion mechanisms than Ni-5Cr because the Cr depletion range in Ni-20Cr covers multiple grains. Since the grain boundary diffusion coefficient of Cr in nickel is usually ten times higher than the volume diffusion coefficient at 700°C, the grain boundary diffusion certainly plays an important role in the Cr depletion. Additionally, the voids and slits observed in certain areas in Ni-20Cr suggest the relationship between microstructure and corrosion resistance. As shown in Figure 56, an IPF map, SEM image and EDS maps of Cr were collected from the same area in Ni-20Cr. An EDS line scan crossing multiple grains and grain boundaries was acquired to quantitatively analyze the Cr depletion along this scanning path (Figure 56(c)). Comparing the SEM image with EDS Cr map, the Cr depleted grains show a relatively rough cross-section compared to other grains. Slits and voids are observed in the rough grains. The 10 seconds etching process doesn't change Cr concentration in these grains because EDS characteristic x-ray excitation volume can be 1-3 μ m in diameter for most elements at 15kV incident electrons. Therefore, the rough grains are susceptible to lose Cr during corrosion in high temperature molten FLiBe. From the IPF image, the rough grains favor to [101] orientation. From EDS line scan (Figure 56(c)), the Cr concentration in these grains is about 5 wt.% lower than neighbor grains, but it increases slightly at the grain boundary between two attacked grains. In the EDS mapping of Cr, the Cr depletion along the grain boundary was not observed mainly due to the

limited differentiation capability of the EDS mapping technique. Without the formation of precipitates, the grain boundaries in Ni-5Cr and Ni-20Cr are too thin to be differentiated by EDS mapping although Cr depletion occurred in these grain boundaries.

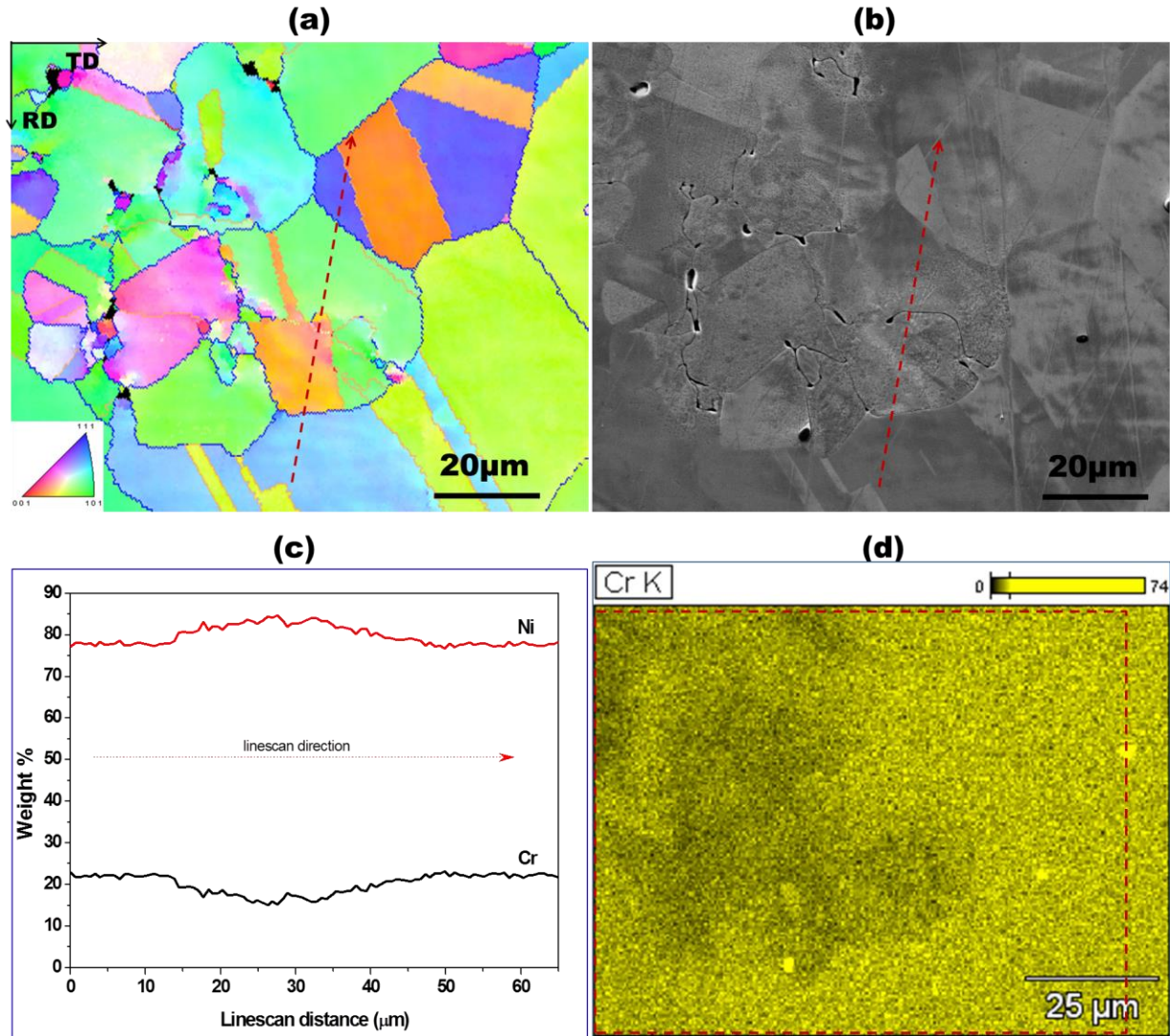


Figure 56: (a) EBSD inverse pole figure [001] with grain boundary map (blue line: 15°-180° regular grain boundary; orange line: CSL $\Sigma 3$), (b) cross-sectional SEM image, (c) Ni and Cr concentration profiles (wt.%) along the EDS line scanning path labeled in (a, b), and (d) EDS Cr map in the same area as EBSD and SEM for the Ni-20Cr tested in molten FLiBe for 1000 hours.

To identify the spatial orientation of the grains and grain boundaries where Cr depleted, the misorientation angle of specific grains 1, 2 and 3 that represent different corrosion resistance to molten fluoride salt were measured. As shown in Figure 57, 3-D crystal geometries and Kikuchi patterns of three grains labeled in the IPF and SEM images were analyzed. The misorientation angle relative to [001] is about 18° , 30° and 40° for grains 1, 2, and 3 respectively. The grain boundary type is usually characterized by neighboring grains' misorientation angle. Table 8 lists the neighboring grains misorientation angles of visible grain boundaries (slits) in the SEM image. The neighboring grains misorientation angle between grain 1 and grain 2 and 3 is in a range of 35° - 50° where Cr is favorable to deplete. Differently, no Cr depletion occurred in all CSL grain boundaries, which indicates the variance of grain boundary corrosion resistance to molten fluoride salt in term of Cr depletion.

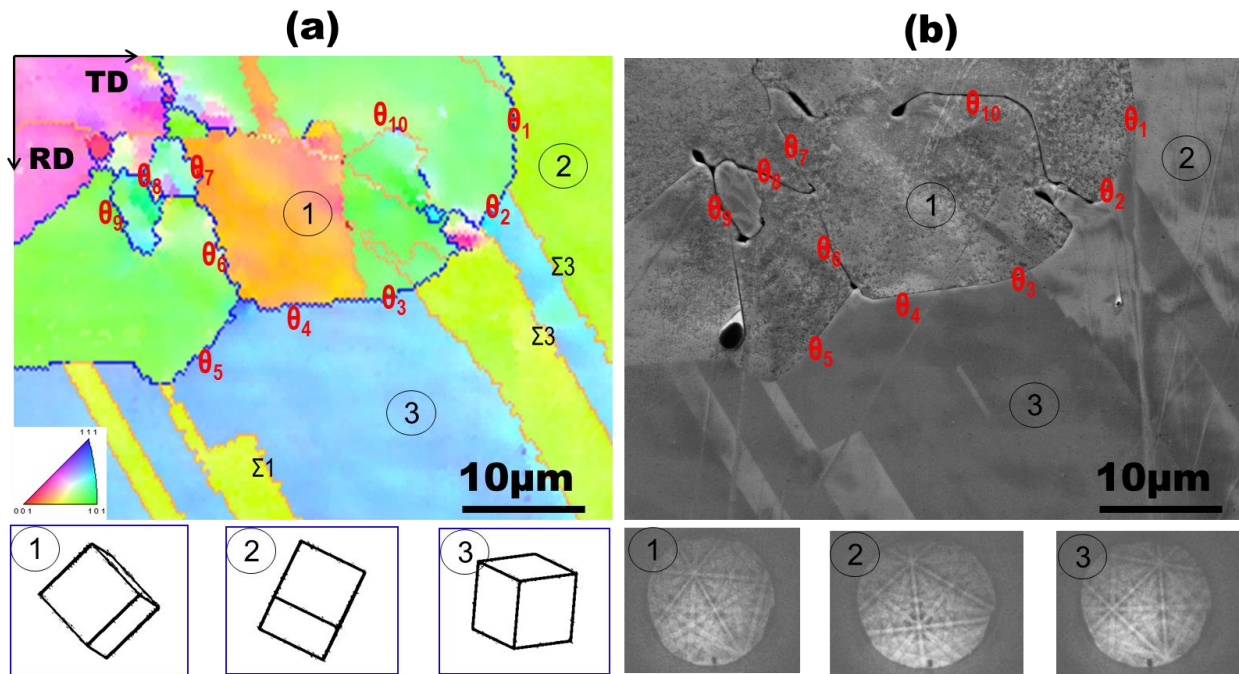


Figure 57: (a) EBSD inverse pole figure relative to [001] direction and (b) SEM image in the same area as EBSD. The lattice orientation and Kikuchi patterns on three individual grains are presented.

Table 8: Neighboring grains misorientation angle for the grain boundaries labeled in Figure 57.

Grain boundary	Misorientation angle (°)	Grain boundary	Misorientation angle (°)
θ_1	34.9	θ_6	43.2
θ_2	37.4	θ_7	39.8
θ_3	38.7	θ_8	51.6
θ_4	50.7	θ_9	32.1
θ_5	35.7	θ_{10}	58.6

3.1.13 Chemical state of Cr on post-corrosion alloys surface

X-ray photoelectron spectroscopy is a surface-sensitive quantitative spectroscopic technique to measure the elemental compositions on sample surface in a depth range of less than 10 nm. This technique was employed to analyze the chemical states of Cr on the surface of Ni-5Cr and Ni-20Cr alloys. The XPS Cr (2p) spectra on the surface of as-received Ni-20Cr, and FLiBe-exposed Ni-5Cr and Ni-20Cr for 1000 hours are shown in Figure 58. Table 9 summarizes the detected XPS Cr (2p) peaks and their corresponding chemical compound of Cr. According to the XPS spectra, the chemical state of Cr on the surface of as-received Ni-20Cr is mainly composed of Cr metal and Cr_2O_3 oxide. A protective oxide film of Cr_2O_3 usually forms on the Cr containing alloy surface at room temperature, especially for the polished surface. However, no Cr metal and Cr_2O_3 was detected on the post-corrosion Ni-5Cr and Ni-20Cr surface, indicating zero Cr metal on surface after corrosion testing in molten FLiBe. On the post-corrosion Ni-20Cr surface, two Cr (2p) peaks with relatively high binding energy were observed, resulting from the residual CrF_2 on the corrosion surface. The existence of CrF_2 on the cleaned corrosion surface of Ni-20Cr is probably due to the specific surface morphology. As shown in Figure 59(a), a thin, porous structure layer formed on the surface of post-corrosion Ni-20Cr that was cleaned by soaking in deionized water for 24 hours. The corrosion product of CrF_2 might be incorporated in this porous structure layer so that it is difficult to completely dissolve by statically soaking in water. To remove it, this Ni-20Cr sample was further ultrasonically cleaned in water. As exhibited in Figure 59(b), the porous structure layer disappeared after ultrasonic cleaning. After this step, CrF_2 was not detected on the Ni-20Cr surface. This

analysis demonstrates that the Cr metal concentration on post-corrosion alloys' surface is zero, which provides a significant boundary condition of $[Cr] = 0$ as $x=0$ and $t>0$.

In the earlier published report on the corrosion behavior of INOR-8 in fluoride fused salt, the concentration of Cr on alloy surface was assumed to equal the concentration of Cr ions in the molten salt at equilibrium state[72]. This was under the assumption of zero Cr impurity in the initial salt and only one oxidizing reaction with Cr by the means of $Cr + 2UF_4 \rightarrow CrF_2 + 2UF_3$. Based on the general impurities specification in MSRE salt, the concentration of Cr in salt is only 25ppm (0.0025% in weight). Compared to the Cr concentration in alloys ($\geq 5\%$), the $C_s=0.0025\%$ is negligible. Therefore, it is reasonable to apply the boundary condition of $C_s=0$ for developing a long-term corrosion prediction model.

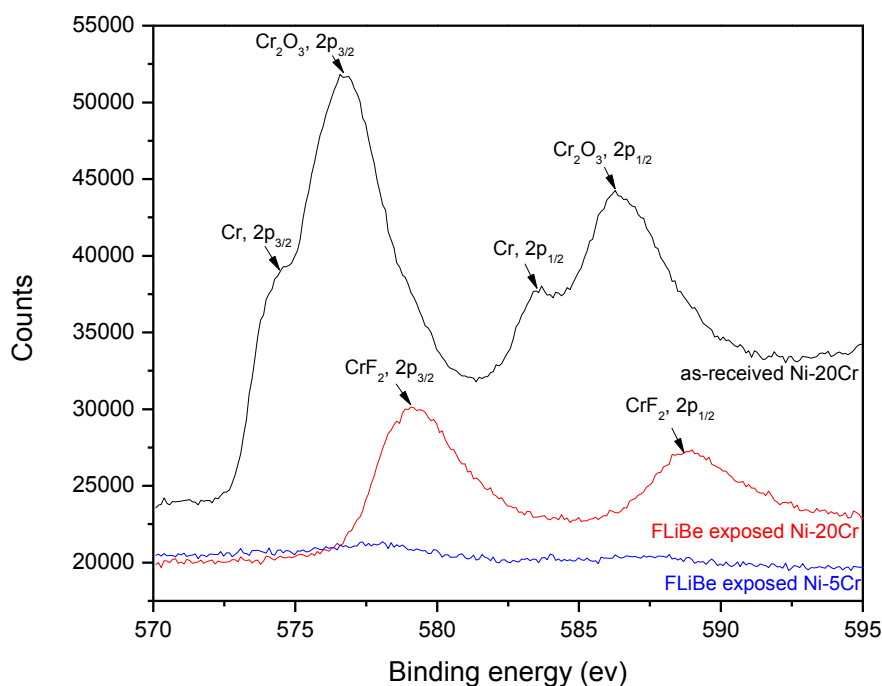


Figure 58: K-alpha XPS Cr-2p spectra of as-received Ni-20Cr (black), post-corrosion Ni-20Cr (red) and post-corrosion Ni-5Cr (blue) after testing in molten FLiBe for 1000 hours, focusing on the range of Cr binding energy from 570ev to 595ev.

Table 9: XPS Cr (2p) peaks and corresponding chemical state of Cr on sample surface.

Alloy sample	Surface condition	Cr (2p) peak	Chemical state
as-received Ni-20Cr	fine polished	2p _{3/2} , 2p _{1/2}	Cr ₂ O ₃
Post-corrosion Ni-20Cr	cleaned in water	2p _{3/2} , 2p _{1/2}	Cr
Post-corrosion Ni-5Cr	cleaned in water	-	-

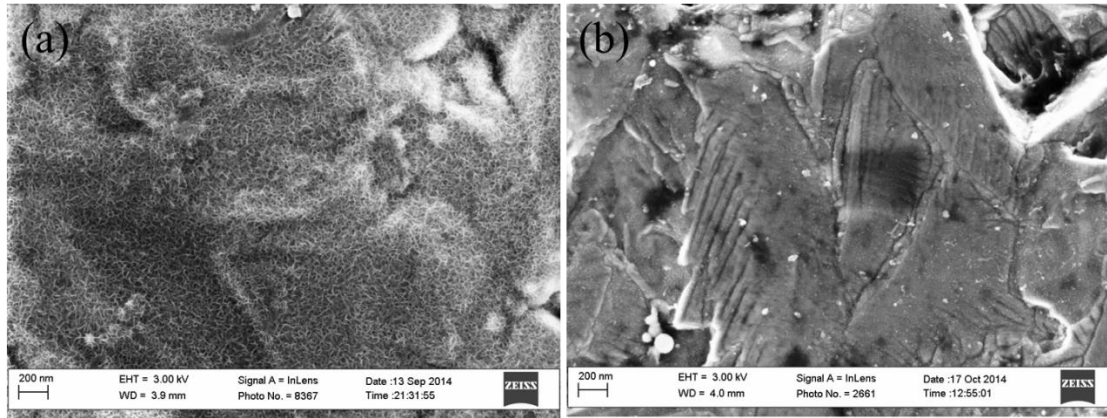


Figure 59: (a) Cleaned surface after soaking in deionized water for 24 hours and (b) further ultrasonically cleaned surface for the FLiBe-exposed Ni-20Cr for 1000 hours.

3.1.14 Discussion about Cr depletion approach in Ni-Cr alloys

Figure 60 and Figure 61 show the quantitative results of Cr concentration profiles in post-corrosion Ni-Cr model alloys based on EDS line-scan. Each line-scan path crosses the maximum Cr depletion region that is referred in the observation of EDS Cr mappings. The line-scan direction is from the unaffected substrate to corrosion surface. From these Cr concentration profiles, the Cr depletion distance is 6.5 μ m, 19.6 μ m, and 23.6 μ m for Ni-5Cr, and 24.3 μ m, 74.5 μ m, and 143.7 μ m for Ni-20Cr, exposed to molten FLiBe for 50 hours, 500 hours and 1000 hours respectively. These data are close to the measurements from the EDS Cr mappings. From these Cr concentration profiles, it was observed that the Cr concentration drops down dramatically from the unaffected substrate (no Cr depletion) to the Cr depleted region and then maintains at about half of initial Cr concentration in Ni-5Cr, but gradually decreases in Ni-20Cr. This phenomenon might also be related to the alloys' microstructure.

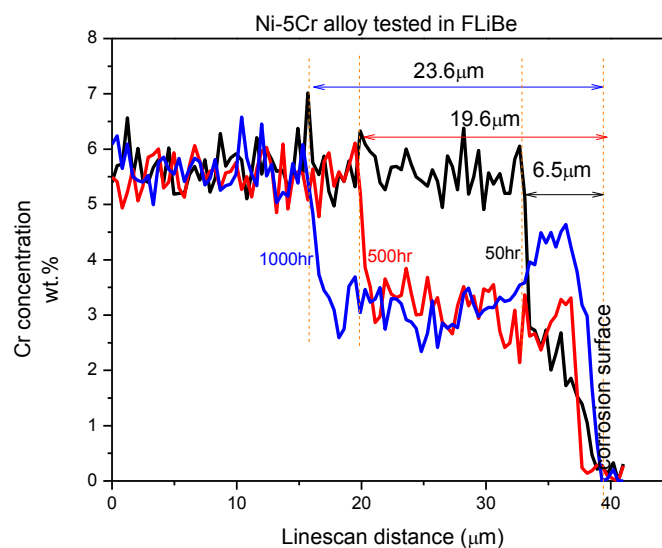


Figure 60: Cr concentration profiles (EDS line-scan) in Ni-5Cr alloys that were exposed to molten FLiBe for 50, 500 and 1000 hours.

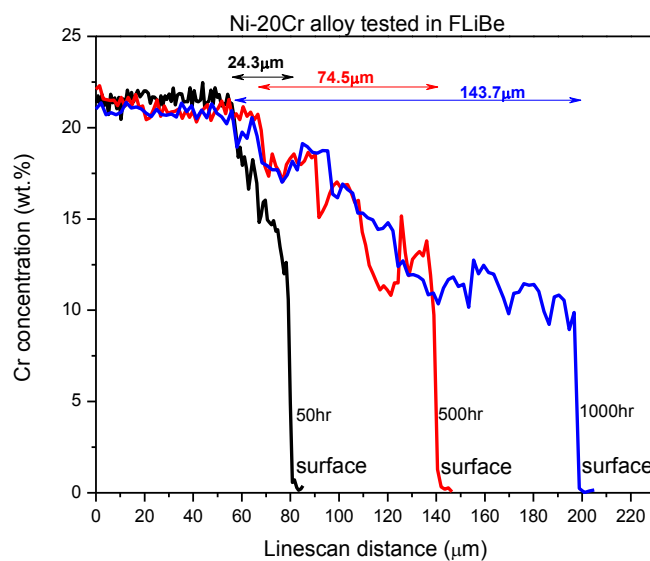


Figure 61: Cr concentration profiles (EDS line-scan) in Ni-20Cr alloys that were exposed to molten FLiBe for 50, 500 and 1000 hours.

As mentioned earlier, the Cr diffusion mechanism is strongly dependent on alloys' microstructure. Based on above analyses, the grain size might be an important factor affecting Cr diffusion rate. As illustrated in Figure 62, the Cr depleted region in Ni-20Cr covers multiple grain layers (grain size $\sim 30\mu\text{m}$), but it only covers a single grain layer (grain size $\sim 100\mu\text{m}$) in Ni-5Cr. This means that some grain boundaries are involved in the Cr depleted region in Ni-20Cr. In other words, grain boundaries play a more important role in the Cr depletion in Ni-20Cr than in Ni-5Cr. Since the average grain size in Ni-5Cr is larger than the Cr depletion distance, volume diffusion is predominant approach causing Cr depletion in Ni-5Cr. This phenomena was reported by R. B. Evans for the investigation of self-diffusion of Cr in nickel-base alloys[48].

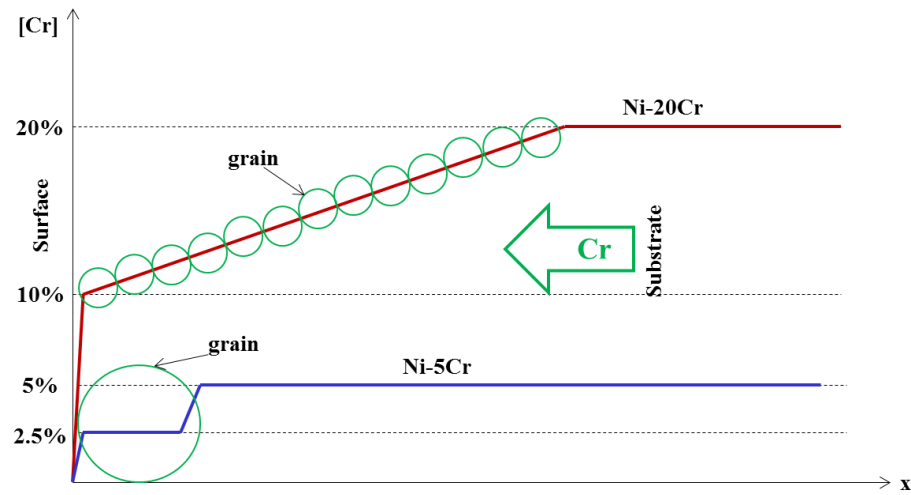


Figure 62: Schematic illustration of Cr concentration profile in Ni-5Cr and Ni-20Cr during corrosion in molten FLiBe.

The dramatic drop of Cr concentration in the region near the corrosion surface was observed in all post-corrosion Ni-Cr model alloys. Since the area fraction of grains to grain boundaries is significant in the near-surface layer, the volume diffusion mainly contributes to the Cr depletion in this shallow layer. This layer is about $0.5\text{-}1\mu\text{m}$ range according to the EDS line-scan profiles. Therefore, the surface layer was usually attacked much faster than the inside, as presented in the SEM images of the corrosion surface (Figure 46).

The precipitates in grain boundaries appear to affect the overall Cr outward diffusion coefficient especially for grain boundary dominant diffusion. In high purity (99.95%) Ni-5Cr and Ni-20Cr, no precipitates formed in the grain boundary of annealed and corroded samples. The Cr diffusion through alloys' grain boundary without precipitates is usually much faster than the alloys with the precipitates in grain boundary because the grain boundary precipitates inhibit Cr outward diffusion. Additionally, the chromium carbide precipitates formed in most commercial alloys initiate a Cr depleted zone in grain boundaries, as demonstrated in Figure 63. Was calculated that the Cr concentration at grain boundary-matrix interfaces decreases with increasing carbon content in alloys[66]. For example, a number of carbide precipitates formed in aged 316 stainless steel and Hastelloy N[91], [94], [101], [102].

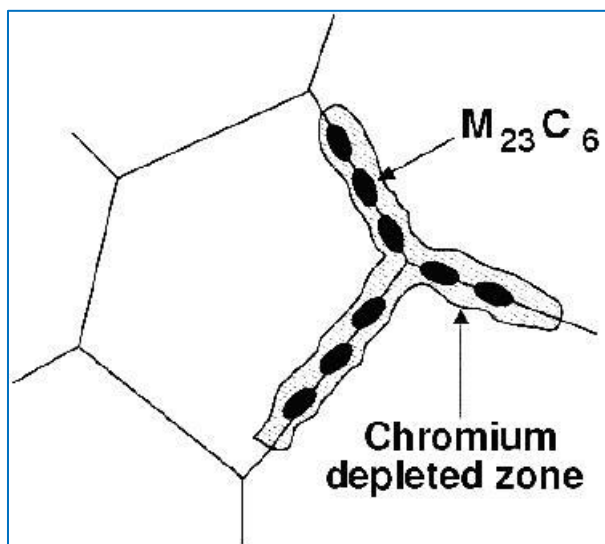


Figure 63: Typical Cr depletion at local region nearby grain boundary due to the formation of $Cr_{23}C_6$ precipitate.

3.1.15 Summary

High purity Ni-5Cr and Ni-20Cr model alloys were evaluated in argon back-filled and molten FLiBe environment at 700°C for 50 hours, 500 hours and 1000 hours in order to get a more fundamental understanding of alloy corrosion in molten FLiBe environment. The microstructure of annealed and

corroded samples was analyzed using multiple techniques. A protective Cr_2O_3 film formed on the annealed sample surface, which induced 0.5-1 μm Cr depletion but also protected alloys from further degradation. Grain size and grain orientation in cold rolled Ni-5Cr changed during annealing. Cr depletion was observed in all FLiBe-exposed alloys as deep as 140 μm after 1000 hours corrosion according to the observation of cross-sectional EDS Cr mappings. Cr depletion in the form of intergranular corrosion appeared severe and Cr depletion induced lattice parameter shrinkage in the near surface layer. Lattice parameter decreased by 0.33pm and 1.49pm for Ni-5Cr and Ni-20Cr after 1000 hours corrosion. Although the preferential Cr depletion along grain boundaries was observed in the etched cross-section of Ni-20Cr, it was not captured by the EDS mapping technique because the Cr depleted zone was too narrow to be differentiated by using this technique. The attack depth in terms of maximum Cr depletion distance was quantitatively analyzed. Effective diffusion coefficient D_{eff} was calculated from weight loss under an assumption of Cr depletion induced weight change during corrosion in molten FLiBe.

By analyzing alloys' microstructural evolution during corrosion in molten FLiBe, an understanding was developed of the contributions of grain (or volume) diffusion and grain boundary diffusion to the overall diffusion coefficient. In Ni-5Cr, the volume diffusion was observed as the dominant mechanism of Cr depletion. The grains with a misorientation angle relative to [001] direction in a range of 35°-50° were preferentially attacked by molten FLiBe, and the grains with misorientation angle far from this range had better corrosion resistance. In smaller grain-sized Ni-20Cr, the grain boundary diffusion was observed in etched cross-sectional SEM images, but couldn't be differentiated using EDS mapping. The grain boundaries were characterized using neighboring grains' misorientation angles. The preferentially attacked grain boundaries (as slits in SEM image) have misorientation angle in a range of 35°-50°. In all tested specimen, the CSL grain boundaries exhibited the best corrosion resistance to molten fluoride salt.

The state of Cr on the corrosion alloys' surface was analyzed through measuring the Cr (2p) bonding energy using XPS. The concentration of Cr metal is zero on alloy surface after corrosion in molten FLiBe.

This measurement provides a valuable boundary condition for calculating corrosion attack depth in terms of the maximum Cr depletion distance.

3.2 Corrosion of Hastelloy N in high temperature FLiBe

3.2.1 Overview

The Fluoride Salt-Cooled High-Temperature Reactor (FHR) is being actively considered as the next generation nuclear reactor because it offers, among other benefits, a high degree of passive safety and high thermal efficiency[2], [103], [104]. The primary coolant in FHR will most likely be Li^7 enriched FLiBe salt, which has a low neutron cross section and residual radioactivity, and high volumetric heat capacity, boiling point, and thermal conductivity[24]–[26].

Among the structural materials being considered for FHR is Hastelloy N, a Ni-based alloy which was originally developed during the Molten Salt Reactor Experiment (MSRE) program at the Oak Ridge National Laboratory (ORNL) specifically for a combination of corrosion resistance in molten fluoride salts and air-side oxidation resistance[53], [63], [72], [87], [105]–[108]. Most of the MSRE investigations were conducted in fuel-bearing molten fluoride (e.g., $\text{LiF-BeF}_2\text{-ZrF}_4\text{-ThF}_4\text{-UF}_4$) salts that were eventually used in the molten salt reactor developed under this program. An example of one significant experiment in the MSRE program was a flow loop of this salt constructed with Hastelloy N which operated successfully for 9.2 years in the temperature range of 560°C (cold section) to 700°C (hot section)[53]. Examination of the inner surface of the flow loop after this long-term test showed a Cr depleted attack depth of 100 μm in the hot section and deposition of Cr on the colder section of the loop. The outer air-side surface of the Hastelloy N loop exhibited an oxide layer with thickness of about 50 μm . This long-term corrosion test and other investigations suggested that Hastelloy N has good compatibility with molten fluoride salt and acceptable oxidation resistance in air[53], [108].

Nuclear graphite has been considered for use in high-temperature gas-cooled nuclear reactors and was used in the MSRE because of its excellent performance in high temperature and intense radiation environment[11], [27], [28]. The success of graphite used in MSRE has prompted the selection of graphite as matrix for fuel pebbles and structural material for FHR. However, the corrosion of Hastelloy N in molten FLiBe salt in the presence of graphite has not been investigated. With this background, the present work was undertaken to evaluate the corrosion performance and mechanisms of Hastelloy N in enriched FLiBe salt at 700°C with and without the presence of graphite. The corrosion test temperature of 700°C is the presently proposed outlet temperature of the FHR.

3.2.2 Characterization methods

The corrosion studies of Hastelloy N in purified FLiBe were listed in Table 6. The nominal composition of the alloy as provided by the manufacturer was shown in Table 4. The purified FLiBe and the graphite crucible used for the corrosion tests in this work are shown in Figure 64.

Following corrosion tests at 700°C for 1000 hours, Hastelloy N coupons were cleaned in deionized water for 24 hours, and air dried at room temperature (Figure 65(a)). Sample mass and dimensions were measured before and after corrosion tests for calculating weight change per unit area.

Additionally, to understand the thermal effect on the evolution of Mo rich precipitates in Hastelloy N, a series of annealing tests of Hastelloy N at 850°C for 20-500 hours were accomplished.

Characterization of the surface and near-surface regions of the samples were performed using x-ray diffraction (XRD, Siemens STOE), and scanning electron microscopy (SEM, LEO 1530) equipped with energy dispersive spectroscopy (EDS). Additionally, focused ion beam (FIB, Zeiss 1540XB CrossBeam) milling was employed to reveal the cross-sectional microstructure in the near-surface region of the material. A Titan scanning transmission electron microscopy (STEM, FEI) equipped with a high-angle annular dark-field (HADDF) detector and EDS system was also applied to identify the structure of nano-

sized carbide particles and Ni_3Fe phase underneath corrosion surface. For quantitatively analyzing the depth of attack, elemental line-scan composition profiles were conducted on samples cross-section from substrate to the exposed surface.

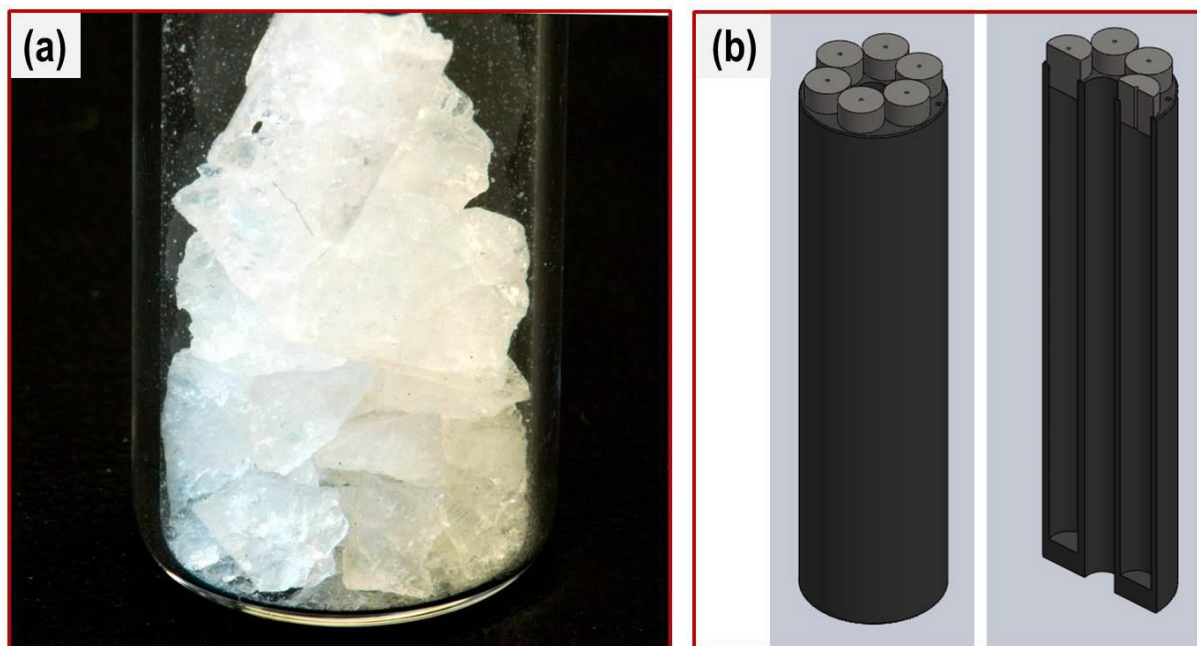


Figure 64: (a) Purified Li-enriched FLiBe salt at room temperature used in this study and (b) depictions of graphite crucible used in this study for conducting corrosion tests. Pure nickel liner was inserted into the compartments in effect providing a nickel containment for the corrosion test.

3.2.3 Weight change

The weight loss for the samples after corrosion tests in pure nickel capsule was only $0.124\text{mg}/\text{cm}^2$ which translates to about $1.226\mu\text{m}/\text{year}$ assuming uniform corrosion. This low corrosion rate is attributed to the inert nickel capsule and the purity of the salt used in this study. However, the samples tested in graphite capsule showed a weight gain of about $0.165\text{ mg}/\text{cm}^2$.

Under assumption of diffusion controlled corrosion for the Hastelloy N in nickel capsule, the overall diffusion coefficient was calculated to be $8.72 \times 10^{-19}\text{ m}^2/\text{sec}$ at 700°C using Equation (21), which is lower

than the Hastelloy N in fueled molten fluoride salt (containing 1%UF₄), $\sim 2.9 \times 10^{-18}$ m²/sec[72]. This indicates that the corrosion rate of alloy in non-fueled FLiBe is lower than that in UF₄ dissolved FLiBe.

3.2.4 Surface morphology of post-corrosion Hastelloy N

Figure 65(a) shows photograph of these samples and no significant corrosion attack was observed in these initial visual examinations. Higher magnification surface examinations (Figure 65(c) and Figure 65(d)) of the Hastelloy N samples after corrosion tests showed conclusive evidence of corrosion attack. The initially polished surface (Figure 65(b)) exhibited an increase in surface roughness and developed a porous structure for the samples tested in pure nickel capsule (Figure 65(c)). The formation of this porous surface is initially indicative of dissolution of alloying elements likely Cr from the alloy into the molten salt[71], [109]. For the samples tested in graphite containment, particle phases with diameter ranging from several tens of nano-meters to about 1.5μm covered the entire surface (Figure 65(d)). These particle phases formed due to the presence of graphite in the corrosion environment were likely responsible for the weight gain exhibited by the samples after corrosion testes.

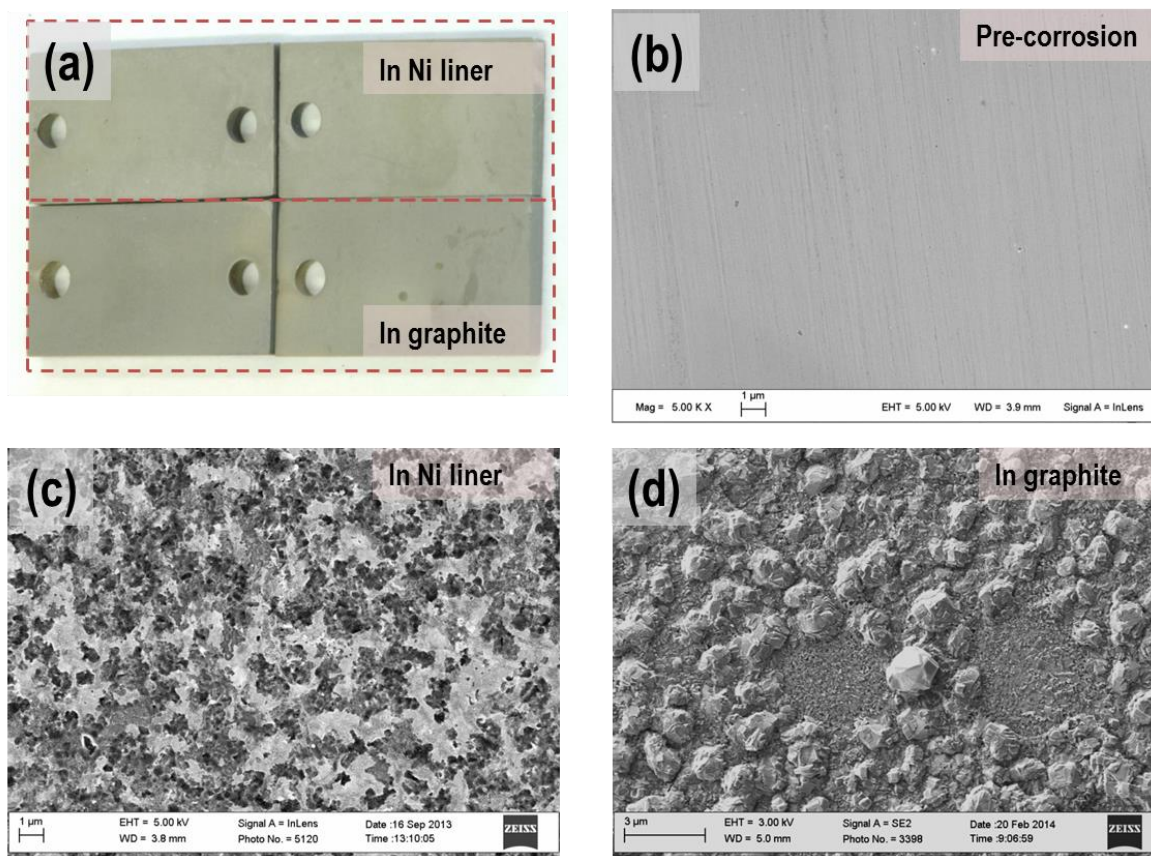


Figure 65: (a) Hastelloy N samples after corrosion testing in FLiBe salt in nickel and graphite capsule at 700°C for 1000 hours. (b), (c) and (d) SEM images showing surface morphology of Hastelloy N before and after corrosion tests in nickel and graphite capsules, respectively.

3.2.5 Elemental analysis on corrosion surface

The compositions of the surface features shown in Figure 65(c) and (d) were analyzed using the SEM-EDS technique and the results are shown in Figure 66. As shown in Figure 66(a), this porous layer formed on the samples tested in nickel capsule consisted of nickel enriched surface with Mo and Si rich precipitates in the size range from hundreds nanometers to several microns. The discontinuous, weak Cr map (Figure 66(a-2)) mainly resulted from the near-surface layer underneath porous surface because of a few microns x-ray escape depth while applying 15keV accelerating voltage for EDS scanning. For the samples tested in graphite capsules (Figure 66(b)), relatively high Cr concentration was observed on the

particulate phases and Mo and Si was not detected in the particulates. This suggests that the particulate phases are Cr-carbide particles formed due to the reaction between carbon from graphite source and Cr in the salt. Similar to samples tested in nickel capsules, Mo and Si rich precipitates were also observed on the sample surface.

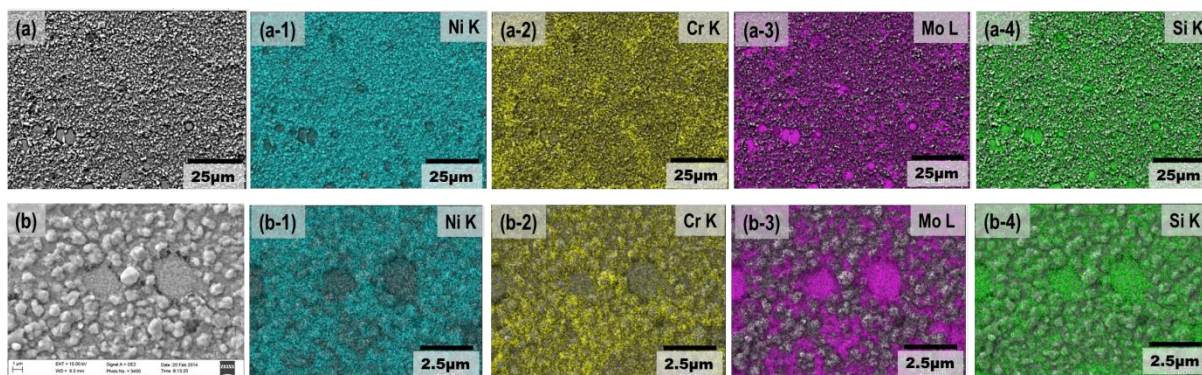


Figure 66: EDS elemental mappings of Hastelloy N corrosion surface after testing molten FLiBe in nickel (a, scale bar 25µm) and in graphite capsule (b, scale bar 2.5µm).

3.2.6 XRD analysis on corrosion surface

XRD was employed to investigate the phases in the near-surface regions of samples after corrosion tests. Figure 67 shows XRD patterns of Hastelloy N before and after corrosion tests in nickel and graphite capsules. The characteristic peaks of the matrix FCC austenite phase are clearly identifiable on the three types of samples[89], [110]. Additionally, the characteristic peaks of MoSi_2 (PDF card 01-072-6181) phase were detected on both types of post-corrosion Hastelloy N samples. Mo is known to be relatively inert in molten fluoride salt environment. In next subsection, the results showing that at high temperatures, the precipitates preferentially formed at grain boundaries in Hastelloy N potentially mitigate outward diffusion of Cr along grain boundaries will be presented. Furthermore, for the samples tested in graphite capsule (Figure 67(c)), in addition to MoSi_2 precipitates, the carbides of Cr_3C_2 , Cr_7C_3 , and Mo_2C were identified by the XRD pattern[111]–[116]. This analysis is consistent with EDS analysis of post-corrosion alloy surface shown in Figure 66(b). The Ni_3Fe was speculated to form in sample near-surface layer due

to the severe depletion of Cr from Hastelloy N and thermal diffusion of Mo toward either surface or grain boundary.

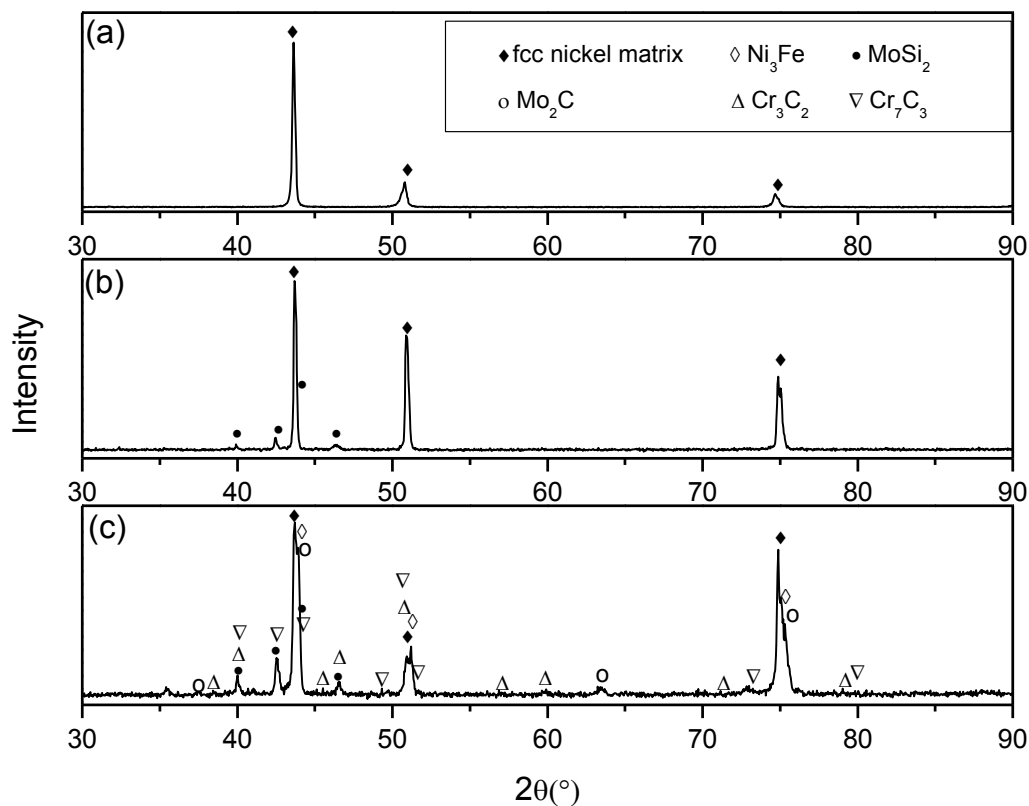


Figure 67: X-ray diffraction patterns of the near-surface regions of Hastelloy N (a) as-received condition, and (b) and (c) after corrosion testing in FLiBe salt at 700°C for 1000 hours in nickel and graphite capsule, respectively.

3.2.7 Microstructural instability of Hastelloy N at high temperature

Figure 68 shows cross-sectional SEM images and EDS elemental mappings of as-received Hastelloy N and annealed Hastelloy N samples. In as-received alloy, the Mo- and Si-rich round phases with diameter varying from hundreds nanometers to about five microns are randomly distributed in grains.

After annealing, the precipitates with relatively high concentration of Mo and Si formed at grain boundary. The precipitates coarsened and became discontinuous network at grain boundary with increasing of annealing time. This observation of Mo-rich precipitates nucleating and coarsening at grain boundary indicates the microstructural instability of Hastelloy N at high temperature. This Mo- and Si-rich precipitate evolution at high temperature might changes the corrosion resistance of Hastelloy N in molten fluoride salts. In recent publications, the effect of Mo content in Hastelloy N on corrosion was reported by F. Ouyang et.al.[96], [117]. It was concluded that long-term corrosion rate of Hastelloy N and Hastelloy B3 in molten FLiNaK was controlled by the outward diffusion of Cr and Mo. The study only discussed the relationship between Mo content in alloys and corrosion rate. The mechanism of Mo effect on corrosion behavior has not been well understood. From this annealing test, the migration of Mo-rich phase to grain boundary during high temperature exposure certainly mitigates Cr outward diffusion particularly along grain boundary.

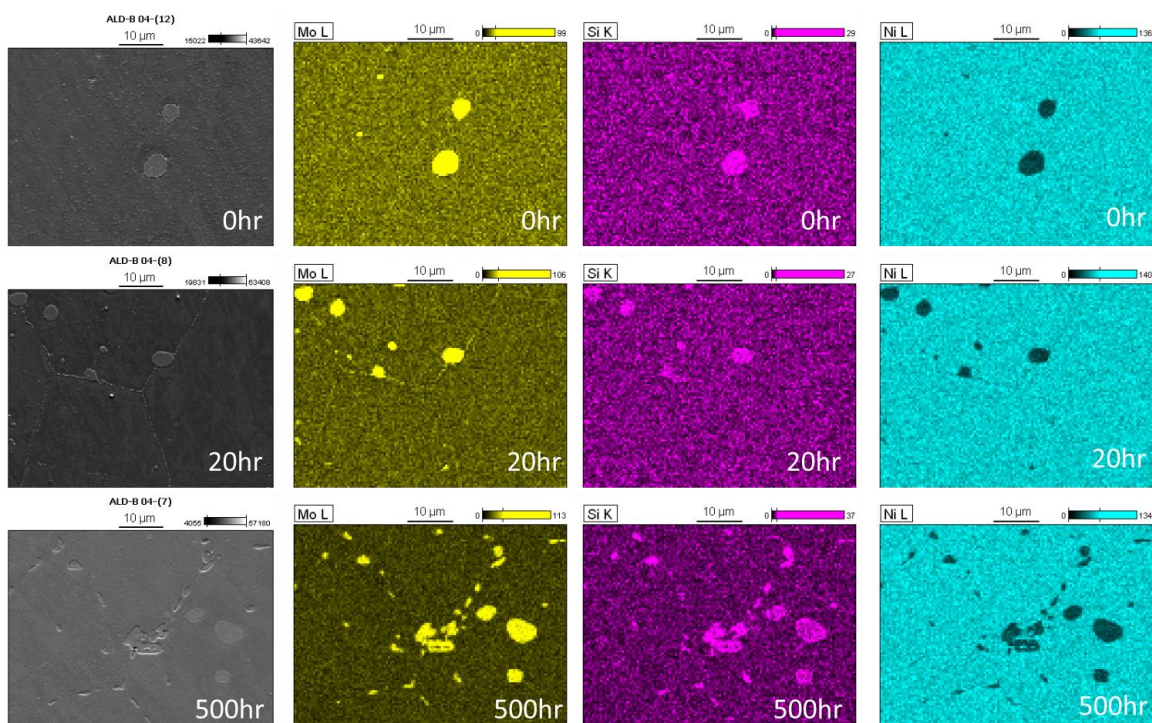


Figure 68: Cross-sectional SEM images and EDS mappings showing the Mo rich precipitates and the elemental distribution of Mo, Si and Ni of as-received and annealed Hastelloy N samples. Annealing temperature was 850°C. Scale bar is 10μm.

3.2.8 Microstructure of FIB milled cross-section

Further examination of the near-surface regions of post-corrosion Hastelloy N samples was performed by focused ion beam (FIB) milling of the surface (Figure 69). As observed in these FIB-SEM images, pores extend to ~200 nm into the substrate of the sample tested in pure nickel capsule (Figure 69(b)), indicating that the porous structure shown in plan-view image in Figure 69(a) extends to this depth below the surface. The void formation mainly results from outward diffusion of Cr and vacancy condensation analogous due to the Kirkendall effect observed in diffusion couples. As shown in Figure 69(c) and (d), the samples tested in graphite capsule exhibited a different near-surface microstructure. High magnification SEM image (Figure 69(c)) clearly showed three different shapes of carbides particles on corrosion surface, corresponding to Cr_3C_2 , Cr_7C_3 and Mo_2C as identified by XRD. Large size particles

on surface have different response to FIB milling electrons from alloy matrix, which caused rough cross-section as shown in Figure 69(d). Underneath the corroded surface, cavities were observed in the vicinity of MoSi_2 precipitates. The formation of these cavities is a result from the massive depletion of Cr from the region underneath the precipitates. Meanwhile, the Cr and some of the Mo in Hastelloy N matrix in near-surface region also thermally diffused to the sample surface to react with carbon and formed carbides particles. As a consequence of substantial Cr depletion and Mo diffusion outward, a layer of Ni_3Fe compound formed underneath the surface at 700°C . These microstructural observations are in agreement with XRD analysis (Figure 67(c)). Additionally, carbide containing layer was observed under Ni_3Fe phase layer. The dark features shown in Figure 69(d) were identified as Cr_{23}C_6 particles and had a diameter of tens nanometers by scanning transmission electron microscopy (STEM) analysis (Figure 70(d)).

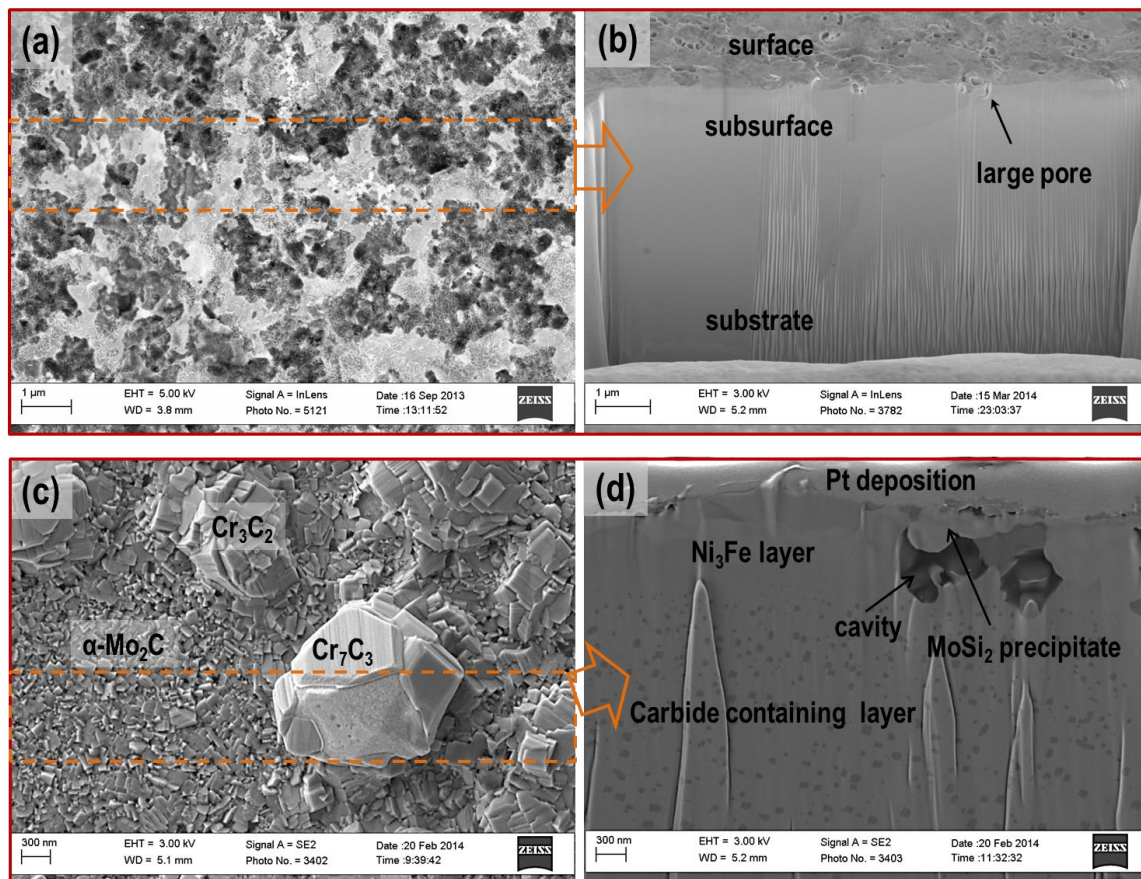


Figure 69: SEM images showing corrosion surface and FIB milled cross section underneath framed area (orange line) for the Hastelloy N tested in FLiBe salt at 700°C for 1000 hours in (a, b) nickel capsule and (c, d) graphite capsule, respectively.

3.2.9 Carbide particles formed within Hastelloy N

Under STEM, multiple layers from surface to substrate were clearly observed in the Hastelloy N sample tested in graphite capsule. As shown in Figure 70(a), a FIB lift-out samples encompassed about 7 μm depth below the corrosion surface. In near-surface layer (Figure 70(b)), TEM diffraction patterns identified regions 1 and 2 to be Ni₃Fe phase and nickel matrix. Figure 70(b) also presents the distribution of carbide particles formed underneath Ni₃Fe layer, becoming larger and more scattered in deeper regions. A close view in Figure 70(c) shows the spherical morphology of these particles within Hastelloy N matrix. The elemental compositions of these particles were quantitatively identified using STEM-EDS technique

(Figure 70(c)). High concentration of Cr, Mo and C was detected on a particle and the nominal compositions of Cr and Mn to C was approximately 23 to 6 in atom%. Combining these analyses, the nanosized particles formed in Hastelloy N matrix were identified as $(\text{Cr, Mn})_{23}\text{C}_6$. A few Mn substituted Cr lattice sites in Cr_{23}C_6 . Therefore, it was referred to Cr_{23}C_6 in this paper rather than $(\text{Cr, Mn})_{23}\text{C}_6$.

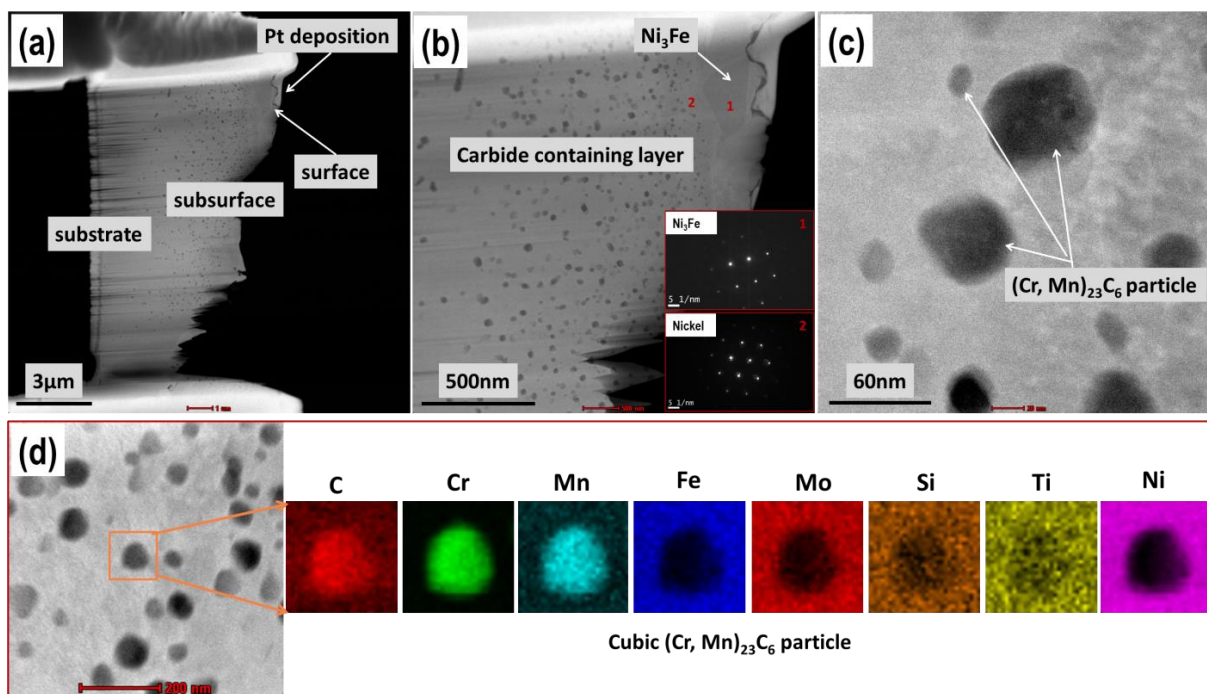


Figure 70: STEM images and EDS mapping showing the microstructure features in near-surface layer of the Hastelloy N tested in graphite capsule. (a) full view of a FIB lift-out sample, (b) a region in near-surface layer with TEM diffraction patterns in region 1 of Ni_3Fe layer and region 2 of Hastelloy N matrix, (c) close view of nanosized carbide particles within Hastelloy N matrix, and (d) quantitative elemental mapping (C, Cr, Mn, Fe, Mo, Si, Ti and Ni) of a particle marked by a square.

3.2.10 Cross-sectional microstructure of post-corrosion Hastelloy N

Cross-sectional SEM-EDS examination was performed to quantify the depth of corrosion attack in Hastelloy N tested in pure nickel and graphite capsule. Figure 71(a) shows a cross-sectional SEM image and EDS maps on the same region of the sample tested in pure nickel capsule. Mo and Si rich precipitates were observed both at grain boundary and in the vicinity of grain boundaries. EDS maps also identified

Mo and Si shown earlier in Figure 66(a). Cr depletion preferentially along grain boundary was only observed to a depth of about 3.5 μm . This observation suggests that the Cr depletion occurred predominantly through grain boundary diffusion D_{gb} .

The samples tested in graphite capsule were analyzed similarly with the SEM-EDS technique and showed dramatically different microstructure in the near-surface regions. Figure 71(b) shows a cross-sectional SEM image in the near-surface region of the material. Grain boundary attack was clearly observed, and Mo- and Si-rich precipitates were also observed both at grain boundaries and on the corrosion surface. This is similar to the observations made for samples tested in the nickel capsule. However, carbide particles (Cr_{23}C_6) were observed at depths ranging from approximately 2 μm to 9 μm from corrosion surface. These particles correspond to the black features observed in FIB milled cross-sectional SEM image shown in Figure 68(d) and STEM images in Figure 70(b). This carbide containing layer results from the reaction between the Cr in Hastelloy N matrix and the inward diffusing carbon from the molten FLiBe. The carbon in molten salt originally emanated from graphite crucible. Additionally a layer of about 1.4 μm in thickness underneath surface was devoid of any precipitate particles. This layer was identified as Ni_3Fe compound by XRD and STEM analyses. EDS mappings of principal elements also showed higher concentration of Fe in this layer. It is speculated that the Cr in the near-surface region diffuses outward to react with the inwardly diffusing carbon in the initial stage of corrosion and forms the chromium carbide phase. Mo thermally diffuses toward either grain boundary or surface, and then forms carbides phase particles on surface (as observed in SEM image in Figure 65(d) and Figure 69(c)). Meanwhile, the carbon in FLiBe salt diffused inwardly and reacted with Cr in deeper Hastelloy N matrix because the diffusion rate of carbon through nickel matrix $D_{C/Ni}$ ($\sim 10^{-10} \text{ m}^2/\text{sec}$) is much faster than Cr $D_{Cr/Ni}$ ($\sim 10^{-15} \text{ m}^2/\text{sec}$)[46], [68], [118]. As a result, after the initial stage of corrosion, the newly-formed chromium carbide particles (Cr_{23}C_6) stabilize Cr in Hastelloy N matrix. Thus no Cr is observed in the Ni_3Fe layer even though Cr concentration gradient existed. In the EDS maps, high concentrations of Cr and Mo were observed on corrosion surface, which corresponds to the Cr_3C_2 , Cr_7C_3 , Mo_2C , and MoSi_2

precipitate phases. Furthermore, high concentration of Cr was observed at the near-surface grain boundaries suggesting that Cr in Hastelloy N preferentially diffuses toward grain boundaries.

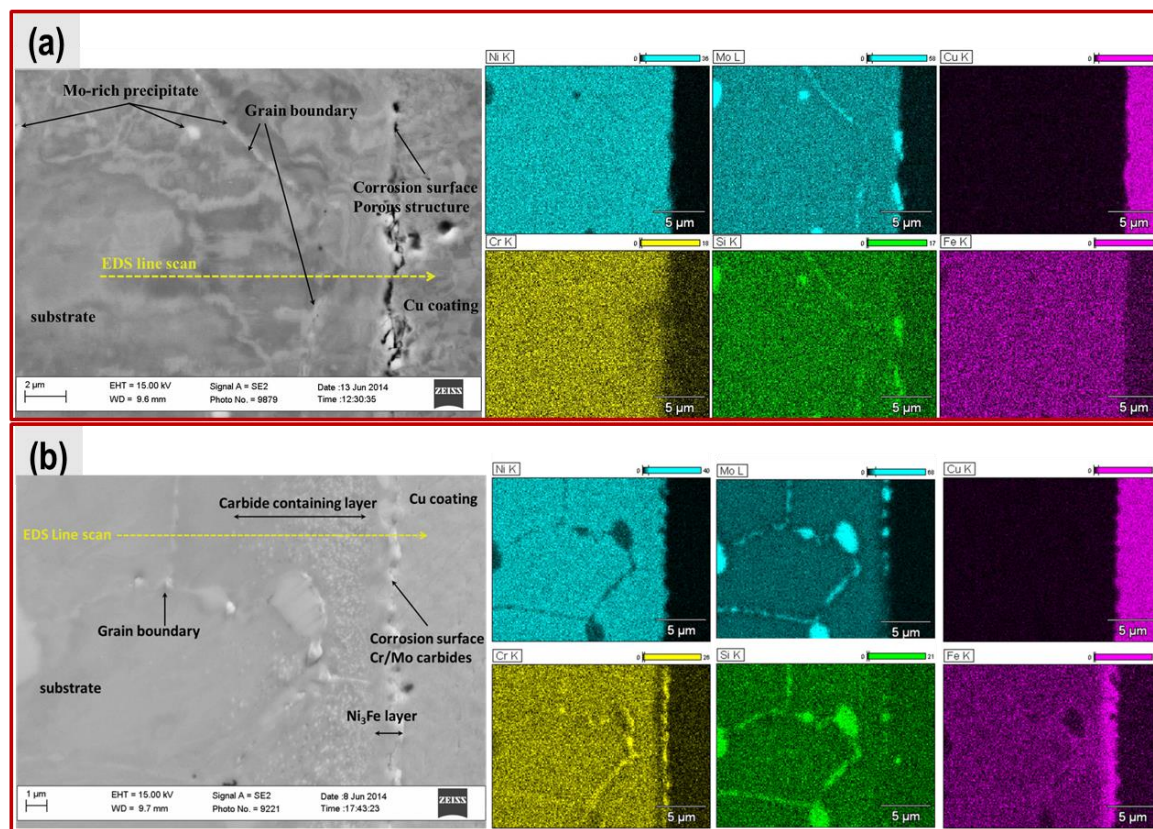


Figure 71: SEM-EDS analysis of Hastelloy N samples tested in (a) nickel capsule and (b) graphite capsule. Cu coating was electroplated on sample surface prior to polishing. Yellow dashed arrows in cross-sectional SEM images denote the traces of EDS line-scan.

3.2.11 Quantitative analysis of graphite effect on Hastelloy N corrosion

The concentration profiles of principal elements shown in Figure 72 and Figure 73 in post-corrosion Hastelloy N subsurface were collected by EDS line-scan along the dashed arrows labeled in the SEM images in Figure 71. The concentration profiles in Figure 72 (tested in pure nickel capsule) indicate Cr depletion depth of approximately 2.1 μm. However, the Cr depletion along the grain boundaries extended to about 3.5 μm using a cut-off criteria of 5% (Cr content of Hastelloy N is 7%). As a result, the Hastelloy

N corroded in FLiBe salt in pure nickel capsule at 700°C for 1000 hours was attacked about 3.5μm, which is consistent with EDS Cr map shown in Figure 71(a). In Figure 73 (tested in graphite capsule), multiple corrosion-affected layers with varying structures and compositions are separated by vertical dashed lines which correspond to the observations in the cross-sectional SEM images (Figure 69(d)) and TEM images (Figure 70). The profile of Cr shows about 0.6μm of a very high concentration zone which corresponds to the chromium carbides particles formed in the surface. About 1.4μm deep zone underneath carbides particles corresponds to Ni₃Fe alloy layer where the concentrations of Mo and Cr decreased but Fe and Ni increased. In a grain boundary about 10μm below the surface, the concentrations of Mo and Cr were higher than alloy matrix, which indicates the thermal diffusion of Mo and Cr preferentially toward grain boundaries within Hastelloy N. In the carbide containing layer of approximately 7μm in thickness, the Cr concentration remains constant at the values slightly higher than Hastelloy N matrix. The Gibbs free energy of formation per mole carbon was calculated using thermodynamic software of HSC7.0 (in Figure 74). In the environment with limited carbon source (through thermal diffusion inward to Hastelloy N), the chromium carbide of Cr₂₃C₆ was preferentially formed at 700°C. As a result, the Hastelloy N tested in graphite capsule exhibited a total corrosion attack depth zone of about 9μm region which consists of a 7μm carbide containing layer, 1.4μm Ni₃Fe layer, and 0.6μm layer of carbides particles.

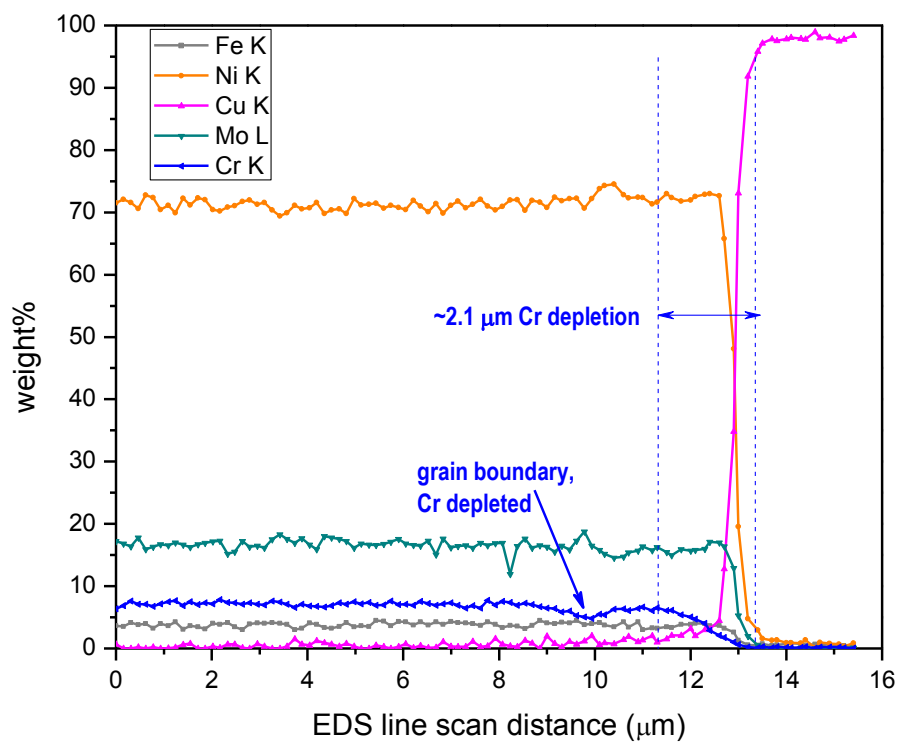


Figure 72: Quantitative concentration profiles of the main elements in the near-surface of Hastelloy N tested in pure nickel capsule.

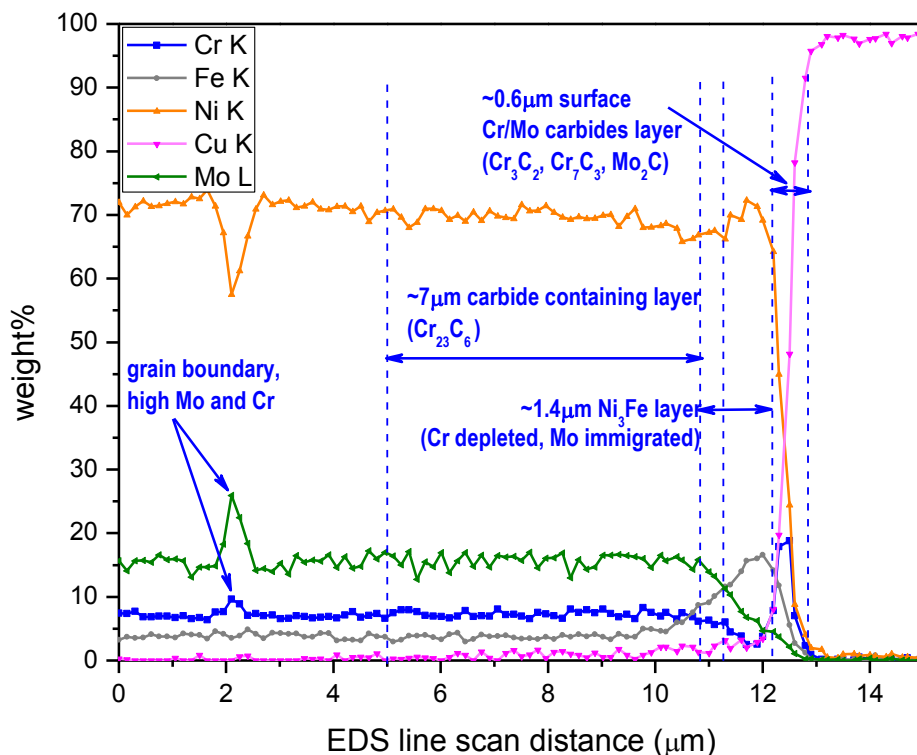


Figure 73: Quantitative concentration profiles of main elements in the near-surface of Hastelloy N tested in graphite capsule.

3.2.12 Kinetics of carbides formation

According to the calculation of Gibbs free energy of formation, shown in Figure 74, Cr_{23}C_6 is more thermodynamically favorable than other carbides at 700°C , however, Cr_3C_2 , Cr_7C_3 , and Mo_2C were observed as final products of corrosion on Hastelloy N surface in molten FLiBe during tests carried out in graphite capsules. On alloy surface that directly contacted with molten salt containing abundant carbon source, the chemical reaction $\text{Cr}_{23}\text{C}_6 + \text{C} \rightarrow \text{Cr}_7\text{C}_3$ occurred and consumed Cr_{23}C_6 .

Comparing the analyses of Hastelloy N samples tested in FLiBe salt in pure nickel and graphite corrosion capsules, the samples tested in graphite capsule showed a corrosion affected depth about $5.5\mu\text{m}$ greater as compared to those tested in nickel capsule. Pure nickel is highly stable in molten fluoride salts

and the attack in Hastelloy N in this nickel capsule was only from the corrosion of FLiBe salt. However, the carbon source from graphite capsule wall in molten FLiBe affected Hastelloy N to a greater extent due to the formation of a carbide containing layer. Although the formation of this carbide containing layer changes the microstructure and properties of the near-surface layer, the formation of the highly stable Cr_{23}C_6 appears to stabilize Cr in alloy from dissolving in the molten FLiBe, and may provide an engineering solution to mitigate corrosion in Hastelloy N in the long-term.

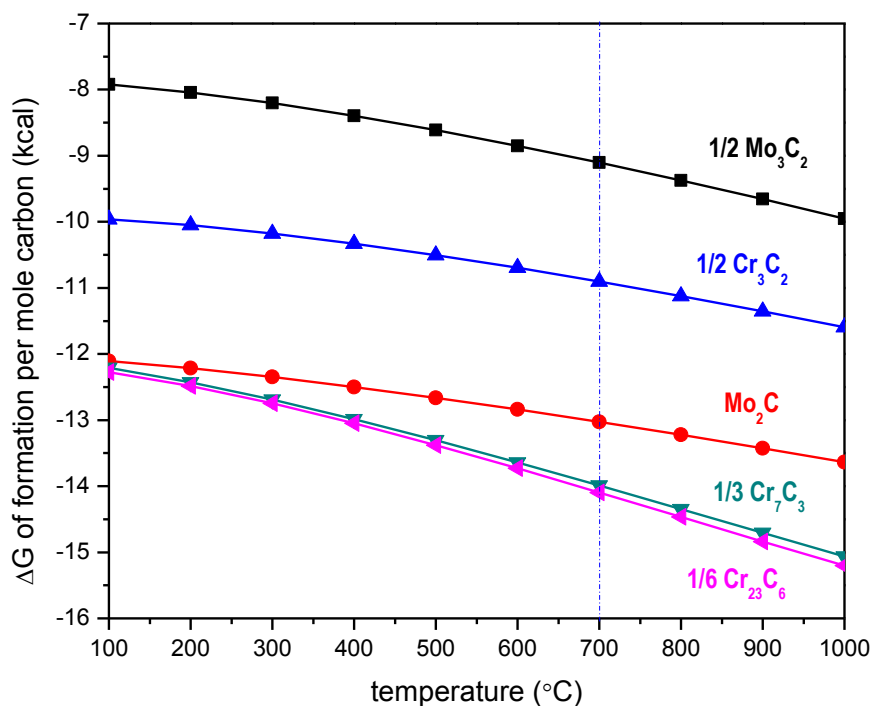


Figure 74: Gibbs free energy of formation (ΔG) of carbides per mole carbon as a function of temperature, calculating with HSC7.0.

3.2.13 Summary

Corrosion tests of Hastelloy N, a low chromium, high molybdenum nickel-based alloy have been carried out in purified $2^7\text{LiF}\text{-BeF}_2$ (66-34 mole%) molten salt at 700°C for 1000 hours, using all

precautions necessary for handling beryllium and fluorine bearing salts. Tests were performed in pure nickel and graphite capsules. The microstructural changes at the surface and in near-surface regions of the samples as a result of corrosion were evaluated using SEM-EDS analysis, FIB milling, XRD and STEM techniques. For samples tested in nickel capsules, a porous structure of about 200nm deep formed at the surface and the depth of corrosion attack as measured by chromium depletion extended to a depth of 3.5 μ m. MoSi₂ precipitate particles were also observed and presumed to form primarily due to thermal effects. For samples tested in graphite capsules, in addition to the formation of Cr₃C₂, Cr₇C₃ and Mo₂C particles on surface, massive chromium depletion and concurrent formation of Ni₃Fe phase layer approximately 1.4 μ m deep was observed in near surface region. Underneath this, a layer containing Cr₂₃C₆ particles was observed in Hastelloy N matrix, approximately 7 μ m deep. Chromium depletion was not observed in this layer. In terms of the depth of microstructural changes induced by corrosion, the presence of graphite accelerates corrosion; however the stabilization of chromium as carbide phase may potentially mitigate Cr depletion in the long-term which is the primary mechanism of corrosion in molten fluoride salts.

3.3 Corrosion of 316 stainless steel in high temperature FLiBe

3.3.1 Overview

The Fluoride-Salt-Cooled High-Temperature Reactor (abbreviated conventionally as FHR) is emerging as a leading reactor concept for the next generation nuclear reactors[1], [2], [103]. The FHR features molten fluoride salt as the primary coolant, which provides for a number of potential benefits such as high degree of passive safety, solubility for many fission products, atmospheric pressure operation, high thermal efficiency, and lower spent fuel per unit energy[24], [26], [56]. However, corrosion of structural materials in molten fluoride salts is an important consideration which must be understood and mitigated for the successful fruition of the FHR. The protective oxide layer relied upon for corrosion resistance in most high temperature environments has a propensity to dissolve in molten

salt[36], [44], [119]. The containment alloy for the FHR should not only exhibit minimum corrosion in the molten fluoride salt coolant, but it should also exhibit high air-side oxidation resistance and creep strength at the intended high temperatures of FHR operation. These unique needs were recognized in the earlier Aircraft Nuclear Program (ANP) and the Molten Salt Reactor Experiment (MSRE) in the United States between 1950 and 1970 which led to the successful development and operation of the molten salt-cooled reactor[53], [120]. These programs used a $\text{NaF-ZrF}_4\text{-UF}_4$ and $\text{LiF-BeF}_2\text{-ZrF}_4\text{-UF}_4$ salt where the uranium fuel was dissolved in the molten salt coolant. Extensive corrosion studies in these programs demonstrated the strong propensity of chromium in the test alloys to dissolve in the molten fluoride salts. Rigorous experimentation eventually led to the development of Hastelloy-N, a Ni-based alloy low in Cr (7 wt.%) and high in Mo (16 wt.%) that exhibited outstanding long-term corrosion resistance in long-term corrosion tests in thermal flowing loops, as well as good air-side corrosion resistance. However, Hastelloy-N is not code certified in the ASME Boiler Pressure Vessel Code under sections I, III, B31.1, and B31.3, and therefore cannot presently be used in a commercial reactor without extensive testing[121].

Unlike the MSRE, the recent FHR design proposes to use a non-fuel bearing FLiBe salt as primary coolant with TRISO fuel particles submerged in this coolant[1], [2]. Although the containment material for FHR has not been decided, 316 stainless steel is being actively considered because of its existing code certification at the intended FHR operation temperatures. Experiments associated with MSRE using flow loops have shown 316 stainless steel to have acceptable corrosion resistance in molten FLiBe at 650°C, particularly when the redox potential of the salt was controlled with beryllium additions[44]. Lastly, nuclear graphite has been selected as an in-core material for the FHR because of its high temperature strength and chemical resistance to molten fluoride salts. Recent work has shown that graphite when present in conjunction with structural alloys in molten fluoride salt, FLiNaK can adversely affect their corrosion performance[35], [80].

With the above background, the present study was aimed at investigating the corrosion behavior of 316 stainless steel in molten FLiBe salt at the designed FHR outlet temperature of 700°C under static

test conditions. The tests were performed in 316 stainless steel and graphite capsules to determine the effect of the presence of graphite on corrosion.

3.3.2 Characterization methods

Table 5 lists the nominal chemical composition of material. Two 316 stainless steel samples with polished surface were suspended in each capsule using 316 stainless steel wires. For the corrosion tests, the crucible was heated in a ceramic furnace to 700°C in the glove box where it was maintained for exposure durations of 1000, 2000, and 3000 hours. These corrosion test times are longer than those reported in literature and were used to improve accuracy in corrosion rate measurements and conduct experiments well past the initial impurity-driven corrosion stage. The corrosion temperature of 700°C was selected to meet the intended FHR outlet temperature.

The mass and dimensions of corrosion samples were measured and compared to the pre-corrosion measurements to calculate weight change (mg/cm^2) as an initial metric of the extent of corrosion. The microstructure of the corrosion layer was characterized using x-ray diffraction (XRD), and scanning electron microscopy (SEM) equipped with energy dispersive spectroscopy (EDS). The corrosion surface of one 3000 hour test sample was ground in small increments to analyze the phase transitions in the near surface layers by XRD. Additionally, all samples were mounted and polished to observe their cross-sectional microstructure from the corrosion surface to inner substrate using SEM-EDS and Electron Backscatter Diffraction (EBSD) techniques. The affected depth in the alloy was evaluated by measuring the maximum Cr depletion depth using EDS analysis. EBSD analysis was performed on LEO 1530 SEM incorporated with TSL (TexSEM Laboratory, Inc.) Orientation Imaging Microscopy (OIM). Alpha phase and gamma phase of iron were pre-loaded into OIM data collection system to identify both phases distribution. Grain size distribution, grain orientation, phase distribution as well as grain boundary character distribution were collected from the same region as EDS scanning. Collected EBSD data was then cleaned up using TSL-OIM data analysis software, as standard cleanup processes[77], [78], [122]. Scanning Transmission Electron Microscope (STEM, Titan, FEI) and EDS

techniques were employed to analyze the microstructure of carbides formed within near surface region. A sample tested in graphite capsule for 3000 hours was selected for STEM analysis. Bright field and dark field STEM images were collected from an area near to corrosion surface. The composition of particles was analyzed using STEM-EDX technique.

3.3.3 Weight change

The results of weight change measurements after corrosion tests are shown in Figure 75. In all cases the samples experienced a loss in weight due to corrosion indicating a material dissolution mechanism, and this weight loss increased with exposure time. Up to 2000 hours, the weight loss was higher for the samples tested in graphite capsules as compared to the samples tested in stainless steel capsules, while at 3000 hours, the weight loss for the two capsule material tests were approximately identical. Herein, it should be noted that the net weight losses for the samples tested in graphite capsules should be higher as chromium carbide particle formation in the alloy matrix almost certainly resulted in weight gain after corrosion tests. This will be discussed later through microstructure analyses.

As the depletion of Cr becomes pronounced in the near-surface, the chromium inside the sample diffuses outwards due to a concentration gradient. The rate of Cr depletion therefore depends on its thermal diffusion coefficient in 316 stainless steel. As Cr is depleted deeper within the sample, grain boundaries rather than grains, become the preferred path of Cr migration because of their higher diffusion coefficient[47], [50]. Assuming a constant diffusion source, the weight change (ΔM) due to Cr depletion as a function of time can be expressed as Equation (19). According to this formula, the effective diffusion coefficient (D_{eff}) of Cr in the 316 stainless steel samples tested in 316 stainless steel capsules, without graphite, was calculated to be $4.2 \times 10^{-19} \text{ m}^2/\text{s}$ at 700°C , which is in the range of the reported $D_{\text{Cr/316ss}} = 10^{-19} \sim 10^{-17} \text{ m}^2/\text{s}$ at 700°C [47], [50]. Therefore, the weight loss of 316 stainless steel in FLiBe occurred as proportionally to the square root of corrosion time, shown in Figure 75, indicating thermal diffusion-controlled corrosion[45].

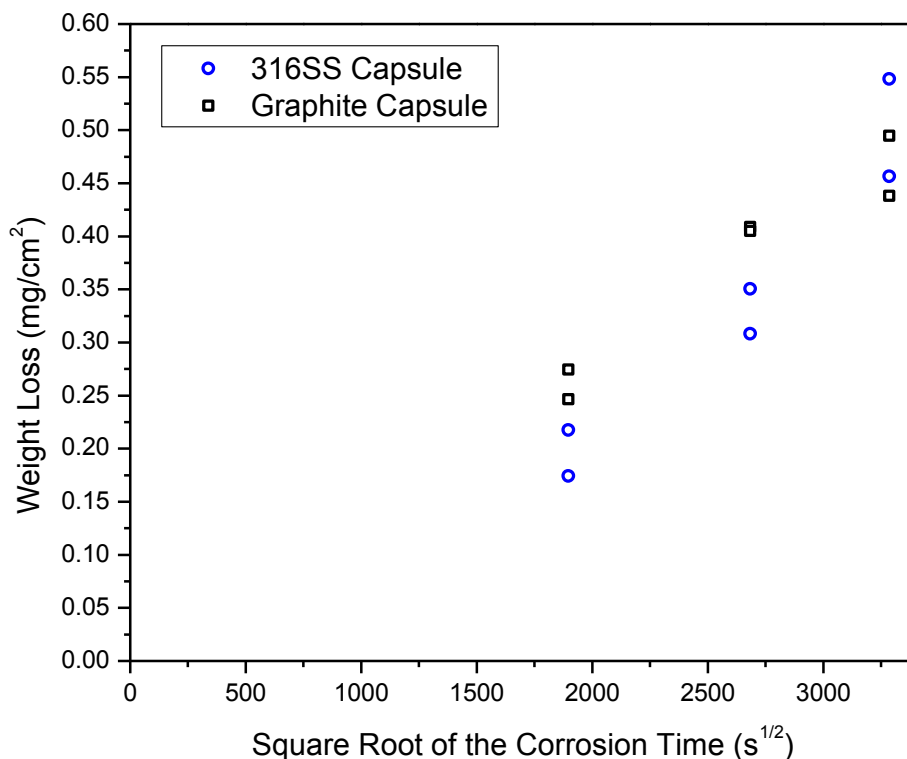


Figure 75: Weight measurements for 316 stainless steel samples tested at 700°C in molten FLiBe salt in 316 stainless steel and graphite corrosion capsules (two samples in each capsule) as a function of square root of corrosion time.

3.3.4 Observation on corrosion surface

The surface images of various samples after the corrosion tests are shown in Figure 76. All samples clearly showed evidence of corrosion attack particularly along the grain boundaries, although there is evidence of attack on the grains as well. As expected, the degree of attack is seen to increase with exposure time. The samples tested in the graphite capsules had wider grain boundary attack than those tested in 316 stainless steel capsules. These initial observations indicate that graphite accelerates the corrosion attack to 316 stainless steel and is to some extent consistent with the trends in weight loss

measurements shown in Figure 75. Additionally, pitting is observed on the grains of all samples and there is evidence of round particulate phases adhered to the surface.

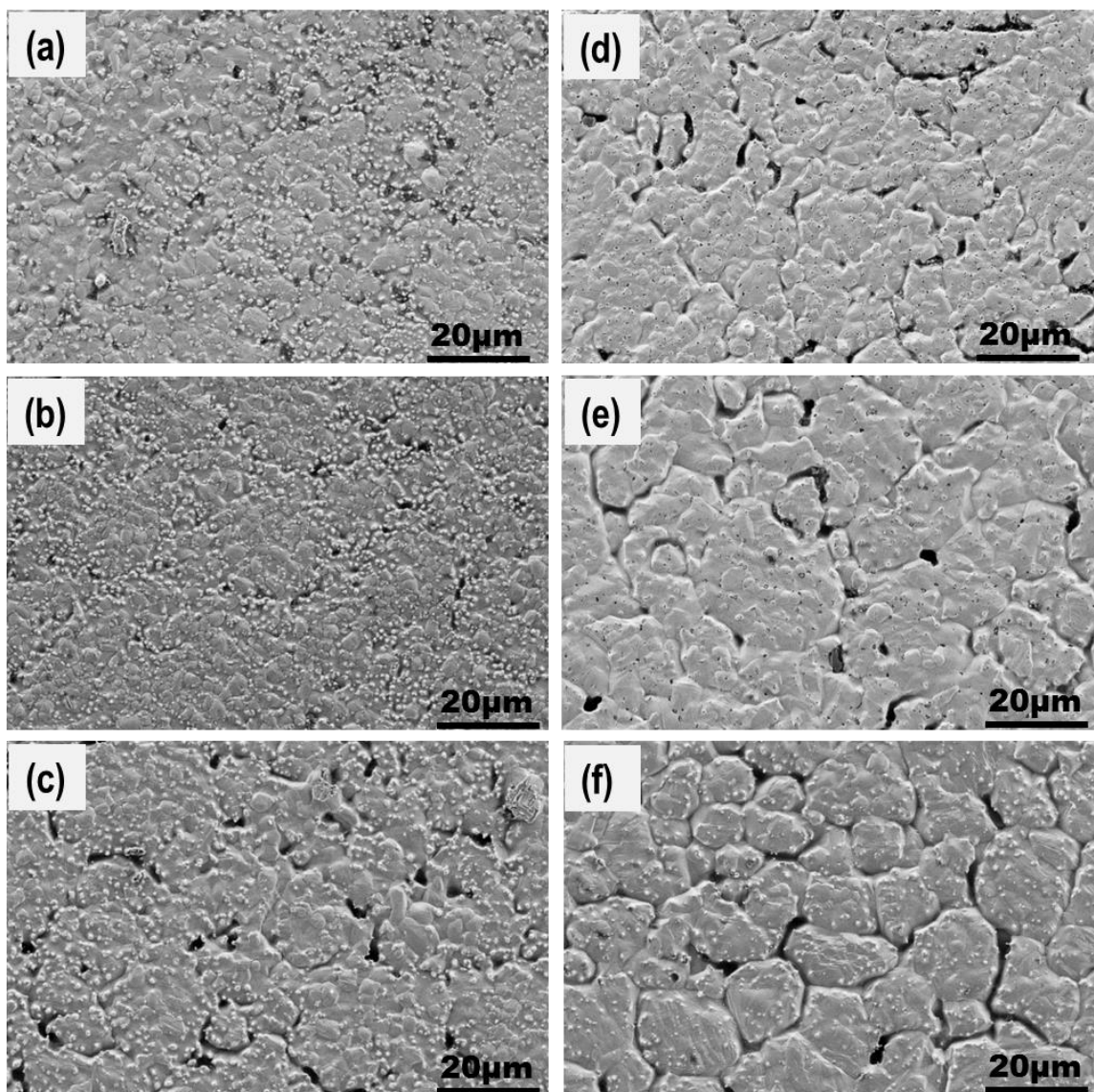


Figure 76: Surface SEM images of 316 stainless steel samples after corrosion testing under different conditions. a, b, and c in 316 stainless steel capsules, and d, e, and f in graphite capsules for 1000, 2000, and 3000 hours, respectively.

3.3.5 Microstructure of particulate phase on corrosion surface

Figure 77 shows SEM images of the surface of the samples exposed for 3000 hours in 316 stainless steel and graphite capsule tests, along with Mo element EDS x-ray mapping of the surface. A large number of Mo-rich precipitate particles were detected on the corrosion surface regardless of capsule material. The formation of these precipitates appears to be a consequence of Cr depletion at the surface which increases the activity of Mo and Si in the near-surface regions and promotes the precipitation of MoSi_2 phase. Molybdenum is known to be quite inert to molten fluoride salts, however pure silicon is prone to attack in this environment[36]. The formation of MoSi_2 precipitates prevents the fluoridation of Si.

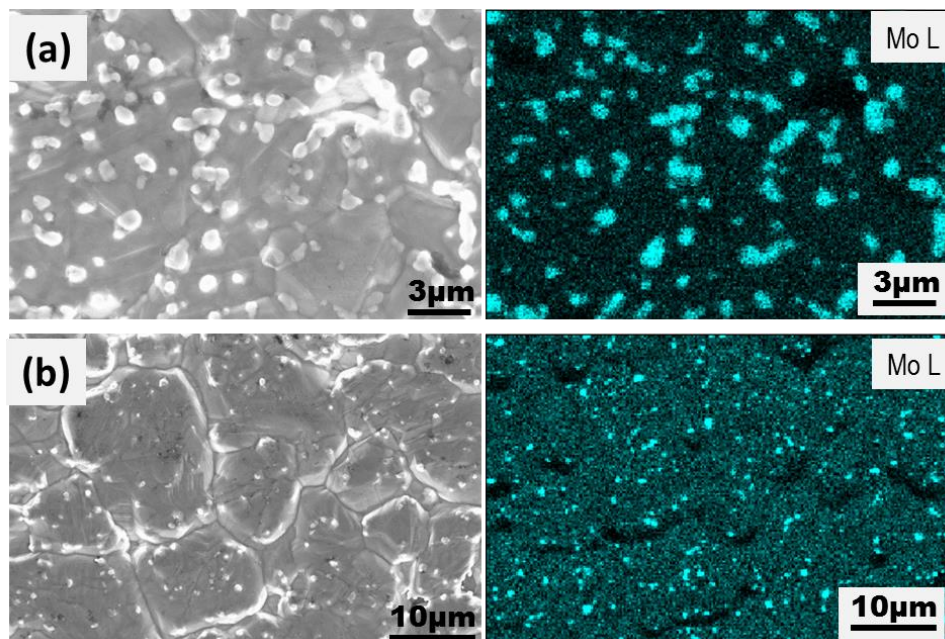


Figure 77: EDS maps showing Mo-rich precipitates on the corrosion surface of 316 stainless steel samples tested in (a) 316 stainless steel lined capsule and (b) graphite capsule after 3000 hours exposure to molten FLiBe salt at 700°C.

High magnification SEM images of the surface of the samples tested for 3000 hours, shown in Figure 78, provide further insights into the corrosion mechanisms. For the samples tested in a graphite capsule, as shown in Figure 78(b), deep, steep cleavage was observed at the grain boundary, indicative of more severe attack than those in 316 stainless steel capsule. These samples also contained hexagonal

Cr_7C_3 crystals and spherical Mo-rich particles on the corrosion surface. The Cr_7C_3 crystals were embedded in grains, protruding out from the edges, while the Mo-rich particles reside on the tip of Cr_7C_3 crystals. For the samples tested in the 316 stainless steel lined capsule, shown in Figure 78(a), only the spherical Mo-rich particles were observed on the corrosion surface. Compared to Figure 78(b), the grain boundary was not attacked as steeply. The difference in the surface microstructure of the two types of samples demonstrates the acceleration effect of graphite.

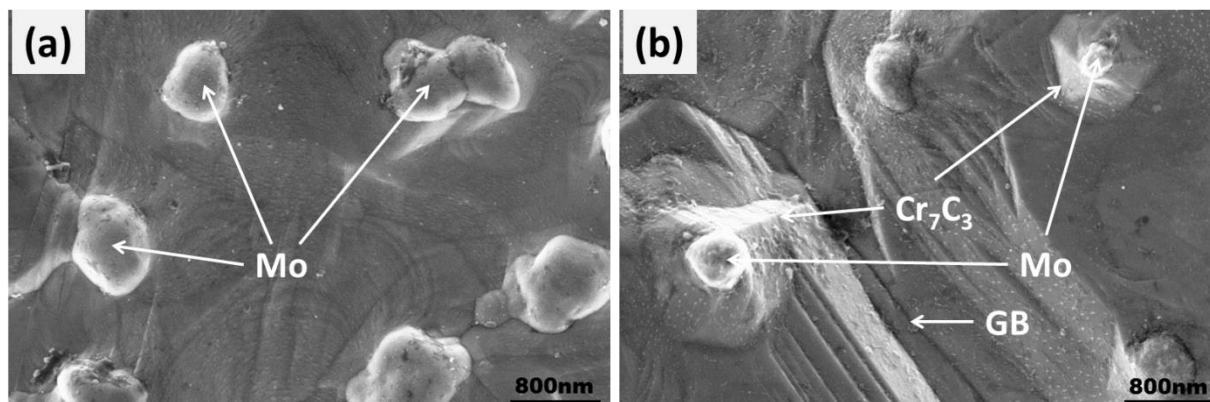


Figure 78: High magnification (20,000 \times) SEM images of the 316 stainless steel sample's corrosion surface after corrosion testing in (a) 316 stainless steel capsule and (b) graphite capsule for 3000 hour. Mo denotes Mo-rich phase and GB denotes grain boundary.

3.3.6 XRD analysis on corrosion surface

The phase content of the corrosion layer was further analyzed using XRD technique. Figure 79 shows the XRD patterns of the as-received samples and samples tested for 3000 hours in the two capsule materials. After corrosion, the characteristic peak intensity of austenite phase (γ phase) decreased with the (220) peak shrinking and the (111) and (200) peaks completely disappearing. The characteristic peaks of α -ferrite phase generated as indicated by the appearance of (200), (211) and (110) peaks. Main peak (110) of both α -ferrite phase and α' -martensite phase overlapped on XRD pattern. The α' -martensite phase in the as-received sample might have been introduced during the cold-working of the alloy during sheet fabrication[123], [124]; the formation of α -ferrite phase is attributable to the corrosion process.

The XRD patterns (Figure 79) also successfully identified tetragonal MoSi_2 (PDF card 01-072-6181) on the corrosion test samples' surface from both types of capsules material, but Cr_7C_3 (PDF card 04-002-2449) only on the corrosion surface tested in graphite capsules[125]. XRD pattern presents MoSi_2 main peaks of (004) and (112) both at around $2\theta=46.2^\circ$ and (110) at $2\theta=39.7^\circ$. MoSi_2 peaks are relatively weak due to the relatively low concentration of these precipitates. Main characteristic peaks of hexagonal Cr_7C_3 crystal such as (421) at $2\theta=44.3^\circ$ and (420) at $2\theta=39.3^\circ$ overlapped with other peaks, and a weak peak of (202) at $2\theta=42.6^\circ$ in XRD pattern due to its relatively low percentages in sample[125].

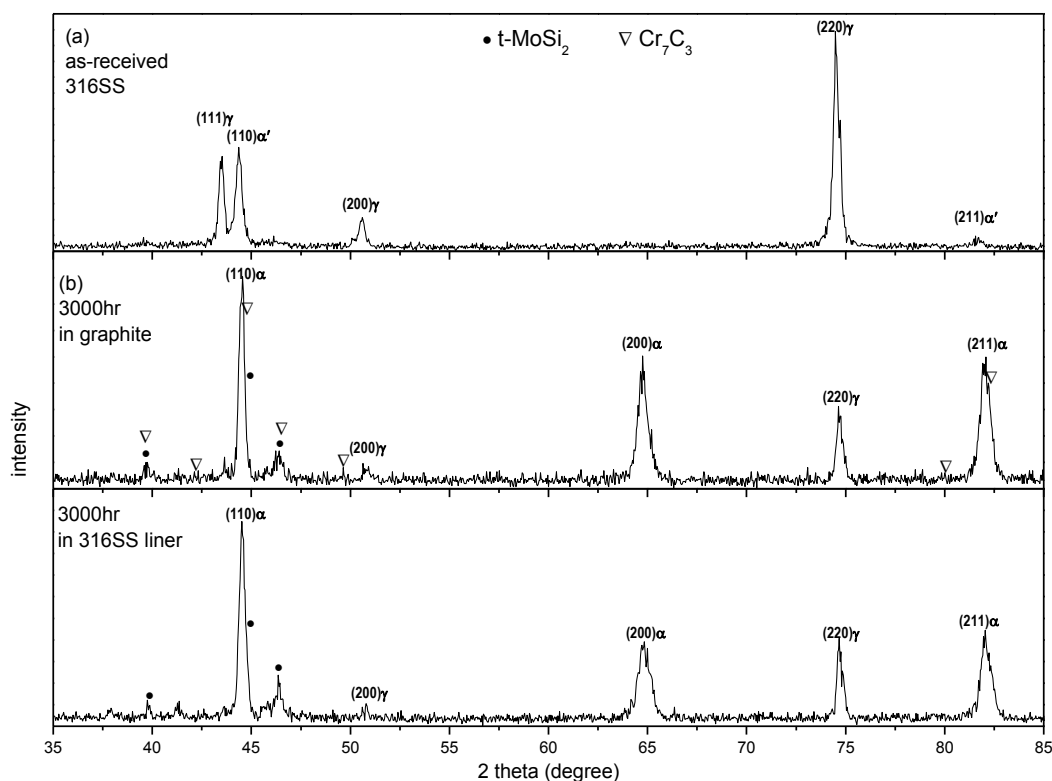


Figure 79: XRD patterns collected from the surface of (a) as-received 316 stainless steel, (b) 316 stainless steel tested in a graphite capsule, and (c) 316 stainless steel tested in a 316 stainless steel capsule. (b) and (c): both tested for 3000 hours.

3.3.7 Cr depletion induced phase transformation

In order to further confirm that α -ferrite phase formation after corrosion tests was not a thermal effect, and to ascertain the depth of the ferrite transformation, the surface of the samples from the corrosion test was ground slightly and re-analyzed using XRD. As shown in Figure 80, XRD patterns of the incrementally ground 3000 hour corrosion test surfaces shows the gradual resurgence of the γ phase. After removing 45-50 μm from the surface, the XRD pattern appears identical to that of the as-received sample. The α -ferrite phase was dominant for only 5-10 μm into the sample which, as will be shown later, is on the same order as the corrosion attack depth.

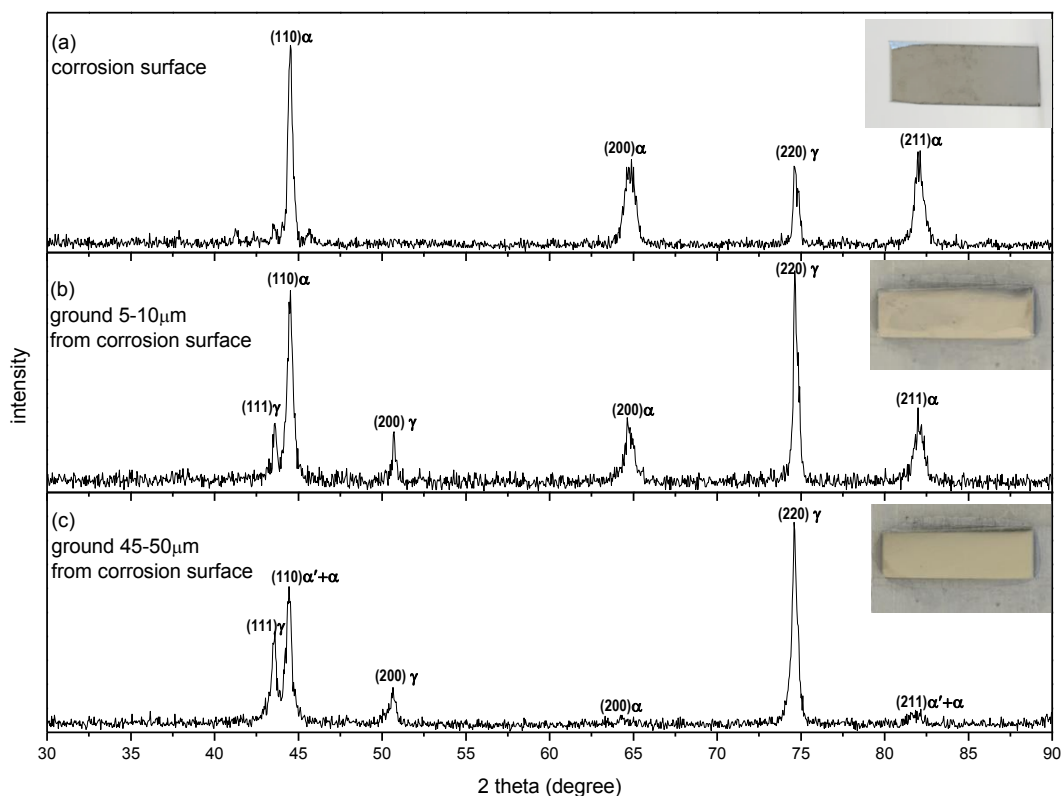


Figure 80: XRD patterns scanned on (a) the original corrosion surface tested in 316 stainless steel capsule for 3000 hours, (b) the surface after grinding down 5 μm to 10 μm below the original surface of the sample in (a), and (c), the surface after grinding down 45 μm to 50 μm below original corrosion surface of the sample in (a). Photographs on right side show the XRD scanned surface.

3.3.8 Cross-sectional microstructure

The depth of the corrosion attack and the internal microstructure of the corrosion layer were examined in sample cross-sections under the SEM. Figure 81(a-c) shows the images of samples tested in 316 stainless steel capsules and Figure 81(d-f) shows the samples tested in graphite capsules, each for 1000, 2000 and 3000 hours respectively. For the samples tested in graphite capsules, the randomly distributed particulate phases in the 316 stainless steel matrix are chromium carbide particles which were previously observed protruding from the grain boundaries in the plan view images (Figure 78(b)). These particles formed as inwardly diffusing carbon reacted with outwardly diffusing chromium. Increase in corrosion test time resulted in an increase in depth of the region containing these particles from approximately $5\mu\text{m}$ at 1000 hours, to deeper than $50\mu\text{m}$ after 3000 hours. As expected, these chromium carbide particles were not observed in the samples tested in 316 stainless steel capsules due to the absence of carbon source in the molten salt. Additionally, in all of the cross-sectional SEM images, M_{23}C_6 type carbide precipitates were observed at grain boundaries, which usually formed in 316 stainless steel during high temperature aging[90], [91], [102]. The samples exposed to salt for 3000 hours in the graphite capsule were marked by the recession of corrosion surface, particularly at the grain boundary. As shown in Figure 81(f), a crack developed several microns deep into alloy along grain boundary. It corresponds to the observation of a deep cleavage at grain boundary shown in Figure 78(b). This heavy attack at the grain boundary was not observed in the samples tested in 316 stainless steel capsules.

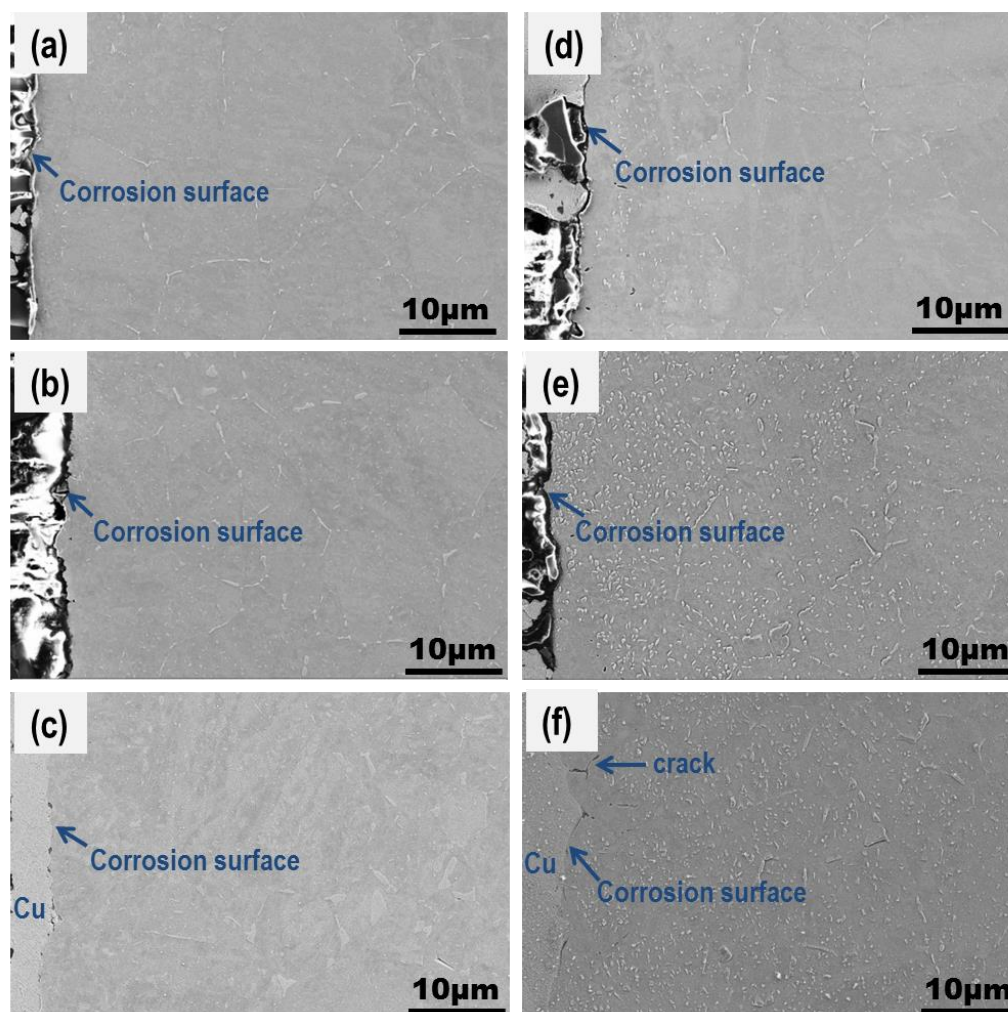


Figure 81: Cross-sectional SEM images of 316 stainless steel samples after corrosion tests; (a), (b), and (c) tested in 316 stainless steel capsules, and (d), (e) and (f) tested in graphite capsules for 1000, 2000, and 3000 hours respectively. Please note that samples in (c) and (f) were electroplated a Cu layer for edge protection.

3.3.9 Intergranular corrosion attack in alloy

The depth of corrosion attack was measured in terms of the maximum Cr depletion distance using EDS elemental maps for Cr as shown in Figure 82. Based on this criterion, the affected corrosion attack depth was found to be from 6.4µm to 11.5µm for the samples tested in 316 stainless steel capsules, and from 13.7µm to 22.5µm for the samples tested in graphite capsules for corrosion time from 1000 hours

to 3000 hours. As expected, increasing the corrosion test time increased the affected depth; testing in graphite capsules doubled the maximum Cr depletion depth. The EDS maps also showed Cr depletion through volume diffusion in a shallow region near the corrosion surface. This can be seen in Figure 82(d) where volume Cr depletion accounts for a layer approximately $3\mu\text{m}$ thick. This observation indicates that volume diffusion is dominant mechanism for the Cr depletion during initial corrosion stage due to the large projected area ratio of grain to grain boundary on corrosion surface. Additionally, the contrast between Cr concentration in the grain boundary and substrate is higher for the samples in graphite capsule than those in 316 stainless steel capsule, which corresponds to the more severe Cr depletion in grain boundary. This difference further suggests the acceleration effect of graphite on Cr depletion.

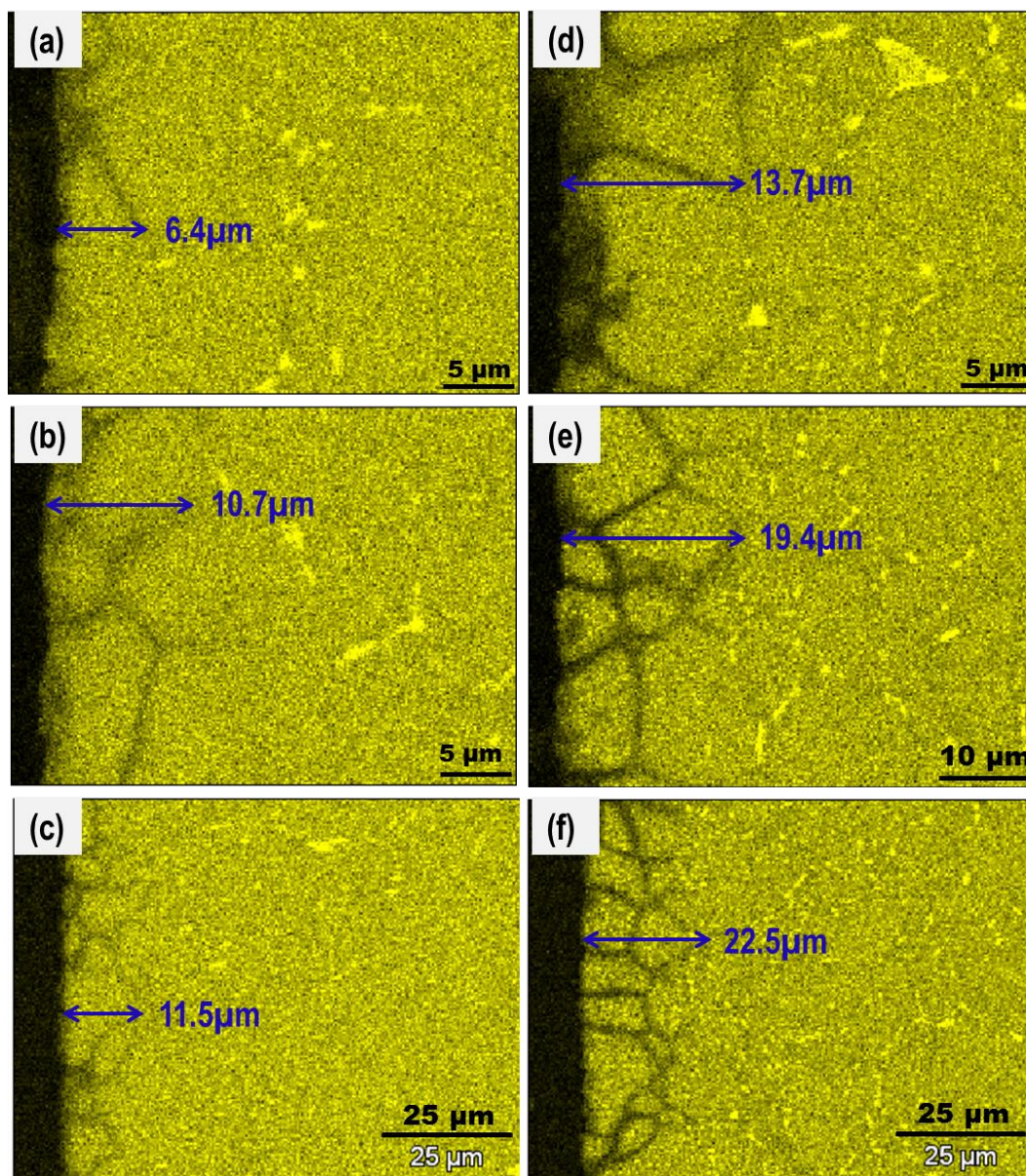


Figure 82: EDS maps showing Cr distribution in near surface layer of corroded 316 stainless steel samples: (a), (b), and (c) tested in 316 stainless steel capsules and (d), (e), and (f) tested in graphite capsules at 700°C for 1000, 2000, and 300 hours. Maximum Cr depletion distance was labeled in each EDS Cr map.

3.3.10 Quantitative analysis of Cr depletion

Figure 83 shows the concentration profiles of main elements Fe, Cr and Ni in 316 stainless steel. The Cr depletion profile was observed as gradually decreasing from initial concentration of [Cr]=17% to zero on corrosion surface. A plateau ([Cr] = 8%) appeared in the Cr profile in Figure 83(b) suggests Cr depletion from the grains in near surface region of the sample tested in graphite capsule. This observation further confirms the corrosion accelerating effect of graphite in molten salt by way of Cr depletion. From Cr profiles, the Cr depletion distance is about 14 μ m and 20 μ m for the samples tested in 316 stainless steel capsule and graphite capsule respectively for 3000 hours. The profiles of EDS line-scan are highly dependent on the selection of scanning path, particularly for the inhomogeneous Cr distribution due to preferential grain boundary corrosion.

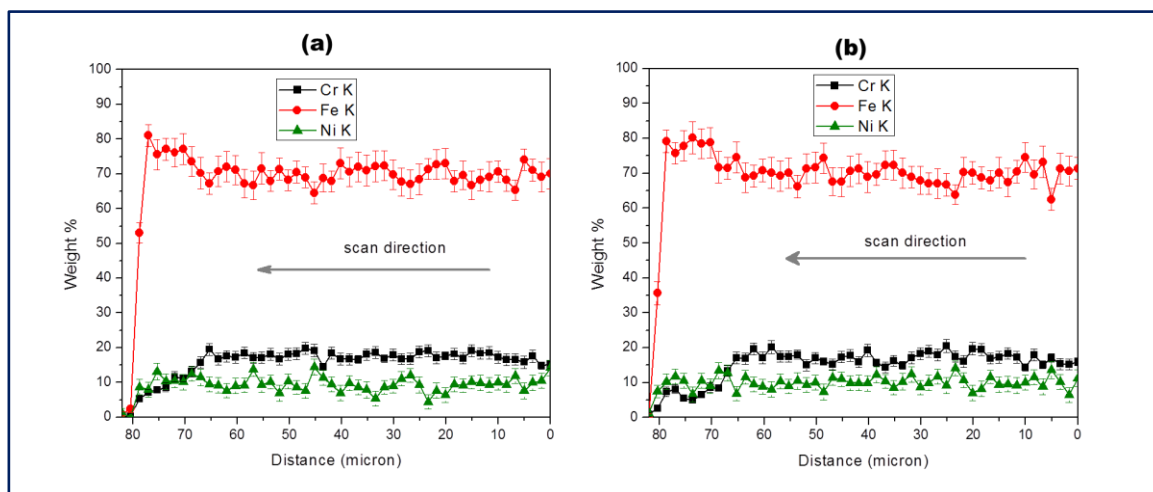


Figure 83: Main elements Cr, Fe and Ni concentration profiles in the near-surface region of 316 stainless steel samples (a) tested in 316 stainless steel capsule and (b) tested in graphite capsule for 3000 hours.

The complicated Cr distribution map also suggests the complexity of corrosion rate calculation. The conventional corrosion rate calculation from the weight loss was based on the assumption of uniform Cr depletion, by the means of $\chi = \frac{\Delta M}{AC_0 \rho}$. From above observation and analysis, Cr depletion is not uniform

within alloys. Therefore, the conventional calculation method underestimates the real corrosion rate in terms of the maximum Cr depletion distance.

3.3.11 Prediction of corrosion attack depth

Based on the maximum Cr depletion distance measured from EDS Cr mappings, the long-term corrosion attack depth can be predicted at least to a first approximation from the logarithmically fitting curves as shown in Figure 84. The fits predicted an attack depth of 17.1 $\mu\text{m}/\text{year}$ and 31.2 $\mu\text{m}/\text{year}$ for the samples tested in 316 stainless steel capsules and graphite capsules respectively[76].

In the MSRE literature, the void layer observed under an optical microscope was considered to be Cr depletion layer, and the attack depth was calculated based on weight loss by assuming uniform Cr depletion from tested alloy[105]. Our studies using SEM and EDS to identify the depth of corrosion attack indicates that MSRE literature underestimated the corrosion attack depth values. Overall, comparing 316 stainless steel to the corrosion resistance of Hastelloy-N in liquid fluoride salts, reported approximately 25 $\mu\text{m}/\text{year}$ at the temperature up to 704°C, the corrosion attack depth of 316 stainless steel in FLiBe at 700°C of 17.1 $\mu\text{m}/\text{year}$ and 31.2 $\mu\text{m}/\text{year}$ is in an acceptable range[45], [53].

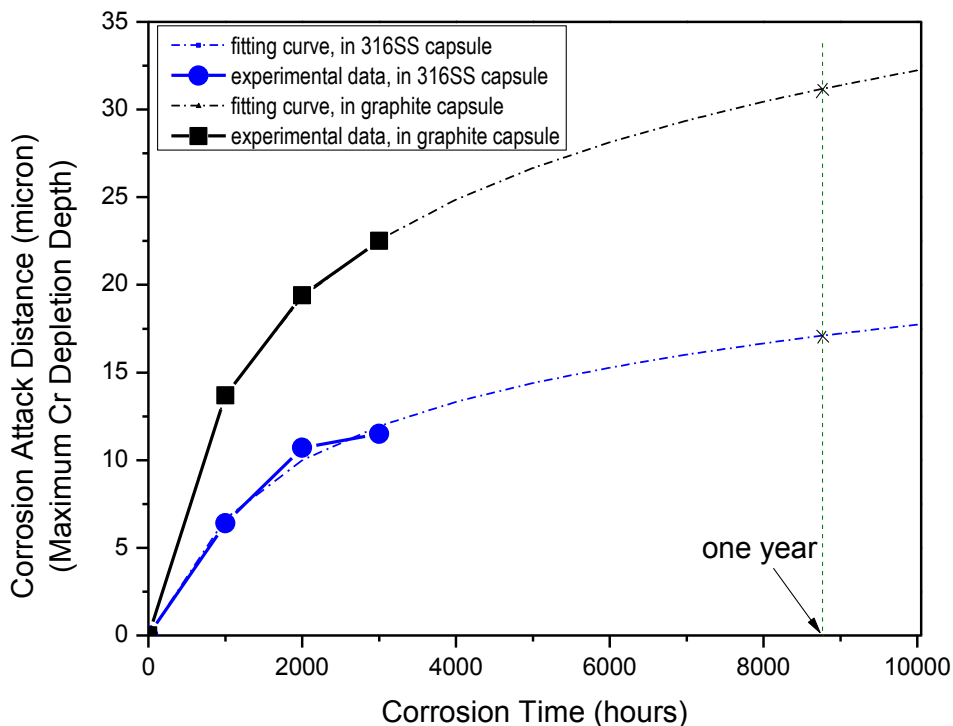


Figure 84: The depth of corrosion attack, in terms of maximum Cr depletion depth, as a function of corrosion time. Experimental data is indicated by a solid line, while the fit is indicated by the dashed line. The fit predicted $17.1\mu\text{m}/\text{year}$ of corrosion in 316 stainless steel capsules and $31.2\mu\text{m}/\text{year}$ in graphite capsules.

3.3.12 Grain boundary dependence of Cr depletion

As shown in Figure 85, the cross-sectional microstructure, elemental distribution, grain size distribution, grain orientation and phase distribution as well as grain boundary map in the same region were obtained by combining SEM-EDS with EBSD techniques. In this same region, SEM images and EDS mappings were first collected prior to EBSD scanning. Figure 85(a) presents precipitates at grain boundaries and the grains with different contrast. Figure 85(b-d) exhibits EDS mappings of Cr, Fe and Ni. Concentration of Fe and Ni is relatively higher at the grain boundaries where Cr significantly depleted. Figure 85(e-h) displays EBSD results including auto grain map, inverse polar figure (IPF), α

phase (red) distribution, and image quality combined with grain boundary maps and α phase, at the same region as cross-sectional SEM and EDS mappings. These images suggest that (1) Cr only depleted along high angle grain boundaries (15-180°, blue lines), not in coincident sites lattice (CSL) grain boundaries such as $\Sigma 3$ (orange lines), and (2) α phase particularly developed in the area where Cr substantially depleted, in a distance from 2 μm to 6 μm to surface. These results correlate the Cr depletion, phase transformation with grain boundary types. Massive Cr depletion in high angle grain boundaries enriched Fe and Ni components and then induced the formation of secondary α -ferrite phase at 700°C. The misorientation angle between the two adjacent grains (signified by grain boundaries in orange) was calculated to be 60°, which further identifies the $\Sigma 3$ grain boundary. Based on these findings, $\Sigma 3$ grain boundary has the relative high corrosion resistance to molten fluoride salts at high temperature with respects to the Cr depletion. In practice, a grain boundary engineering solution is applicable to improve high temperature corrosion resistance of 316 stainless steel in FLiBe. Moreover, the newly-formed α phase might change alloy radiation resistance in practical application because of the different radiation response between α -ferrite and γ -austenite phase[74], [126].

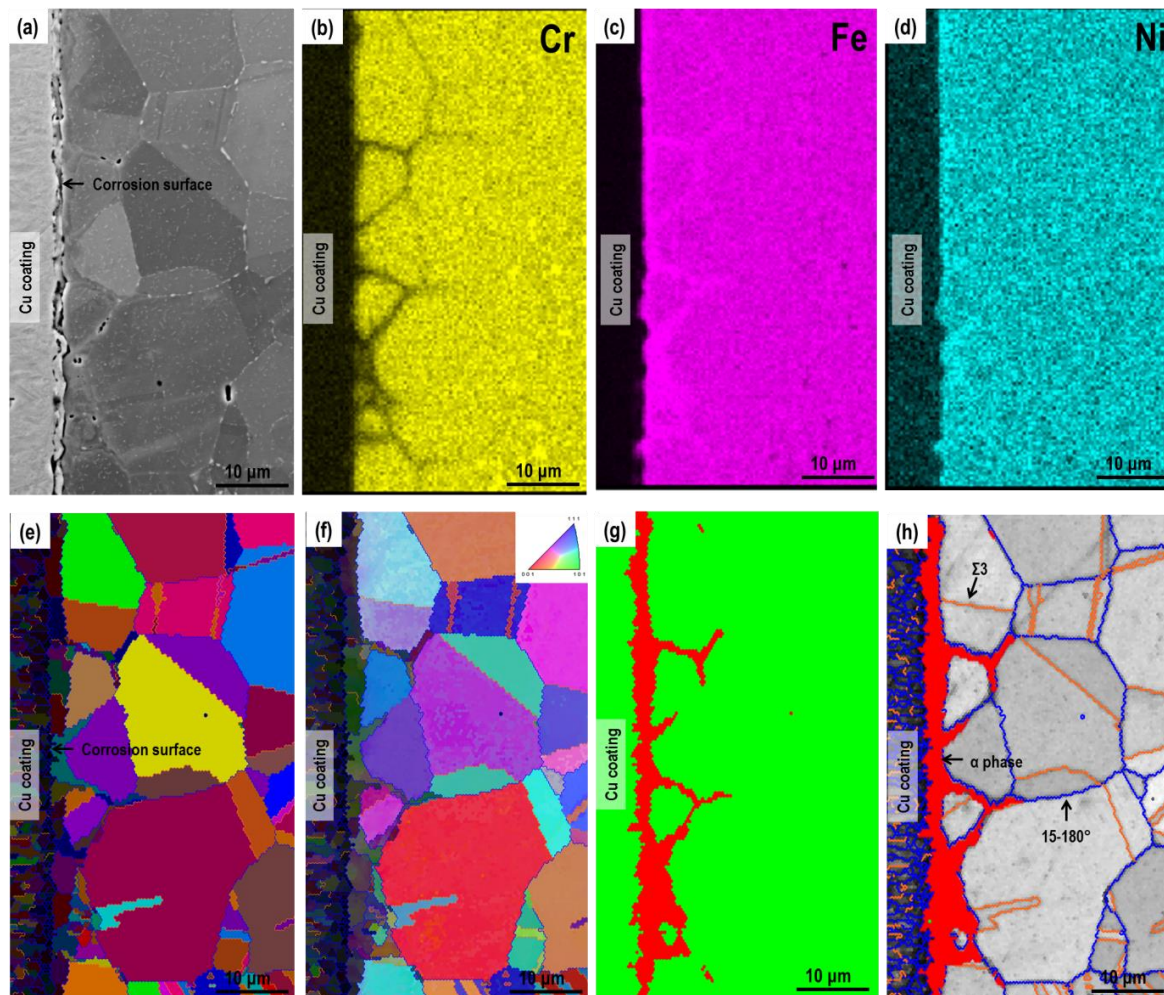


Figure 85: (a) cross-sectional SEM image, (b-d) EDS Cr, Fe and Ni map and (e-h) EBSD images in same near-to-surface area of 316 stainless steel tested in graphite capsule for 1000 hours. (e) grain distribution, (f) inverse polar figure [001], (g) α phase (red) distribution and (h) grain boundary and α phase maps overlapped on image quality (blue lines and orange lines denote 15-180° and $\Sigma 3$ grain boundaries respectively).

3.3.13 Microstructure of carbides formed within alloy

Figure 86 shows STEM images of a FIB lift-out of 316 stainless steel tested in graphite capsule for 3000 hours. This FIB sample covers a range of approximately 15 μm thick from surface to interior. The final thickness of this FIB milled sample was about 100nm. As shown Figure 86(a), a voids produced

during milling sample to electron transparency and a large number of carbides particles (bright gray) with various shapes randomly distributed within alloy. As shown in Figure 86(b) and Figure 86(c), two specific locations in Figure 86(a) were further magnified to observe the microstructural features of particles. Figure 86(b) displays the cross-section of a MoSi_2 particle (~300nm in diameter) formed on alloy surface, corresponding to the round particles in Figure 78(b). A grain boundary extended to surface was clearly observed in this region. Figure 86(c) focuses on the carbide particles of Cr_7C_3 , Mo_2C , and Al_4C_3 . Their compositions were analyzed using STEM-EDS techniques (Figure 87) and the formation was discussed later. Figure 86(d) presents an area framed in Figure 86(b), including a triple grain boundary junction and M_{23}C_6 precipitates in grain boundaries. The thickness of M_{23}C_6 precipitate band is about 10nm resulting from the alloy sensitization at 700°C.

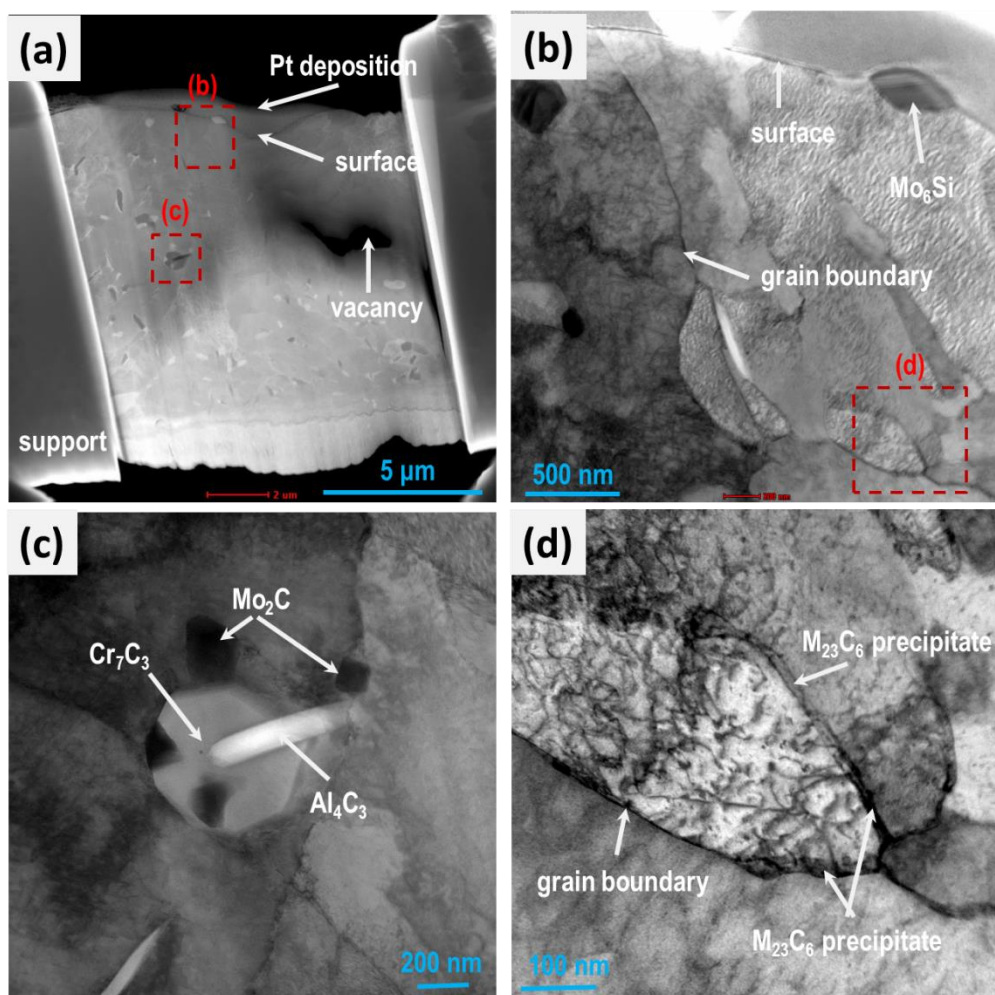


Figure 86: STEM images of a 316 stainless steel tested in graphite capsule for 3000 hours, (a) STEM image, (b) and (c) STEM images on a specific location framed in (a), and (d) STEM image on a triple grain boundary junction framed in (b).

To identify the structure of carbide particles formed within alloy matrix, the compositions on each particular particle were collected using STEM-EDS technique, as shown in Figure 87. In addition to the Fe from alloy matrix, the EDS spectra exhibited high concentration of Mo, Cr and Al on round particle 1, hexagonal particle 2 and needle-like particle 3 respectively. Combining with the calculation of Gibbs free energy of carbides formation, particles 1, 2 and 3 shown in STEM image are very likely to be Mo_2C , Cr_7C_3 and Al_4C_3 . The diameter of Cr_7C_3 particle is approximate 600nm, much larger than other type carbide particles. This is consistent with the cross-sectional observation.

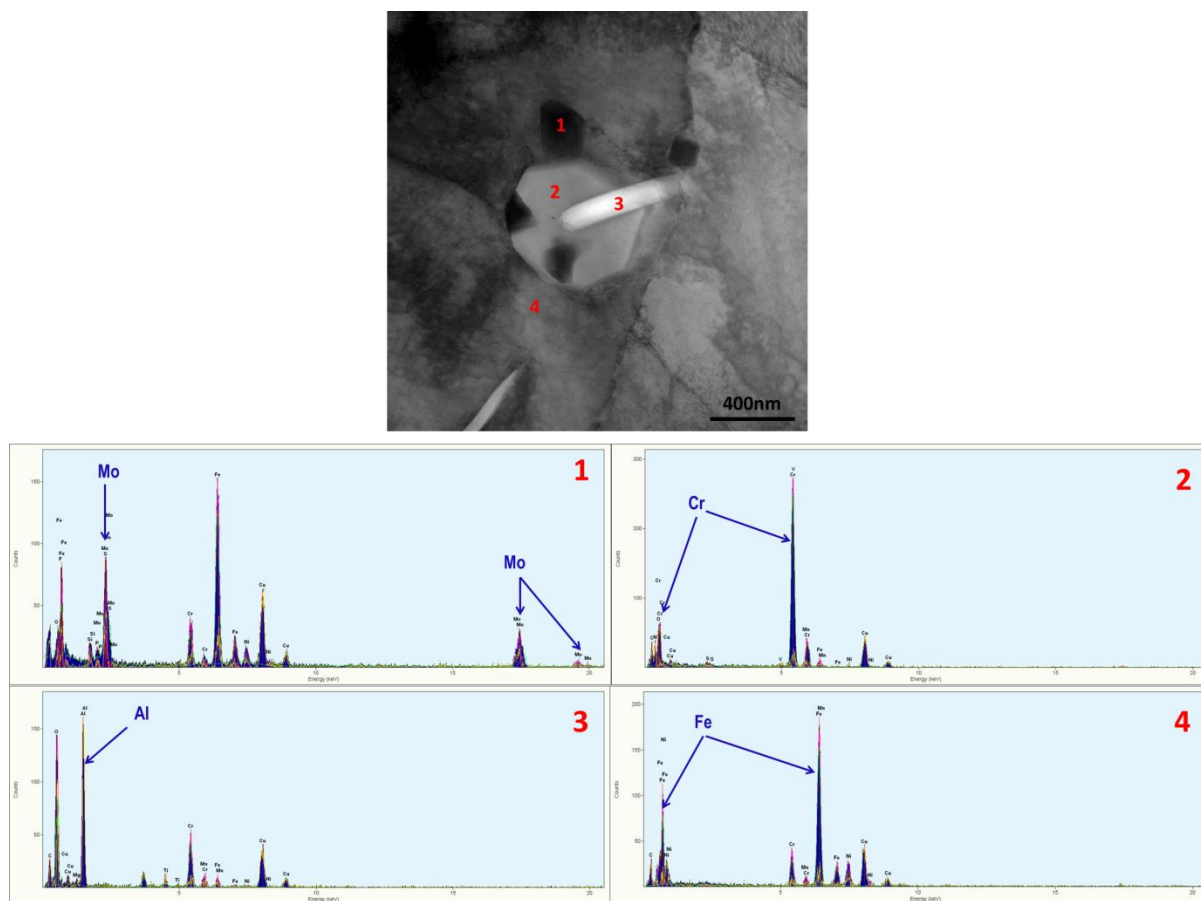


Figure 87: STEM image and EDS spectra corresponding to the red digit 1, 2, 3 and 4 in STEM image. Primary metallic matrix element is highlighted in each EDS spectrum.

3.3.14 Thermodynamics of carbides formation

The corrosion behavior of the 316 stainless steel samples in the graphite capsules was different from those observed for stainless steel capsules. The graphite capsule was found to liberate carbon particles in the presence of salt although the graphite capsule was cleaned and baked. As shown in Figure 88, the FLiBe salt collected from graphite corrosion capsule was dissolved in water. The particle size distribution in the FLiBe solution shows the range of graphite particles from 50 nm to 6349 nm.

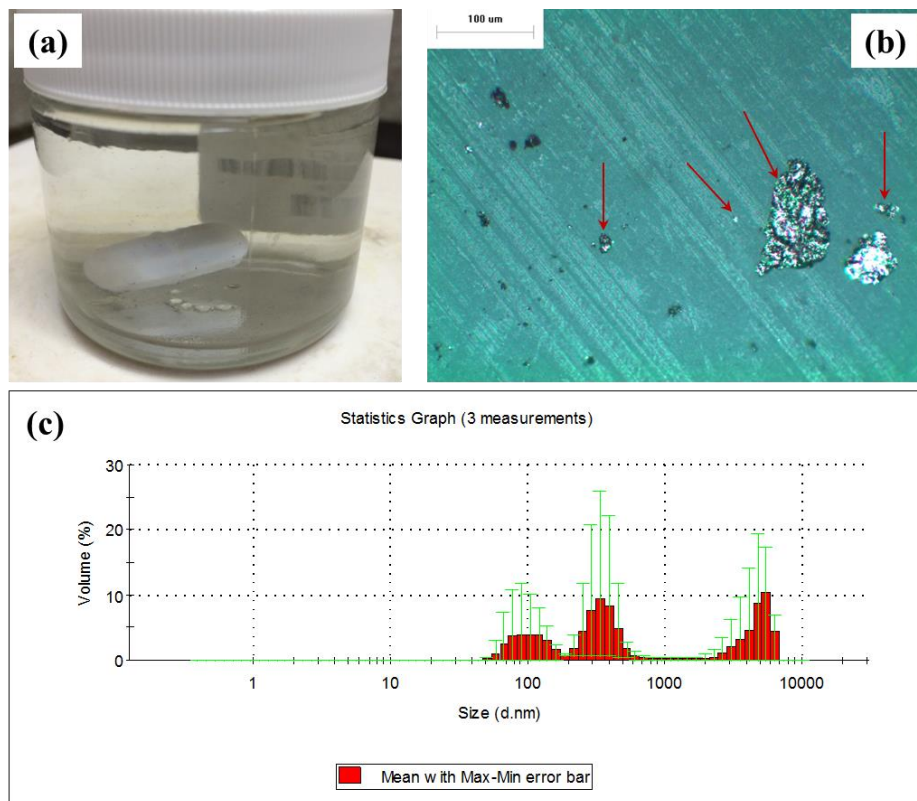
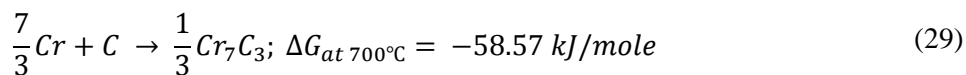
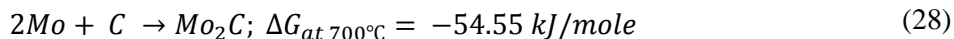
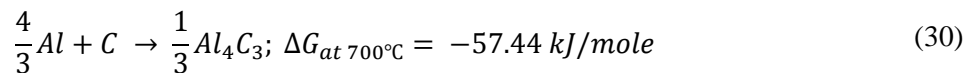


Figure 88: (a) solution of the FLiBe salt collected from graphite corrosion capsule (0.173g salt in 60 ml deionized water), (b) filtered graphite particles (denoted with red arrows) from the solution and (c) particle size distribution of the graphite in FLiBe salt.

Although carbon is chemically inert to salt, it was found to migrate through the salt and react with the stainless steel surface to form chromium carbides. Furthermore, the faster inward diffusion rate of carbon through 316 stainless steel ($D_{C/316ss}=10^{-15} \text{ m}^2/\text{s}$ at 700°C) allowed reactions with the outward diffusing chromium ($D_{Cr/316ss}=10^{-20} \text{ m}^2/\text{s}$ at 700°C) to form chromium carbide particles within the alloy matrix[47], [50], [127]. Similarly, the inward diffusion carbon also reacted with Al and Mo within alloy to form Al_4C_3 and Mo_2C . The negative Gibbs free energy of carbides formation (ΔG in Equation 31-33) at 700°C suggests the occurrence of the following reactions.





These reactions within alloy could have increased samples' weight. Therefore, the net weight loss of the samples tested in the graphite capsules was the value of Cr depletion caused by fluoridation minus the weight gain due to newly-formed carbides within alloy. The real weight loss due to Cr depletion for the samples in graphite capsules should be higher than the measured value shown in Figure 75.

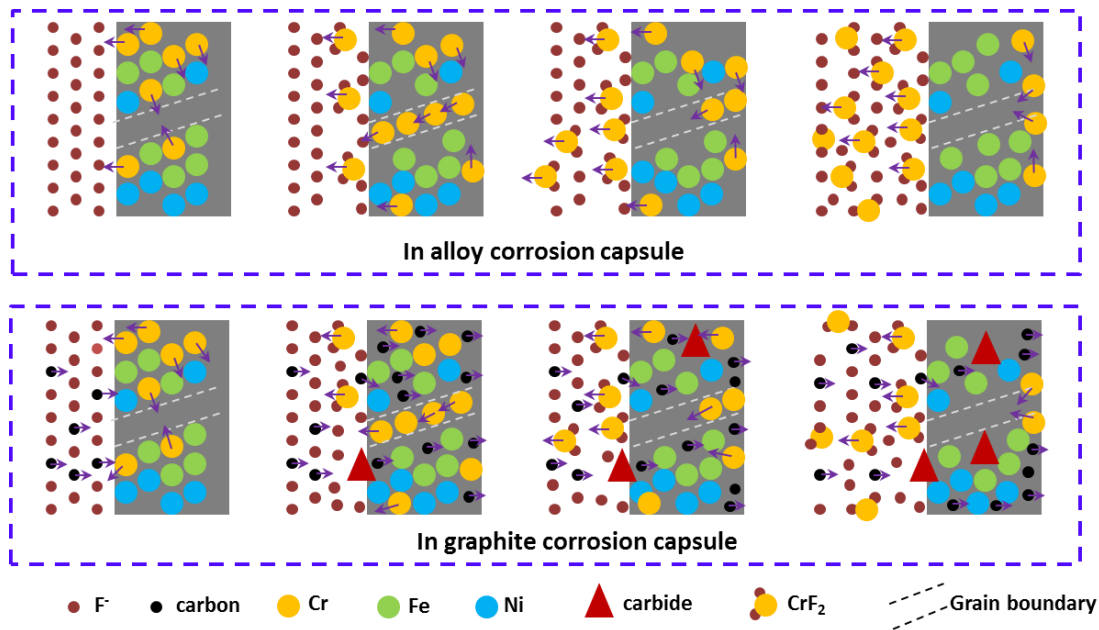


Figure 89: Schematic representation of the 316 stainless steel corrosion processes in molten FLiBe in 316 stainless steel capsule and in graphite capsule materials.

Figure 89 schematically represents the progress of corrosion of 316 stainless steel in molten FLiBe in the absence and in the presence of graphite. Without graphite effect, the Cr (yellow) in near surface region migrates toward both corrosion surface and grain boundary at high temperature. The Cr in grain boundary diffuses outward to react with fluorine ions and dissolves into molten salt. In the graphite corrosion capsule, carbon moves to alloy surface and reacts with surface Cr to form carbide particles on surface. In high temperature molten salt, carbon continuously diffuses inward to alloy matrix and reacts with the Cr within alloy matrix to form carbide particles inside. Fast-diffusing carbon migrates deeper than Cr depletion region to develop a carbide particles containing layer that is deeper than the maximum Cr depletion distance (in Figure 81 and Figure 82).

3.3.15 Redox potential effect on corrosion

In order to investigate the effect of salt redox potential on the corrosion of 316 stainless steel in molten FLiBe, the purified salt was further reduced by adding Be metal. The redox potential of hydrofluorination purified and Be reduced FLiBe was measured using a compact electrochemical probe via an in-situ dynamic beryllium electrode, about -0.45V and -0.49V (reference $E_{\text{HF/H}_2}^0 = 0$ at $\sim 500^\circ\text{C}$) respectively. These values indicate that the FLiBe used in this study was slightly more oxidizing than MSRE fuel salt which ranged from about -0.75V to -0.60V while translating to the same unit and choosing same standard reference electrode HF/H₂. Based on the MSRE experience, the difference in the redox potential between purified and Be reduced FLiBe used for corrosion tests is very small.

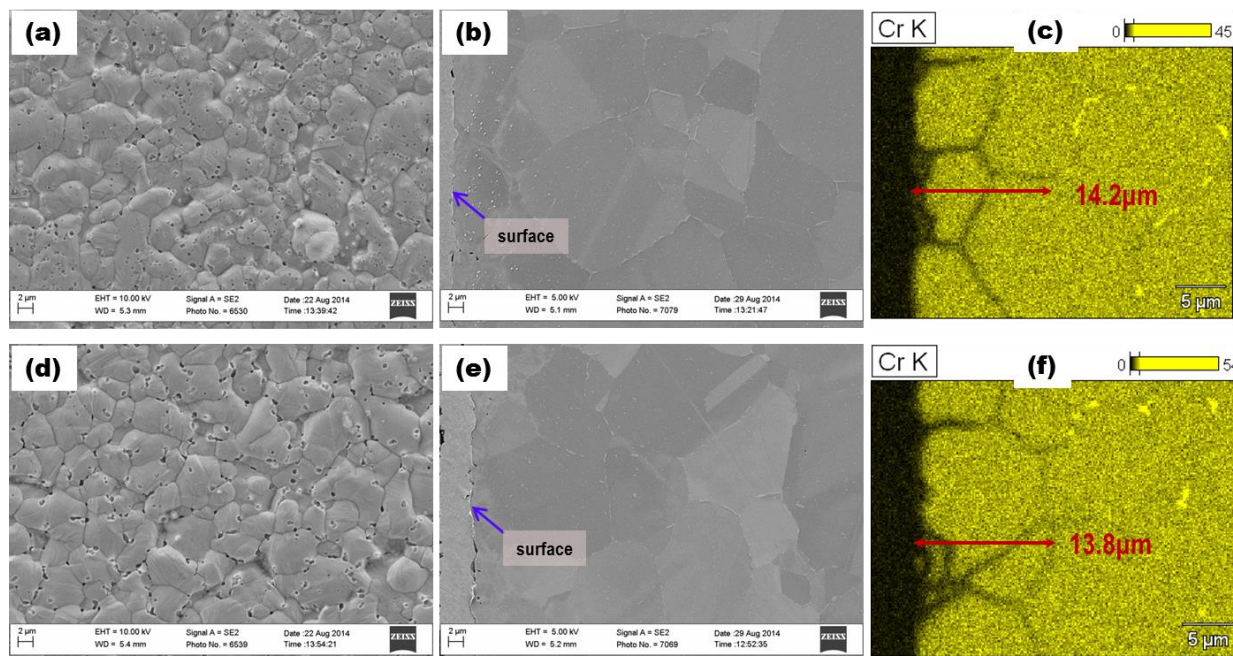


Figure 90: Surface SEM image, cross-sectional SEM image and EDS Cr mapping of 316 stainless steel sample tested in (a, b, c) purified FLiBe and (d, e, f) Be metal reduced FLiBe salt in graphite crucible at 700°C for 1000 hours.

After 1000 hours corrosion in graphite capsules, all samples lost weight of about $-0.45\text{mg}/\text{cm}^2$. Figure 90 shows the similar microstructure of corrosion surface and cross-section in near surface region for the corrosion samples in both FLiBe salts with slightly difference (0.1V) in the redox potential. On the corrosion surface, the intergranular corrosion attack and pitting was observed. In the near surface

region, the preferential Cr depletion along grain boundary was observed. In deeper regions, a number of chromium carbides precipitate formed in grain boundary, but not in the Cr depleted grain boundaries due to the absence of Cr.

It was speculated that the redox potential of both FLiBe salts (with and without Be addition) were comparable during corrosion tests. Therefore, the final corrosion results in both salts are similar. To conduct corrosion test in a constant redox potential salt, a redox potential controlled corrosion system was designed by applying external power supply to adjust and maintain salt redox potential at a desired level. This will be described in the future work section in Chapter 5.

3.3.16 Summary

Corrosion of 316L stainless steel in ^7Li -enriched molten FLiBe salt at 700°C was investigated for exposure durations of up to 3000 hours. The salt was subjected to a hydrofluorination purification treatment prior to the corrosion tests which were performed in both 316 stainless steel and graphite capsules. Corrosion in all cases was dominated by the dissolution of the Cr in the alloy into the salt and corrosion attack occurred predominantly along the grain boundaries of the stainless steel. The corrosion tests performed in graphite capsules exhibited about twice the attack depth compared to those tested in 316 stainless steel capsules indicating that the presence of graphite had an accelerating effect on the corrosion of stainless steel. In both cases Cr depletion at the surface promoted the formation of MoSi_2 precipitates at the surface. For the samples tested in graphite crucibles, hexagonal Cr_7C_3 round Mo_2C , and needle-like Al_4C_3 particulate phases was clearly observed through the depth of the corrosion layer, due to inward diffusion of C into the alloy matrix. Cr_{23}C_6 precipitate was also observed at grain boundary under STEM due to thermal effect. The affected corrosion attack depth as measured from SEM-EDS analysis ranged from $6.4\text{ }\mu\text{m}$ to $11.5\text{ }\mu\text{m}$ for the samples tested in 316 stainless steel capsules, and from $13.7\text{ }\mu\text{m}$ to $22.5\text{ }\mu\text{m}$ for the samples tested in graphite capsules. Based on experimental results of the maximum Cr depletion distance, the attack depth per year was predicted to be $17.1\text{ }\mu\text{m}/\text{year}$ and $31.2\text{ }\mu\text{m}/\text{year}$ for the samples tested in 316 stainless steel capsules and graphite capsules respectively.

XRD analysis showed that the corrosion layer primarily consisted of α -ferrite phase due to massive Cr depletion at high temperature. EBSD crystallographic analysis suggests that the Cr depletion only took place along high angle grain boundaries ($15-180^\circ$) and substantial Cr depletion from alloy induced phase transformation from γ -austenite to α -ferrite phase. The CSL $\Sigma 3$ grain boundary has relatively high corrosion resistance to molten fluoride salt at high temperature.

The corrosion tests in molten FLiBe with varying redox potential present similar corrosion results because of the comparable redox potential of the salt with the dissolving of Cr ions into molten salt. A redox potential controlled corrosion system is required to investigate the redox potential effect on corrosion.

3.4 Discussion

In this section, a thermal diffusion controlled corrosion model for long-term corrosion prediction was developed based on the understanding of the corrosion behavior of the four alloys (investigated in this study) in molten FLiBe salt. The conventional thermal diffusion model, constant diffusion source moving from alloys' surface into substrate, was selected as comparison since the Cr diffusion direction in the alloys in molten fluoride salt occurs from inside the alloy to surface. The validation of this model specifically applied to estimate the depth of corrosion attack of alloys in molten fluoride salt has been discussed by comparing modeled profiles to experimental results. Additionally, the effects of grain boundary precipitates and the presence of graphite on the corrosion behavior of alloys in molten fluoride salt are also discussed.

3.4.1 Thermal diffusion controlled corrosion model (TDCCM)

The latest conceptual molten fluoride salt-cooled high-temperature reactor (FHR) is designed for 60 years life-time. One challenge for the development of FHR is the compatibility of structural alloys with molten fluoride salt because of the inherent corrosivity from molten fluoride salt. To predict the corrosion attack depth of the structural alloys for long exposure durations, an engineering model based on experimental data is required.

Based on the understanding the corrosion behavior of a series of corrosion tests including Ni-Cr binary alloys, Hastelloy N as well as 316 stainless steel in high purity FLiBe at 700°C for up to the duration of 3000 hours, a thermal diffusion controlled corrosion model (TDCCM) was derived from Fick's second law. Then the Cr depletion profile in the alloys at any corrosion time can be estimated using TDCCM from which the corrosion attack depth in terms of the maximum Cr depletion distance can be determined.

The differences between conventional thermal diffusion and molten salt corrosion induced Cr depletion are illustrated in Figure 91. The conventional diffusion with constant concentration on surface follows the line depicted in orange color, and the Cr depletion within alloys in molten fluoride salts follows the line depicted in blue. Typical examples of conventional thermal diffusion couples include the diffusion of carbon into stainless steel and the diffusion of chromium isotope into Inconel[48], [127]. Both these diffusion studies involve diffusion of species from target material's surface into substrate. The diffusion direction of conventional diffusion is therefore opposite to what occurs in the molten salt corrosion where Cr depletion occurs by outward diffusion of Cr from the inside of the alloy to its surface. Table 10 summarizes the main boundary conditions for both models under an assumption of constant diffusion potential for inward and outward diffusion.

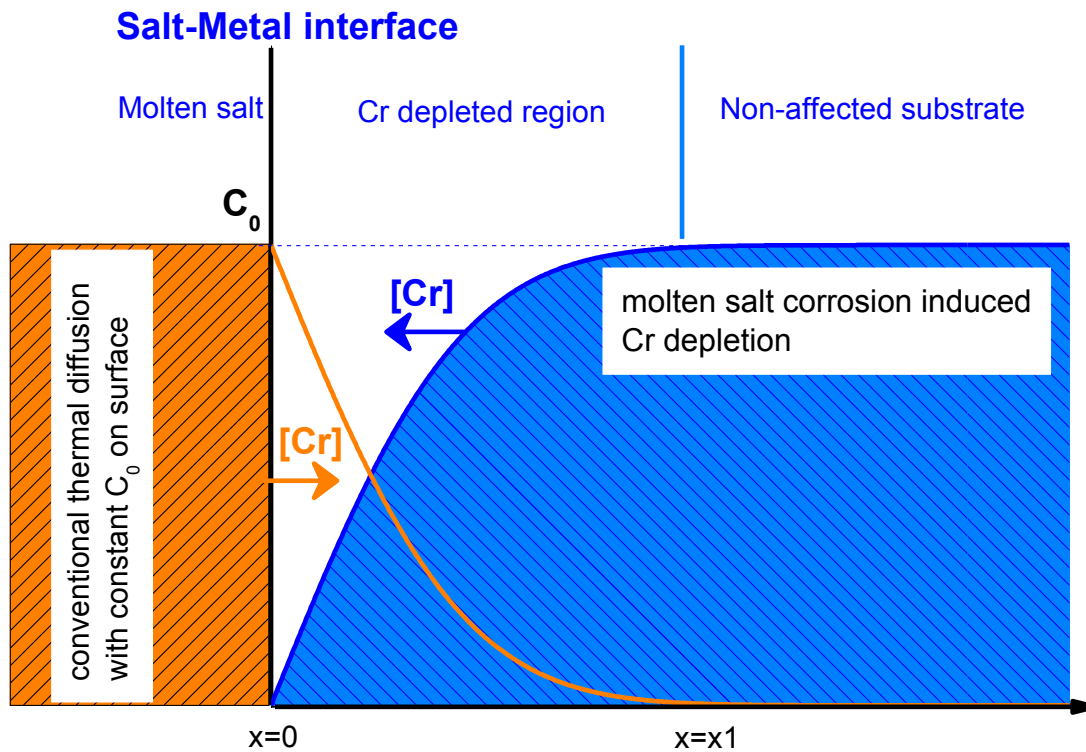


Figure 91: Schematic illustration of conventional thermal diffusion of infinite diffusion source in infinite medium, and the Cr depletion from the alloy into the molten fluoride salts.

For the alloys in high temperature molten fluoride salt, it was hypothesized that the Cr in alloys diffuses to surface and instantly reacts with molten salt and dissolves into the molten salt. For both diffusion models, the overall diffusion coefficient was assumed to be independent on the history of alloys. It was also assumed that at high temperature, homogeneous diffusion occurs.

Table 10: Main boundary conditions for the models of conventional thermal diffusion and the Cr depletion due to corrosion in molten fluoride salts.

	Conventional thermal diffusion, infinite source, infinite medium	Cr depletion in the alloys in high temperature molten fluoride salts
Boundary conditions	$C(x, 0) = 0, x > 0$ $C(0, t) = C_0$ $C(x, t) = 0 \text{ as } x \rightarrow \infty$	$C(0, 0) = C_0$ $C(0, t) = 0, t > 0$ $C(x, t) = C_0 \text{ as } x \rightarrow \infty$
Fundamental theory	$\frac{\partial C}{\partial t} = D \frac{\partial^2 C}{\partial x^2}$	
Diffusion solution	$C(x, t) = C_0 \cdot \operatorname{erfc}\left(\frac{x}{2\sqrt{Dt}}\right)$	$C(x, t) = C_0 \cdot \operatorname{erf}\left(\frac{x}{2\sqrt{Dt}}\right)$

Since the long-term corrosion attack for the alloys in molten fluoride salts is controlled by Cr thermal diffusion[48], [72], the model derivation starts from classical Fick's second law. Two typical thermal diffusion cases are (1) doping with fixed amount (N) of dopant and (2) doping with a fixed surface concentration (C_0). The solutions of Fick's second law for these two cases are respectively expressed as:

$$C(x, t) = \frac{N}{\sqrt{\pi Dt}} e^{-x^2/4Dt} \quad (31)$$

and

$$C(x, t) = \int_x^\infty dC(x, t) = \int_x^\infty \frac{C_0}{\sqrt{\pi Dt}} e^{-u^2/4Dt} du = C_0 \operatorname{erfc}\left(\frac{x}{2\sqrt{Dt}}\right) \quad (32)$$

where error function: $\operatorname{erf}(z) = \frac{2}{\sqrt{\pi}} \int_0^z e^{-y^2} dy$, and complementary error function: $\operatorname{erfc}(z) = 1 - \operatorname{erf}(z)$, and D is diffusion coefficient, x is diffusion distance, and t is diffusion time. The typical inward diffusion concentration profiles as a function of distance for case (2) are shown in Figure 92(a).

For the molten salt corrosion induced Cr outward depletion, as presented in Figure 92(b), the concentration of Cr equals to constant C_0 (initial concentration in alloy) as $x > x_1 > 0$. The diffusion source of Cr within the alloy is divided into infinitely thin slabs with thickness of du . Under the assumption of

surface Cr concentration $C(x=0, t>0)=0$, the integration of all slabs that contribute to the Cr depletion from position x to 0 at time t is:

$$C(x, t) = \int_0^x dC(x, t) = \int_0^x \frac{C_0}{\sqrt{\pi Dt}} e^{-u^2/4Dt} du = C_0 \operatorname{erf}\left(\frac{x}{2\sqrt{Dt}}\right) \quad (33)$$

Equation (35) termed as thermal diffusion controlled corrosion model (TDCCM) in this study. This model assumes surface Cr concentration $C_s=0$ (already confirmed by XPS analysis). If the Cr concentration on alloy surface equals to the Cr ions in molten salt at equilibrium steady-state as reported by J. H. DeVan[72], here $C_s=0.0035\%\rho_{\text{FLiBe}}$ (35ppm Cr in the corrosion FLiBe salt measured by NAA, $\rho_{\text{FLiBe}}=1.94\text{g/cm}^3$ at 700°C) is substituted into Equation 26. Then, the Cr depletion distance is only about $0.002\mu\text{m}$ deeper than the result calculated using TDCCM model.

In this study, the TDCCM model was applied to predict the corrosion attack depth of alloys in molten fluoride salts after corrosion time t . In this model, the critical constant D , defining as overall or effective diffusion coefficient of Cr in alloys, can be calculated from the experimental measurements of weight change (ΔM). Assuming a constant Cr concentration (C_0) in alloys, the weight change due to Cr depletion as a function of time is expressed as

$$\Delta M = 2AC_0 \sqrt{\frac{Dt}{\pi}} \quad (34)$$

where A is exposure area, D is the overall diffusion coefficient of Cr in alloys, and t is the corrosion time. Equations (33) and (34) have been employed by R. B. Evans to calculate Cr diffusion coefficient in nickel-base alloys by immersing alloys specimen into the hot molten salt in which Cr^{51} isotopes was added[48].

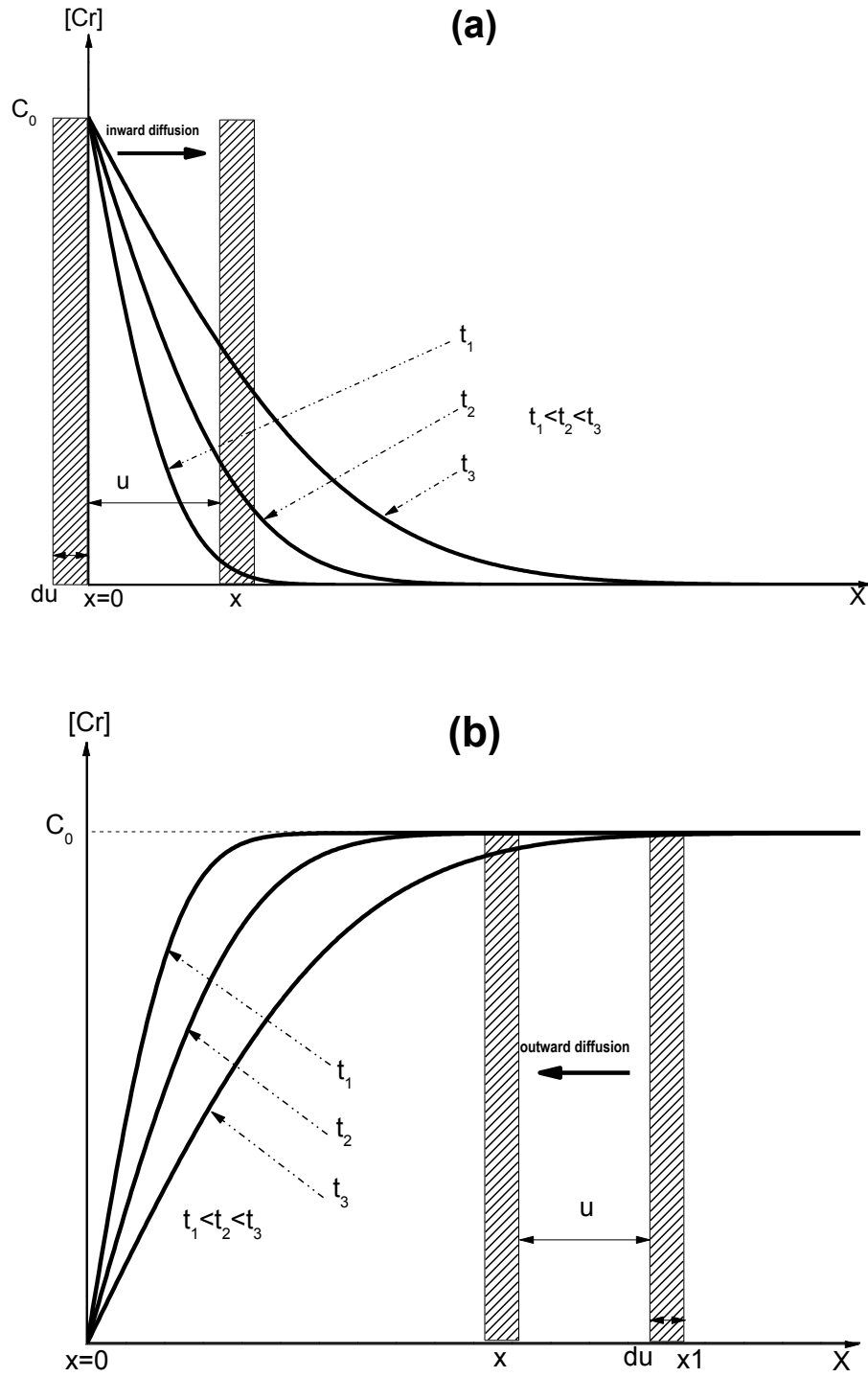


Figure 92: Typical concentration profiles of (a) conventional thermal diffusion for the cases with infinite diffusion source through infinite medium, and (b) molten salt corrosion induced Cr depletion profiles by the means of outward diffusion from alloy into molten salt.

The calculated overall diffusion coefficient D is a combination of grain boundary diffusion (D_{gb}) and volume diffusion (D_v). Although this diffusion direction is opposite to the conventional thermal diffusion, the Cr concentration gradient/potential is the driving force for both the corrosion induced Cr outward diffusion and conventional inward diffusion. Therefore, the conventional thermal diffusion theories can be applied here.

In polycrystalline metals the overall diffusion coefficient can be modeled using Hart's equation $D = fD_{gb} + (1-f)D_v$, where f is the volume fraction of grain boundaries in a polycrystal. A segregation factor (s) may be introduced into the grain boundary diffusion term if the studied element tends to segregate to the grain boundaries[67]. The volume diffusion coefficient and grain boundary diffusion coefficient can be expressed as D_v (or $s\delta D_{gb}$) = $D_0 \exp(-Q/RT)$, where δ is grain boundary width, usually assumed to be 0.5nm, D_0 is pre-exponential factor, R is noble gas constant, and T is temperature in Kelvin, but they are in a wide range in reports[47], [50], [67], [95]. These diffusion results can be applied to the calculation of D in the TDCCM. From EBSD grain boundary maps, f can be easily calculated by assuming 0.5nm grain boundary width. However, according to the microstructural analysis in this study, the alloys' microstructure significantly changed during corrosion tests in high temperature molten salt. This is a big challenge to the determination of D_{gb} . Therefore, the overall D in this study was roughly calculated from the weight loss.

Substituting the effective diffusion coefficient into TDCCM Equation (33), the Cr depletion profiles for all four alloys tested in molten FLiBe was calculated for any corrosion duration. Figure 93 presents all calculated Cr depletion profiles at the corrosion times (50 hours to 3000 hours) and 365 days. These profiles provide a good estimation of corrosion attack depth in terms of the maximum Cr depletion distance from surface. Table 11 summarizes the experimental results ($\pm 2\% C_0$ error involved) and the calculated data. The calculated distance is from the alloy surface ($C(x=0, t>0)=0$) to the point where the Cr concentration is in a range of 98% C_0 -100% C_0 .

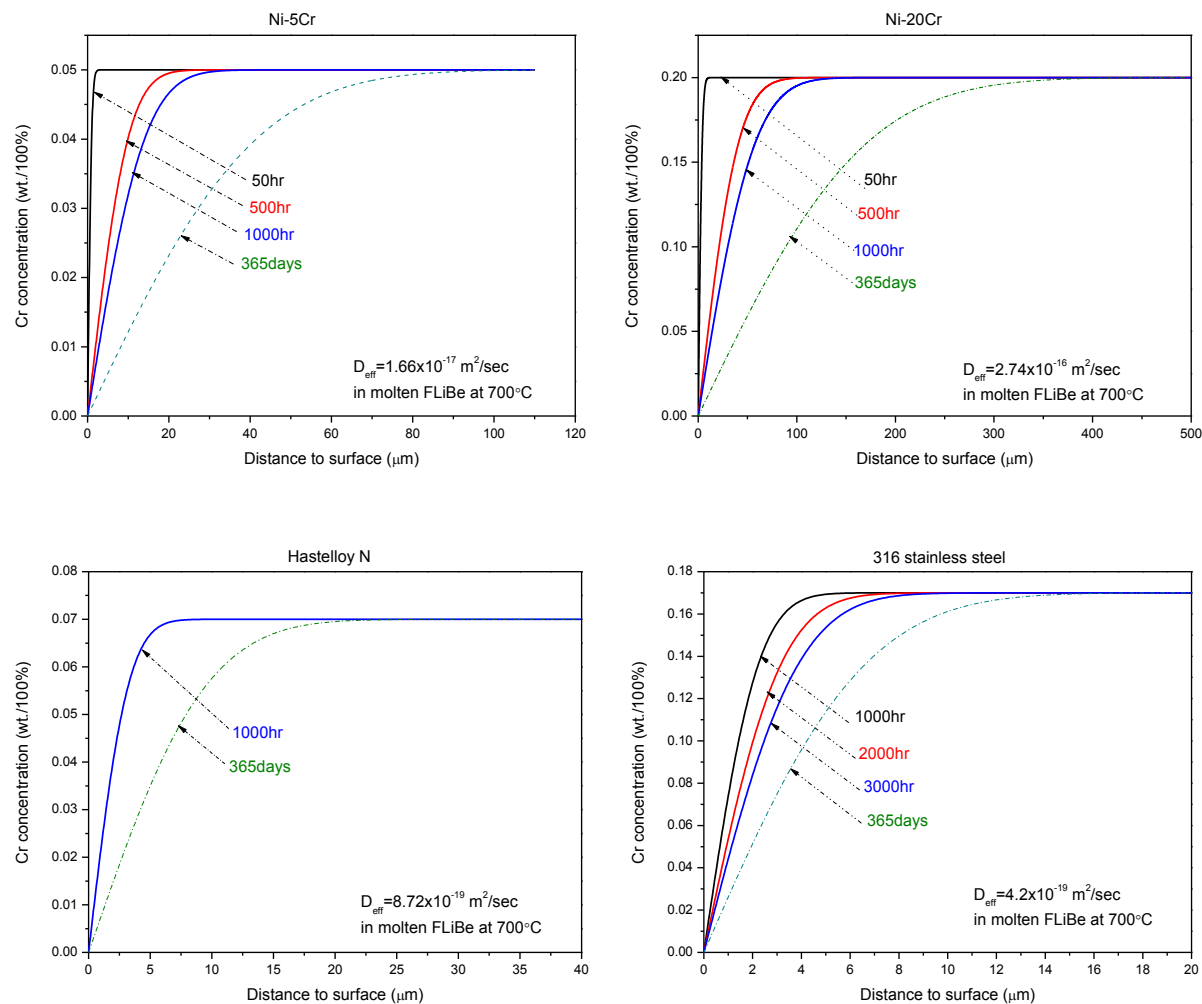


Figure 93: Cr depletion profiles of the four alloys investigated in this study as a function of the distance, calculated using the TDCCM.

3.4.2 Validation of TDCCM

The TDCCM prediction, despite several assumptions discussed above, were readily validated by the experimental results. As shown in Figure 94, the experimental Cr concentration profiles measured by using SEM-EDS technique for the longest corrosion time (up to 3000 hours) of each tested alloy are overlapped on the calculated profiles. All calculated profiles fit reasonably well with the experimental results except for Ni-20Cr. The calculated Cr diffusion coefficient in Ni-20Cr is the highest among all alloys. Therefore, Cr quickly migrates to the near surface region in certain depth, especially for the initial

corrosion stage in a shallow region. It is believed that the Cr depletion profile in Ni-20Cr become closer to the calculated one for longer corrosion times. The minor discrepancy observed between the model and experimentally determined values for Ni-20Cr alloy for longer exposure time warrants further investigation.

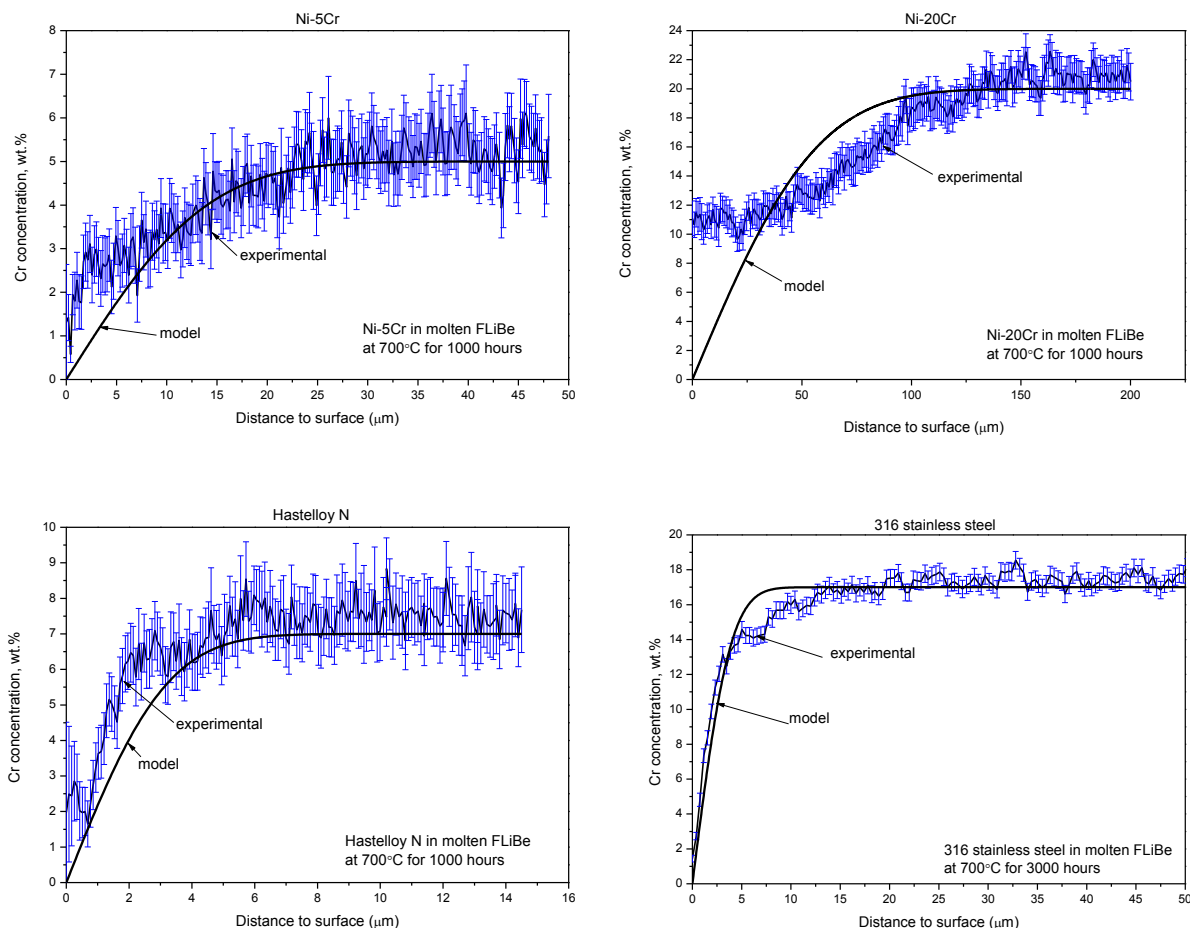


Figure 94: Comparison of calculated and experimental (averaged) Cr depletion profiles for Ni-5Cr, Ni-20Cr, 316 stainless steel and Hastelloy N in molten FLiBe at 700°C.

The experimental and calculated maximum Cr depletion distances for all alloys tested in this study are summarized in Table 11. The last column of calculated range shows the importance of cut-off criterion for determining the maximum Cr depletion distance. The experimental results are close to or in the range of calculated data when $\pm 2\% C_0$ error and criterion of $98\% C_0$ - $100\% C_0$ range, respectively, are applied.

Table 11: Calculated effective diffusion coefficient of Cr in alloys, the experimental and calculated maximum Cr depletion distance in the alloys tested in molten FLiBe at 700°C.

Specimen and liner	Calculated D_{eff} (m ² /sec) from weight loss	Corrosion time (hour)	Maximum Cr depletion distance (μm)	
			Experimental* (error $\sim \pm 2\% C_0$)	Calculated (98% C_0 -100% C_0)
Ni-5Cr (in nickel)	1.66×10^{-17}	50	5.4	1.6-3.7
		500	17.9	18.1-34.9
		1000	21.7	25.4-41.3
		8760	-	75.2-115.1
Ni-20Cr (in nickel)	2.74×10^{-16}	50	18.2	6.3-13.9
		500	84.5	73.2-121.3
		1000	140.8	103.4-171.5
		8760	-	305.6-530.2
Hastelloy N (in nickel)	8.72×10^{-19}	1000	5.5	5.8-13.5
		8760	-	17.2-29.5
316 stainless steel (in 316 stainless steel)	4.2×10^{-19}	1000	6.4	4.0-7.6
		2000	10.7	5.7-11.5
		3000	11.5	7.1-12.7
		8760	-	12.0-18.9

* Based on the results of EDS mapping of Cr element.

The calculated annual Cr depletion distance of Ni-20Cr is approximately 4 times of Ni-5Cr. This suggests that the Cr concentration gradient (i.e. concentration potential) primarily drives Cr outward diffusion in alloys. However, the initial Cr concentration in the commercial alloy of Hastelloy N and 316 stainless steel is not proportional to the Cr depletion distance because of the complicated microstructural evolution of commercial alloys during corrosion in high temperature molten FLiBe. Using TDCCM, the annual Cr depletion distance was calculated to be 17.2-29.5 μm/year for the Hastelloy N in nickel capsule and 12.0-18.9 μm/year for the 316 stainless steel in 316 stainless steel capsule, respectively. Based on the TDCCM calculations, the corrosion resistance of 316 stainless steel in molten FLiBe at 700°C is comparable to Hastelloy N. Here it should be noted that the calculated Cr depletion profile is strongly dependent on the effective diffusion coefficient (D_{eff}) and many factors affect D_{eff} such as the microstructural evolution of alloys in high temperature molten salt. The tested 316 stainless steel in this work has about 0.0225% carbon and chromium carbides precipitates were observed to form at grain boundaries during corrosion tests at 700°C. These grain boundary carbides probably can potentially mitigate the Cr diffusion in the 316 stainless steel. In actual FHR service,

considerable amount of graphite is present in the core. The graphite in molten salt in this study has been found to liberate carbon that diffused into the tested 316 stainless steel and Hastelloy N then carbides formed in the alloys.

As discussed above, the TDCCM can be used to predict the high temperature, long-term corrosion attack depth of alloys in molten fluorides salt which is costly and also a challenge to corrosion system. Although the expression of this model doesn't present the microstructural effects on the Cr depletion, the effective diffusion coefficient (D_{eff}) calculated from the weight loss actually includes all factors that affect Cr depletion. The main contribution of this TDCCM model is to provide a first level approximation of the corrosion attack depth in structural alloys in high temperature molten fluoride salts.

3.4.3 Effect of grain boundary precipitates on Cr depletion

Numerous investigations on the effect of grain boundary precipitates on the intergranular corrosion cracking have been reported for several alloys such as 304 stainless steel, 316 stainless steel, 2124 Al alloy and Inconel 690[88], [90], [98], [102], [128]–[131]. The formation of the grain boundary precipitates such as M_7C_3 and $M_{23}C_6$ type carbides initiate a Cr depletion zone around the precipitates in the grain boundary at high temperature. For example, it was reported that the intergranular stress corrosion cracking of 304 stainless steel depended on the minimum Cr concentration, spacing of carbides and the width of Cr depleted zone at grain boundary[88]. The presence of a semi-continuous distribution of carbides in grain boundaries promoted intergranular corrosion cracking. However, the effect of grain boundary precipitates on the Cr outward diffusion in the alloys that are immersed in molten fluoride salt has not been reported. Herein, the relationship between newly-formed precipitates in alloys' grain boundary and Cr depletion rate is discussed.

As shown in Figure 95, a large amount of chromium carbide precipitates formed in the grain boundaries of 316 stainless steel, and molybdenum silicide precipitates formed in the grain boundaries of Hastelloy N, but as expected no such precipitates formed at the grain boundaries of Ni-5Cr and Ni-20Cr. All four alloys experienced 1000 hours corrosion test in molten FLiBe at 700°C. The sampled areas in Figure 95 are within the bulk of each sample where the molten salt corrosion doesn't impact the

microstructure. From the calculated D_{eff} (Table 11), the Cr diffuses about 2-3 orders of magnitude faster through Ni-5Cr and Ni-20Cr than Hastelloy N and 316 stainless steel, although the initial Cr concentration is similar between Ni-5Cr (~5%) and Hastelloy N (~7%), and between Ni-20Cr (~20%) and 316 stainless steel (~17%). This suggests that the formation of the precipitates in grain boundary could dramatically retard the Cr outward diffusion in alloys, particularly for the grain boundary diffusion.

In general, the chromium carbide precipitates formed in grain boundaries promote a Cr depleted zone in the region adjacent to the precipitates (Figure 63), which reduces stainless steel oxidation resistance in high temperature environment because Cr is the essential element to protect alloys from oxidation[94], [128], [130]. But unlike the protective oxide films, the Cr is susceptible to be consumed in molten fluoride salt[35], [36], [40], [96], [132]. It is expected that the Cr depleted-zone nearby the grain boundaries due to the formation of chromium carbide precipitates enhances the corrosion resistance of 316 stainless steel to molten fluoride salt, particularly for intergranular corrosion attack. In Hastelloy N, the Mo-rich precipitate nucleates and coarsens in grain boundaries when the alloy is exposed to high temperature[53], [96]. The Mo-rich precipitates in grain boundaries dramatically improve the corrosion resistance of Hastelloy N in molten fluoride salt because Mo is immune to molten fluoride salts (Figure 5). Therefore, the formation of the grain boundary chromium carbides in 316 stainless steel and Mo-rich precipitates in Hastelloy N could mitigate Cr outward depletion rate. Without the grain boundary precipitates in Ni-5Cr and Ni-20Cr, the overall Cr depletion rate is high, which is consistent with the calculated diffusion coefficient (D_{eff}) (in Table 11).

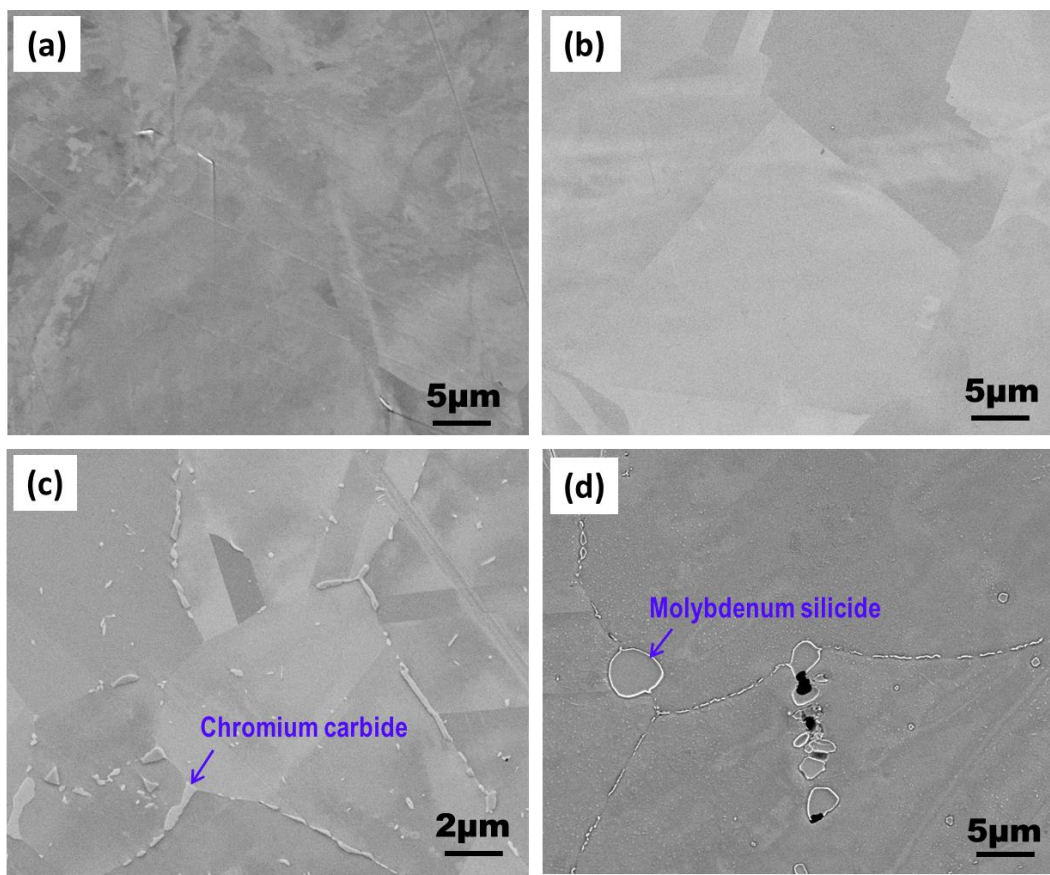


Figure 95: Cross-sectional SEM images focusing on the grain boundaries in the bulk alloy: (a) Ni-5Cr, (b) Ni-20Cr, (c) 316 stainless steel, and (d) Hastelloy N. All samples exposed to molten FLiBe at 700°C for 1000 hours.

From the corrosion point of view, the formation of grain boundary precipitates is beneficial to the alloys corrosion resistance in molten fluoride salt. However, it should be noted that the grain boundary precipitates could dramatically influences alloy mechanical properties.

3.4.4 Effect of crystallographic texture on the alloys corrosion

In materials science terminology, texture refers to the distribution of crystallographic orientation of a polycrystalline specimen. In polycrystalline alloys, the characters of texture generally include grain size, spacing orientation of grains as well as misorientation angle of grain boundary. EBSD is widely applied to characterize these microstructural features. Figure 96(a) presents the spacing orientation of grains and grain boundaries distribution in the cross-section of a Ni-20Cr specimen tested in molten FLiBe for

1000 hours. To obtain a configuration parallel to the corrosion surface, original EBSD data was rotated -90° about RD using OIMTM data analysis software. Quantitative texture analysis is shown in Figure 96(b), presenting the orientation of crystal clusters. Figure 96(c) is the misorientation profile along the EDS line scan (in Figure 56). Point-to-origin means the misorientation from a point on the vector to the point at the origin of the vector (blue), and point-to-point means the misorientation from a point on the vector to the previous point on the vector (orange).

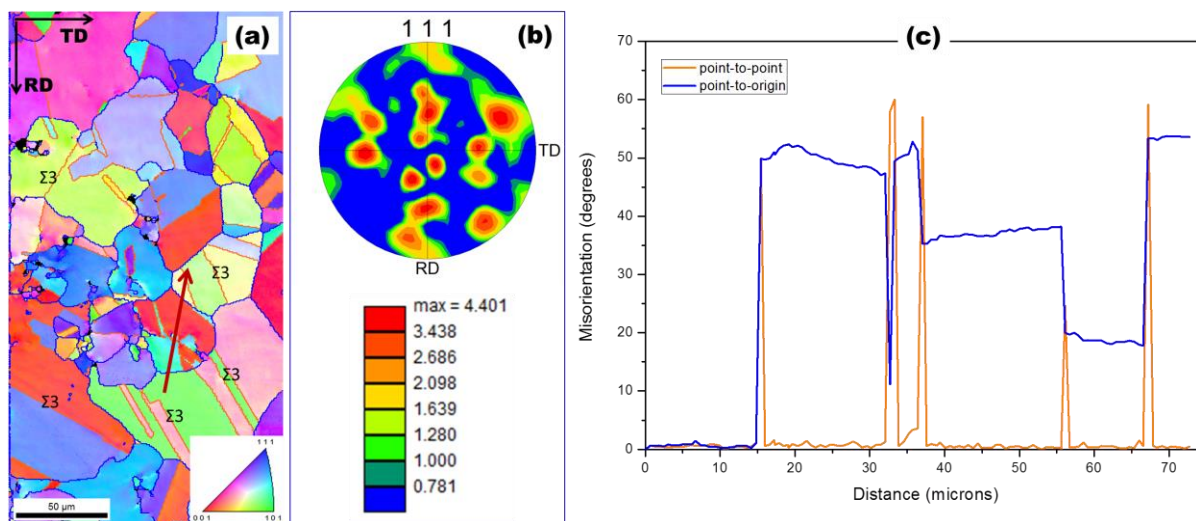


Figure 96: (a) Inverse pole figure (IPF) to [001] after rotating -90° about RD axis, (b) pole figure (PF) and (c) misorientation profile along the red arrow trace labeled in (a) for the Ni-20Cr sample tested in molten FLiBe at 700°C for 1000 hours. Grain boundaries distribution map overlapped on IPF, blue lines denote high angle regular grain boundaries (15° - 180°), and orange lines denote CSL $\Sigma 3$ grain boundaries.

Combination of EBSD crystallographic texture analysis with EDS technique is an approach to understand the correlation between alloy texture and corrosion resistance. From the misorientation profile and EDS line-scan in the cross-section of Ni-20Cr, it is known that the Cr depletion preferentially occurred along the grain boundaries with misorientation angle approximately 35° - 50° between neighboring grains. The CSL $\Sigma 3$ grain boundaries showed high corrosion resistance to molten fluoride salt for all four tested alloys in this study. This is because the grain boundary Cr diffusion was

selective with respect to boundary plane type. It is known that the energy of low-angle CSL grain boundaries is dependent on the degree of misorientation between neighboring grains. CSL $\Sigma 3$ grain boundaries have relatively low energy compared to other types of boundaries. Therefore, the Cr did not diffuse to low-angle CSL $\Sigma 3$ grain boundaries, and the CSL $\Sigma 3$ s have low propensity for Cr depletion. Additionally, CSL $\Sigma 3$ grain boundaries have also been reported to immune the chromium carbide precipitation in 316 stainless steel[102].

3.4.5 Effect of graphite on the alloys corrosion

In this study, the corrosion tests of commercial Hastelloy N and 316 stainless steel in graphite capsule were accomplished to understand the graphite effect on alloys' corrosion behavior in molten FLiBe. In the presence of graphite in the corrosion environment, Hastelloy N gained weight after 1000 hours corrosion due to the formation of numerous carbides particles on surface and in alloy's matrix, and 316 stainless steel lost more weight than the ones without graphite for 1000-3000 hours corrosion due to acceleration effect of graphite on Cr outward diffusion.

A large number of carbide particles Mo_2C , Cr_3C_2 and Cr_7C_3 formed on Hastelloy N surface and nano-sized $(\text{Cr}, \text{Mn})_{23}\text{C}_6$ particles formed within Hastelloy N matrix as deep as $7\mu\text{m}$ from surface after 1000 hours corrosion in molten FLiBe. On the other hand, on 316 stainless steel surface only hexagonal Cr_7C_3 protruded out from the edge of deep attacked grain boundaries, and in 316 stainless steel matrix round Mo_2C , needle-like Al_4C_3 and Cr_7C_3 particles formed as deep as $50\mu\text{m}$ after 3000 hours corrosion test in molten FLiBe. The use of graphite corrosion capsule doubled corrosion attack depth in terms of the maximum Cr depletion distance in comparison with the samples tested in 316 stainless steel capsule.

As discussed earlier, the corrosion of structural alloys in molten fluoride salt is governed by the thermal diffusion of Cr in alloys, and carbon diffuses much faster than Cr in both Fe and Ni base alloys. Microstructural analysis (mainly using SEM-EDS technique) in this study suggests that the newly-formed carbides particles layer is deeper than the observable Cr depletion distance in Hastelloy N and 316 stainless steel tested in graphite capsules. Therefore, the carbon diffusion in alloys determines the depth of carbides particles formed in the alloys. Additionally, the newly-formed chromium carbides

within alloys stabilize Cr by the mean of chemical bonding with carbon, which might enhance alloys' long term corrosion resistance to molten fluoride salt. In this regard, it may be advisable to run longer corrosion tests to understand how the chromium carbide particles improve alloys' corrosion resistance. From literature review, during MSRE program the carburization phenomenon was observed in some Hastelloy N parts that were in contact with graphite. A sacrificial shim was placed between Hastelloy N and graphite to deal with the carburization problem[33].

Chapter 4 Conclusions

In support of structural materials development for FHR, corrosion of candidate structural alloys in the potential primary coolant molten salt FLiBe at designed outlet temperature of 700°C has been studied. Because of the hygroscopicity and toxicity of FLiBe salt, specific facilities such as glove box with controlled atmosphere and salt transfer system were designed and fabricated for safely handling the FLiBe salt in various states. Corrosion tests of two commercial candidate FHR alloys Hastelloy N and 316 stainless steel were successfully conducted in molten FLiBe in different material capsules, Hastelloy N in pure nickel and IG-110 graphite and 316 stainless steel in 316 stainless steel and IG-110 graphite. To achieve a more fundamental understanding of corrosion mechanisms, particularly Cr depletion into the salt, Ni-5Cr and Ni-20Cr binary alloys were also evaluated. To separate thermal effects from corrosion-induced effects, these two binary alloys were also heat treated in Ar filled quartz tubes at the same temperature as corrosion tests (700°C). After corrosion tests, the maximum Cr depletion distance was measured to evaluate their corrosion resistance to molten FLiBe. Finally, based on the understanding of these four alloys' corrosion results, a model for long-term corrosion prediction was developed to predict the Cr depletion depth in structural alloys after long term corrosion in molten.

From the studies of Ni-5Cr and Ni-20Cr binary alloys in Ar filled quartz tubes and the corrosion tests in molten FLiBe in pure nickel capsules, the following general conclusion were achieved: (1) the surface of thermally annealed alloys consisted of a protective Cr_2O_3 film ($\sim 1.6 \mu\text{m}$ thick) that induced slight Cr depletion ($\sim 1 \mu\text{m}$ thick) underneath surface; (2) intergranular corrosion was dominant in the near-surface regions of the samples tested in molten FLiBe; (3) lattice parameter shrank by 0.33pm and 1.49pm respectively for Ni-5Cr and Ni-20Cr near-to-surface layer where substantial Cr depleted after 1000 hours corrosion in molten FLiBe; (4) the Cr depletion rate of the alloys was governed by the overall thermal diffusion coefficient of Cr in the alloy that was calculated to be $D_{\text{eff}} = 1.66 \times 10^{-17} \text{ m}^2/\text{sec}$ for Ni-5Cr and $D_{\text{eff}} = 2.74 \times 10^{-16} \text{ m}^2/\text{sec}$ for Ni-20Cr; (6) the Cr concentration on the corroded alloys' surface (C_s) was

observed to be near zero as determined by XPS analysis; (7) the grains with misorientation angle relative to [001] direction in a range of 35°-50° were favored to be attacked in molten FLiBe salt.

From the 1000 hours corrosion tests of Hastelloy N in molten FLiBe in both pure nickel capsule and graphite capsule, the following conclusions were arrived at: (1) an about 200nm deep porous structure layer formed in the near-surface regions of the Hastelloy N tested in nickel capsule; (2) the corrosion attack depth as measured by Cr depletion extended to a depth of 3.5 μ m (5wt.% Cr cut-off criterion) for the Hastelloy N tested in nickel capsules; (3) regardless of capsule material, MoSi₂ precipitates formed at the grain boundaries in the alloy mainly due to thermal effects; (4) for samples tested in graphite capsules, the formation of Cr₃C₂, Cr₇C₃ and Mo₂C phase particles were observed in the near-surface region of Hastelloy N; (5) massive Cr depletion and concurrent formation of a ~1.4 μ m Ni₃Fe phase layer occurred in the near surface region of the Hastelloy N tested in graphite capsule; (6) fast C inward diffusion resulted in the formation of a nano-sized Cr₂₃C₆ particles layer extending to approximately 7 μ m in depth; (7) the newly-formed chromium carbides at the grain boundaries in Hastelloy N potentially stabilized Cr against dissolution due to corrosion.

From the long-term corrosion tests of 316 stainless steel in molten FLiBe in both 316 stainless steel and graphite capsule, the following conclusions were arrived at: (1) intergranular corrosion was the dominant corrosion mechanism; (2) for tests performed in graphite capsules the accelerated Cr depletion was higher by a factor of two compared to those tested in 316 stainless steel capsules; (3) substantial Cr depletion at surface promoted the formation of MoSi₂ precipitates; (4) hexagonal Cr₇C₃, round Mo₂C, and needle-like Al₄C₃ particulate phases formed through the entire corrosion layer due to the inward diffusion of carbon to alloy matrix; (5) nano-sized Cr₂₃C₆ precipitate formed at grain boundary due to thermal effect; (6) the corrosion attack depth measured by SEM-EDS analysis ranged from 6.4 μ m to 11.5 μ m for the samples tested in 316 stainless steel capsules, and from 13.7 μ m to 22.5 μ m for tests in graphite capsules for 1000 to 3000 hours, respectively; (7) massive Cr depletion in the corrosion layer induced a γ -austenite to α -ferrite phase transformation in the corrosion layer; (8) within 316 stainless steel, the Cr

depletion occurred predominantly along the random high angle grain boundaries (15-180°); (9) CSL $\Sigma 3$ s grain boundaries were relatively immune to corrosion to molten fluoride salt in terms of Cr depletion.

With respect to the corrosion attack depth as measured by the maximum Cr depletion distance, the corrosion of 316 stainless steel and Hastelloy N were comparable. The presence of graphite in molten FLiBe accelerated Cr depletion rate at initial corrosion stage, but the formation of carbides particles within alloys' matrix is expected to stabilize Cr from dissolution in the long term.

Based on the experimental data and physical corrosion mechanisms, a model for long-term corrosion prediction of Cr-containing alloys in FLiBe salt has been developed specifically for corrosion in molten FLiBe salt at 700°C. The model uses Cr concentration profile $C(x, t)$ as a function of corrosion distance in the material and duration fundamentally derived from the Fick's diffusion laws. This model was validated with reasonable accuracy for the four alloys by fitting the calculated profiles with experimental data and can be applied to evaluate corrosion attack depth over the long-term. The critical constant of the overall diffusion coefficient (D_{eff}) in this model can be quickly calculated from the experimental measurement of alloys' weight loss due to Cr depletion. While many factors affect the D_{eff} such as the grain boundary type, grain size, precipitates, initial Cr concentration as well as temperature, this model provides a methodology for estimating corrosion attack depth of alloys in molten fluoride salts.

The model predicts corrosion rate of 75.2 $\mu\text{m}/\text{year}$, 305.6 $\mu\text{m}/\text{year}$, 17.2 $\mu\text{m}/\text{year}$, and 12.0 $\mu\text{m}/\text{year}$ for Ni-5Cr (5wt.% Cr), Ni-20Cr (20wt.% Cr), Hastelloy N (7wt.% Cr) and 316 stainless steel (17wt.% Cr), respectively, in the molten FLiBe without graphite at 700°C using a cut-off criterion of $[\text{Cr}] = 98\% C_0$.

Chapter 5 Future work

In addition to the investigations presented in this thesis, the radiation induced damage and the redox potential of molten salt also play important roles in the evaluation of structural alloys performance in molten fluoride salt for the FHR application. Some preliminary designs were completed for studying these two effects on alloys' corrosion in molten salt.

5.1 Irradiation effect on alloys corrosion in molten salt

As reported by E. a. Kenik and J. T. Busby, the irradiation-induced degradation to the alloys in irradiation environment might become life-limiting concerns at the high damage levels[74]. The forms of degradation include radiation hardening, embrittlement, dimensional stability, radiation-induced segregation (RIS) and precipitation, transmutation effects and irradiation-induced stress corrosion cracking. According to our earlier corrosion tests, the radiation-induced segregation probably becomes a major factor affecting Cr depletion preferentially along grain boundary. Basically, there are two mechanisms that contribute to the radiation-induced segregation, (1) inverse Kirkendall mechanism where solute atoms interact with the vacancy flux and (2) interstitial drag mechanism where undersized solute atoms preferentially interact with the flux of self-interstitials and migrate toward defect sinks. The depletion of chromium and enrichment of nickel and possibly silicon was observed at grain boundary in irradiated stainless steel and nickel alloys[29], [30], [32], [74]. Therefore, with respect to the Cr depletion preferentially along grain boundaries for the alloys in high-temperature molten fluoride salts, it is expected that RIS may have a mitigating effect on the corrosion rate. With this concern, this work involved the proton irradiation of 316 stainless steel followed by static corrosion tests in molten FLiBe at 700°C.

Prior to irradiation experiment, the radiation damage profile was calculated using SRIM 2010, setting threshold value of 40 eV displacement energy and 0 eV lattice binding energy, as shown in Figure 97. Assuming the beam energy completely transfers to target atoms, ionization, phonon, and lattice binding energy (0eV), the incident particle energy (E_i^0) equals to $E_i^T + E_i^I + E_i^P + E_i^B$. Following

this calculation, a constant 0.5 dpa radiation damage region is expected when 2.0 MeV proton beam is applied to hit 316 stainless steel samples. As demonstrated in Figure 97, constant radiation damage was introduced into the layer from surface to about 10 μ m deep where alloy may be expected to undergo Cr depletion along grain boundaries.

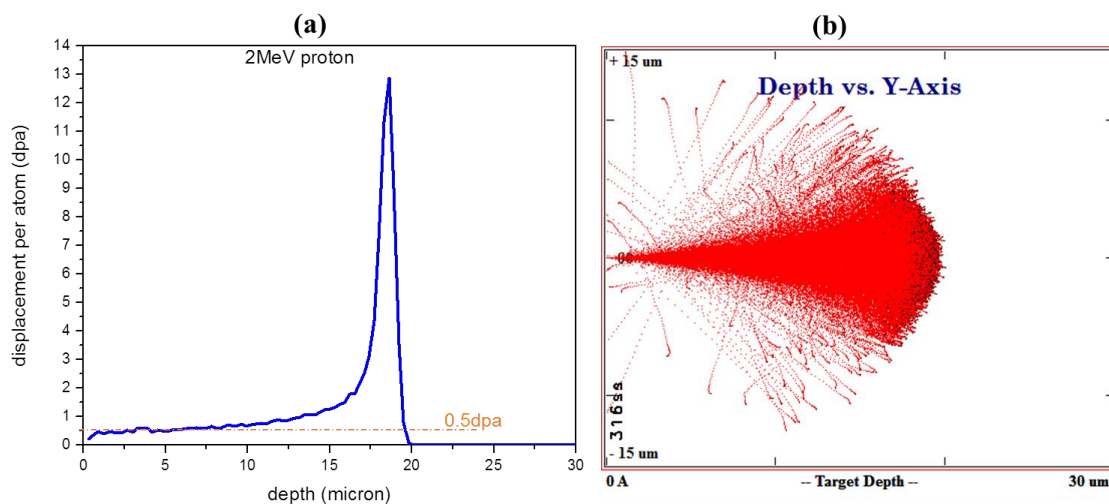


Figure 97: (a) Profile of displacement per atom (dpa) vs. depth and (b) 2 dimensions tracing path of incident protons showing the radiation damage distribution in 316 stainless steel, calculated using The Stopping and Range of Ions in Matter (SRIM, 2010) with Quick Kinchin-Peace calculation mode.

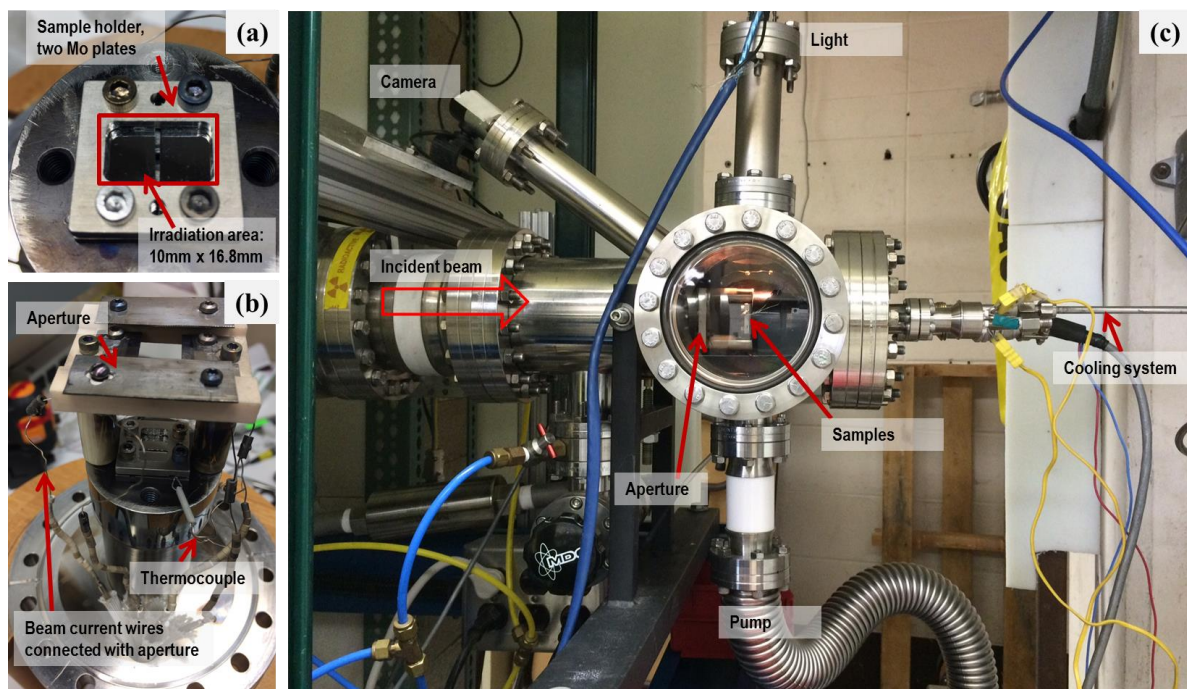


Figure 98: (a) two 316 stainless steel samples mounted on Mo plates on stage, (b) assembled sample holder and aperture on stage, and (c) samples loaded into beam line chamber equipped with assisting facilities of cooling system and IR camera.

Figure 98 shows the configuration of the sample stage, sample holder, aperture as well as the beam chamber for the irradiation experiment. A cooling system was attached to the back of sample stage for controlling the radiation temperature at about 450°C. Based on our experience, this temperature can be achieved if 2.0MeV proton beam current is controlled at about 12 μ A. Using the equipment in the Ion Beam Laboratory (IBL) at the University of Wisconsin-Madison, 0.5dpa constant damage was accumulated after 70 hours radiation. The real radiation temperature was maintained at 420 \pm 15°C. As shown in Figure 99(b), the irradiated area on 316 stainless steel appears blue yellow.

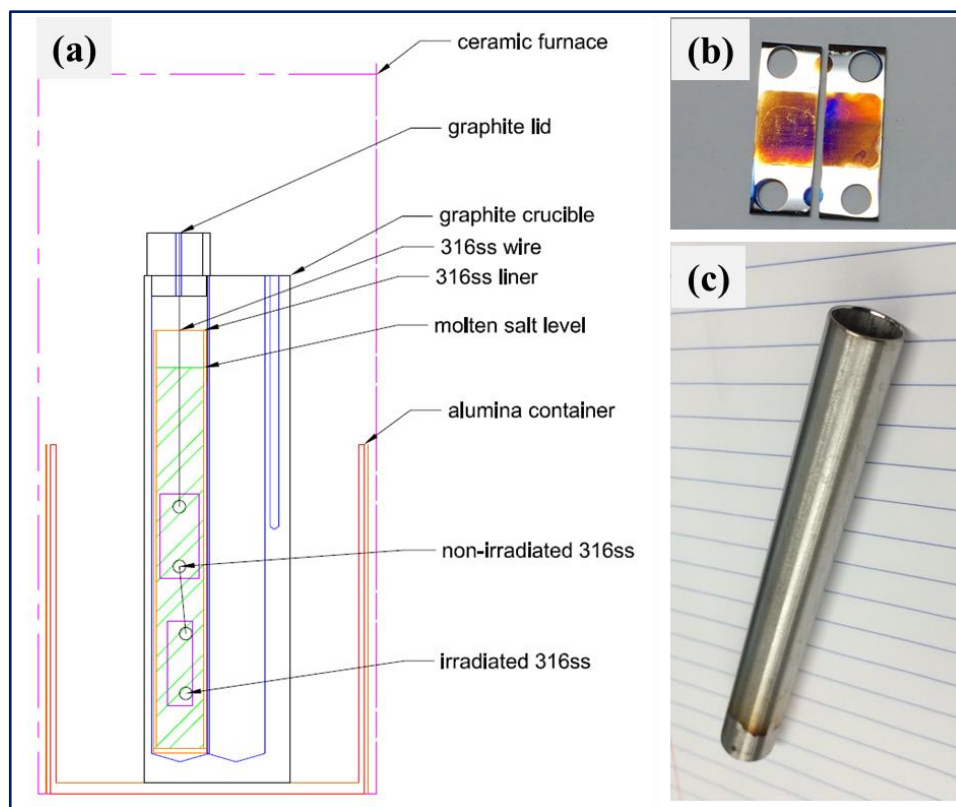


Figure 99: (a) Schematic illustration diagram of corrosion experiment for testing irradiated samples, (b) irradiated 316 stainless steel samples and (c) 316 stainless steel liner for conducting corrosion tests of irradiated and non-irradiated 316 stainless steels in molten FLiBe at 700°C.

Figure 99 (a) illustrates the corrosion system for evaluating the radiation effect (mainly radiation induced segregation at grain boundaries) on the corrosion behavior of 316 stainless steel in molten FLiBe. A non-irradiated (as control sample) and an irradiation specimen are simultaneously suspended in molten FLiBe in a 316 stainless steel corrosion crucible. The work is expected to be synergistic with the corrosion tests performed in FLiBe in the Massachusetts Institute of Technology Research Reactor (MITR) under neutron irradiation conditions.

However, after proton irradiation, the irradiated 316 stainless steel samples unexpectedly exhibited measureable level of radioactivity due to Co impurity in the 316 stainless steel. The trace Co in the 316 stainless steel comes from the nickel that was used to manufacture austenitic stainless steel. Based on the radiation safety policy in the University of Wisconsin-Madison, these irradiated samples could not be immediately tested, but will be tested once the radioactivity level drops.

5.2 Redox potential controlled corrosion tests

In MSRE, the redox potential of molten fluoride salt was adjusted by dipping Be rod into molten salt[22]. The addition of Be reductant into convection corrosion loop reduced the weight change of 316 stainless steel[57]. In our static corrosion tests, the redox potential of molten FLiBe was supposed to be adjusted by Be metal addition. However, the electrochemistry measurement showed that only ~0.1V difference in the redox potential between purified FLiBe and Be reduced FLiBe salt. The microstructure of the 316 stainless steel samples tested in both salts for 1000 hours therefore showed similar Cr depletion distance from surface (Figure 90). Furthermore, the corrosion product of chromium fluoride dissolved in molten salt changes initial redox potential during corrosion in molten FLiBe. With these concerns, a redox potential controlled corrosion system was designed, as shown in Figure 100. In this system, two electrical circuits are included to measure salt redox potential vs. the reference electrode $E_{\text{Ni}^{2+}/\text{Ni}}$ and to reduce salt by applying an external DC power supply. In the boron nitride capsule, 10% NiF_2 and balance FLiBe salt is filled and a pure nickel rod (1.6mm in diameter) is immersed into molten salt. Mo was selected as anode and cathode because of its excellent stability in molten fluoride salt. In the center of salt, a Mo rod (1.6mm in diameter) and a Mo tubing (3.2mm in diameter) are positioned at the same height, but they are electronically separated using boron nitride isolator. The Mo tubing also served as a sheath of thermocouple that monitors the molten FLiBe temperature. Samples suspended in molten salt are separated from all electrodes by using boron nitride isolator. A glassy carbon crucible was selected as molten FLiBe container for this corrosion test.

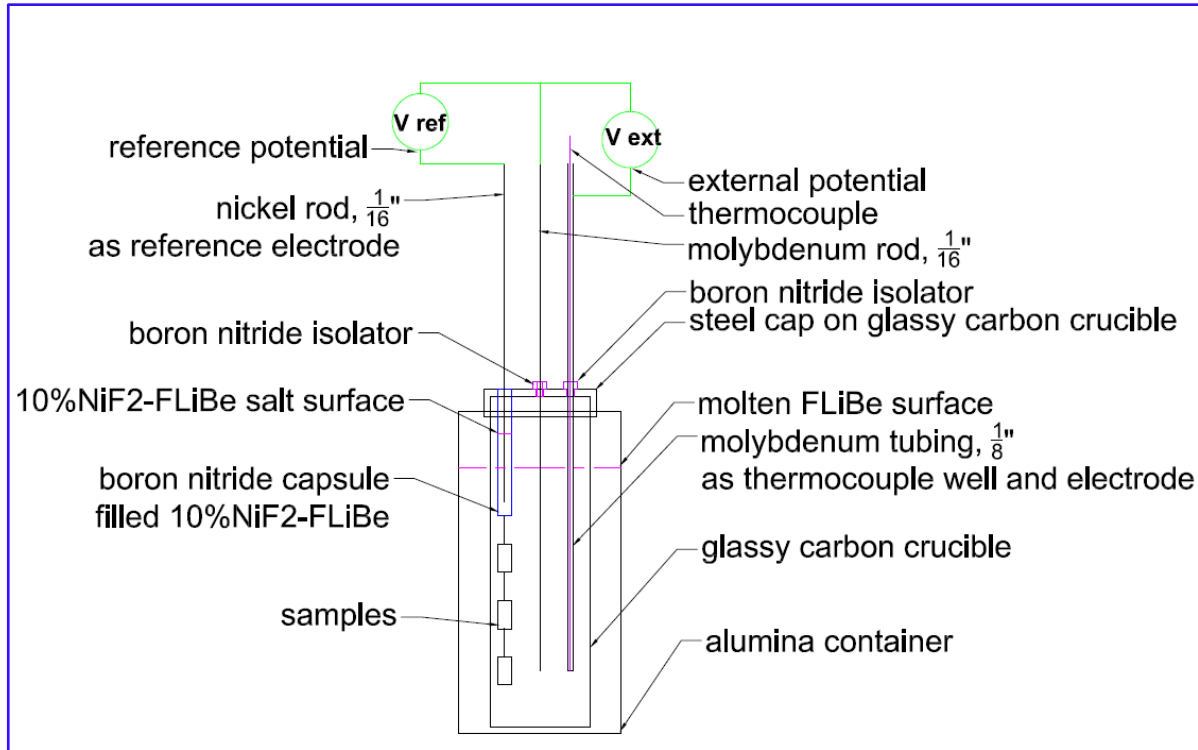
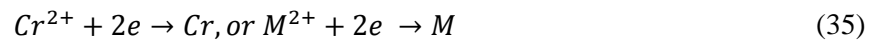


Figure 100: Diagram of redox potential controlled corrosion system.

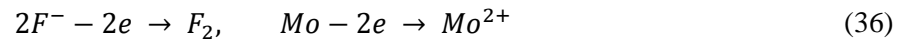
During corrosion tests, two main half-cell reactions take place on cathode and anode at certain external potential V_{ext} by the means of the following reactions.

On cathode:



where M is impurities ions, depending on V_{ext} , the reaction productions were reduced. The external voltage is controlled in the desired range where the main metal ions of salt are not reduced.

On anode:



where negative ions such fluorine ions are reduced, or the electrode material Mo is oxidized, depending on the salt condition.

The baseline of the reference electrode equals to $E_{Ni^{2+}/Ni \text{ vs HF/H}_2} = 0.473V$ in 10% NiF_2 balanced FLiBe at 700°C. The redox potential (vs. Ni^{2+}/Ni standard reference) of molten FLiBe equals to the sum of supplied external voltage (E_{ext}) from DC power supply and the potential difference (E_{ref}) between the FLiBe in glassy carbon crucible and the 10% NiF_2 balanced FLiBe in boron capsule, $E = E_{ext} + E_{ref}$. The

reference potential can be measured on-line. Therefore, this system enables the on-line controlling of the redox potential of molten salt. The accuracy of the voltage control is controlled at $\pm 0.01\text{V}$.

Following this design, the redox potential controlled corrosion system was fabricated, as shown in Figure 101. A 3D drawing in Figure 101(a) clearly presents the positions of all electrodes. The pictures in Figure 101(b) and (c) show the assembled redox potential controlled corrosion system. To avoid ground issue, a 316 stainless steel rod is welded on the steel cap. This rod is connected with ground wire. An extra thermocouple in ceramic furnace monitors furnace temperature during corrosion tests.

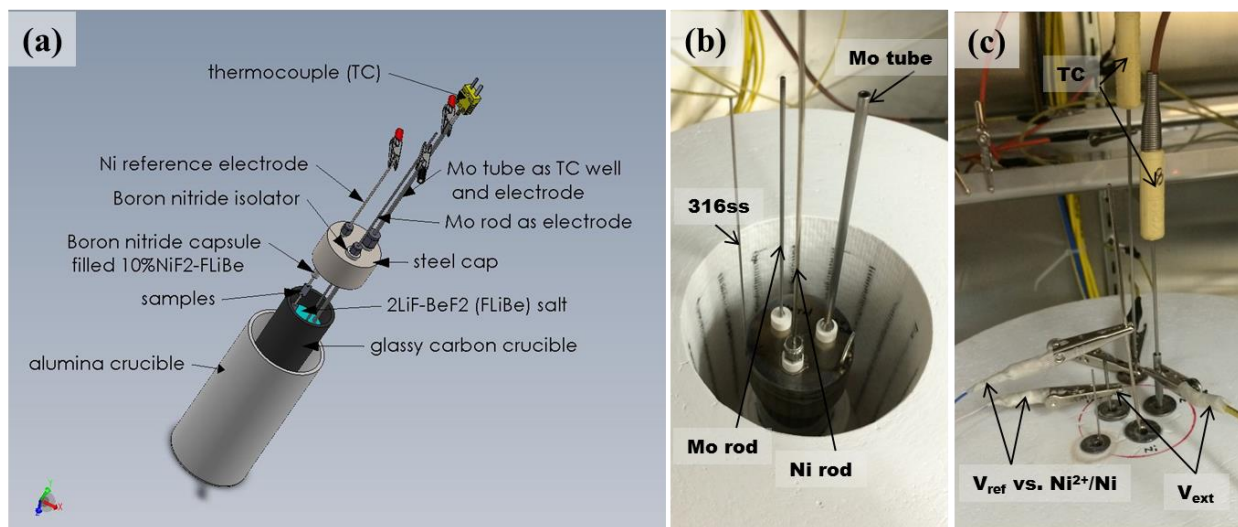


Figure 101: (a) 3D schematic drawing of redox potential controlled corrosion system, (b) prepared corrosion system in furnace, and (c) corrosion setup with reference voltage measurement and external power supply connection.

Bibliography

- [1] G. F. Flanagan, D. E. Holcomb, and S. M. Cetiner, “FHR Generic Design Criteria, ORNL/TM-2012/226,” 2012.
- [2] T. R. Allen, S. Ball, E. Blandford, T. Downar, G. Flanagan, C. W. Forsberg, E. Greenspan, D. Holcomb, L. W. Hu, R. Matzie, J. McGaha, D. Mears, M. Memmot, P. F. Peterson, J. Rushton, R. Schleicher, F. Silady, A. Stanculescu, C. Stoots, and R. Wright, “Fluoride-Salt-Cooled, High-Temperature Reactor (FHR) Integrated Research Project Workshop 1,” 2013.
- [3] T. R. Allen, K. Sridharan, L. Tan, W. E. Windes, J. I. Cole, D. C. Crawford, and G. S. Was, “Materials challenges for generation IV nuclear energy systems,” *Nuclear Technol.*, vol. 162, no. June, 2008.
- [4] M. W. Rosenthal, P. R. Kasten, and R. B. Briggs, “Molten-Salt Reactors---History, Status, and Potential,” 1969.
- [5] H. G. MacPherson, “Molten-salt reactor program, Quarterly progress report, ORNL-2799,” Sep. 1959.
- [6] L. E. McNeese, “Molten-Salt Reactor Program Semiannual Progress Report for Period Ending February 28, 1975, ORNL-5047,” 1975.
- [7] B. H. Webster, “Quality-assurance practices in construction and maintenance of the molten-salt reactor experiment, ORNL-TM-2999,” 1970.
- [8] M. W. Rosenthal, R. B. Briggs, and P. N. Haubenreich, “Molten-salt reactor program semiannual progress report, ORNL-4622,” 1971.
- [9] F. Lantelme and H. Groult, “Corrosion in Molten Salts,” in *Molten Salts Chemistry, From Lab to Applications*, 1st ed., Elsevier, 2013, pp. 241–267.
- [10] P. Peterson, “Overview of the current status of the UCB Mark-1 PB-FHR commercial prototype design effort,” 2014.
- [11] H. G. Macpherson, “The Molten Salt Reactor Adventure,” *Nucl. Sci. Eng.*, vol. 90, pp. 374–380, 1985.
- [12] W. B. Cottrell, R. C. Briant, J. H. Buck, and A. J. Miller, “Quarterly progress report on aircraft nuclear propulsion project, ORNL-1294,” 1952.
- [13] R. C. Briant, A. J. Miller, and W. B. Cottrell, “Aircraft nuclear propulsion project, quarterly progress report, ORNL-1227,” 1952.
- [14] W. D. Manly, G. M. Adamson, J. H. Coobs, J. H. DeVan, D. A. Douglas, E. E. Hoffman, and P. Patriarca, “Aircraft reactor experiment-metallurgical aspects, ORNL-2349,” 1957.
- [15] J. A. Lane, “Aircraft Reactor Experiment,” in *Aqueous Homogeneous Reactors*, vol. 853, J. A. Lane, Ed. 1957.
- [16] C. A. Brandon and J. A. Conlin, “MSRE capsul irradiation experiment,” *ORNL-TM-870*, 1964.
- [17] J. R. Engel, “MSRE design and operations report, part XI-A, Test program for ^{233}U operation, ORNL-TM-2304,” 1968.

- [18] C. Wong and B. Merrill, "Relevant MSRE and MSR Experience," 2004.
- [19] D. T. Ingersoll, "Status of Physics and Safety Analyses for the Liquid-Salt-Cooled Very High-Temperature Reactor (LS-VHTR), ORNL-TM-2005-218," 2005.
- [20] C. Forsberg, "LS-VHTR Overview : Factors Impacting Refueling," 2006.
- [21] W. R. Grimes, "Chemical Research and Development for Molten Salt Breeder Reactors, ORNL-TM-1853," 1967.
- [22] W. R. Grimes, "Molten-salt reactor chemistry," *Nucl. Appl. Technol.*, vol. 8, no. February, p. 137, 1970.
- [23] O. Benes, C. Cabet, S. Delpech, P. Hosnedl, V. Ignatiev, R. Konings, D. Lecarpentier, O. Matal, C. Renault, and J. Uhler, "Assessment of Liquid Salts for Innovative Applications," *Rev. Rep. Liq. salts Var. Appl.*, 2009.
- [24] D. F. Williams and K. T. Clarno, "Evaluation of salt coolants for reactor applications," *Nucl. Technol.*, vol. 163, no. 3, pp. 330–343, 2008.
- [25] D. F. Williams, L. M. Toth, and K. T. Clarno, "Assessment of candidate molten salt coolants for the advanced high-temperature reactor (AHTR), ONRL-TM-2006/12," 2006.
- [26] V. Khokhlov, V. Ignatiev, and V. Afonichkin, "Evaluating physical properties of molten salt reactor fluoride mixtures," *J. Fluor. Chem.*, vol. 130, no. 1, pp. 30–37, Jan. 2009.
- [27] P. Yvon and F. Carré, "Structural materials challenges for advanced reactor systems," *J. Nucl. Mater.*, vol. 385, no. 2, pp. 217–222, Mar. 2009.
- [28] T. Allen, J. Busby, M. Meyer, and D. Petti, "Materials challenges for nuclear systems," *Mater. Today*, vol. 13, no. 12, pp. 14–23, Dec. 2010.
- [29] T. R. Allen, L. Tan, G. S. Was, and E. A. Kenik, "Thermal and radiation-induced segregation in model Ni-base alloys," *J. Nucl. Mater.*, vol. 361, no. 2–3, pp. 174–183, Apr. 2007.
- [30] P. Ahmedabadi, V. Kain, K. Arora, I. Samajdar, S. C. Sharma, and P. Bhagwat, "Radiation-induced segregation in desensitized type 304 austenitic stainless steel," *J. Nucl. Mater.*, vol. 416, no. 3, pp. 335–344, Sep. 2011.
- [31] N. Wanderka, A. Bakai, C. Abromeit, D. Isheim, and D. N. Seidman, "Effects of 10 MeV electron irradiation at high temperature of a Ni-Mo-based Hastelloy," *Ultramicroscopy*, vol. 107, no. 9, pp. 786–90, Sep. 2007.
- [32] A. Etienne, B. Radiguet, N. J. Cunningham, G. R. Odette, R. Valiev, and P. Pareige, "Comparison of radiation-induced segregation in ultrafine-grained and conventional 316 austenitic stainless steels," *Ultramicroscopy*, vol. 111, no. 6, pp. 659–63, May 2011.
- [33] H. E. McCoy and J. R. Weir, "Materials Development for Molten-Salt Breeder Reactors, ORNL-TM-1854," 1967.
- [34] R. L. Jones and K. H. Stern, "New eras in molten salt corrosion research," in *Ind. Eng. Chem. Prod. Res. Dev.*, 1980, pp. 158–165.

- [35] R. S. Sellers, W. J. Cheng, M. H. Anderson, K. Sridharan, C. J. Wang, and T. R. Allen, "Materials corrosion in molten LiF-NaF-KF eutectic salt under different reduction-oxidation conditions," in *Proceedings of ICAPP*, 2012.
- [36] L. C. Olson, J. W. Ambrosek, K. Sridharan, M. H. Anderson, and T. R. Allen, "Materials corrosion in molten LiF-NaF-KF salt," *J. Fluor. Chem.*, vol. 130, no. 1, pp. 67–73, Jan. 2009.
- [37] M. S. Sohal, M. A. Ebner, P. Sabharwall, and P. Sharpe, "Engineering Database of Liquid Salt Thermophysical and Thermochemical Properties," 2010.
- [38] J. W. Ambrosek, "Molten Chloride Salts for Heat Transfer in Nuclear Systems," University of Wisconsin-Madison, 2011.
- [39] J. C. Sager, "The Measurement and Control of the Redox Potential of Molten FLiNaK Salt," University of Wisconsin-Madison, 2013.
- [40] J. W. Koger, "Chromium depletion and void formation in Fe-Ni-Cr alloys during molten salt corrosion and related processes.pdf," in *Advances in corrosion science and technology*, 1974, pp. 245–318.
- [41] D. F. Williams and L. M. Toth, "Chemical Considerations for the Selection of the Coolant for the Advanced High-Temperature Reactor," 2005.
- [42] J. H. Shaffer, "Preparation and handling of salt mixtures for the molten salt reactor experiment, ORNL-4616," 1971.
- [43] F. Group, "White Paper of FHR Integrated Research Project Workshop 4," 2013.
- [44] J. R. Keiser, J. H. DeVan, and D. L. Manning, "The Corrosion Resistance of Type 316 Stainless Steel to Li₂BeF₄, ORNL/TM-5782," 1977.
- [45] J. R. Keiser, "Compatibility studies of potential molten-salt breeder reactor materials in molten fluoride salts, ORNL-TM-5783," 1977.
- [46] S. P. Murarka, M. S. Anand, and R. P. Agarwala, "Diffusion of Chromium in Nickel," *J. Appl. Phys.*, vol. 35, no. 4, p. 1339, 1964.
- [47] R. Braun and M. Feller-Kniepmeier, "Diffusion of chromium in α -iron," *Phys. Status Solidi*, vol. 90, no. 2, pp. 553–561, Aug. 1985.
- [48] R. B. Evans, J. H. DeVan, and G. M. Watson, "Self-diffusion of chromium in nickel-base alloys, ORNL-2982," 1961.
- [49] H. O. Nam, a. Bengtson, K. Vörtler, S. Saha, R. Sakidja, and D. Morgan, "First-principles molecular dynamics modeling of the molten fluoride salt with Cr solute," *J. Nucl. Mater.*, vol. 449, no. 1–3, pp. 148–157, 2014.
- [50] A. F. Smith, "The Diffusion of Chromium in Type 316 Stainless Steel," *Met. Sci.*, vol. 9, no. 1, pp. 375–378, Jan. 1975.
- [51] T.-F. Chen, G. P. Tiwari, Y. Iijima, and K. Yamauchi, "Volume and Grain Boundary Diffusion of Chromium in Ni-Base Ni-Cr-Fe Alloys," *Mater. Trans.*, vol. 44, no. 1, pp. 40–46, 2003.

- [52] A. Langley, "Hydrogen trapping, diffusion and recombination in austenite stainless steels," *J. Nucl. Mater.*, vol. 129, pp. 622–628, 1984.
- [53] J. W. Koger, "Evaluation of Hastelloy N alloys after nine years exposure to both a molten fluoride salt and air at temperatures from 700 to 560C, ORNL-TM-4189," 1972.
- [54] L. Olson, K. Sridharan, M. Anderson, and T. Allen, "Nickel-plating for active metal dissolution resistance in molten fluoride salts," *J. Nucl. Mater.*, vol. 411, no. 1–3, pp. 51–59, Apr. 2011.
- [55] D. Olander, "Redox condition in molten fluoride salts Definition and control," *J. Nucl. Mater.*, vol. 300, no. 2–3, pp. 270–272, Feb. 2002.
- [56] S. Delpech, C. Cabet, C. Slim, and G. S. Picard, "Molten fluorides for nuclear applications," *Mater. Today*, vol. 13, no. 12, pp. 34–41, Dec. 2010.
- [57] J. R. Keiser, J. H. DeVan, and E. J. Lawrence, "Compatibility of molten salts with type 316 stainless steel and lithium," *J. Nucl. Mater.*, vol. 86, pp. 295–298, 1979.
- [58] J. Zhang, "Electrochemistry of actinides and fission products in molten salts - Data review," *J. Nucl. Mater.*, vol. 447, no. 1–3, pp. 271–284, 2014.
- [59] E. L. Compere, S. S. Kirsliis, E. G. Bohlmann, F. F. Blankenship, and W. R. Grimes, "Fission Product Behavior in the Molten Salt Reactor Experiment, ORNL-4865," 1975.
- [60] J. R. Keiser, "Status of tellurium-Hastelloy N studies in molten fluoride salts, ORNL-TM-6002," 1977.
- [61] D. A. Petti, P. A. Demkowicz, J. T. Maki, and R. R. Hobbins, "TRISO-coated particle fuel performance," *Compr. Nucl. Mater.*, pp. 151–213, 2012.
- [62] V. K. Afonichkin, A. L. Bovet, V. V. Ignatiev, A. V. Panov, V. G. Subbotin, A. I. Surenkov, A. D. Toropov, and A. L. Zhrebtsov, "Dynamic reference electrode for investigation of fluoride melts containing beryllium difluoride," *J. Fluor. Chem.*, vol. 130, no. 1, pp. 83–88, Jan. 2009.
- [63] R. B. Briggs, "Molten-salt reactor program semiannual progress report, ORNL-3708," Oak Ridge National Laboratory, 1963.
- [64] H. E. McCoy, "The INOR-8 Story," 1969.
- [65] B. Kelleher, G. Zheng, M. Anderson, K. Sridharan, and G. Cao, "Purification of Non Uranium Bearing Fluoride Salts for Nuclear Applications," in *Transactions of the American Nuclear Society*, 2013, vol. 109, no. 1971, pp. 1079–1081.
- [66] G. S. Was and R. M. Kruger, "A thermodynamic and kinetic basis for understanding chromium depletion in Ni-Cr-Fe alloys," *Acta Metall.*, vol. 33, no. 5, pp. 841–854, May 1985.
- [67] T.-F. Chen, Y. Iijima, K. Hirano, and K. Yamauchi, "Diffusion of chromium in nickel-base Ni-Cr-Fe alloys," *J. New Mater. Electrochem. Syst.*, vol. 169, pp. 285–290, 1989.
- [68] J. D. Tucker, R. Najafabadi, T. R. Allen, and D. Morgan, "Ab initio-based diffusion theory and tracer diffusion in Ni-Cr and Ni-Fe alloys," *J. Nucl. Mater.*, vol. 405, no. 3, pp. 216–234, Oct. 2010.

- [69] M. Mizouchi, Y. Yamazaki, Y. Iijima, and K. Arioka, "Low Temperature Grain Boundary Diffusion of Chromium in SUS316 and 316L Stainless Steels," *Mater. Trans.*, vol. 45, no. 10, pp. 2945–2950, 2004.
- [70] P. E. A. Turchi, L. Kaufman, and Z.-K. Liu, "Modeling of Ni–Cr–Mo based alloys: Part II — Kinetics," *Calphad*, vol. 31, no. 2, pp. 237–248, Jun. 2007.
- [71] L. C. Olson, "Materials corrosion in molten LiF–NaF–KF eutectic salt," University of Wisconsin-Madison, 2009.
- [72] J. H. DeVan and R. B. Evans, "Corrosion behavior of reactor materials in fluoride salt mixtures, ORNL-TM-0328," 1962.
- [73] J. C. Fisher, "Calculation of Diffusion Penetration Curves for Surface and Grain Boundary Diffusion," *J. Appl. Phys.*, vol. 22, no. 1, p. 74, 1951.
- [74] E. A. Kenik and J. T. Busby, "Radiation-induced degradation of stainless steel light water reactor internals," *Mater. Sci. Eng. R Reports*, vol. 73, no. 7–8, pp. 67–83, Jul. 2012.
- [75] V. Ignatiev and A. Surenkov, *Material Performance in Molten Salts*, 1st ed., vol. 5. Elsevier Inc., 2012.
- [76] G. Zheng, B. Kelleher, G. Cao, M. Anderson, T. Allen, and K. Sridharan, "Corrosion of 316 Stainless Steel in High Temperature Molten Li₂BeF₄ (FLiBe) Salt," *J. Nucl. Mater.*, vol. 461, pp. 143–150, 2015.
- [77] Y. Palizdar, R. C. Cochrane, R. Brydson, R. Leary, and A. J. Scott, "Accurate analysis of EBSD data for phase identification," *J. Phys. Conf. Ser.*, vol. 241, p. 012104, Jul. 2010.
- [78] T. G. Woodcock and O. Gutfleisch, "Multi-phase EBSD mapping and local texture analysis in NdFeB sintered magnets," *Acta Mater.*, vol. 59, no. 3, pp. 1026–1036, Feb. 2011.
- [79] J. W. Koger, "Corrosion of type 304L stainless steel and Hastelloy N by mixtures of boron trifluoride, air, and argon, ORNL-TM-4172," 1972.
- [80] W. J. Cheng, R. S. Sellers, M. H. Anderson, K. Sridharan, C. J. Wang, and T. R. Allen, "Zirconium effect on the corrosion behavior of 316L stainless steel alloy and Hastelloy-N superalloy in molten fluoride salt," *Nucl. Technol.*, vol. 183, pp. 248–259, 2013.
- [81] R. S. Sellers, "Impact of reduction-oxidation agents on the high temperature corrosion of materials in LiF–NaF–KF," University of Wisconsin, Madison, 2012.
- [82] V. V. Ignat'ev, a. I. Surenkov, I. P. Gnidoi, V. I. Fedulov, V. S. Uglov, a. V. Panov, V. V. Sagaradze, V. G. Subbotin, a. D. Toropov, V. K. Afonichkin, and a. L. Bove, "Investigation of the corrosion resistance of nickel-based alloys in fluoride melts," *At. Energy*, vol. 101, no. 4, pp. 730–738, Oct. 2006.
- [83] W. E. Clark, L. Rice, and D. N. Hess, "Evaluation of Hastelloy F and other corrosion-resistant structural materials for a continuous centrifuge in a multipurpose fuel-recovery plant, ORNL-3787," 1965.
- [84] J. W. Koger and A. P. Litman, "Mass transfer between Hastelloy N and Haynes Alloy No. 25 in a molten sodium fluoroborate mixture, ORNL-TM-3488," 1971.
- [85] J. W. Koger and A. P. Litman, "Compatibility of Hastelloy N and Croloy 9M with NaBF₄–NaF–KBF₄ (90–4–6 mol%) fluoroborate salt, ORNL-TM-2490," 1969.

- [86] S. Downey, P. N. Kalu, and K. Han, "The effect of heat treatment on the microstructure stability of modified 316LN stainless steel," *Mater. Sci. Eng. A*, vol. 480, no. 1–2, pp. 96–100, May 2008.
- [87] R. E. Gehlbach and H. E. McCoy, "Phase instability in Hastelloy N," in *International Symposium on Structural Stability in Superalloys*, 1968, pp. 346–366.
- [88] S. M. Bruemmer, B. W. Arey, and L. A. Charlot, "Influence of Chromium Depletion on Intergranular Stress Corrosion Cracking of 304 Stainless Steel," *Corrosion*, no. January, 1992.
- [89] J.-C. Zhao, M. Larsen, and V. Ravikumar, "Phase precipitation and time-temperature-transformation diagram of Hastelloy X," *Mater. Sci. Eng. A*, vol. 293, no. 1–2, pp. 112–119, Nov. 2000.
- [90] H. U. Hong, B. S. Rho, and S. W. Nam, "Correlation of the M₂₃C₆ precipitation morphology with grain boundary characteristics in austenitic stainless steel," *Mater. Sci. Eng. A*, vol. 318, pp. 285–292, 2001.
- [91] H. U. Hong and S. W. Nam, "The occurrence of grain boundary serration and its effect on the M₂₃C₆ carbide characteristics in an AISI 316 stainless steel," *Mater. Sci. Eng. A*, vol. 332, pp. 255–261, 2002.
- [92] D. K. Schreiber, M. J. Olszta, and S. M. Bruemmer, "Grain boundary depletion and migration during selective oxidation of Cr in a Ni-5Cr binary alloy exposed to high-temperature hydrogenated water," *Scr. Mater.*, vol. 89, pp. 41–44, 2014.
- [93] Y. Smda, I. G. C. Wood, F. H. Stott, D. P. Whittle, and B. D. B. A. S. Ow, "Intergranular oxidation and internal void formation in Ni-40 % Cr alloys," *Corros. Sci.*, vol. 21, no. 8, pp. 581–597, 1981.
- [94] H. Sahlaoui, H. Sidhom, and J. Philibert, "Prediction of chromium depleted-zone evolution during aging of Ni–Cr–Fe alloys," *Acta Mater.*, vol. 50, no. 6, pp. 1383–1392, Apr. 2002.
- [95] D. D. Pruthi, M. S. Anand, and R. P. Agarwala, "diffusion of chromium in Inconel-600," *J. Nucl. Mater.*, vol. 64, pp. 206–210, 1977.
- [96] F.-Y. Ouyang, C.-H. Chang, and J.-J. Kai, "Long-term corrosion behaviors of Hastelloy-N and Hastelloy-B3 in moisture-containing molten FLiNaK salt environments," *J. Nucl. Mater.*, vol. 446, no. 1–3, pp. 81–89, Mar. 2014.
- [97] S. K. Rai, A. Kumar, V. Shankar, T. Jayakumar, K. Bhanu Sankara Rao, and B. Raj, "Characterization of microstructures in Inconel 625 using X-ray diffraction peak broadening and lattice parameter measurements," *Scr. Mater.*, vol. 51, no. 1, pp. 59–63, Jul. 2004.
- [98] L. H. Chan, H. Weiland, S. Cheong, G. S. Rohrer, and A. D. Rollett, "The correlation between grain boundary character and intergranular corrosion susceptibility of 2124 Al alloy," in *Applications of Texture Analysis-15th International Conference on Textures of Materials*, 2008.
- [99] S. M. Schlegel, S. Hopkins, and M. Frary, "Effect of grain boundary engineering on microstructural stability during annealing," *Scr. Mater.*, vol. 61, pp. 88–91, 2009.
- [100] L. P. Bonfrisco and M. Frary, "Effects of crystallographic orientation on the early stages of oxidation in nickel and chromium," *J. Mater. Sci.*, vol. 45, pp. 1663–1671, 2010.
- [101] K. J. Kim, J. Ginsztler, and S. W. Nam, "The role of carbon on the occurrence of grain boundary serration in an AISI 316 stainless steel during aging heat treatment," *Mater. Lett.*, vol. 59, no. 11, pp. 1439–1443, May 2005.

- [102] R. Jones, V. Randle, and G. Owen, "Carbide precipitation and grain boundary plane selection in overaged type 316 austenitic stainless steel," *Mater. Sci. Eng. A*, vol. 496, no. 1–2, pp. 256–261, Nov. 2008.
- [103] C. W. Forsberg, P. F. Peterson, and P. S. Pickard, "Molten-Salt-Cooled Advanced High-Temperature Reactor for Production of Hydrogen and Electricity," in *Nuclear Technology, American Nuclear Society*, 2003, pp. 1–25.
- [104] D. F. Williams, "Assessment of candidate molten salt coolants for the NGNP-NHI heat-transfer loop, ORNL-TM-2006/69," 2006.
- [105] L. S. Richardson, D. E. Vreeland, and W. D. Manly, "Corrosion by molten fluorides, ORNL-1491," 1953.
- [106] H. E. McCoy and B. McNabb, "Intergranular cracking of INOR-8 in the MSRE, ORNL-4829," 1972.
- [107] K. R. Peters, D. P. Whittle, and J. Stringer, "Oxidation and hot corrosion of nickel-based alloys containing molybdenum," *Corros. Sci.*, vol. 16, pp. 791–804, 1976.
- [108] R. Weiju, D. F. Wilson, G. Muralidharan, and D. E. Holcomb, "Considerations of Alloy N for fluoride salt-cooled high-temperature reactor applications," in *ASME 2011 Pressure Vessels and Piping Division Conference*, 2011, pp. 1–12.
- [109] G. Zheng, B. Kelleher, G. Cao, K. Sridharan, M. Anderson, and T. Allen, "Investigation of 2LiF-BeF₂ (FLiBe): Salt Transfer, Corrosion Tests and Characterization," in *Transactions of the American Nuclear Society*, 2013, vol. 109, pp. 259–260.
- [110] V. Shankar, K. Bhanu Sankara Rao, and S. L. Mannan, "Microstructure and mechanical properties of Inconel 625 superalloy," *J. Nucl. Mater.*, vol. 288, no. 2–3, pp. 222–232, Feb. 2001.
- [111] Y. G. Gogotsi and R. A. Andrievski, *Materials science of carbides, nitrides and borides*. Gogotsi1998, 1998.
- [112] A. Paul, J. Lim, K. Choi, and C. Lee, "Effects of deposition parameters on the properties of chromium carbide coatings deposited onto steel by sputtering," *Mater. Sci. Eng. A*, vol. 332, no. 1–2, pp. 123–128, Jul. 2002.
- [113] S. Gomari and S. Sharafi, "Microstructural characterization of nanocrystalline chromium carbides synthesized by high energy ball milling," *J. Alloys Compd.*, vol. 490, no. 1–2, pp. 26–30, Feb. 2010.
- [114] A. Zikin, I. Hussainova, C. Katsich, E. Badisch, and C. Tomastik, "Advanced chromium carbide-based hardfacings," *Surf. Coatings Technol.*, vol. 206, no. 19–20, pp. 4270–4278, May 2012.
- [115] H. Wang, Z. Wang, and S. Chen, "Preparation of molybdenum carbides with multiple morphologies using surfactants as carbon sources," *J. Solid State Chem.*, vol. 194, pp. 19–22, Oct. 2012.
- [116] P. Xiao, Y. Yan, X. Ge, Z. Liu, J.-Y. Wang, and X. Wang, "Investigation of molybdenum carbide nano-rod as an efficient and durable electrocatalyst for hydrogen evolution in acidic and alkaline media," *Appl. Catal. B Environ.*, vol. 154–155, pp. 232–237, Jul. 2014.
- [117] F.-Y. Ouyang, C.-H. Chang, B.-C. You, T.-K. Yeh, and J.-J. Kai, "Effect of moisture on corrosion of Ni-based alloys in molten alkali fluoride FLiNaK salt environments," *J. Nucl. Mater.*, vol. 437, no. 1–3, pp. 201–207, Jun. 2013.
- [118] B. S. Berry, "Diffusion of carbon in nickel," *J. Appl. Phys.*, vol. 44, no. 8, p. 3792, 1973.

- [119] P. Calderoni, P. Sharpe, H. Nishimura, and T. Terai, "Control of molten salt corrosion of fusion structural materials by metallic beryllium," *J. Nucl. Mater.*, vol. 386–388, pp. 1102–1106, Apr. 2009.
- [120] D. R. Holmes, "New corrosion-resistant high temperature heat exchanger materials," *Corros. Sci.*, vol. 8, no. 8, pp. 603–622, 1968.
- [121] H. J. White, "Haynes International Capabilities: HASTELLOY N alloy, ORNL," HAYNESS, International, 2010.
- [122] L. Tan, X. Ren, K. Sridharan, and T. R. Allen, "Corrosion behavior of Ni-base alloys for advanced high temperature water-cooled nuclear plants," *Corros. Sci.*, vol. 50, no. 11, pp. 3056–3062, Nov. 2008.
- [123] A. Das, P. C. Chakraborti, S. Tarafder, and H. K. D. H. Bhadeshia, "Analysis of deformation induced martensitic transformation in stainless steels," *Mater. Sci. Technol.*, vol. 27, no. 1, pp. 366–370, Jan. 2011.
- [124] B. R. Kumar, A. K. Singh, B. Mahato, P. K. De, N. R. Bandyopadhyay, and D. K. Bhattacharya, "Deformation-induced transformation textures in metastable austenitic stainless steel," *Mater. Sci. Eng. A*, vol. 429, no. 1–2, pp. 205–211, Aug. 2006.
- [125] T. Y. Xing, X. W. Cui, W. X. Chen, and R. S. Yang, "Synthesis of porous chromium carbides by carburization," *Mater. Chem. Phys.*, vol. 128, no. 1–2, pp. 181–186, Jul. 2011.
- [126] P. J. Maziasz, "Overview of microstructural evolution in neutron-irradiated austenitic stainless steels," *J. Nucl. Mater.*, vol. 205, pp. 118–145, 1993.
- [127] R. P. Agarwala, M. C. Naik, M. S. Anand, and A. R. Paul, "Diffusion of carbon in stainless steel," *J. Nucl. Mater.*, vol. 36, pp. 41–47, 1970.
- [128] H. Sahlaoui, K. Makhoulf, H. Sidhom, and J. Philibert, "Effects of ageing conditions on the precipitates evolution, chromium depletion and intergranular corrosion susceptibility of AISI 316L: experimental and modeling results," *Mater. Sci. Eng. A*, vol. 372, no. 1–2, pp. 98–108, May 2004.
- [129] Y. F. Yin and R. G. Faulkner, "Model predictions of grain boundary chromium depletion in Inconel 690," *Corros. Sci.*, vol. 49, pp. 2177–2197, 2007.
- [130] M. Matula, L. Hyspecka, M. Svoboda, V. Vodarek, C. Dagbert, J. Galland, Z. Stonawska, and L. Tuma, "Intergranular corrosion of AISI 316L steel," *Mater. Charact.*, vol. 46, no. 2–3, pp. 203–210, Feb. 2001.
- [131] C. Hu, S. Xia, H. Li, T. Liu, B. Zhou, W. Chen, and N. Wang, "Improving the intergranular corrosion resistance of 304 stainless steel by grain boundary network control," *Corros. Sci.*, vol. 53, no. 5, pp. 1880–1886, May 2011.
- [132] M. Kondo, T. Nagasaka, A. Sagara, N. Noda, T. Muroga, Q. Xu, M. Nagura, A. Suzuki, and T. Terai, "Metallurgical study on corrosion of austenitic steels in molten salt LiF–BeF₂ (Flibe)," *J. Nucl. Mater.*, vol. 386–388, pp. 685–688, Apr. 2009.